

# Liquid phase *in situ* spectroscopic investigations of heterogeneous catalysts

Présentée le 6 novembre 2020

à la Faculté des sciences de base  
Groupe Kröcher  
Programme doctoral en chimie et génie chimique

pour l'obtention du grade de Docteur ès Sciences

par

**Thibault Xavier Florian FOVANNA**

Acceptée sur proposition du jury

Prof. H. Girault, président du jury  
Prof. O. Kröcher, Dr D. Ferri, directeurs de thèse  
Prof. E. C. Groppo, rapporteuse  
Prof. T. Bürgi, rapporteur  
Prof. V. Tileli, rapporteuse



“Cerca trova”

*Palazzo Vecchio – Firenze*

“Fluctuat nec mergitur”





# Acknowledgements

I would like to deeply thank Prof. Oliver Kröcher for giving me the opportunity to do my PhD in his lab.

The extent of the results obtain during the thesis would not have been so great with the supervision of Dr. Davide Ferri and Dr. Maarten Nachtegaal.

I am gratefull for the time, patience and amazing work provided by Marcel Hottiger in the workshop. Without him, the setup and cells would have remained drawings on paper.

I have to thank Martin Elsener for his help in the lab and his shared knowledge. Also thanks to him, I started jogging.

Dr. Ivo Alxneit is the longest office mate I had here at PSI and so far. Many thanks to his dayly greetings and farwell. Always a please to talk about science, music and art with you.

When I started my PhD, I could not have had a better team to start, Adrian, Andrey, Patrick, thanks to you three for taking me under your care and sharing your experience at all the levels, you guys truly are diamonds! Also on the otherside of the river, knowledge, help, advices from Jerick, Julia, Valentina and René was very precious. Many thanks to Jerick and Julia for the beamtimes spent together.

Then the new generation of the ACS group that arrived, starting with Rob, Maneka, Adam, Miren, Fillipo, Dominik, Tanja. You have been all an amazing group.

Then there are the friends, Christopher, Erich, Andreas, with who daily complains and happiness were shared around a beer or some Glühwein. I am particularly gratefull to Dr. Christophe Baranowski with whom I have travelled and collaborated he is the best!

I want to give a special thank you to two people who are at the origin of this thesis. Francis Perritaz, who allowed me to make my frist, steps as a lab technician in chemistry. Dr. Pietro Tanasini, who showed me the way of going further and put the seed of going further. To both of you, thank you.

I also want to thank my family, my mother and brother. My grand mother, my father. My grands father who always acted as my lawer and believed in me.



# Abstract

The development and combination of spectroscopic methods at the solid-liquid interface is a key challenge in order to allow effective improvement of new heterogeneous catalytic processes. Since we are facing climate changes, ecology concerns raising awareness about how resources are used, processed, recycled and that feedstock or raw material provenance is also becoming a concern, new routes of producing chemicals are explored so that we could achieve sustainable economy without compromising on quality and technological advances. Synthesis of bulk, fine chemicals often involve a catalytic step with some of them occurring at the solid-liquid interface. Biomass valorization heavily relies on catalytic reactions in a solvent medium thus in order to improve these processes and allow upscaling, development of adequate catalytic materials is crucial. The rational development of such materials is achieved by trial and error or structure-activity investigations which allow to better understand the crucial catalytic properties of the newly synthesized material.

Structure-activity studies are often conducted *in situ* by investigation of the material with a chosen physico-chemical method, while the desired reaction is taking place at the surface of the catalyst. If in addition, the activity and selectivity of the reaction are assessed simultaneously, the experiment is labeled under the term *operando*. To perform such studies, the right tools and methods have to be available to the researchers. For this purpose, three spectroscopic cells and a setup were developed and are presented to make such tools accessible to the scientific community for studies of catalytic solid-liquid-gas interfaces at temperature as high as 180°C and pressure as high as 16 bar. The combination of vibrational spectroscopy, specifically attenuated total infrared spectroscopy (ATR-IR) with X-ray absorption spectroscopy (XAS) was chosen in order to obtain a larger picture with most versatile methods for such investigations.

The work is structured as follow:

Chapter 1 covers a brief introduction on the applications of heterogeneous catalysis for biomass valorization, a fundamental overview of IR spectroscopy, ATR-IR, XAS, X-rays diffraction (XRD) and temperature programmed reduction (TPR) with relevant resources from scientific literature as an overview of the existing knowledge in each field.

In chapter 2 the spectroscopic cells developed and utilized for the investigations in this project, together with a dedicated setup allowing performing *in situ* experiments to study solid-liquid-gas interfaces at elevated pressures and temperatures.

Chapter 3 covers the investigation of PdO nanoparticles (NP) supported on Al<sub>2</sub>O<sub>3</sub> during *in situ* reduction by hydrogen in cyclohexane solvent and the mechanistic outcomes from this study by the combination of XAS/XRD/ATR-IR. This study revealed the stepwise reduction process of conversion of PdO to Pd further reduced to PdH. In depth, analysis of the XAS data allowed investigating the mechanism involved in both reactions, which lead to the conclusion that PdO reduction was following a nucleation mechanism, while PdH formation is occurring via the shrinking core mechanism.

In chapter 4 is described the *in situ* quantification of PdH phase during furfural hydrogenation over a commercial Pd/Al<sub>2</sub>O<sub>3</sub> material was investigated by the combination of TPR experiments performed (i) in the lab and (ii) at the synchrotron. Kinetics of PdH consumption could be quantified *in situ* in a solvent medium. Analysis of the data by combination of multivariate curve resolution alternating least square (MCR-ALS) and linear combination fitting (LCF) allowed to follow, during furfural transient pulse, the behavior of four Pd phases; PdO, Pd, PdH and PdC.

Chapter 5 covers the development of a novel material, supported Ru nanoparticles on Al<sub>2</sub>O<sub>3</sub> promoted with P loading. This material was tailored for the catalytic transfer hydrogenation of furfural. Characterization of the material showed that promotion with phosphorus of the Ru/Al<sub>2</sub>O<sub>3</sub> lead to smaller Ru NP, introduction of Brønsted sites and greater stability of the material towards Ru leaching. It is demonstrated how *in situ* ATR-IR and XAS are efficient techniques for investigation of the structure-activity relationship for material development.

Chapter 6 demonstrates the application of modulation excitation (ME) combined with phase sensitive detection (PSD) and ATR-IR. The study was conducted over a zeolite material for the synthesis of polyoxymethylene ethers, which is a promising fuel for diesel engines. Competition for active sites between the reactants and water, which prevents the adsorption of trioxane on the Brønsted sites thus driving the reaction to proceed via a less preferred mechanism leading to slower kinetics.

**Keywords:** solid-liquid interface, X-ray absorption spectroscopy, attenuated total reflection infrared spectroscopy, X-ray diffraction, transient investigation, modulation excitation

# Résumé

Le développement et la combinaison de méthodes spectroscopiques à l'interface solide-liquide est un défi majeur afin de permettre une amélioration efficace de nouveaux processus catalytiques hétérogènes. Étant donné que nous sommes confrontés aux changements climatiques, l'écologie concerne la sensibilisation à la manière dont les ressources sont utilisées, traitées, recyclées et que la provenance des matières premières ou des matières premières devient également une préoccupation, de nouvelles voies de production de produits chimiques sont explorées afin que nous puissions parvenir à une économie durable sans compromettre qualité et avancées technologiques. La synthèse de produits chimiques fins en vrac implique souvent une étape catalytique, certains d'entre eux se produisant à l'interface solide-liquide. La valorisation de la biomasse repose fortement sur des réactions catalytiques en milieu solvant donc pour améliorer ces procédés et permettre une mise à l'échelle, le développement de matériaux catalytiques adéquats est crucial. Le développement rationnel de ces matériaux est réalisé par essais et erreurs ou études de structure-activité qui permettent de mieux comprendre les propriétés catalytiques cruciales du matériau nouvellement synthétisé.

Les études de structure-activité sont souvent menées in situ par investigation du matériau avec une méthode physico-chimique choisie, tandis que la réaction souhaitée se déroule à la surface du catalyseur. Si en plus, l'activité et la sélectivité de la réaction sont évaluées simultanément, l'expérience est étiquetée sous le terme *operando*. Pour réaliser de telles études, les bons outils et méthodes doivent être mis à la disposition des chercheurs. A cet effet, trois cellules spectroscopiques et un montage ont été développés et sont présentés pour rendre ces outils accessibles à la communauté scientifique pour des études d'interfaces catalytiques solide-liquide-gaz à une température aussi élevée que 180 ° C et une pression aussi élevée que 16 bars. La combinaison de la spectroscopie vibrationnelle, spécifiquement la spectroscopie infrarouge totale atténuée (ATR-IR) avec la spectroscopie d'absorption des rayons X (XAS) a été choisie afin d'obtenir une image plus grande avec les méthodes les plus polyvalentes pour de telles enquêtes.

Le travail est structuré comme suit:

Le chapitre 1 couvre une brève introduction sur les applications de la catalyse hétérogène pour la valorisation de la biomasse, un aperçu fondamental de la spectroscopie IR, ATR-IR, XAS,

diffraction des rayons X (XRD) et la réduction programmée en température (TPR) avec des ressources pertinentes de la littérature scientifique comme un aperçu des connaissances existantes dans chaque domaine.

Dans le chapitre 2, les cellules spectroscopiques développées et utilisées pour les investigations de ce projet, avec une configuration dédiée permettant d'effectuer des expériences in situ pour étudier les interfaces solide-liquide-gaz à des pressions et des températures élevées.

Dans le chapitre 3 couvre l'étude des nanoparticules de PdO (NP) supportées sur  $\text{Al}_2\text{O}_3$  pendant la réduction in situ par l'hydrogène dans le solvant cyclohexane et les résultats mécanistes de cette étude par la combinaison de XAS / XRD / ATR-IR. Cette étude a révélé le processus de réduction par étapes de la conversion de PdO en Pd encore réduit en PdH. En profondeur, l'analyse des données XAS a permis d'étudier le mécanisme impliqué dans les deux réactions, ce qui a conduit à la conclusion que la réduction de PdO suivait un mécanisme de nucléation, tandis que la formation de PdH se produit via le mécanisme de rétrécissement du noyau.

Dans le chapitre 4, la quantification in situ de la phase PdH au cours de l'hydrogénation furfurale sur un matériau commercial Pd /  $\text{Al}_2\text{O}_3$  a été étudiée par la combinaison d'expériences TPR réalisées (i) en laboratoire et (ii) au synchrotron est décrite. La cinétique de la consommation de PdH a pu être quantifiée in situ en milieu solvant. L'analyse des données par combinaison de résolution de courbe multivariée alternant les moindres carrés (MCR-ALS) et l'ajustement de combinaison linéaire (LCF) a permis de suivre, pendant l'impulsion transitoire, le comportement de quatre phases Pd; PdO, Pd, PdH et PdC.

Le chapitre 5 couvre le développement d'un nouveau matériau, des nanoparticules de Ru supportées sur  $\text{Al}_2\text{O}_3$  promues avec une charge P. Ce matériau a été conçu pour l'hydrogénation par transfert catalytique du furfural. La caractérisation du matériau a montré que la promotion avec le phosphore du Ru /  $\text{Al}_2\text{O}_3$  conduit à des NP de Ru plus petits, à l'introduction de sites de Brønsted et à une plus grande stabilité du matériau vis-à-vis de la lixiviation du Ru. Il est démontré que les ATR-IR et XAS in situ sont des techniques efficaces pour étudier la relation structure-activité pour le développement de matériaux.

Le chapitre 6 montre l'application de l'excitation par modulation (ME) combinée à la détection sensible à la phase (PSD) et à l'ATR-IR. L'étude a été menée sur un matériau zéolitique pour la synthèse d'éthers de polyoxméthylène, qui est un carburant prometteur pour les moteurs

diesel. Compétition pour les sites actifs entre les réactifs et l'eau, qui empêche l'adsorption du trioxane sur les sites de Brønsted forçant la réaction à se dérouler via un mécanisme moins préféré conduisant à une cinétique plus lente.

Mots-clés : interface solide-liquide, spectroscopie d'absorption de rayons-X, réflectance totale atténuée, diffraction des rayons-X, méthodes transientes, spectroscopie de modulation du signal





# Contents

<b>Abstract</b>	<b>vii</b>
<b>Contents</b>	<b>xiii</b>
<b>1. Introduction</b>	<b>15</b>
1.1. Context	16
1.2. X-ray absorption spectroscopy	19
1.3. Attenuated total reflectance infrared spectroscopy	20
1.4. X-ray diffraction	21
1.5. Modulation excitation and phase sensitive detection	22
1.6. Temperature programmed reduction	24
1.7. Scope of the thesis	24
<b>2. Spectroscopic cells and setup</b>	<b>27</b>
2.1. Introduction	28
2.2. XAS/XRD cell	29
2.3. Tandem cell	33
2.4. Setup	39
<b>3. Investigation of PdO reduction in liquid phase</b>	<b>41</b>
3.1. Introduction	42
3.2. Experimental	43
3.3. Results and discussion	45
3.4. Conclusion	53
<b>4. In situ quantification of PdH</b>	<b>55</b>
4.1. Introduction	56
4.2. Experimental	57
4.3. Results and discussion	60
4.4. Conclusion	70
<b>5. RuP</b>	<b>71</b>
5.1. Introduction	72
5.2. Experimental	73
5.3. Results and discussion	76
5.4. Conclusion	85
<b>6. OME</b>	<b>87</b>
6.1. Introduction	88
6.2. Experimental	91
6.3. Results and discussion	94
6.4. Conclusion	109

<b>7. Conclusions and outlook</b>	<b>111</b>
<b>Appendices</b>	<b>115</b>
<b>List of references</b>	<b>134</b>
<b>List of contribution</b>	<b>147</b>
<b>Curriculum Vitae</b>	<b>149</b>

# Chapter 1: Introduction

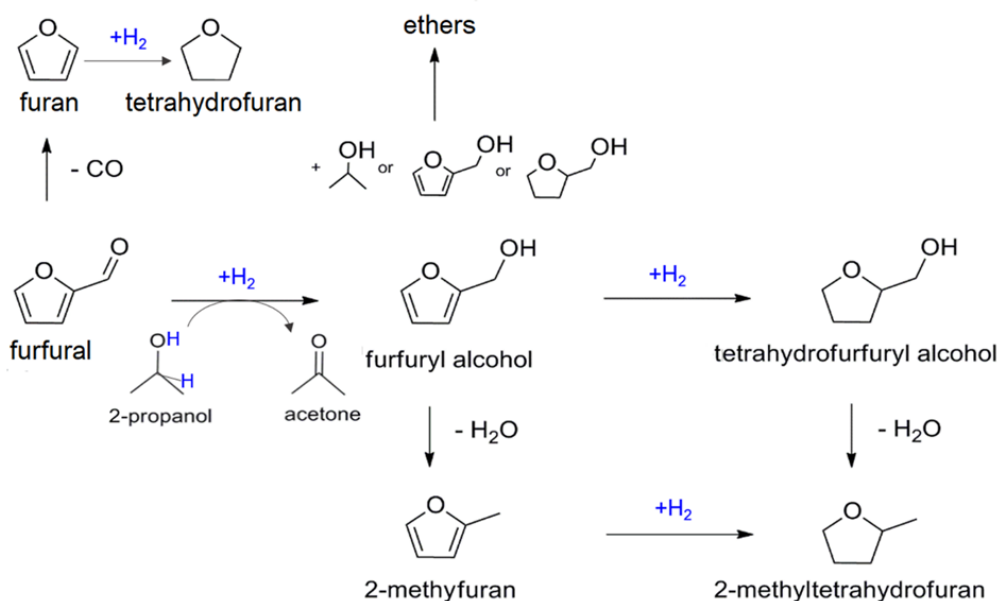
## 1.1 Context

Numerous valuable processes relevant to nature and technologic applications take place at solid-liquid interfaces. Enzymatic reactions, production of fine and bulk chemicals, electrochemistry among other involve such interface. There, fundamental understanding can help improving the process.<sup>1</sup> With challenges such as climate change, energy production and aging of population, the demand for the production of fuels, chemicals is under constant pressure to meet economical and societal requirements. Both fine and bulk chemical industries together with energy production rely mostly on fossil resources as feedstock. The environmental changes implicated with the use of such feedstock, sustainable substitutes are explored.

Biomass is an ecological alternative source chemicals and fuels. However, due to the diversity of biomasses and the complex transformations necessary to obtain pure chemicals new processes are required. The biomass sources are multiple such as wood based, aquatic, animal or human biomass wastes and even their combination.<sup>2</sup> The range of chemicals that can be obtained is as diverse as the heterogeneity of the sources. Conversion of biomass is categorized into three classes; bio-catalytic process, chemo-catalytic process and chemical modifications of biopolymers. Each leads to a different range of products, platform molecules, pool of molecules or functional biopolymers. The final products can find applications from fine chemical synthesis to bulk chemical such as surfactants and additives.<sup>3,4</sup> In this work, we will focus on solid-liquid interface spectroscopic and diffraction investigations of value added chemicals obtained from biomass, such as furfural and polyoxymethylene dimethyl ethers, which undergo catalytic transformation on solid catalysts in liquid phase.

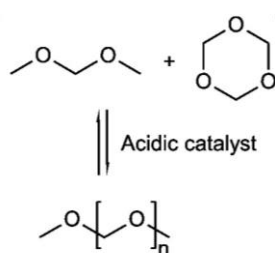
Furfural is an example of a building block from hemicellulose-derived pentoses, which can be transformed into various compounds of industrial interest.<sup>5</sup> The hydrogenation of furfural can proceed along several pathways leading to various useful chemicals such as tetrahydrofuran, furan, 2-methylfuran and furfuryl alcohol (**Scheme 1.1**).<sup>6</sup> The latter is the result of a selective single-step reduction of the carbonyl group of furfural and is a key intermediate in the production of lysine, ascorbic acid (vitamin C), polymers, synthetic fibers, rubbers, resins and lubricants.<sup>7</sup> The conventional catalytic hydrogenation process currently used for producing furfuryl alcohol requires high temperature (130-200°C) and pressure (up to 30 bar) and toxic elements, i.e. copper chromite.<sup>8</sup> Therefore, the development of heterogeneous catalytic

processes operating under milder conditions and with less-toxic elements remains a priority to achieve a more sustainable industrial process.



**Scheme 1.1.** Reaction pathways for the catalytic hydrogenation of furfural.

Polyoxymethylene dimethyl ethers (OME) have recently gained attention as substitute of Diesel. Their soot-free combustion produces cleaner exhaust emissions. They can be produced from methanol, a biomolecule. However the reaction shows best conversions when the OME are produced from trioxane with dimethoxymethane on an acid catalyst (**Scheme 1.2**). Zeolite H-Beta has been evaluated as the most performant material. However, the reaction suffers from the presence of water, found as an impurity in the reactants or as a by-product; the kinetics are greatly slowed but no further investigations have been conducted.<sup>9</sup>



**Scheme 1.2.** Reaction equation of OME synthesis.

The level of complexity of the catalytic system increases in liquid phase reactions due to additional mutual interactions when compared a to solid-gas phase system. As shown in **Figure 1.1**, the additional component with respect to the gas phase, the solvent, might interact with all other components, i.e. the metal nanoparticle, the metal oxide support, the reactant (furfural) and the dissolved gas (hydrogen). The solvent might also affect the intermediate species of a given chemical reaction.<sup>10</sup> The presence of a liquid does not interfere significantly

with X-ray absorption spectroscopy (XAS) measurements because the solvent is mostly transparent to high energy photons. On the other hand, addition of the solvent introduces higher complexity in studies with vibrational spectroscopy, because of the strong absorption of the IR radiation. Thus overlapping with the spectral region of the adsorbed species, causing challenges in the observation and identification of the latter. Finally, because the solvent interacts with the dispersed metal phase, the solvent can become a reducing agent in certain cases, such as 2-propanol.

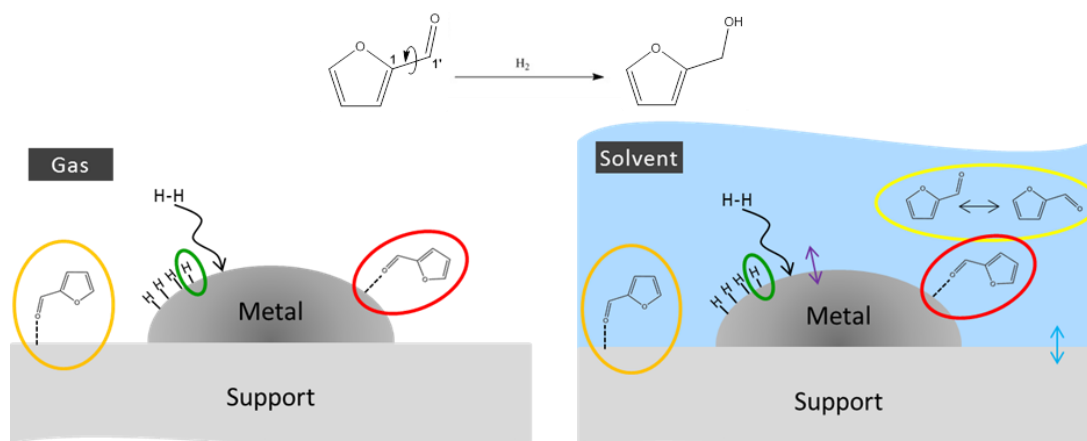


**Figure 1.1:** Interactions present in gas phase (left) and liquid phase (right). Furfural hydrogenation is taken as example. Interactions are highlighted in purple arrow: solvent-metal, blue arrow: solvent-support, green: hydrogen-metal, yellow: furfural-solvent, orange: furfural-support, red: furfural-metal.

The interpretation of catalytic processes and material properties is heavily enhanced by *in situ* or *operando* studies leading to fundamental understanding of the structure of the material under reaction conditions. However, interpretations of the data and results obtained from such investigations are often hampered by the complex data, especially in the case of vibrational studies. Untangling the contribution from the solvent, the reactant, the support and spectator species to observe intermediate or adsorbate species can become a very complex task. Transient experiment, where the reactive system is observed not under steady state conditions but while reacting to a stimulus, can facilitate such investigations.

To study and understand heterogeneous catalytic processes, a combination of techniques is often required.<sup>11–13</sup> To probe reactions at the solid-liquid interface, it was chosen to combine XAS with attenuated total reflection infrared spectroscopy (ATR-IR). The combination of vibrational spectroscopy with XAS has already proven a powerful combination, both for solid-gas and solid-liquid interface investigations due to the complementarity of the two techniques.<sup>14</sup>

## 1.2 X-ray absorption spectroscopy

X-ray absorption spectroscopy is an element specific bulk technique that yields information about the local structural and compositional environment of an absorbing atom. It is a short range method that probes from the first up to the second or third coordination shell of neighboring atoms. Knowledge about the oxidation state, bond distances, coordination number and geometry and nature of the surrounding atoms can be obtained.<sup>15</sup> The presence of a liquid does not interfere significantly with X-rays of high energy due to the great penetration depth therefore the solvent is mostly transparent during the measurement.

The interaction of X-rays photons with the energy matching the one of a core electron, the latter is then expelled to become a photo-electron and creating a vacancy, which is then filled by an electron from a higher energy level and emission of X-rays photons can be observed.

The absorption of X-rays follows the Lambert-Beer law:

$$I_t = I_0 e^{-\mu d} \quad \text{Eq. 1.3}$$

where  $I_t$  and  $I_0$  are the transmitted and incident beam intensities,  $d$  is the beam path through the sample and  $\mu$  is the absorption coefficient.

XAS spectra can be separated in two regions. The X-ray near edge structure (XANES) and the extended X-ray absorption fine structure (EXAFS). Below the absorption edge, the pre-edge is found.

The oxidation state is the main information that can be deduced from the XANES. Oxidation states of an element are characterized by the edge position, shifting to higher energies while increasing the oxidation state will induce the white line features. The white line is one of the first very intense wiggle just after the edge. The white line intensity is also correlated with the oxidation state and the nature of the atoms surrounding the absorber element. Information about the nature of the surrounding atoms are also present in the XANES, since this part of the spectrum is the signature of electronic transition of the electron to the empty states. Therefore, if the core atom is bound to an electronic donating or withdrawing group, the shape of the white line will be affected. Consequently, it is possible to differentiate between the various ligands. Usually, analysis of the XANES can be performed by linear combination fitting. It is even possible to quantify the proportion of each reference in a sample, by collecting spectra of reference compounds with known ligands, oxidation state, conformation.

Due to the high energies of the X-rays photons, XAS benefits from a high penetration through materials, while working at K-edges. L-edge would provide more surface level information. However, energy levels of the L-edge photons are not suited for experimental constraints for *in situ* investigations.

XAS has been widely applied for the investigations of various catalytic systems both for solid-gas and solid-liquid interfaces.<sup>14,16</sup>

### 1.3 Attenuated total reflectance infrared spectroscopy

Attenuated total reflectance infrared spectroscopy (ATR-IR) is characterized by the use of an Internal Reflective Element (IRE) with a high refractive index, which acts as an infrared carrier; common materials used as IRE are reported in **Table 1.1**.

**Table 1.1:** most common material used as IRE

Material	Refractive index ( $n_{\text{IRE}}$ )	Limitations/properties
Diamond (C)	2.42	Expensive
Zinc selenide (ZnSe)	2.42	Limited to pH between 5 and 9
Silicon (Si)	3.45	Not transparent below 1500 $\text{cm}^{-1}$ , not suitable for pH above 12
Germanium (Ge)	4.0	Fragile, max 150°C
KRS-5 (Thallium bromo-iodide)	2.35	Fragile, toxic, soluble in bases

Total internal reflection is achieved when radiations propagate in an optically dense medium ( $n_{\text{IRE}}$  = refractive index of the IRE) and reaches an optically rare medium ( $n_{\text{sample}}$  = refractive index of the sample environment) at an angle of incidence ( $\theta$ ) greater than the critical angle ( $\theta_c$ ) as shown in **Figure 1.2**. This produces an evanescent electromagnetic field ( $E$ ), that is generated into the sample, whose amplitude decreases exponentially from the surface ( $z$ ) as shown in Eq 1.1:

$$E = E_0 e^{-z/d_p} \quad \text{Eq. 1.1}$$

where  $E_0$  corresponds to the amplitude of the electric field at the interface. The penetration depth ( $d_p$ ) is defined as the distance required to decrease the electric field amplitude to  $e^{-1}$  (Eq 1.2):



$$d_p = \frac{\lambda}{n_{IRE} 2\pi \sqrt{\sin^2 \theta - \left(\frac{n_{sample}}{n_{IRE}}\right)^2}} \quad \text{Eq. 1.2}$$

where  $\lambda$  the wavelength. Typical values for  $d$  are comprised between 0.1-5  $\mu\text{m}$ . Therefore, only a very small volume of the sample is probed. This makes the use of ATR-IR advantageous compared to transmission mode, especially when involving a solvent strongly absorbing in the IR range.

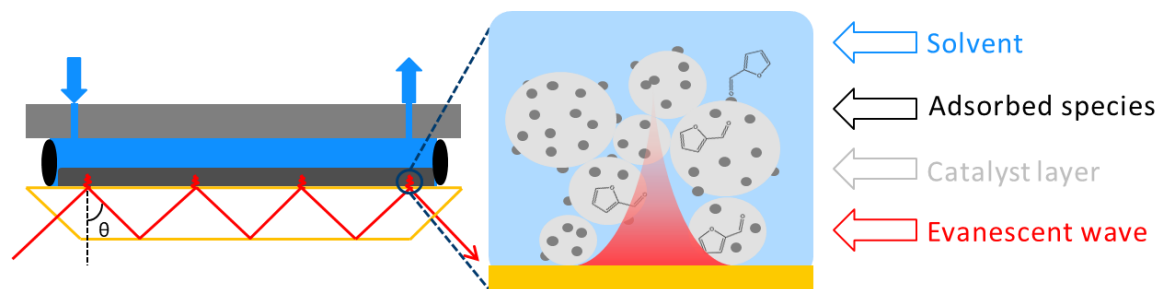


**Figure 1.2:** Principle of ATR-IR spectroscopy

ATR-IR is an established method for *in situ* studies at the solid-liquid interface.<sup>17–21</sup> Coordination of a molecule to a metal surface produces noticeable shifts of the fundamental vibrational modes in the IR spectrum with respect to the gas and liquid state.<sup>11,22–26</sup> Examples like benzyl alcohol oxidation or the Knoevenagel reaction demonstrated that the ATR-IR mode is suitable to identify adsorbed species at the surface of the catalyst in a liquid environment providing fundamental understanding of the reaction mechanisms.<sup>27,28</sup>

## 1.4 X-ray diffraction

X-ray diffraction (XRD) is the elastic scattering of X-rays photons by atoms in a periodic lattice producing constructive interference.<sup>29</sup> XRD patterns display the intensity of diffracted X-rays as a function of the scattering angle  $2\theta$ . Often in synchrotron light, the scattering vector length is used instead of  $2\theta$ :

$$Q = \frac{4\pi}{\lambda} \sin \theta \quad \text{Eq. 1.4}$$

where  $\lambda$  is the wavelength of the incident monochromatic light. Lattice structural parameters are derived by the Bragg law:

$$n\lambda = 2d \sin \theta \quad \text{Eq. 1.5}$$

where  $n$  is the order of the reflection,  $d$  the distance between two lattice planes.

In catalyst characterization, diffraction patterns are mainly used to identify the crystallographic phase present in the material and how these may change under exposure to reaction conditions. XRD is a long-range order method and require large arrangement of crystalline lattice. One parameter that is often of interest is the crystallite size, such as for supported nanoparticles, which can be deduced using the Scherrer equation<sup>30</sup>:

$$L = \frac{K\lambda}{\beta \cos \theta} \quad \text{Eq. 1.6}$$

where L is the particle size, K is a constant and  $\beta$  the full width at half maximum of the peak. However, if the material present too small crystallites regions or too disordered, diffraction pattern becomes irrelevant. The use of synchrotron radiation and high energy X-rays allows for narrow peaks and short time acquisition leading it to a suitable method for *in situ* investigations of catalytic materials because of the higher resolution and short time acquisition.<sup>31–33</sup>

## 1.5 Modulation excitation and phase sensitive detection

As a special type of transient experiment to investigate complex systems, modulation excitation (ME) spectroscopy is an established method for *in situ* investigation of solid catalysts. It is used to enhance signals responding to changes in the reaction environment.<sup>34–37</sup> This methodology eases the process of peaks attribution and evidence of adsorbate species. The principle is to stimulate the reactive environment by applying a periodic change (modulation) such as concentration, temperature, pressure, light, electric potential to the reactive system while monitoring the response of the system with the desired spectroscopy/diffraction technique. It is important that the system is reversible. The ME is employed, because by modulating the system several times, it allows to average the acquired signal, increasing the signal to noise ratio. This is a crucial step, since usually transition state and adsorbed molecules are either short lived or present in low concentration, as a consequence difficult to observe. Improving the signal quality by averaging, greatly improves the possibility to observe such species.

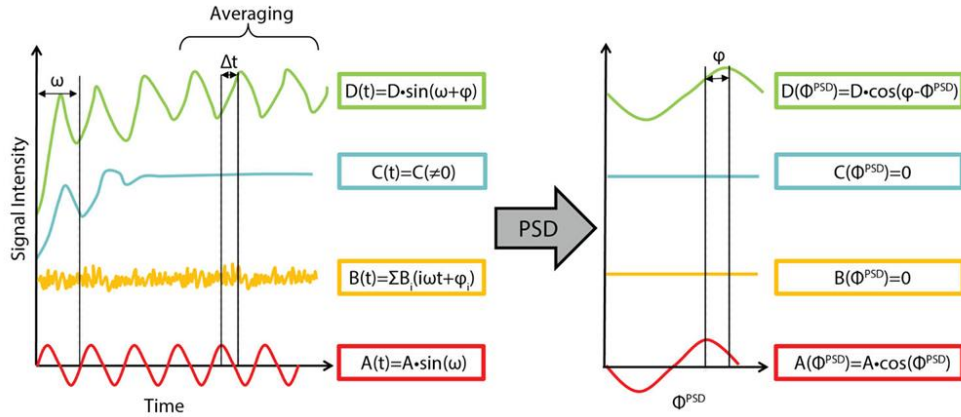


**Figure 1.3:** Principle of ME-PSD, illustration from ref <sup>38</sup>.

Phase sensitive detection is used in combination with ME. The information contained in a single spectrum is composed of the vibrational bands of the solvent, the reactant and the various adsorbed species on both the Pd nanoparticles and the  $\text{Al}_2\text{O}_3$  support. While we are interested specifically in the observation of the adsorption mode of furfural on the Pd nanoparticles. The data set is composed of spectra or diffractograms at different times within the modulation period (so called time-resolved). After averaging, the time-resolved data are processed through the PSD algorithm (Eq.1.7) transforming the data into the phase-domain or phase-resolved data.

$$A_k^{\varphi_k^{PSD}}(\nu) = \frac{2}{T} \int_0^T A(\nu, t) \sin(k\omega t + \varphi_k^{PSD}) dt \quad \text{Eq. 1.7}$$

Where  $T$  is the modulation period,  $A(\nu, t)$  the intensity of the signal as a function of wavenumber and time  $t$ ,  $\omega$  is the frequency of the external stimulation,  $n$  is the demodulation frequency and  $\varphi^{PSD}$  is the demodulation phase angle. The integer variable  $n = 1, 2, 3, \dots$  determines the frequency at which the time dependent signals are demodulated, for  $n = 1$  the demodulation frequency is equal to the stimulation frequency,  $n = 2, 3, \dots$  harmonic frequencies are obtained. The signal intensity in the phase-resolved data varies harmonically as  $\varphi^{PSD}$  varies between 0 and  $2\pi$ . The phase signal reaches the maximum amplitude when  $\varphi^{PSD}$  is equal to the phase lag  $\varphi$ . For a linear system, the demodulated response will be zero when  $n \neq 1$ . The advantage of the phase-resolved dataset is that it contains only the information about the components that respond to the external stimulation. Static signals like spectator species, the solvent, the support are cancelled as shown in **Figure 1.3**.<sup>34,38,39</sup>

## 1.6 Temperature programmed reduction

Temperature programmed reduction is nowadays a standard characterization method of catalytic material. The sample is heated under reducing atmosphere (usually hydrogen) and the consumption of reducing agent is followed as a function of temperature.<sup>40</sup> This measure allows to evaluate the reducibility of a material. In depth information can be obtained while changing the heating rate: shift of the maxima of temperature reduction as a function of heating rate allows to quantify the activation energy of reduction of a material. If it is possible to follow the reduction process under steady state conditions, the mechanisms of reduction can be determined. Two major mechanisms have been discussed in literature: the shrinking core model and the nucleation model.<sup>41</sup> This methodology can be applied *in situ* combined with spectroscopic methods such as XAS, and ATR-IR among others.

## 1.7 Scope of the thesis

The aim of the present thesis is to investigate processes taking place at catalytic solid-liquid interfaces using the complementary information of state-of-the-art spectroscopy and diffraction methods such as X-ray absorption spectroscopy (XAS), infrared spectroscopy and X-ray diffraction (XRD). The processes involving reduction, adsorption and reaction at metal nanoparticles, metal oxide supports and zeolitic materials will be followed *in situ* exploiting transient experiments in which the environment around the catalytic material is altered and with adequate time-resolution. In order to allow for such type of experiments, i.e. transient conditions and combination of complementary characterization techniques, technical development of suitable cells, employable under relevant temperature, pressure and flow conditions needs to be performed. Application of single-transient experiments in combination with chemometric methods and of multiple-transient experiments according to the paradigm of the modulation excitation method in combination with phase sensitive detection will allow to gain fundamental level understanding of such complex systems that goes beyond what is currently obtained in a liquid environment. Catalytic processes that are relevant for biomass conversion and sustainable chemistry have been selected, because the liquid environment is key to these systems.

When information from two complementary characterization techniques such as XAS and IR spectroscopy is combined, experiments are typically performed separately but especially with different cells that have been optimized for each technique. Repeating experiments in various

cells introduces bias such as temperature distribution along the catalyst bed and flow dynamics (residence time) variations that complicate the comparison of the independent datasets. Direct combination of the two techniques in a single spectroscopic cell enabling either a single experiment or repetition of exactly the same experiment at synchrotron facilities and in the laboratory provides an essential tool that allows direct combination of the complementary results.

Liquid phase furfural hydrogenation on metal-based heterogeneous catalysts is taken as the first main probe reaction. Because many aspects of the behavior of solid catalysts in liquid environment are largely unknown, a systematic study is performed aiming at following the structure of Pd/Al<sub>2</sub>O<sub>3</sub> catalysts in the main steps of the reaction, thus from reduction to reaction conditions.

A combination of *in situ* XAS and XRD will be exploited to study the reduction behavior of supported PdO nanoparticles prior to use in the catalysis. This elementary step will provide valuable insight in the capabilities of the two methods both in terms of achievable temporal resolution and data quality. The two methods are sensitive to the various Pd phases that can be in principle formed, PdO, metallic Pd, Pd hydrides and Pd carbide-like species. Identification of hydrides and differentiation from metallic Pd and carbide-like species is crucial using X-rays because these species may appear simultaneously in the whole process from catalyst reduction to reaction. The reactivity of this species is then equally crucial for the understanding of the catalytic process. Sufficient sensitivity of the spectroscopy/diffraction methods is required because we want to follow precisely the fate of these species in transient experiments requiring second to sub-second time-resolution. The use of chemometric methods such as multivariate curve resolution will allow to obtain for the first time the possibility to quantify the concentration of these species and follow their consumption during reaction, e.g. in the presence of furfural.

Coupling of XAS and ATR-IR for the investigation of furfural hydrogenation is carried out with the aim of gaining fundamental understanding of the interaction of furfural with supported metal nanoparticles. ATR-IR should provide the complementary information about coordination and reaction of furfural on supported nanoparticles under the reactive environment in the liquid phase. It should be mentioned that while the reaction is largely studied, mechanistic interpretation relying on *in situ/operando* experiments in liquid phase is still missing.

Furfural hydrogenation will be investigated also under catalytic transfer hydrogenation conditions on novel materials based on Ru/Al<sub>2</sub>O<sub>3</sub> modified with Phosphorous. The various spectroscopy/diffraction techniques will be used to obtain information on the role of Phosphorous on activity and stability of the modified catalyst compared to the standard Ru/Al<sub>2</sub>O<sub>3</sub> material.

Finally, in the second probe reaction, IR spectroscopy in the ATR mode will be used to explore the surface properties of Beta zeolite in the presence of the reactants used for OME synthesis and to determine the nature of the kinetic effect of water on this reaction. Vibrational spectroscopy on zeolites in liquid environment is rare, while in marked contrast it is state-of-the-art in gas phase catalytic processes. By this probe reaction, we aim at gaining both molecular view of the catalytic process but also at providing possibly novel molecular aspects of the behaviour of zeolites in the liquid environment. For this purpose, rather than conventional steady-state experiments, the material and the reaction will be explored by combining ATR-IR with modulation excitation and phase sensitive detection. This will provide enhanced spectroscopic data allowing us to interrogate at a molecular level the interaction of the zeolite active sites, silanols and Brønsted acid sites, with the reactants.

## Chapter 2: Spectroscopic cells and setup

## 2.1 Introduction

To acquire *in situ* or *operando* data on a catalytic system, two essential components are required: the spectroscopic cell or reactor and a setup. In this chapter, the three cells used in this work will be discussed, together with the setup that has been designed and built to fulfill the requirements for *in situ* and *operando* investigations at relevant temperatures and pressures for selected heterogeneous catalytic processes in continuous mode. Since transient methods (including modulation excitation) are precious to obtain knowledge on reactive intermediates, transition states and adsorbed species, fast switching of solutions, low dead volume and flow dynamics were considered as the main parameters for cell development.

The cell for X-rays was adapted from previous work.<sup>42,43</sup> This cell was chosen because it has been proven suitable for XAS and XRD experiments under gas phase conditions and it provides an accurate and stable temperature control and heat distribution within the catalyst bed. This property is not easily achievable with a capillary cell that is often used as continuous reactor while performing synchrotron light based experiments.<sup>44</sup> Here, adaptation to liquid phase operation is demonstrated.

The ATR-IR cell was manufactured based on the design extensively described in literature.<sup>45</sup> It was successfully tested for resistance to pressure up to 12 bar. Together with this cell a setup that has been reported in literature has also been used for some parts of the work and will not be further discussed in this chapter.

The tandem cell has been developed during this project. The design emerged from the aspiration to combine ATR-IR spectroscopy and XAS within one cell. This combination of techniques has previously been applied to cells designed for solid-gas interface studies while solid-liquid interface investigations but only in separated cells and reactors.<sup>12,27</sup> As often discussed when designing and employing a cell or reactor for a specific technique, biases in the measurements can be introduced that will affect the experiments and the reliability.<sup>44</sup> Therefore, having a unique cell that can be employed for both XAS and ATR-IR allows for a direct comparison of the results obtained with the two spectroscopic methods.

Finally, the setup designed to perform *in situ* and *operando* catalytic experiments under pressure will be presented at the end of this chapter. This setup has been designed in order to perform continuous liquid phase catalytic hydrogenation of furfural but can be adapted to other reactions involving gaseous chemical like oxygen, nitrogen or carbon monoxide or reaction



processes that would require reaction temperature above the boiling point of the solvent. In addition, the setup has been designed to perform modulation excitation under these conditions of temperature and pressure. It has to be specified that the flasks containing the reactive solutions can be pressurized up to 10 bar of gas pressure on the liquid and the reactive lines and components allow keeping the liquid under pressure to maintain the liquid phase and avoid separation of the gas and liquid. It is important to report that a major drawback of solid-liquid-gas systems is the extremely low concentration of the gas in the liquid phase, which leads to low reactant concentration and conversion during the catalytic transformations and limitations for the online detection methods.

## 2.2 XAS/XRD cell

### 2.2.1 Cell design

The cell presented in this section (**Figure 2.1**) has been originally developed and used for investigations of catalytic solid-gas interfaces,<sup>42,43</sup> and was adapted to experiments performed with a pressurized liquid in this work. The ring was modified and the internal hole was reduced to 1 mm diameter. Changing from graphite based windows to polytetrafluoroethylene (PTFE) windows (200  $\mu\text{m}$  thickness) allow operation at pressures up to 14 bar and temperatures as high as 180°C in a continuous liquid flow. PTFE was selected from a variety of window materials for its high photon transmission in the low energy region of X-rays (6-8 keV), its compatibility with a wide range of chemicals and its favorable mechanical properties. Additionally, the aperture in the aluminum back plate was increased to form a cone (included angle of 12,5°) to avoid interference with the acquisition of diffraction pattern.

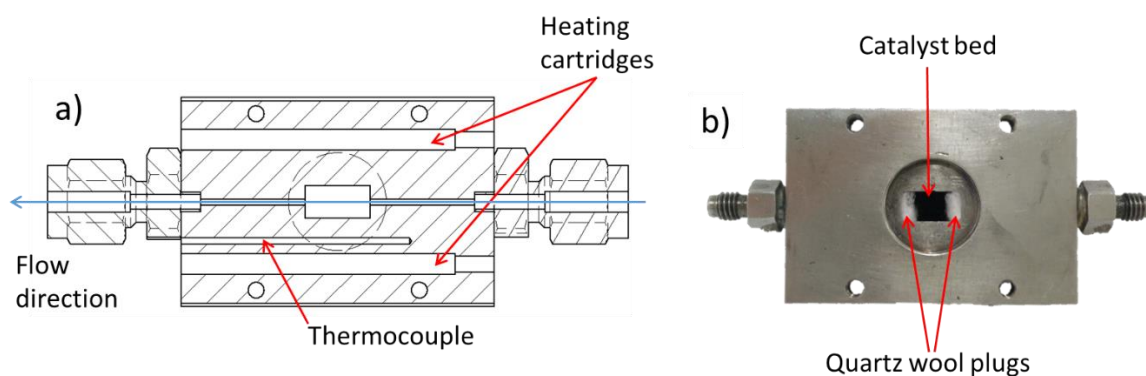


**Figure 1.1:** a) Drawing of the cross section of the XAS/XRD cell. b) Picture of the cell filled with catalyst and quartz wool plugs.

## 2.2.2 Description and characterization of the *in situ/operando* spectroscopic reactor

The transmission for X-rays photons of the PTFE windows and the effect of the window thickness were predicted using the online calculator of the Center for X-ray analysis.<sup>46</sup> The result of this evaluation is shown in **Figure 2.2a** for the energy range of 6-26 keV in which K and L<sub>3</sub>-edges of possible elements of interest are indicated. At the Pd K-edge a transmission of more than 87% is reached for a total window thickness of 800  $\mu\text{m}$ . The transmission increases to about 98% at a total window thickness of 200  $\mu\text{m}$ . At the Fe K-edge, however, the transmission is lower and much more affected by the window thickness: increasing the total window thickness from 200  $\mu\text{m}$  to 800  $\mu\text{m}$  decreases transmission from 45% to 4%, which would result in poor data quality in fast scanning (QEXAFS) measurements. As a compromise, a window thickness of 200  $\mu\text{m}$  (thick curve in **Figure 2.2a**) was chosen for this work. Other light element based materials such as Kapton, polyether ether ketone (PEEK) and graphite were also tested but failed to provide sealing at pressures above 5 bar.

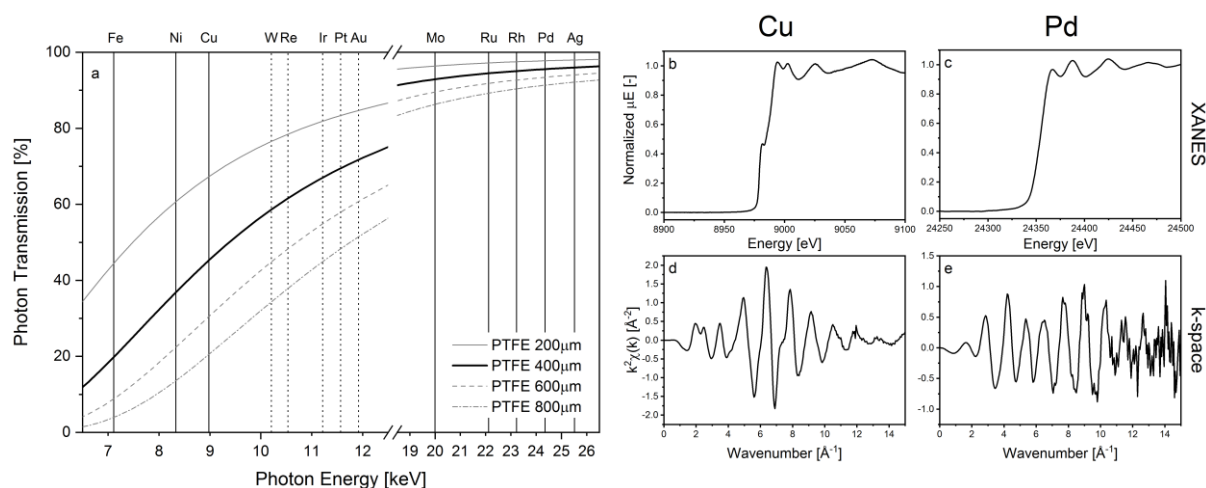


**Figure 2.2:** a) Modeled transmission of cell as function of the X-rays photon energy for different thickness of the windows. Positions of K-edges (straight solid line) and L<sub>3</sub>-edges (straight dotted lines) of typical elements of interest are indicated. XANES spectrum b) and k-space d) of 5 wt.% Cu/Al<sub>2</sub>O<sub>3</sub> at 50°C in 2-propanol. XANES spectrum c) and k-space e) of 5 wt.% Pd/Al<sub>2</sub>O<sub>3</sub> at 50°C in 2-propanol.

The quality of the XAS spectra that can be achieved does not only depend on the window transmission but also on the optical path length, concentration of the absorber, and, in the case of supported metal nanoparticles, on absorbance of the support itself. Experimental results for elements included the energy range (6.5 keV – 25 keV) of **Figure 2.2a** are reported in **Figure 2.2b-e**: Cu/Al<sub>2</sub>O<sub>3</sub> (5 wt.% Cu) and Pd/Al<sub>2</sub>O<sub>3</sub> (5 wt.% Pd) both measured in 2-propanol at 50°C. The XANES spectra acquired during 1 s and the corresponding k-space transformed data are reported as well. The spectrum at the Pd K-edge shows a well-defined

XANES region and an EXAFS region that can be used in a k-space up to at least 12 Å<sup>-1</sup>. According to the calculation shown in **Figure 2.2a**, at the Pd K-edge (24350 eV) data quality is mostly dictated by the optical path length, the metal loading and absorption of the photons by the alumina support. At lower photon energies exemplified by the Cu K-edge spectra, the total absorption from components other than the element of interest (windows, solvent, sample matrix or support) defines the quality of the spectra. Nevertheless, even at the Cu K-edge good quality data can be recorded using a k-space up to 12 Å<sup>-1</sup>.

### 2.2.3 Cell flow dynamics evaluation

The residence time distribution (RTD) of the empty and loaded cell were determined to verify its suitability as a plug flow reactor (PFR).<sup>47,48</sup> Toluene (1 M) in cyclohexane was used as tracer solution and its concentration profile was monitored by following the C=C stretch vibration at 1496 cm<sup>-1</sup> in a transmission infrared flow-cell (CaF<sub>2</sub> windows, 0.2 mm spacer) mounted in a Bruker Vertex 70 spectrometer equipped with a RT-DLaTGS detector. Spectra were recorded from 4000 cm<sup>-1</sup> and 400 cm<sup>-1</sup> continuously every 0.3 s, experiments were performed in triplicate and the tracer profile were averaged.

The peak intensity at 1496 cm<sup>-1</sup> h(t), corresponding to the C=C stretch of toluene, was selected as the indicator of the toluene concentration as a function of time. It is then used to calculate the RTD function E(t) according to:

$$E(t) = \frac{h(t)}{\int_0^{\infty} h(t) dt} \quad \text{Eq. 2.1}$$

from which the mean residence time  $\tau$  can be calculated as:

$$\tau = \int_0^{\infty} tE(t) dt \quad \text{Eq. 2.2}$$

Applying the dimensionless time  $\theta$ :

$$\theta = \frac{t}{\tau} \quad \text{Eq. 2.3}$$

to calculate the normalized RTD function:

$$E(\theta) = \frac{E(t)}{\tau} \quad \text{Eq. 2.4}$$

allows for easier comparison of RTDs with different mean residence times.

**Figure 2.3** shows the  $h(t)$  recorded at the outlet of the cell by infrared spectroscopy.  $h(t)$  increases or decreases fast after the switch. Steady state concentration of toluene is reached after 4 min while after switching off the toluene flow its concentration reaches zero after 5 min at a flow rate of 0.2 mL/min.  $h(t)$  observed is similar to what has been previously published when the unmodified cell was used to study solid-gas systems.<sup>42,43</sup> Thus, we expect the modified cell to be equally well suited for transient experiments and modulation-excitation experiments performed in solid-liquid systems.

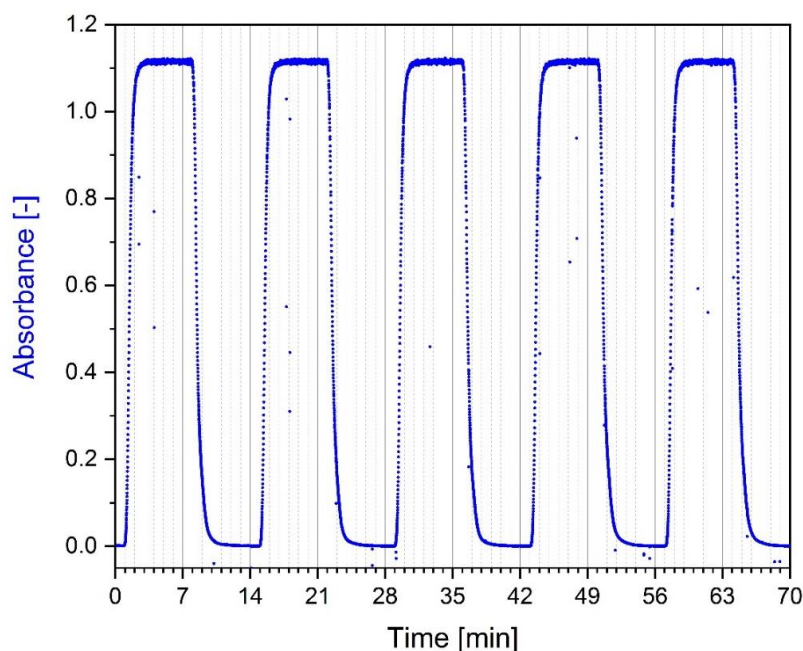


**Figure 2.3:** Concentration profile of toluene in the exiting solution by monitoring the  $1496\text{ cm}^{-1}$  band as a function of time in the spectroscopic cell filled with catalyst and quartz wool.

$E(t)$  for the empty and the filled cell are shown in **Figure 2.4a**. The shape of the peak shows that toluene was detected when the cell is empty. Eq. 2.2 returned mean residence time ( $\tau$ ) values of  $\tau_{\text{empty}} = 165\text{ s}$  and  $\tau_{\text{filled}} = 119\text{ s}$ , respectively. The longer residence time in the empty cell shows that the exchange of solutions requires more time due to a larger exchange volume and to the presence of favored and un-favored flow paths due to the cell design.

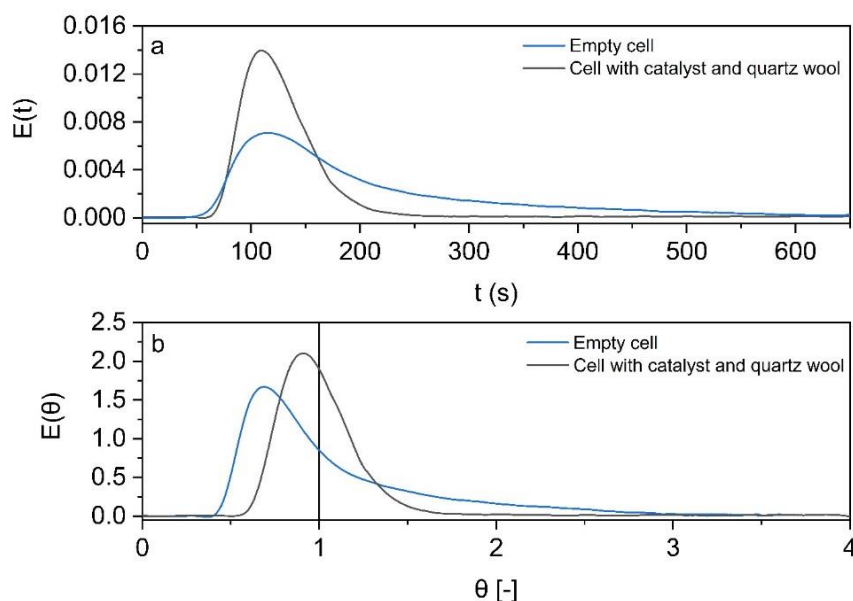


**Figure 2.4:** Residence time distribution functions of the empty cell (blue) and cell filled with catalyst (black). a) Distribution function. b) Normalized distribution function.

$E(\theta)$  shown in **Figure 2.4b** and obtained from Eq. 2.4 allows for a direct evaluation of the reactor type upon normalization of the RTD function. The empty cell exhibits a broader and less symmetric distribution compared with a maximum positioned at 0.53. In the presence of the sample, the normalized RTD function is more symmetric and its maximum is closer to  $\theta = 1$ . Both factors (shape and peak position) indicate that the empty cell is a poor PFR while the filled cell is similar to a PFR.<sup>47,48</sup>

## 2.3 Tandem cell

### 2.3.1 Development of the tandem spectroscopic cell

The principle of the combination of ATR-IR and XAS in one tandem cell is shown in **Figure 2.5**. In the ATR-IR mode, the IR radiation passes through the internal reflection element (IRE). The incident X-rays beam penetrates the catalyst layer from the opposite side and the emitted X-rays are detected in fluorescence mode.

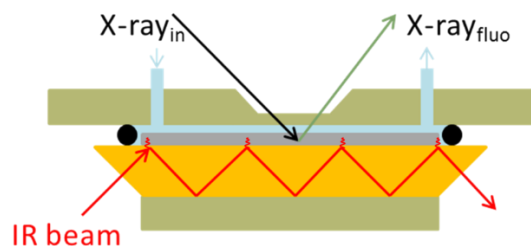


**Figure 2.5:** Principle of combination of ATR-IR and XAS in the tandem-cell. IRE (orange), catalyst layer (grey), solution (blue), cell walls (green), Viton® O-ring (black): the evanescent wave is indicated at every reflection point in the catalyst.

Pressure, flow rate and the nature of the solvent were the parameters for selecting the constituting elements of the setup. The design of the tandem-cell was determined based on pressure requirements and material properties, such as X-rays transparency, elasticity and chemical resistance to the solvents.

As shown in **Figure 2.5**, the IRE serves as the support for the catalyst layer. Although several materials can be chosen as IRE, we selected ZnSe because its refractive index (2.4) allows investigating the catalyst bed with larger penetration depth ( $10\text{ }\mu\text{m}$  at  $1700\text{ cm}^{-1}$ ). The drawback of the use of an IRE is that it forces XAS to be measured in fluorescence mode and it calls for a specific window material transparent to the X-rays. Synthetic diamond was discarded due to machining limitations, brittleness and price. PTFE and PEEK were the materials of choice. These carbon based materials possess low absorption coefficient for X-rays at the desired energies of the Cu to Pd K-edges (8.98 to 24.35 keV, respectively). In order to produce a cell that has flexibility in the operational X-rays energy range, the Cu K-edge was considered as the lowest energy for XAS and the benchmark for data quality. Additionally, the possibility to perform space resolved ATR-IR spectroscopy and XAS in order to probe the catalyst bed at the inlet, center and outlet was considered in the design of the cell.

PEEK was preferred to PTFE because of greater mechanical performance and resistance to deformation. As opposed to the XAS/XRD cell, where PTFE was preferred because of higher elasticity ensuring a better cell sealing of the cell, the lower elasticity of PEEK in the tandem cell is crucial since the XAS window is built within the frame of the cell walls. Therefore, to sustain operation under pressure, it is required that the XAS windows do not deform under pressure. The XAS window presents three slits enabling to probe the catalyst bed by space resolved fluorescence XAS in three different points in correspondence of the inlet, the middle and the outlet of the catalyst layer deposited onto the IRE. The slits are thin enough to allow sufficient transmission of X-rays at the Cu K-edge without deformation up to 6 bar. The

drawings in **Figure 2.6** show the two radiations paths in the cell, the solution flow and the circuit of the fluid for temperature control.

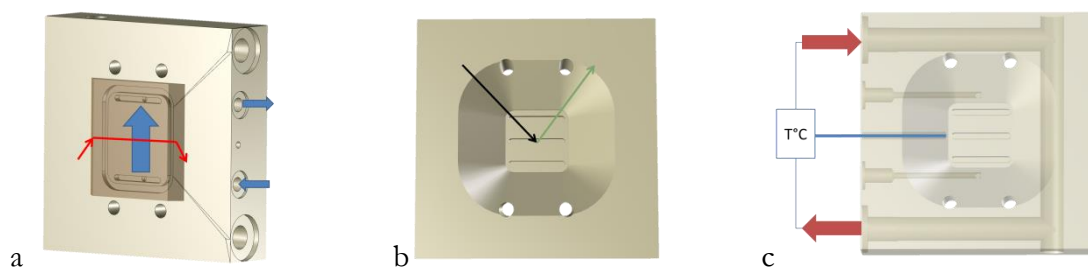


**Figure 2.6:** Design of the tandem-cell. a) Back side of the cell showing the IR beam path in red and the liquid flow path in blue. b) Front side of the cell showing the incident X-rays in black and the emitted X-rays in green. c) Transparent view showing the path of the heating/cooling fluid and the channel for the thermocouple.

**Figure 2.7** shows the tandem-cell mounted on a movable stage of a commercial ATR-IR mirror assembly allowing vertical positioning of the cell. A screw on the back of the cell allows selecting the height of the cell with respect to the IR beam thus to perform space resolved ATR-IR.

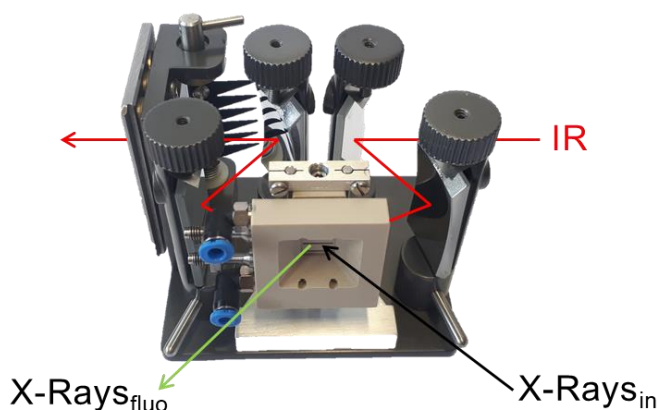


**Figure 2.7:** Tandem cell mounted on the commercial mirror assembly.

The eleven internal reflections in the IRE are shown in **Figure 2.8a**, and imaged by using a laser pointer and a phone camera. The effective number of internal reflections is four due to the fact that the layer is deposited on only one side and the shape of the deposited layer covers a smaller area than the IRE length. The deposition process consists in the sedimentation of the powder and drying of the solvent (usually bi-distilled water). The powder requires to be sieved to at least 50  $\mu\text{m}$  in order to provide a homogeneous and stable catalyst layer as shown in **Figure 2.8b**.



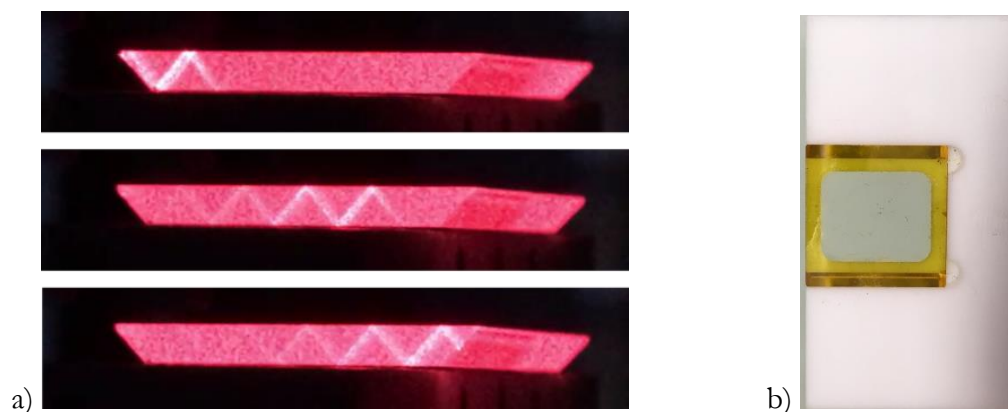


**Figure 2.8:** a) The 11 total internal reflections in the IRE ZnSe. b) Deposition of a layer of 5 wt.% CuO/Al<sub>2</sub>O<sub>3</sub> on the ZnSe IRE.

### 2.3.2 Proof of concept

Two experimental sessions were performed to evaluate the cell. First, the performance of the cell was tested at the Cu K-edge in dry environment and in the presence of 2-propanol at the SuperXAS beamline. Second, the quality of the infrared spectra was verified by performing CO adsorption on 5 wt.% Pd/Al<sub>2</sub>O<sub>3</sub> in 2-propanol solvent.

#### 2.3.2.1 Fluorescence X-ray absorption spectroscopy

The quality of fluorescence XAS spectra was investigated using 5 wt.% CuO/Al<sub>2</sub>O<sub>3</sub> and a passivated implanted planar silicon (PIPS) detector. A ZnSe IRE was used as substrate for the catalyst layer to replicate the conditions used in an hypothetical identical ATR-IR experiment. The spectra in **Figure 2.9a** demonstrate the presence of various peaks besides the features of the Cu K-edge in both dry and wet conditions. Such peaks originate from the diffraction of the X-rays caused by the ZnSe IRE. The IRE acts as a prism diffracting and reflecting the X-rays, which then contribute to the spectrum. The effect of ZnSe IRE is further confirmed by the presence of the absorption edge of Zn K-edge (9659 eV) following the Cu K-edge (8979 eV). The second observation to be made is that when a flow of 2-propanol is carried over the catalyst layer a decrease in edge jump is observed suggesting delamination of the catalytic material from the IRE.

In order to overcome the diffraction contribution of the IRE, a catalyst layer of the same material was deposited onto a glass plate (76 x 26 mm), used for optimal microscopy, which was then loaded into the tandem-cell. **Figure 2.9b** shows the corresponding fluorescence XAS spectra recorded in air. The effect of using an amorphous material greatly improved the quality



of the spectrum and allowed to conclude that the present design of the cell is suitable for XAS experiment in fluorescence mode at energy edges as low as the Cu-K edge.

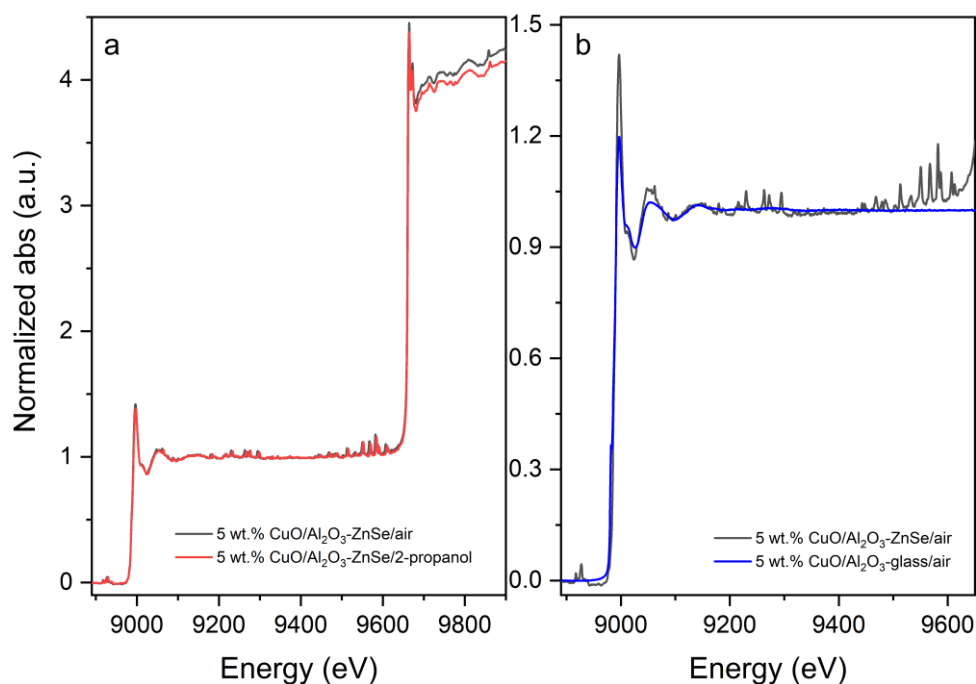


**Figure 2.9:** XANES spectra at the Cu K-edge of 5 wt.% CuO/Al<sub>2</sub>O<sub>3</sub>. a) Catalyst layer in air (black) and in 2-propanol (red) deposited on the ZnSe IRE. b) Comparison between catalyst layers on ZnSe IRE (black) and a glass plate (blue).

### 2.3.2 ATR-IR

For the evaluation of the performance of the cell in ATR-IR spectroscopy, CO adsorption on 5 wt.% Pd/Al<sub>2</sub>O<sub>3</sub> was investigated. After reduction in H<sub>2</sub>-saturated 2-propanol for 1 h at 75°C, a solution of CO-saturated 2-propanol was contacted with the Pd/Al<sub>2</sub>O<sub>3</sub> layer. This procedure was performed also with using the conventional ATR-IR cell. CO adsorption was selected due to the characteristic peaks of CO adsorbed on Pd sites in the region of 2100-1800 cm<sup>-1</sup>.<sup>49</sup>

In the reference experiment with the conventional cell and 25-reflections ZnSe IRE the peaks associated with CO adsorbed on linear binding sites at 2070 cm<sup>-1</sup> are present together with a second broad peak with maximum at 1945 cm<sup>-1</sup> corresponding to bridge and hollow bonded CO (**Figure 2.10a**). The same pattern is recognizable in **Figure 2.10b** for the experiment using the tandem cell. However, the spectrum exhibits lower intensity and especially increased noise. The decrease in intensity is associated mainly with the change in the number of active reflections within the IRE. Based on the cell design, only 9 effective reflections are expected on the 25-reflections IRE, while these are only 4 in the case of the 11-reflections IRE of the

tandem cell. The different alignment of the two cells with IRE of significantly different size on the same vertical mirror unit and the reflection within the crystal likely contribute to decrease the intensity further.

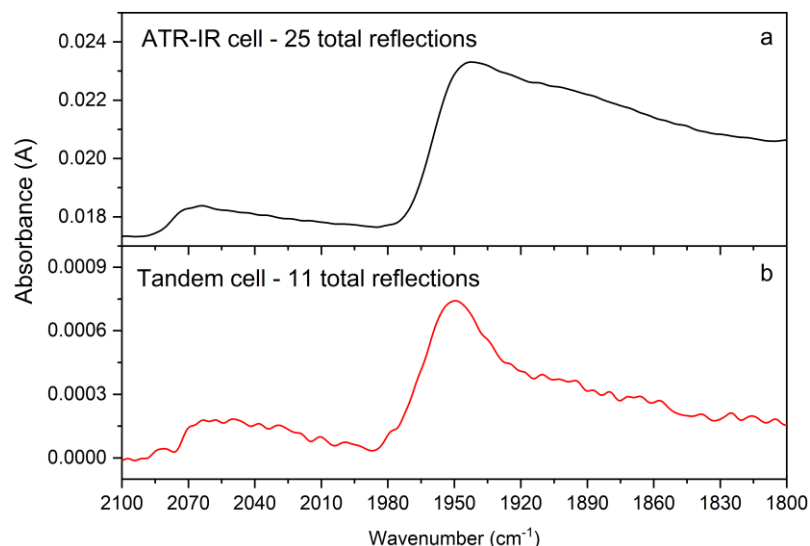


**Figure 2.10:** ATR-IR spectra of adsorbed CO from 2-propanol over 5 wt.% Pd/Al<sub>2</sub>O<sub>3</sub>. a) Standard ATR-IR cell, 25-reflections ZnSe IRE. b) Tandem cell, 11-reflections ZnSe IRE.

### 2.3.3 Conclusions

The main outcome of these experiments is that direct combination of XAS and ATR-IR is not possible in this geometry because of the presence of the IRE contributing to the XAS spectra. The combination can be achieved using a different substrate for the catalyst layer. Then, both spectroscopies can be used in identical but separate experiments. On the side of XAS, no limitation has been observed. The extreme sensitivity of the method to layer delamination which might require first stabilization of the layer prior to *in situ* experiment. On the ATR-IR side, poorer data quality has been obtained compared to a standard cell, which can be solved by tuning the measurement parameters such as number of scans at the expenses of time resolution.

In addition to the improvement of the ATR-IR signal, the characterization of the flow characteristics of the cell is required in order to validate its suitability for transient experiments. Finally, the spatial resolution of the catalyst layer, that is allowed by the cell design, was not yet tested.

## 2.4 Setup

### 2.4.1 Setup components

A schematic of the setup used to measure the RTD and to perform experiments in liquid phase is shown in **Figure 2.11**. Two high-pressure liquid chromatography (HPLC) pumps (Knauer Azura 4.1 P, 10 mL stainless steel head) provide the desired continuous flows of the solvents with low pulsation. H<sub>2</sub>-saturated solutions are obtained by bubbling H<sub>2</sub> in the storage tanks and by flowing the solution through an online gas feeder, with internal H<sub>2</sub> pressure of 5 bar. The gas feeder consists of a 20 cm section of the PTFE tubing jacketed with a stainless steel tube which is pressurized with the desired gas.<sup>50,51</sup> Operation of the gas feeder was demonstrated by saturation experiments with CO<sub>2</sub> in 2-propanol as the CO<sub>2</sub> concentration can easily be monitored by IR spectroscopy.

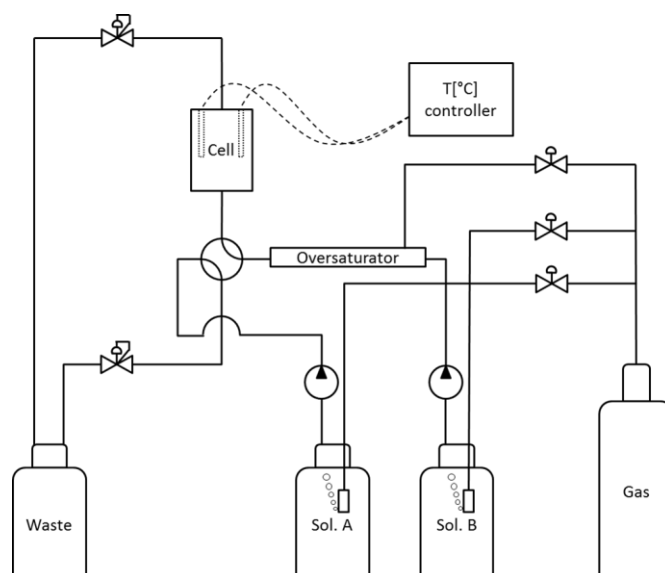


**Figure 2.11:** Flow sheet of the setup.

### 2.4.2 Gas feeder design

The over-saturator was tested with CO<sub>2</sub> as tracer gas because solvated CO<sub>2</sub> can be monitored by infrared spectroscopy following the absorbance of the peak at 2338 cm<sup>-1</sup>. The effects of flow rate and gas pressure inside the over-saturator on the amount of dissolved CO<sub>2</sub> in 2-propanol are reported in **Figure 2.12**.

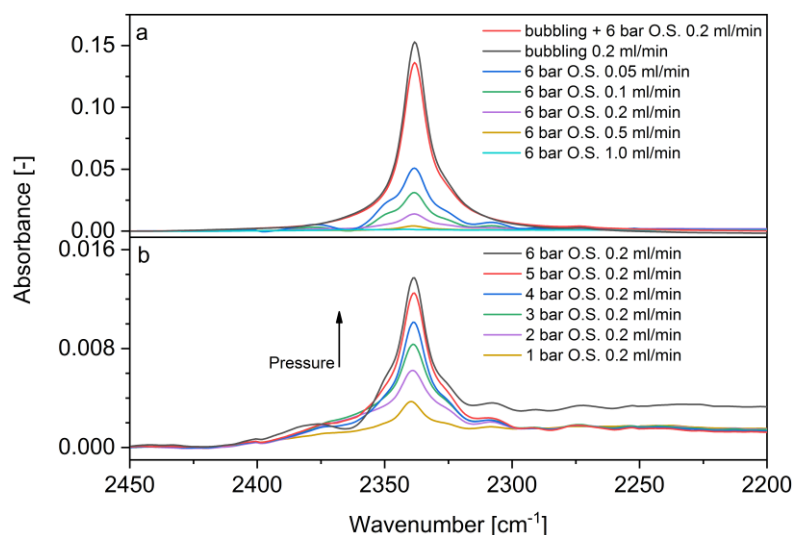


**Figure 2.12:** ATR-IR spectra of CO<sub>2</sub> dissolved in 2-propanol as a function of a) flow-rate and b) pressure in the over-saturator.

At a constant flow rate, increasing the pressure allows to increase the peak intensity associated with solvated CO<sub>2</sub>. At constant CO<sub>2</sub> pressure, almost no CO<sub>2</sub> is dissolved at flow rate as high as 1.0 mL/min. However, decreasing the flow rate to 0.05 mL/min significantly increases the amount of CO<sub>2</sub> dissolved in 2-propanol. In comparison with gas pressure this is the strongest factor to control the amount of gas dissolved.

Much higher CO<sub>2</sub> concentrations are achieved by using the bubbler alone. Operation of the over-saturator at 6 bar CO<sub>2</sub> pressure to the bubbler at a flow rate of 0.2 mL/min increases the total amount of solvated CO<sub>2</sub>. These two experiments combined demonstrate that the device achieves a continuous flow of a liquid over-saturated with a gas. Similar behavior is expected with H<sub>2</sub> and other light gases.

# Chapter 3: Investigation of PdO reduction in liquid phase

The present chapter is based on the manuscript in preparation: T. Fovanna, G. Garin, I. Alxneit, A. H. Clark, S. Checchia, M. Di Michiel, O. Kröcher, M. Nachtegaal, D. Ferri, Combined in situ XAS and XRD studies of solvent-mediated reduction of PdO nanoparticles by hydrogen. T. Fovanna performed the experimental work, analyzed and interpreted most of the data. The manuscript was written with the co-authors.

### 3.1 Introduction

Production of bulk and fine chemicals often involve at least one or more catalytic steps to obtain the commercial product; a heterogeneous catalytic material may endorse the role of the catalyst. As new processes are developed, heterogeneously catalyzed reactions need to be adapted and new challenges are constantly faced. Novel catalysts are developed and studied using a collections of modern analytical spectroscopic and diffraction methods that are often performed *in situ* or under *operando* conditions.<sup>52</sup>

Supported nanoparticles (NPs) of palladium oxide (PdO) or palladium (Pd) are heavily studied as they are involved in many industrial catalytic processes, electrochemistry, and hydrogen storage systems.<sup>53–56</sup> Often the synthesis of such catalysts requires simple to more complex synthetic routes and may imply elaborated pretreatments.<sup>49,57,58</sup> Prior to use, *in situ* reduction of the oxidic passivation layer of Pd NPs formed during storage at ambient conditions is often required as activation step of the catalyst.<sup>59</sup> Reduction of small oxide particles has been studied in the past.<sup>41</sup> The reaction has been modeled considering two different mechanisms based on nucleation or a shrinking core.<sup>40,60,61</sup> The mechanism of PdO reduction under different gas atmospheres has been studied by Su et al.<sup>62</sup> who showed that the reducing gas plays a central role in the understanding of the mechanism. Reduction in methane is best described using a nucleation model, while reduction in hydrogen follows the shrinking core model. To date, no mechanistic study trying to distinguish between the two models has been performed on the reduction of PdO NPs in liquid phase.

In a previous work, a flow cell suited for spectroscopy and diffraction measurements was applied for *operando* studies of gas phase catalyzed reactions combining diffuse reflectance infrared Fourier transform (DRIFT) spectroscopy, X-ray absorption spectroscopy (XAS) and X-ray diffraction (XRD).<sup>42,43</sup> The latter two techniques are well suited to study heterogeneous catalytic systems. They were specifically selected because they are sensitive to the presence and evolution of the various Pd phases and are able to detect hydrogen insertion into the Pd NP.<sup>59,63</sup> To complement these studies the reduction of the supported PdO NP was monitored by attenuated total reflectance infrared (ATR-IR) spectroscopy to observe the formation of water as the product.<sup>27</sup>

Here, we report a study of PdO reduction in a H<sub>2</sub>-saturated liquid using XAS, XRD and ATR-IR. We demonstrate that PdO is reduced first to an intermediate metallic phase, which

is then rapidly converted into palladium hydride. The time resolved XAS allows to establish that reduction of PdO follows a nucleation model while the formation of the hydride follows a shrinking core model.

## 3.2 Experimental

### 3.2.1 Material and chemicals

Pre-reduced 5 wt.% Pd/Al<sub>2</sub>O<sub>3</sub> (type 324, Johnson Matthey) was oxidized by heating the catalyst to 400°C at 5°C/min for 4 h under shallow bed conditions under stagnant air. Hydrogen (99.995 % purity, Carbagas), Argon (99.9990 % purity, Alpha gas), cyclohexane (SupraSolv for gas chromatography MS, Merck) and toluene (HiPerSolv CHROMANORM HPLC grade, VWR Chemicals) were used as received.

*3.2.2 Transmission electron microscopy*-TEM images were recorded with a JEOL 2010 microscope operated at 200 keV, equipped with a LaB<sub>6</sub> filament and a CCD camera (Orios, GATAN). The catalyst powder was deposited on holey carbon film supported on copper grids from sonicated suspensions in 2-propanol. The material was characterized by TEM (**Figure B1-Appendix**) and the particle size distribution (PSD) of the Pd NPs. The PSD appears to be narrow with the mode at 4.0 nm.

### 3.2.3 *In situ* X-ray absorption spectroscopy and X-ray diffraction

Separate experiments applying identical procedures were performed to collect data for X-ray absorption spectroscopy (XAS) and X-ray diffraction (XRD).

The catalyst powder ( $35 \pm 1$  mg) was loaded into the cell equipped with polytetrafluoroethylene (PTFE) windows (each 200  $\mu$ m thick) between quartz wool plugs. The resulting optical path length was 2 mm. The cell was connected to a 4-ways switching valve at the inlet and to a back pressure regulator (BPR assembly 75 psi, Upchurch) mounted at the outlet and set to 5.2 bar. The cyclohexane was saturated with H<sub>2</sub> upon bubbling and oversaturation. The catalyst bed was heated to 70°C and data acquisition was initiated. When the H<sub>2</sub>-saturated cyclohexane entered the cell, at a flow rate of 0.2 mL/min, this point was defined as time  $t = 0$ .

### 3.2.3.1 XAS

Quick scanning extended X-ray absorption fine structure spectra (QEXAFS) were acquired at a rate of 1 Hz at the Pd K-edge (24350 eV) at the SuperXAS beamline of the Swiss Light Source (SLS, Villigen) using 15 cm long ionization chambers filled with 1 bar N<sub>2</sub> and 1 bar Ar as detectors. A Pd foil, mounted between the second and the third ionization chamber served as internal energy reference. The polychromatic beam resulting from the 2.9 Tesla super bend magnet was collimated using a Pt-coated collimating mirror, subsequently monochromatized by a channel-cut Si(111) crystal of the QEXAFS monochromator and finally focused using a Pt-coated toroidal mirror to a spot size of 150 x 150  $\mu\text{m}^2$ .

All spectra were energy corrected, normalized and smoothed using ProXAS.<sup>64</sup> Absolute energy calibration was achieved by aligning the edge position of the sample with that of the simultaneously recorded spectra of a Pd reference foil.

Linear combination fitting (LCF) analysis of the XANES spectra was performed using the corresponding package in Prestoprongo<sup>65</sup> using selected spectra from gas phase experiments as references. EXAFS fitting of selected spectra was performed using the Demeter software package.<sup>66</sup> Spectra were first subjected to background subtraction. Then photo-electron energy was converted to wave-vector  $Q$  by setting the first inflection point of the absorption edge to 24.35 keV. Finally the  $k^2$ -weighted spectra were Fourier transformed in the  $K$ -range of 3-1  $\text{\AA}^{-1}$ . The first Pd-Pd shell of the EXAFS spectra was fitted using an amplitude reduction factor of 0.83 that was obtained from fitting the Pd-foil reference.

### 3.2.3.2 XRD

X-ray diffraction data were collected at a beam energy of 69 keV at the beamline ID 15 (ESRF, Grenoble) using a Pilatus detector positioned 850 mm from the sample position and a beam size of 75  $\mu\text{m}$  x 120  $\mu\text{m}$ . Diffraction patterns were collected during 1 s every 5 min. The first three Pd peaks were fitted to Gaussians (amplitude, center position, width) using the LMFIT software package.<sup>67</sup>

### 3.2.4 *In situ* attenuated total reflectance infrared spectroscopy

An aqueous suspension of the catalyst (10 mg in 1.5 mL) was stirred for 15 min and deposited on a ZnSe internal reflection element (IRE, 45°, 52 x 20 x 2 mm, Crystran) before drying overnight. The crystal was loaded in an in-house built ATR-IR cell, which was mounted in the



sample compartment of the IR spectrometer (Bruker, Vertex 70). The spectrometer was equipped with a liquid-nitrogen cooled mercury cadmium telluride (MCT) detector and a 4-mirrors attenuated total reflectance (ATR) assembly (Specac). Spectra were collected at 40 kHz scanner velocity and  $4\text{ cm}^{-1}$  resolution by averaging 30 scans. The catalyst layer deposited on the IRE was equilibrated at  $70^\circ\text{C}$  for 1 h with cyclohexane saturated with Ar bubbling at 1 bar until (1 h) a stable signal was obtained, which was used as background spectrum. Then,  $\text{H}_2$ -saturated cyclohexane was allowed to enter the ATR-IR cell while spectra were recorded every 5 min.

### 3.3 Result and discussion

#### 3.3.1 *In situ* X-ray diffraction

**Figure 3.1** shows the diffraction patterns recorded during reduction of  $\text{Pd}/\text{Al}_2\text{O}_3$  using  $\text{H}_2$ -saturated cyclohexane at  $70^\circ\text{C}$ . These patterns are a superposition of the contributions of the PTFE windows, the  $\text{Al}_2\text{O}_3$  support and the PdO and Pd nanoparticles. The patterns at the start and the end of the experiment are shown in red and blue, respectively.

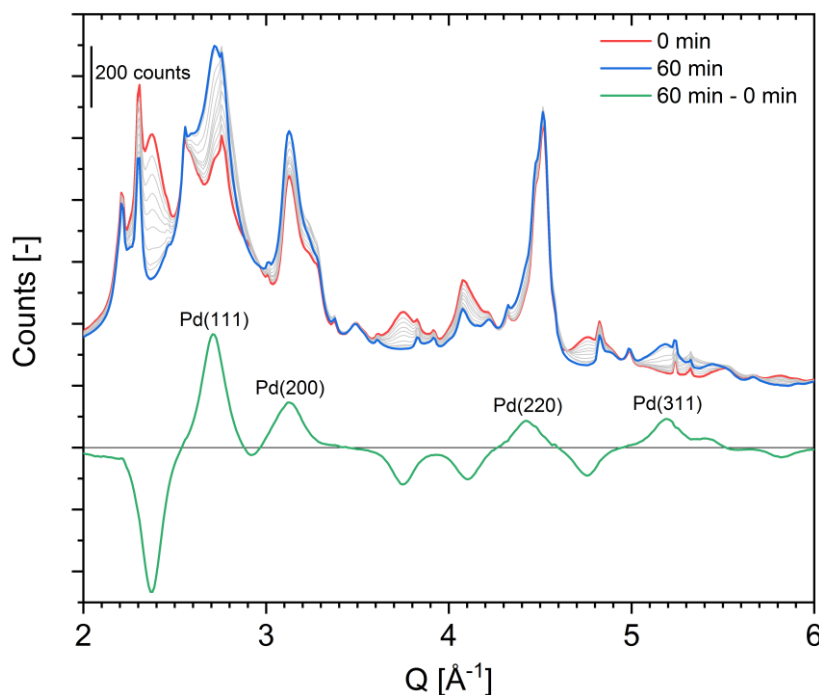


**Figure 3.1:** XRD patterns of  $\text{PdO}/\text{Al}_2\text{O}_3$  recorded at  $70^\circ\text{C}$  in  $\text{H}_2$ -saturated cyclohexane.

Changes due to the conversion of PdO to Pd are clearly visible. The changes become more evident in the difference between the last and first pattern (green). Here, peaks due to Pd appear positive as they are formed, while peaks due to PdO appear negative as they disappear during the reduction.<sup>29</sup> Positive peaks assigned to Pd are located at  $Q = 2.707$  (111),  $3.126$

(200), 4.425 (220), 5.194 (311)  $\text{\AA}^{-1}$  while negative peaks due to PdO are observed at  $Q = 2.367$ , 3.746, 4.105, 4.765  $\text{\AA}^{-1}$ .

The presence of a strong and feature-rich background caused by the PTFE windows (see **Figure B2-Appendix**) and the alumina support prevented a detailed analysis of the data by e.g. Rietveld refinement. A much simpler, qualitative analysis based on difference patterns is presented in the following.

A series of difference patterns ( $P_t - P_0$ ), with  $P_t$  the pattern at time  $t$  and  $P_0$  the first pattern recorded, were generated and the first three positive peaks (Pd(111), Pd(200), Pd(220)) were fitted with Gaussians. For each pattern a single cell parameter ( $a$ ) that defines the position of the three peaks, three amplitudes and a single peak width (indicative of particle size) was determined by a non-linear least squares fit. The time evolution of the unit cell  $a$  parameter is reported in **Figure 3.2a**. Here, cell parameters obtained from the individual peak position are reported to verify that they are consistent with each other and thus fitting of a single cell parameter is allowed. During the first 30 min, the cell parameter values ( $a$ ) oscillate around the value of bulk Pd metal (0.39 nm), then gradually shift to a new value of 0.402 nm over a 20 min period, consistent with lattice expansion and the formation of a PdH phase.<sup>68</sup> Closer inspection of the difference pattern at around 40 min revealed a clear shoulder in all Pd peaks and thus the presence of two different phases. A more detailed analysis was performed assuming all positive peaks to be composed of a linear combination of two phases (Pd and PdH) with different  $a$  parameters (independent of time) and different particle diameters (time dependent). Values of  $a = 0.38905 \pm 1 \cdot 10^{-5}$  nm and  $a = 0.401268 \pm 2 \cdot 10^{-5}$  nm was obtained for the two unit cell dimensions for Pd and PdH phases respectively. The time dependence of the contributions of the three phases (individually normalized) and the relative particle diameters is reported in **Figure 3.2b,c**. The decay of the PdO phase is indicated by the integral of the PdO (111) peak in **Figure 3.2c**. From this **Figure 3.2c** clear picture arises: Initially, PdO is reduced to metallic Pd. In parallel, Pd metal reacts to form a hydride phase, observable by the increasing particle diameter and concentration over time. After 30 min, 80 % of the PdO is reduced and the Pd concentration reaches its maximum value. From this point on, the fraction of Pd and particle diameter start to drop fast as the conversion of Pd into PdH becomes the main reaction. After one hour all PdO has been consumed and only about 20 % Pd remains, while PdH dominates.

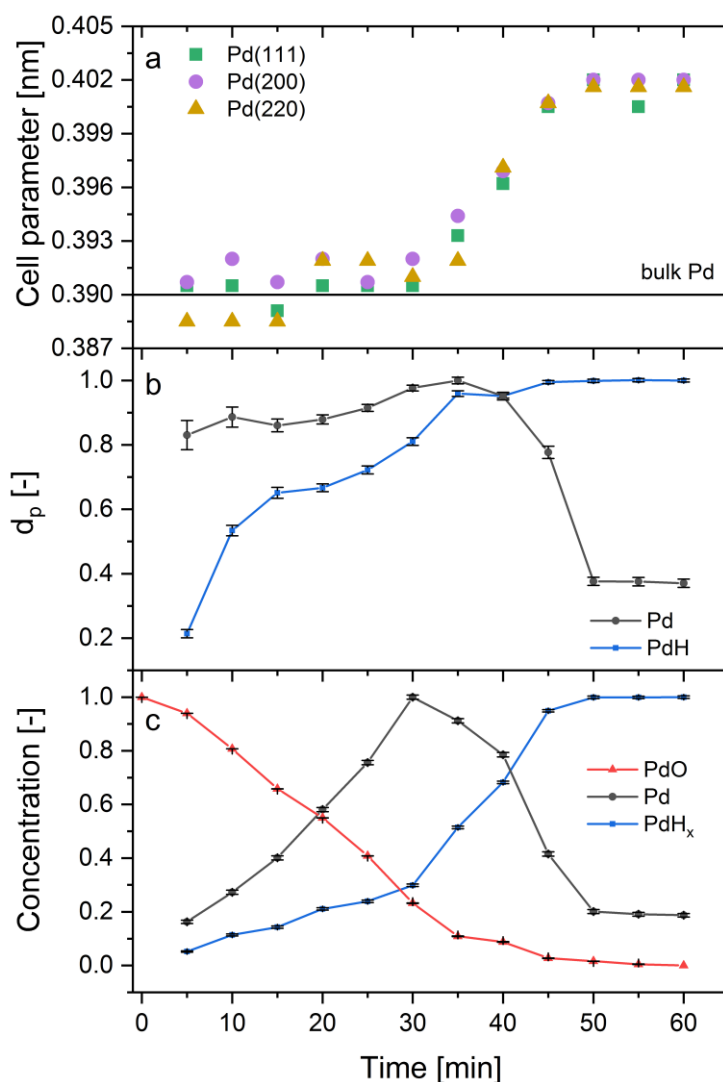


**Figure 3.2:** Time-resolved analysis of the structural XRD parameters extracted during Pd/Al<sub>2</sub>O<sub>3</sub> reduction in H<sub>2</sub>-saturated cyclohexane at 70°C. (a) Cell parameter, (b) relative particle diameter, (c) phase composition.

### 3.3.2 *In situ* X-ray absorption spectroscopy

X-ray absorption spectroscopy (XAS) was used to follow the oxidation state and coordination environment of Pd at the Pd K-edge (22350 eV) in transmission mode using an identical procedure as in the XRD study.

**Figure 3.3a** shows the XANES region of the spectra during the isothermal reduction of PdO/Al<sub>2</sub>O<sub>3</sub> in H<sub>2</sub>-saturated cyclohexane at 70°C. The spectra at  $t = 0$  min is identified as pure PdO by linear combination fitting with reference spectra of bulk PdO and Pd foil. As time progresses, PdO reduces to metallic Pd as confirmed by both, the decreasing white line intensity and the shift of the edge position to lower energies. The reduction is also observable

in the corresponding Fourier transformed spectra of the EXAFS region (**Figure 3.3b**). The signal due to the Pd-O scattering path (at 1.55 Å) decreases over time while the one of the Pd-Pd scattering path (at 2.55 Å) increases accordingly. At  $t = 60$  min only the signature of Pd remains dominant, while arguably a small contribution of PdO could be also identified. Interestingly, the Pd-Pd signature around 2.55 Å shifts to a larger bond length. This indicates an expansion of the lattice consistent with the formation of PdH.

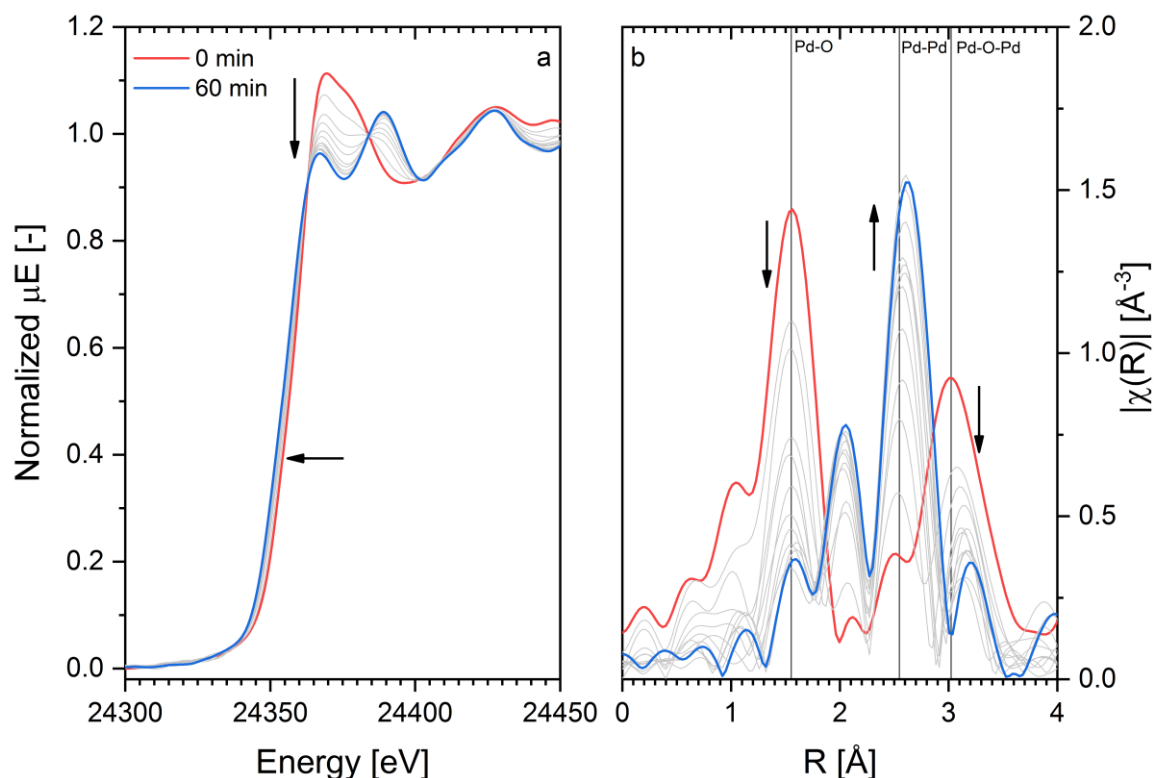


**Figure 3.3:** Time evolution of (a) XANES spectra and (b) of the Fourier transformed K-space during *in situ* reduction of PdO/Al<sub>2</sub>O<sub>3</sub> in H<sub>2</sub>-saturated cyclohexane at 70°C.

In depth investigation of the XANES region, on the complete data set, was performed using linear combination fitting (LCF). To perform LCF, reference spectra are required as input for the analysis. Reference spectrum of PdO in the nanoparticulate state was collected on the original sample at 70°C in air before introducing the solution into the cell. Samples of PdH and Pd required collecting reference spectra *in situ*. Pre-reduced material was equilibrated for 15 min in a gas flow of 10 vol.% H<sub>2</sub>/He at 30°C. The spectrum collected at the end of this procedure was used as PdH<sub>0.4</sub> reference. The evaluation of the hydride fraction was performed by fitting the FT-EXAFS region and using the Pd-Pd bond distance of the first shell.<sup>69</sup> Then, the sample was heated to 160°C under the same H<sub>2</sub>/He atmosphere, the gas flow was switched to He and the sample was cooled to 70°C in He. The last spectrum measured was used as the Pd reference spectrum. The three reference spectra are reported in **Figure B4-Appendix**.

Results of the LCF analysis using the three references (Pd, PdH<sub>0.4</sub>, PdO) are reported in **Figure 3.4a**. The fraction of PdO decreases monotonously to less than 10% after 60 min. As soon as reduction of PdO is initiated both PdH and Pd start to form. The PdH fraction initially rises faster than the Pd fraction and continues to rise until the end of the experiment at  $t = 60$  min. The Pd fraction increases more continuously in the first 30 min then slowly decreases by about 5% until  $t = 60$  min. Thus, Pd is continuously and rapidly converted to PdH. Because conversion to PdH continues, Pd is only an intermediate product of the reduction and its concentration starts to decrease. A comparison of an LCF analysis based solely on two phases (PdO, PdH) only is reported in **Figure B5-Appendix**.

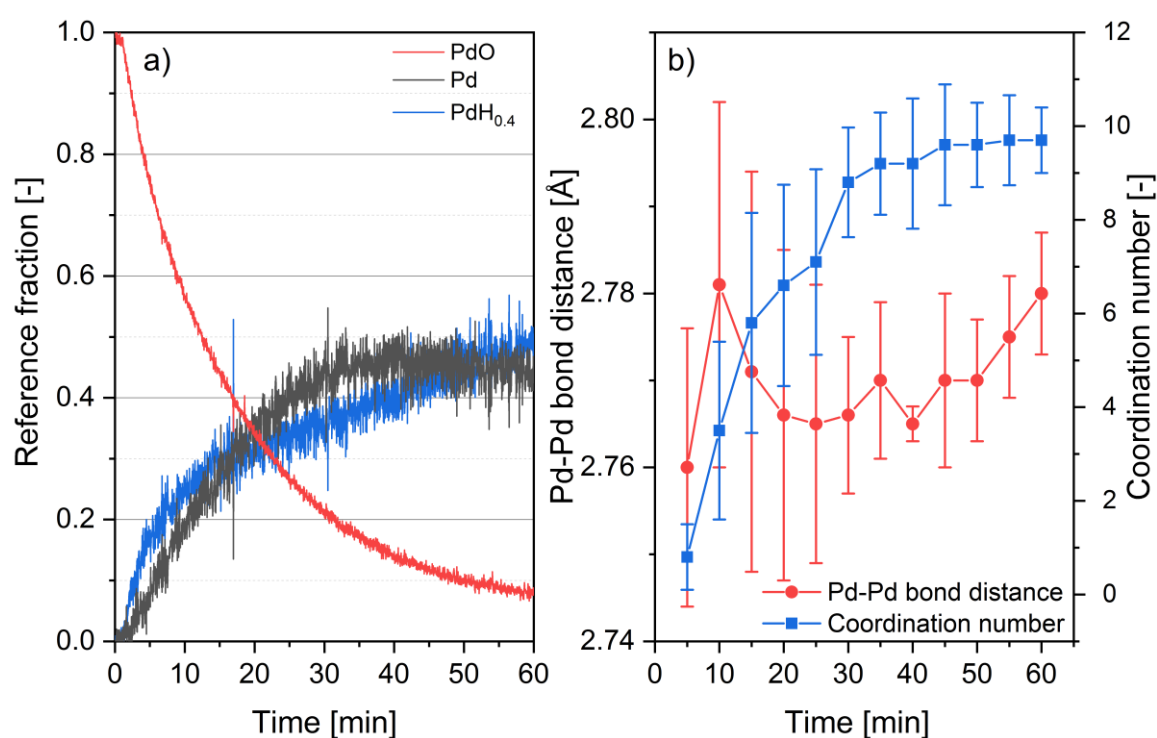


**Figure 3.4:** a) LCF fitting with three reference spectra. b) Time evolution of Pd-Pd bond length and coordination number during *in situ* PdO/Al<sub>2</sub>O<sub>3</sub> reduction in H<sub>2</sub>-saturated cyclohexane at 70°C.

Pd-Pd bond distances and Pd first shell coordination numbers were determined from the FT-EXAFS spectra. Their time evolution is reported in **Figure 3.4b**. The coordination number strongly increases and reaches a nearly constant value of about 9.75 after 45 min. This is a clear indication that the metallic particles grow during the reduction. The Pd-Pd bond distance shows a different behavior. Already after 5 min a clearly higher value than the metallic bulk value (2.74 Å) is observed and remains relatively constant (considering the large error bars). This seems to indicate an expanded Pd-Pd bond distance and thus the presence of inserted hydrogen already at an early stage of the reduction of the PdO phase. Based on the

much larger error in the first 30 min of the experiment, we might speculate about the presence of two phases (Pd and PdH) at this stage of the reaction. At  $t = 60$  min a Pd-Pd bond length of 2.78 Å was observed, which is larger than the value obtained for the Pd foil (2.75 Å).

Both XAS and XRD allow to follow the reduction of the PdO phase to PdH via a Pd intermediate, however the concentration profiles differ. Clear differences are observed in the comparison of the time evolution of the phase compositions obtained by XANES (**Figure 3.4a**) and XRD (**Figure 3.2c**). After 60 min a 20% fraction of PdO remains by XANES while no PdO is observable by XRD. This may be explained by the fact that XRD probes long range order which makes PdO transparent to high energy X-rays at the end of the reduction process, while it is still observable by XANES after 60 min. Another difference is at the end of the process where only 20% of Pd is observed by XRD, while a fraction of 42% is observed by XANES. This is because the material property investigated by the two methods is different. While both EXAFS and XRD allow investigation of local environment on the short or long range XANES probes the changes in electronic transition of the density of states. This allows to investigate the formation or breaking of bonds that both EXAFS and XRD have trouble to investigate in the case of insertion of a light element, such as hydrogen, at low molecular ratio within a metal nanoparticle.<sup>33</sup>

The time evolution of the phase composition obtained from the LCF analysis of the XANES region was analyzed in more detail to shed light onto the mechanism of the PdO reduction to Pd and its further conversion into the PdH phase. The data was analyzed by two different kinetic models: the contracting sphere model and the nucleation model.<sup>70</sup> The mechanism depends on how fast the dissociative adsorption of H<sub>2</sub> takes place on the metal-oxide surface. If the activation of H<sub>2</sub> is fast then the reduction is limited by the diffusion of the reducing agent meaning that the shrinking core model is best to describe the kinetics of reduction. While the nucleation model represents the other extreme, with the activation of H<sub>2</sub> being the slow step and the reduction not limited by diffusion.

The rate law for the contracting sphere model is defined as:

$$1 - (1 - \alpha)^{\frac{1}{n}} = kt + b \quad (3.1)$$

while the nucleation model is described:

$$1 - \alpha = \exp(-kt^n) \quad (3.2)$$

In both equations,  $\alpha$  represents the extent of reduced species,  $k$  the rate constant,  $t$  the time, and  $n$  the dimension of the process. The concentration profile of PdO had to be converted into the fraction of the corresponding reduced phase to allow fitting a growth process. In **Figure 3.5** the results of the fits of all phases to both models are reported. **Figure 3.5a** shows that the consumption of PdO should be described by the nucleation model. This model is able to capture the first 30 min of the reaction before it starts to deviate significantly. The shrinking sphere model, however fails in the whole time interval.

The results obtained for the kinetics of Pd formation is reported in **Figure 3.5b**. Both models seem equally well suited to represent the data up to  $t=30$  min. Both fail at later times, which is expected because at this point, the intermediate Pd phase starts to be consumed. Fitting of the complete concentration profile of PdH reported in **Figure 3.5c** was not possible. After omission of the first 5 min the data can be fitted using the contracting sphere model. No reasonable fit could be obtained with the nucleation model.

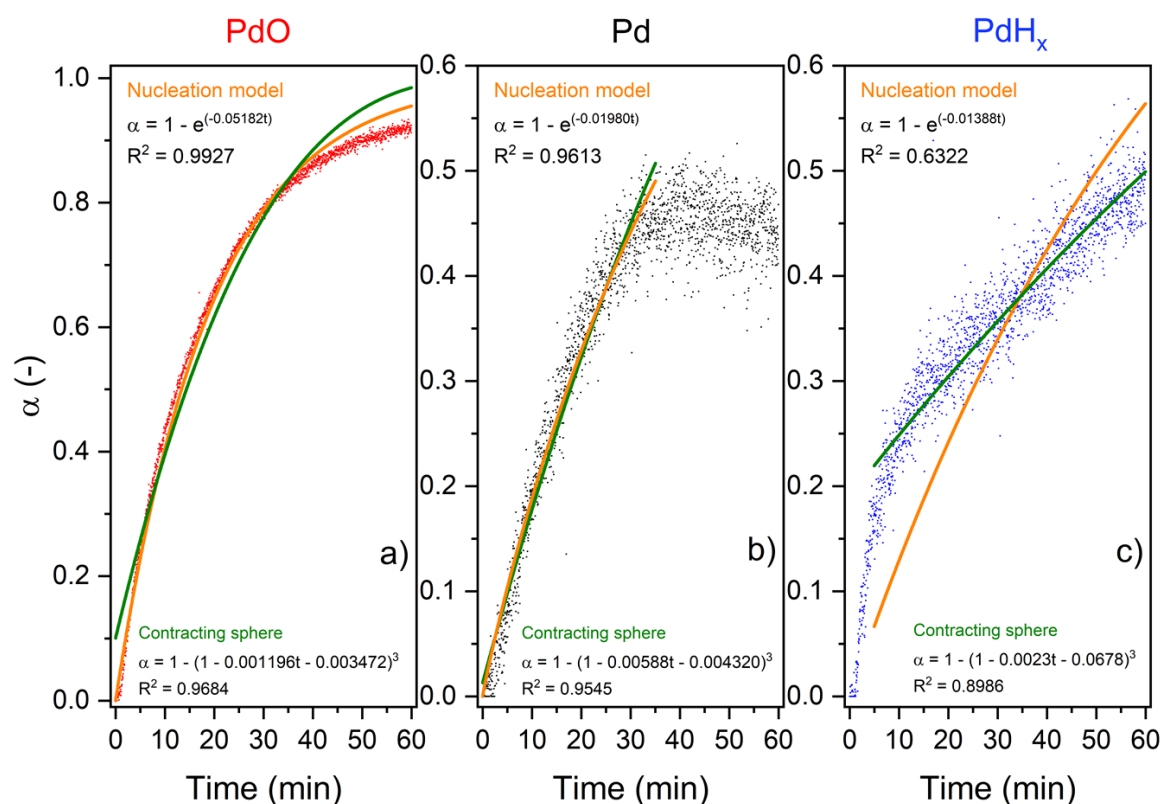
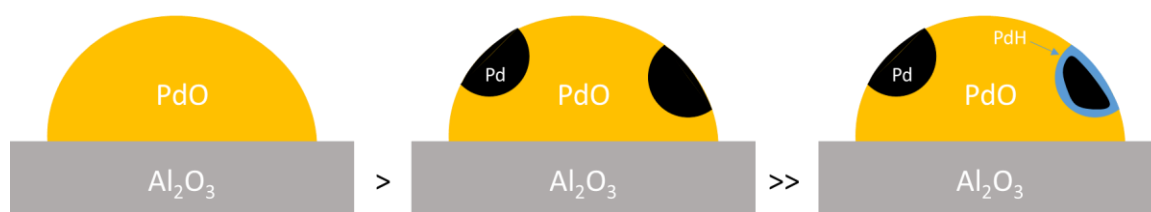


**Figure 3.5:** Results from fitting the LCF-XANES data (black dot) according to the nucleation model (orange) and contracting sphere model (green).

Based on this analysis a reaction mechanism for the reduction of PdO/Al<sub>2</sub>O<sub>3</sub> by H<sub>2</sub>-saturated cyclohexane at 70°C can be proposed as depicted in **Scheme 3.1**. During the initial phase of the reduction, metallic Pd domains nucleate in or at the surface of the PdO phase. These Pd

phase is only an intermediate and is transformed to PdH according to a contracting sphere model. After 60 min PdO is consumed almost completely but the relative amount of the Pd and the PdH phase could not be determined unequivocally. XRD data suggest that only about 10% of Pd remains while XAS data suggest that about 50% remains.



**Scheme 3.1:** Proposed reaction steps for the reduction of PdO and the formation of the PdH phase.

### 3.3.3 *In situ* attenuated total reflectance infrared spectroscopy

Attenuated total reflectance infrared (ATR-IR) spectroscopy was also used to follow the surface occupation at the surface of the catalyst as reported in **Figure 3.6**. In the course of the experiment the baseline changes significantly because of the changes of the refractive index as PdO is reduced to Pd.<sup>27</sup> For easier visualization of the spectral changes that occur, the spectra were aligned at 2385  $\text{cm}^{-1}$ . In addition to the change of refractive index, the formation of water was observed by the increase in intensity of the band at 3274  $\text{cm}^{-1}$ , stretching of the OH ( $\nu_{\text{OH}}$ ), and 1616  $\text{cm}^{-1}$ , water bending mode ( $\delta_{\text{OH}}$ ), of physisorbed water on the  $\text{Al}_2\text{O}_3$  support. The inset of **Figure 3.6** shows the temporal evolution of the point at 2385  $\text{cm}^{-1}$  together with the integrated area in the region of 1564-1722  $\text{cm}^{-1}$ . There is a small delay before the latter peak starts rising, then it reaches a maximum value at 28 min before it starts to continuously decay. The decrease of this signal is an indication that the reduction of PdO generating water is increasingly less important and that the flow of cyclohexane is sufficient to remove the accumulated water. Therefore, this is also an indication that the reduction PdO to Pd approaches completion.



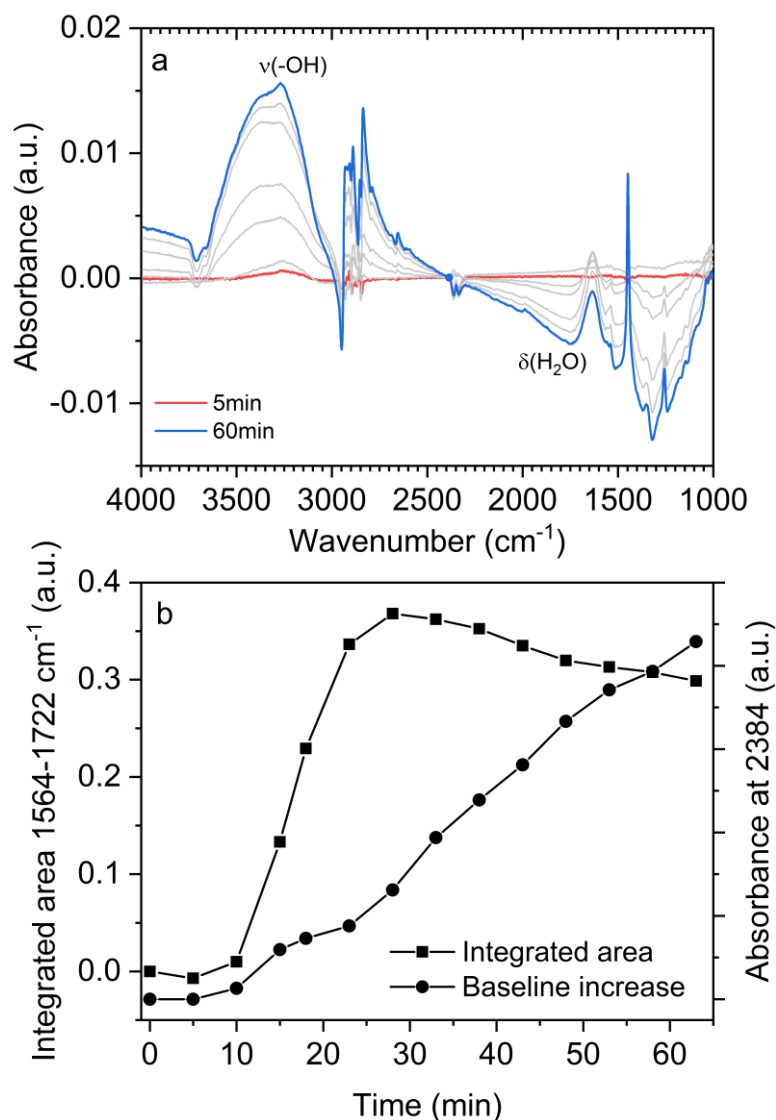


**Figure 3.6:** a) *In situ* ATR-IR spectra of PdO/Al<sub>2</sub>O<sub>3</sub> during reduction in H<sub>2</sub>-saturated cyclohexane, spectra aligned at 2385 cm<sup>-1</sup>. b) Temporal dependence of the integrated surface area between 1564-1722 cm<sup>-1</sup> and at the alignment point at 2385 cm<sup>-1</sup>.

### 3.4 Conclusion

The reduction of PdO/Al<sub>2</sub>O<sub>3</sub> by H<sub>2</sub>-saturated cyclohexane was investigated by *in situ* XAS, XRD and ATR-IR. We could show that a metallic Pd phase forms as intermediate to be further converted to PdH. The three methods show that over the 1 h required for the quasi total reduction of PdO, in the first 30 min the dominant reaction is reduction of PdO, with the concurrent formation of PdH. After 30 min, the reduction of PdO becomes a secondary process and most of the H<sub>2</sub> is used to convert Pd to PdH. Thanks to the high time resolution of XAS measurements, LCF analysis of the XANES allowed to propose a mechanism. PdO

reduction to Pd follows the nucleation model, while the formation of PdH is best described by the shrinking sphere model.

This type of studies allows to elucidate the mechanism of reaction taking place in presence of a liquid phase, as these might be different to when a gas phase is involved. Future studies should also include variations of process parameters such as solvent, temperature or type and concentration of the reductant to study their influence of reaction rates and mechanism.

## Chapter 4: *In situ* quantification of PdH

The present chapter is based on the manuscript in preparation: T. Fovanna, A. H. Clark, M. Nachtegaal, O. Kröcher, D. Ferri, Quantification of Pd hydrides on Pd/Al<sub>2</sub>O<sub>3</sub> in liquid environment. T. Fovanna performed part of the experiments, analyzed and interpreted the data. The manuscript was written with the co-authors.

## 4.1 Introduction

Palladium (Pd) is an established active metal for industrial scale hydrogenation of alkenes or carbonyls, among other functional groups, because of its high reactivity and ability to split hydrogen.<sup>71,72</sup> Pd forms an extensively studied hydride phase, which was first reported by T. Graham for its hydrogen storage properties.<sup>73</sup> Together with the industrial relevance of Pd as a catalyst, the characterization of this hydride phase has been of increasing interest, as it has been identified as the reactive species in hydrogenation reactions,<sup>74,75</sup> in hydrogen storage<sup>76–78</sup> and in electrochemical processes.<sup>74</sup> Most relevant characterization studies aiming at the detection and quantification of Pd hydrides (PdH) have previously been conducted in the gas phase,<sup>74,63,79</sup> while fine chemicals and active pharmaceutical ingredients often rely on liquid-phase catalytic processes.<sup>80</sup> Only a few studies have reported the presence of hydrides in liquid phase.<sup>75,81</sup> However, the utilization of the Pd hydride phase has not been studied so far under *in situ* or *operando* conditions in liquid phase in transient experiments and kinetic studies. Determination of kinetic rate constants of PdH under defined reactive conditions could help rationalizing effects typically associated with solvent properties such as polarity, hydrogen bonding capability and steric hindrance, affecting the hydride reactivity and stability in the liquid phase.

Three major techniques have been exploited to identify Pd hydrides in the gas phase; transmission electron microscopy (TEM),<sup>82</sup> X-ray diffraction (XRD)<sup>63,83</sup> and X-ray absorption spectroscopy (XAS) at both the K and L<sub>3</sub>-edges.<sup>63,83–85</sup> TEM, XRD and EXAFS probe the expansion of the Pd-Pd bonds upon formation of the hydride. However, *in situ* TEM studies in liquid environment is challenging especially because of beam-induced damage. While XRD and XAS do not suffer from major experimental limitations from measurements in liquid phase, they are ambiguous with respect to differentiation between the palladium hydride and palladium carbide phases because lattice expansion is anticipated for both phases in both methods. Hydrides can be identified more easily by characteristic features in X-ray absorption near edge structure (XANES) spectra.<sup>63</sup> The insertion of hydrogen in the Pd-Pd bond of Pd nanoparticles changes the empty density of states thus producing characteristic features in the spectra that enable to distinguish between  $\alpha$ -PdH and  $\beta$ -PdH phases *in situ*.<sup>86</sup> Quantification of the palladium-hydrogen stoichiometry has been achieved from extended X-ray absorption fine structure (EXAFS) spectroscopy using eq. (1) that is based on the measure of the Pd-Pd bond distance in bulk Pd, essentially in a Pd foil.

$$\frac{\Delta R(T)}{R_0(T)} = 0.0666x - 0.0164x^2 \quad \text{Eq. 4.1}$$

where  $\Delta R(T)$  is the change of the Pd-Pd bond distance induced by hydrogen insertion at a given temperature  $T$ ,  $R_0(T)$  the Pd-Pd bond distance in the bare (hydrogen free) nanoparticle at  $T$ , and  $x$  the H:Pd ratio ( $\text{PdH}_x$ ).<sup>79</sup> Eq. 4.1 is accurate for compositions in the  $0 < x < 0.5$  range but the model relies heavily on the accurate determination of bond distances ( $R_0(T)$ ) from the fit of FT-EXAFS data.<sup>74</sup>

Quantification of the hydride phase is key to understand the involvement of hydrides in liquid phase reaction mechanisms. Ideally, high time resolution is a prerequisite to determine the kinetics of their formation and consumption. XAS at the Pd K-edge (quickXAS) offers the advantage of sub-second time resolution required to capture such kinetics. Analysis of the large dataset of time-resolved quickXAS spectra by multivariate curve resolution alternating least square (MCR-ALS)<sup>87</sup> allows to extract spectra of the pure components, i.e. hydride, metallic Pd and PdO, and to quantify the fractions present at each point in time.

In this work, we combine the analysis of XAS spectra by MCR-ALS with temperature-programmed reduction (TPR) as a methodology for quantitative *in situ* determination of formation and consumption of Pd hydrides in gas and liquid phase experiments. This is achieved by combining the time-resolved XAS datasets obtained during hydride formation and desorption in the gas phase and quantification by  $\text{H}_2$ -TPR. MCR-ALS is then used to extract XAS spectra of the pure components present in all datasets. The thus developed quantitative methodology was used to follow the kinetics of hydride consumption during furfural hydrogenation in  $\text{H}_2$ -saturated 2-propanol at  $50^\circ\text{C}$ .<sup>88</sup>

## 4.2 Experimental

### 4.2.1 Materials and Chemicals

The reduced 5 wt.% Pd/ $\text{Al}_2\text{O}_3$  catalyst used in this study was kindly provided by Chimet (Viciomaggio, Italy) and exhibited a surface area of  $125 \text{ m}^2/\text{g}$ . The catalyst was prepared using the method described by Groppo et al.<sup>89</sup>

Hydrogen (Carbagas, 99.995% purity), 10 vol%  $\text{H}_2/\text{He}$  (Messer), helium (Carbagas, 99.9999% purity), 5 vol%  $\text{CO}/\text{Ar}$  (Messer) and 2-propanol (Merck LiChrosolv hypergrade for LC-MS) were used as received, while furfural (Sigma-Aldrich, 99%) was distilled prior to use.

#### 4.2.2 Characterization

*Transmission electron microscopy*-TEM images were taken using a JEOL 2010 microscope equipped with a LaB<sub>6</sub> filament, an energy dispersive X-rays spectrometer (EDS, Oxford Instrument) and a CCD camera (Orius from GATAN) with an acceleration voltage of 200 keV. A single tilt holder was used. The sample was prepared by depositing 5  $\mu$ L of a 2-propanol suspension of the catalyst powder on a holey carbon film supported on a 3 mm copper grid.

*Temperature-programmed reduction*-TPR experiments were carried out in a dedicated instrument (TPDRO 1100, ThermoScientific) equipped with a thermal conductivity detector (TCD). The sample (600 mg) was loaded at the bottom of a quartz reactor and was kept at 30°C in a flow of 10% vol H<sub>2</sub>/Ar (20 mL/min) for 15 min prior to heating. TPR profiles were collected in the temperature range of 30-600°C at and heating rates from 2°Cmin<sup>-1</sup> to 5°Cmin<sup>-1</sup> in the same gas flow. The hydrogen consumption and release were quantified from integration of the peak area and consideration of a response factor determined using a high purity CuO standard (Thermo Electron Corporation).

#### 4.2.3 X-ray absorption spectroscopy

Transmission quick X-ray absorption spectra were obtained at the Pd K-edge (24350 eV, quickEXAFS) at the SuperXAS beamline of the Swiss Light Source (SLS, Villigen) using 15 cm long ionization chambers filled with 1 bar N<sub>2</sub> and 1 bar Ar. Pd foil, mounted between the second and the third ionization chambers was used for internal energy calibration. The polychromatic beam resulting from the 2.9 Tesla superbent magnet was collimated using a Pt-coated collimating mirror, subsequently monochromatized by a channel-cut Si(111) crystal of the QuickXAFS monochromator and finally focused using a Pt-coated toroidal mirror to a spot size of 150  $\mu$ m $\times$ 150  $\mu$ m. Spectra were collected at 2 Hz, but only the spectra obtained while scanning from low to high energy were considered, resulting in a time resolution of one spectrum/sec. *In situ* experiments were carried out using the XAS/XRD cell. In a typical experiment, the sample (35 $\pm$ 1 mg) was firmly fixed between two quartz wool plugs.

During gas phase experiments the cell was connected to mass flow controllers delivering a total flow of 20 mL/min. The sample was heated in 10 vol% H<sub>2</sub>/He flow from 30°C to 170°C at 2°C/min and was then kept in this conditions for 15 min prior to switching to He flow and cooling to 30°C at 2°C/min .

In liquid phase experiments, the cell was connected to a high pressure liquid chromatography (HPLC) Azura P 4.1S pump (10 mL/min stainless steel pump head; Knauer) delivering solutions at a flow rate of 0.2 mL/min. Two back-pressure regulators (5.2 bar; Upchurch Scientific) were connected in series at the outlet of the cell in order to achieve a total pressure of 10.4 bar. The sample was contacted at 30°C with 2-propanol solvent was saturated with bubbling H<sub>2</sub> at 1 bar. After pressure equilibration, the cell was heated to 125°C (10°C/min) and was then held for 1 h. After reduction, the cell was cooled to 50°C and the feedstock solution was changed to a H<sub>2</sub>-saturated 2-propanol solution of furfural (5 mM).

XAS spectra were collected throughout the experiments. All spectra were energy-corrected, normalized and smoothed using a Python script.<sup>64</sup> The processed time-resolved XAS spectra collected during heating in 10 vol% H<sub>2</sub>/He, cooling in He and in the complete liquid phase experiment were processed all simultaneously with principal component analysis (PCA) by fixing the number of components to 3. Then, the whole dataset was submitted to the multivariate curve resolution alternating least squares (MCR-ALS) algorithm with the constraints that the components fraction is comprised between 0 and 1 and is non-negative, and that the total concentration of components sums to unity.<sup>90</sup> This approach results from the nature of MCR-ALS, a method that does not require reference spectra and generates spectra of pure components able to fully describe the system at hand.<sup>87</sup> For this purpose, it requires a data set with the largest diversity of sample state and composition. Feeding the algorithm with a large number of spectra improves the accuracy of the determination of the representative components of the system. Processing all data together by MCR-ALS ensures also the elimination of biases, for example related to ambiguity on whether hydrides deliver the same spectra irrespective of gas and liquid phase. Hence, components are obtained that are able to cope with both reactive environments in a quantitative manner.

Fitting of selected EXAFS spectra was performed using the Demeter software package.<sup>91</sup> Spectra were subjected to background subtraction, converted to the photo-electron wave-vector by setting the first inflection point of the absorption edge to 24.35 keV followed by the Fourier transform of the k<sup>2</sup>-weighted spectra in the range  $k = 3\text{--}11 \text{ \AA}^{-1}$ . The first Pd-Pd shell of the EXAFS spectra was fitted using an amplitude reduction factor of 0.83 that was obtained from the fit of a Pd-foil reference spectrum.

Linear combination fitting (LCF) analysis of the XANES spectra was performed using the corresponding Prestopronto package using selected spectra as references.<sup>92</sup>

#### 4.2.4 Attenuated total reflectance infrared spectroscopy

An aqueous suspension of the catalyst (10 mg in 1.5 mL) was stirred for 15 min and deposited on a ZnSe internal reflection element (IRE, 45°, 52 x 20 x 2 mm; Crystran) before drying overnight under fume hood. The crystal was loaded in an in-house built ATR-IR cell, which was mounted in the IR spectrometer (Bruker, Vertex 70). The IR spectrometer was equipped with a liquid-nitrogen cooled mercury cadmium telluride (MCT) detector and a 4-mirrors ATR assembly (Specac). All spectra were collected at 40 kHz scanner velocity and 4 cm<sup>-1</sup> resolution by averaging 30 scans. The dry catalyst layer deposited on the IRE was equilibrated at 75°C for 1 h with 2-propanol saturated with H<sub>2</sub> bubbling at 1 bar prior to cooling to 50°C until a stable signal was obtained, which was used as background spectrum. Then, a H<sub>2</sub>-saturated 2-propanol solution of furfural (5 mM) was allowed to enter the ATR-IR cell while spectra were recorded consecutively. After 30 min, the exiting solution was analysed by gas chromatography (Trace GC, equipped with HP-5 30 m x 0.025 mm x 0.5 µm Agilent column and a flame ionisation detector, FID). The same procedure was employed for CO adsorption at 50°C by flowing 2-propanol saturated with 5 vol% CO/Ar bubbling at 1 bar after reduction at 75°C as described above.

#### 4.2.5 Diffuse reflectance infrared Fourier transform spectroscopy

CO adsorption from gas phase was followed by DRIFTS. The home-made DRIFT cell<sup>42</sup> fitted with a flat CaF<sub>2</sub> window (d = 25 mm) and loaded with the sample (35 mg) was loaded in a Praying Mantis mirror assembly. In analogy to the liquid phase experiment, the sample was heated to 75°C in a flow of H<sub>2</sub> and reduced for 1 h prior to cooling to 50°C and collection of a background spectrum. Then, CO adsorption was monitored for 30 min while flowing 5 vol% CO/Ar and collecting spectra at 40 kHz scanner velocity and 4 cm<sup>-1</sup> resolution by averaging 50 scans.

### 4.3 Results and Discussion

The catalyst sample was composed of dispersed Pd nanoparticles of average size 2.5±0.5 nm (**Figure C1-Appendix**) on θ-Al<sub>2</sub>O<sub>3</sub> (**Figure C2-Appendix**). The Pd K-edge X-ray absorption data confirmed that the received sample was pre-reduced. A clear first Pd neighbor was observed in the Fourier transformed EXAFS data. However, both XANES and EXAFS data revealed that the reduced state was accompanied by a fraction of oxidized Pd, most likely due to the prolonged exposure to ambient air. Linear combination fit (LCF) of the



XANES region of the sample using the spectra of a Pd foil and of bulk PdO suggests that PdO amounted to 50 %.

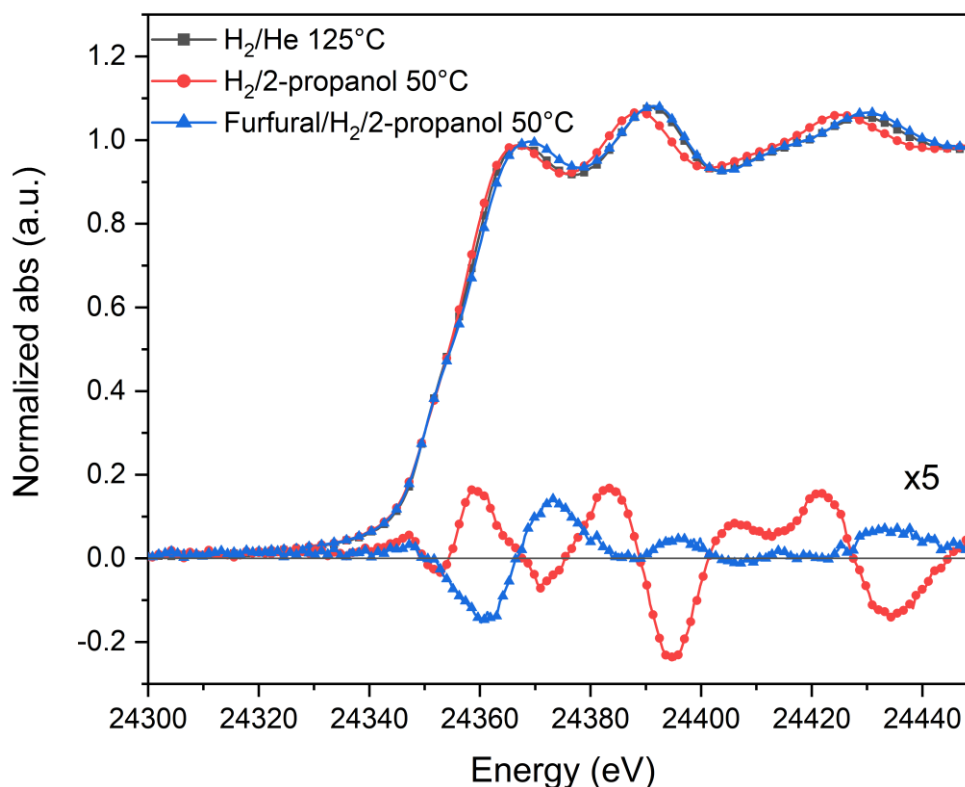


**Figure 4.1:** Pd K-edge XANES spectra of 5 wt.% Pd/Al<sub>2</sub>O<sub>3</sub> obtained in He at 125°C (grey), in H<sub>2</sub>-saturated 2-propanol at 50°C (red) and in H<sub>2</sub>-saturated 2-propanol solution of furfural (5 mM). Difference XANES spectra obtained by subtracting the XANES spectrum obtained in He from the other two spectra.

**Figure 4.1** shows the transmission Pd K-edge X-rays absorption spectra of 5 wt.% Pd/Al<sub>2</sub>O<sub>3</sub> collected at 50°C after reduction in H<sub>2</sub>-saturated 2-propanol at 125°C followed by 30 min exposure to a H<sub>2</sub>-saturated solution of furfural (5mM) together with that of the same catalyst reduced at 125°C in an identical gas phase experiment. Comparison with the reference Pd foil suggests that the catalyst was in reduced state after reduction at 50°C in 2-propanol and at 125°C in gas phase. While the two spectra are close to identical, a shift of the spectrum obtained in H<sub>2</sub>-saturated 2-propanol can be discerned that is typically attributed to the formation of hydrides.<sup>63</sup> This shift can be better appreciated in the difference spectra obtained after subtraction of the spectrum of Pd/Al<sub>2</sub>O<sub>3</sub> after gas phase reduction from the other two spectra (**Figure 4.1**). The difference spectra are not featureless contrary to what might be expected upon subtraction of spectra of reduced catalysts. The XANES features that are related to hydrides are clearly visible when furfural is absent (**Figure 4.1-red**).<sup>63</sup> In contrast,

the features have vanished after introduction of the furfural solution and have been replaced by new features.<sup>63</sup>

Besides XANES, EXAFS also provides evidence of hydride formation from the average value of the Pd-Pd bond distance. In **Table 4.1** are reported the results of the fitting of FT-EXAFS of the related spectra during liquid phase experiment. Because the use of EXAFS data in eq. 4.1 requires the knowledge of  $R_0(I)$  and  $\Delta R(I)$ , two spectra were obtained at 50°C and at 125°C while cooling in He after gas phase reduction at 180°C. The two spectra should represent bare Pd metal nanoparticles free of hydrogen. The bond distance of the first Pd neighbour in the three spectra is reported in **Table 4.1** together with the corresponding hydride concentration determined according to Eq. 4.1<sup>79</sup> and to the methodology described in the following. While the H:Pd stoichiometry obtained by EXAFS fitting and Eq. 4.1 is lower than that obtained by combination of TPR and XANES, it has to be recalled that Eq. 4.1 considers bulk Pd and that Pd nanoparticles may behave differently.<sup>93</sup> Moreover, carbon insertion affects also in a very similar way the average Pd-Pd bond distance determined by EXAFS making this method ambiguous. Hence, XANES appears more reliable and its use is described in the following.

**Table 4.1:** EXAFS fit of the Pd first shell during 2-propanol (IPA) experiment. FUR = furfural.

	N	R	$\sigma^2$	$\Delta E$	Red. $\chi^2$	PdH <sub>x</sub>	PdH <sub>x</sub>
	[ <sup>-</sup> ] <sup>a</sup>	[Å] <sup>b</sup>	[ <sup>-</sup> ] <sup>c</sup>	[ <sup>-</sup> ] <sup>d</sup>	[ <sup>-</sup> ] <sup>e</sup>	[ <sup>-</sup> ] <sup>f</sup>	[ <sup>-</sup> ] <sup>g</sup>
125°C IPA/H <sub>2</sub>	10.1 ± 0.4	<b>2.794</b> ± 0.003	0.0100 ± 0.0004	4.2 ± 0.3	47.6	0.36	-
50°C IPA/H <sub>2</sub>	9.9 ± 0.3	<b>2.804</b> ± 0.002	0.0086 ± 0.0003	4.2 ± 0.2	36.2	0.43	0.37
50°C FUR/IPA/H <sub>2</sub>	9.5 ± 0.4	<b>2.751</b> ± 0.003	0.0074 ± 0.0004	4.9 ± 0.3	106.5	0.05	0.00

<sup>a</sup> Coordination number. <sup>b</sup> Pd-Pd bond distance. <sup>c</sup> Pseudo Debye Waller factor. <sup>d</sup> Energy shift. <sup>e</sup> Reduced chi square. <sup>f</sup> x in PdH<sub>x</sub> obtained from Eq 4.1 and EXAFS analysis. <sup>g</sup> x in PdH<sub>x</sub> by TPR/XAS.

#### 4.3.1 Gas phase experiments

Temperature programmed reduction by hydrogen (TPR) was performed to quantify the amount of hydrogen desorbed from and consumed by the catalyst. **Figure 4.2** shows three consecutive TPR measurements from 30°C to 180°C (TPR-1), from 30°C to 400°C (TPR-2) and from 30°C to 600°C (TPR-3). The aim of the consecutive TPR was to investigate the effect of the end temperature of each ramp on the amount of desorbed and consumed hydrogen. Prior to each TPR experiment, the catalyst was kept in a reducing flow of 10 vol%

H<sub>2</sub>/Ar for 15 min in order to reduce the oxide layer created by the long exposure of the sample to ambient air. The negative peak (H<sub>2</sub> release) centred at 56°C in the three consecutive TPR sequences is readily attributed to desorption of hydrogen from decomposition of hydrides<sup>89,94</sup>. The similar areas of this peak in TPR-1 and TPR-2 suggest that heating the sample to 180°C did not affect significantly the proportion of the hydride phase. Based on calibration of the thermal conductivity signal with CuO providing the amount of desorbed hydrogen and on the amount of Pd loaded in the experiment, the H:Pd ratio was 0.41 (PdH<sub>0.41</sub>) for TPR-1 and TPR-2.

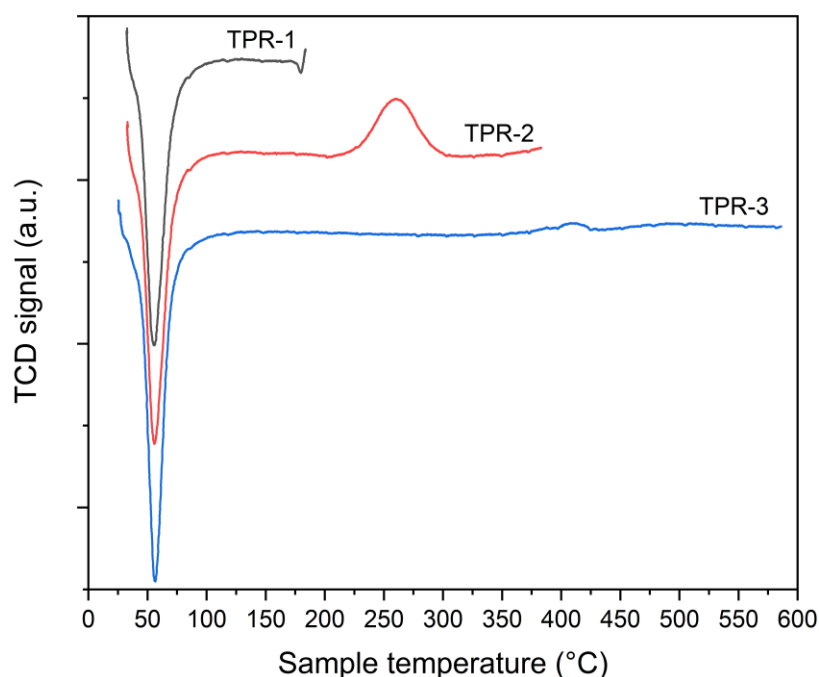


**Figure 4.2:** TPR experiments on 5 wt.% Pd/Al<sub>2</sub>O<sub>3</sub> from 30°C to 180°C (black, TPR-1), 30°C to 400°C (red, TPR-2) and 30°C to 600°C (blue, TPR-3). Conditions: 10 vol% H<sub>2</sub>/Ar, 2°C/min.

In TPR-2 performed up to 400°C, a positive peak (H<sub>2</sub> consumption) appeared at 260°C that reflects the reduction of the residual PdO observed by XAS. It corresponds to a H:Pd ratio of 0.07, thus indicating that 7% of Pd remained as PdO and was reduced only at 260°C. Because more Pd metal was obtained at the end of TPR-2, the negative peak of hydrides was accordingly larger in TPR-3, while the positive peak at 260°C was absent indicating unambiguously that Pd reduction was complete after reduction at 400°C (TPR-2). The amount of desorbed hydride increased from TPR-1/TPR-2 to TPR-3 corresponding to an increase of H:Pd ratio from 0.41 to 0.47, thus consistently with the value of hydrogen consumed for the reduction of PdO in TPR-2. These values of PdH<sub>x</sub> are coherent with previous work and are characteristic of the  $\beta$ -PdH phase<sup>74,78,63,85,95</sup>.

Heating and cooling segments of TPR experiments carried out at different ramping rates (2-5 °C/min; **Figure 4.3**) returned values of the energy of desorption and adsorption of H<sub>2</sub> of 1 and 1.3 kJ/mol, respectively, in agreement with the fact that hydrogen adsorption-desorption on Pd metal does not require activation.<sup>40</sup>

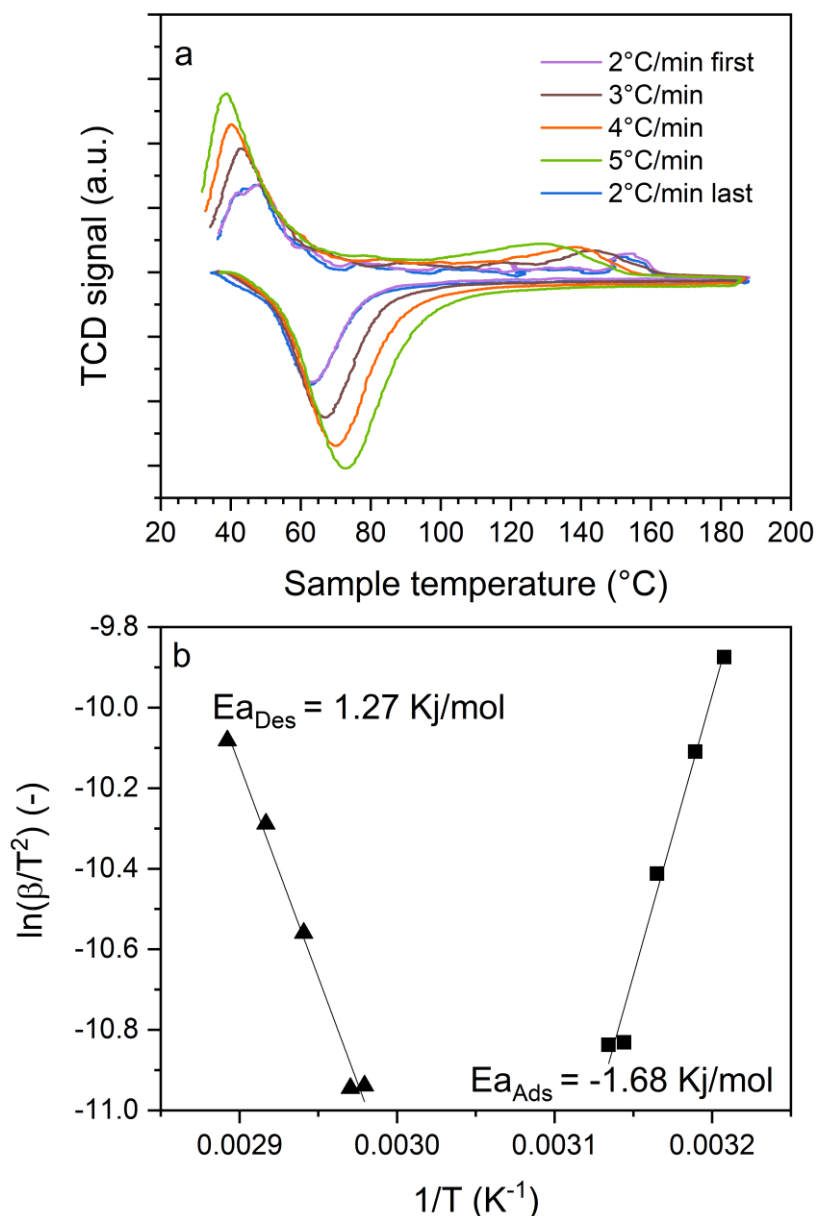


**Figure 4.3:** a) TPR experiments at various heating and cooling ramps (2-5°C·min<sup>-1</sup>). b) Arrhenius plots for adsorption-desorption of Pd hydrides.

The TPR procedure was repeated in the XAS cell in order to assign a spectrum to the PdH<sub>x</sub> fraction established by TPR on the same sample. Various factors, including particle shape and temperature of reduction, can affect the amount of hydrogen stored in the Pd nanoparticles<sup>78,94</sup>. After reduction at 30°C, the catalyst was heated to 160°C to enable observation of desorption of the hydrides by XAS, similar to TPR-1 in **Figure 4.2**. Finally, the gas flow was switched to

He to obtain the reference spectrum of the bare Pd nanoparticles and the sample was cooled to 30°C. Pd nanoparticles are termed bare at this point because hydrides have desorbed. The complete time-resolved XAS dataset measured in the two segments (heating and cooling) was analyzed using MCR-ALS. **Figure 4.4** combines the integrated area of the TCD signal obtained in TPR-1 and the fraction of hydrides obtained from MCR-ALS analysis of the XAS dataset as a function of temperature after a more elaborated data analysis which is described in **Figure 4.5**. Both curves exhibit the same shape. The difference of desorption temperature ( $\Delta T = 9^\circ\text{C}$ ) obtained from the first derivative of the profiles (**Figure C3-Appendix**) is reasonable when considering the differences in geometry, temperature recording and temperature gradients between the TPR reactor and the XAS cell.

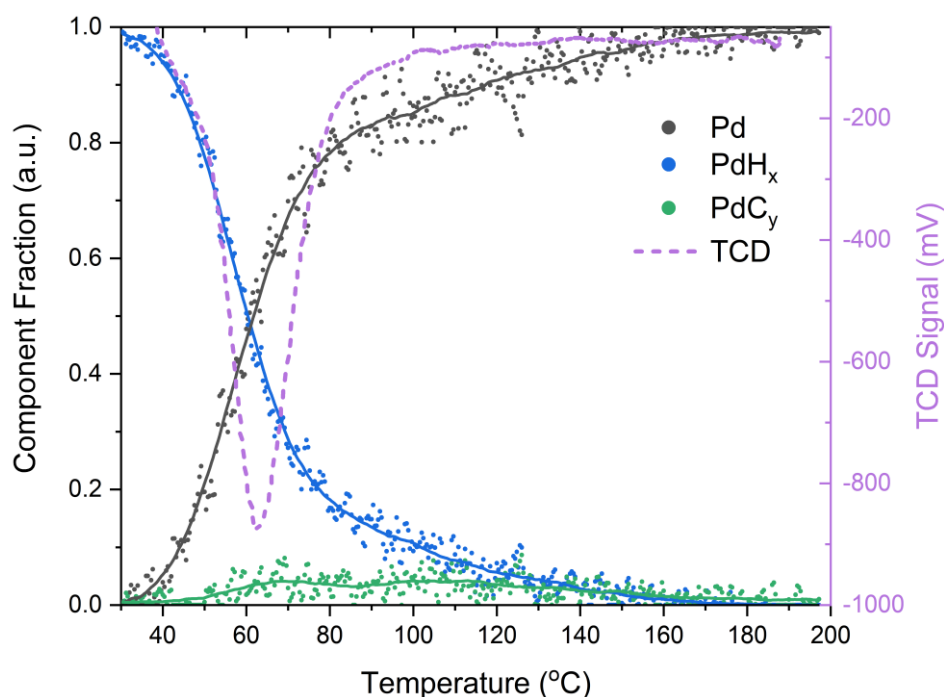


**Figure 4.4:** MCR-ALS of *in situ* XANES spectra obtained while heating 5 wt.% Pd/Al<sub>2</sub>O<sub>3</sub> in 10 vol% H<sub>2</sub>/He to 160°C at 2°C/min. The integrated TCD signal during a similar TPR experiment is also shown.

The procedure to obtain the four components shown in **Figure 4.6** is schematically represented in **Figure 4.5** and is described as follows:

- a) The data set containing the TPR experiment in H<sub>2</sub>/Ar was loaded into the MCR-ALS program. Then PCA returned that two component were necessary to describe the dataset. The data were then processed using MCR-ALS, applying the non-negativity constraint to the spectral components and the component concentrations to sum to one. Analysis returned a concentration profile and two pure components-Pd and PdH<sub>0.4</sub>, which will be used as input later.

- b) The data set containing the liquid phase experiment with furfural was loaded into the MCR-ALS program. The data were then processed using MCR-ALS but including three initial guesses, Pd and PdH<sub>0.4</sub>, and the last spectrum from the analysed dataset, applying the same constraints as in step a. Using these spectra, MCR-ALS analysis returned three refined pure components-Pd, PdH<sub>x</sub> and PdC<sub>y</sub>.
- c) For the sake of comparison the TPR dataset was reanalysed by linear combination fitting (LCF) using Pd-Pd<sub>0.40</sub>-PdC<sub>y</sub>. The returned profile was consistent with the one obtained in step **a** and no contribution of PdC<sub>y</sub> was observed.
- d) Finally, the dataset with the furfural switch in 2-propanol was analysed by LCF using four components, Pd (step **a**)-PdH<sub>0.4</sub> (step **a**)-PdC<sub>y</sub> (step **b**) – PdO. PdO was obtained by measuring a sample of supported PdO nanoparticles on Al<sub>2</sub>O<sub>3</sub>. The procedure returned the concentration profile show in **Figure 4.6**.

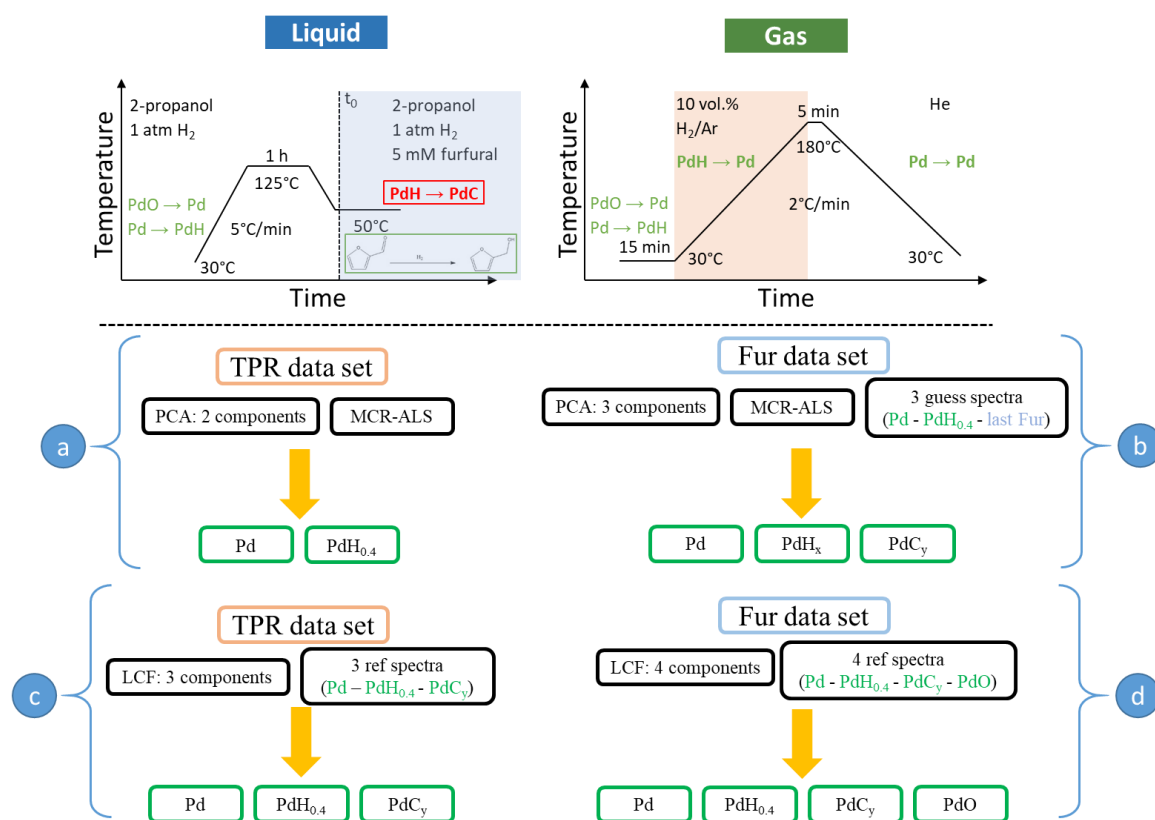


**Figure 4.5:** Fitting procedure used in the present work. This work was performed after processing of the data (normalization and energy correction) using ProQEXAFS.<sup>64</sup>

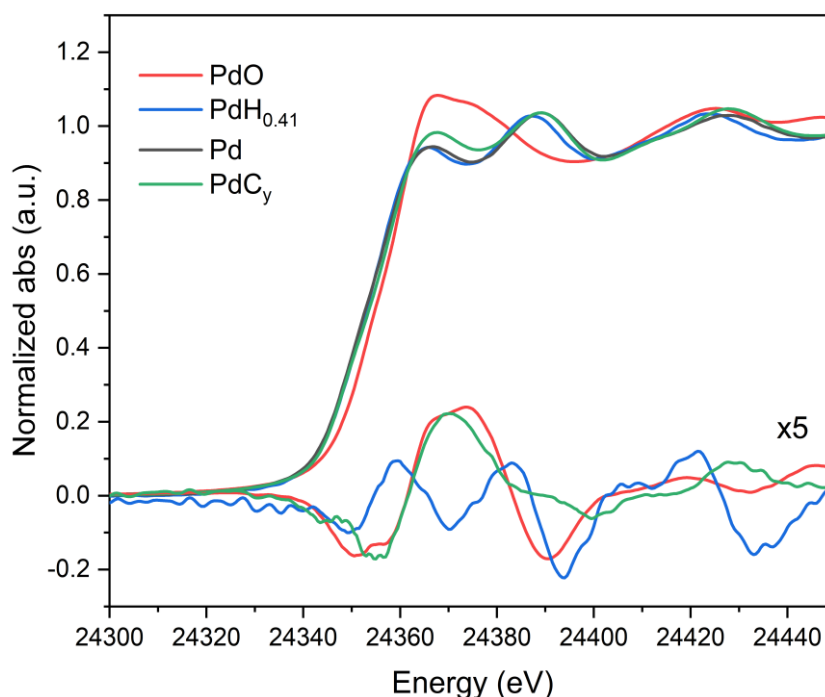


**Figure 4.6:** MCR-ALS refined components used in the LCF procedure for analysis of the XAS-TPR and of the liquid phase kinetic.

#### 4.3.2 Liquid phase experiments

Similar to the gas phase, it was necessary to reduce the oxide phase present on the catalyst in the experiment in the liquid environment. For this purpose, a  $H_2$ -saturated 2-propanol solution was passed through the catalyst bed at  $125^\circ C$  for 1 h. After this reductive treatment, the XANES spectrum of **Figure 4.1** exhibited the same features observed for the Pd hydrides in the gas phase experiments<sup>96</sup>. However, **Figure 4.4** clearly shows that hydrides desorb below  $70^\circ C$  in gas phase experiments. Hence, the stability of hydrides increases significantly in the liquid environment in the temperature regime where bare Pd metal is observed in the gas phase.

Utilization of the hydrides generated under these experimental conditions is a central topic for liquid-phase catalysed hydrogenation reactions. Hence, the above procedure to quantify the fraction of hydrides present on  $Pd/Al_2O_3$  in the liquid environment using MCR-ALS and the dataset of the gas phase experiments (**Figure 4.4**) was repeated by adding the dataset of time-resolved XAS spectra during furfural hydrogenation. The traces in **Figure 4.7** show the temporal evolution of the various Pd species obtained by MCR-ALS starting from the point where a  $H_2$ -saturated solution of furfural was admitted to the catalyst bed to enable liquid phase hydrogenation. The right y-axis scale of **Figure 4.7** is adapted from the gas phase experiment shown in **Figure 4.4**.

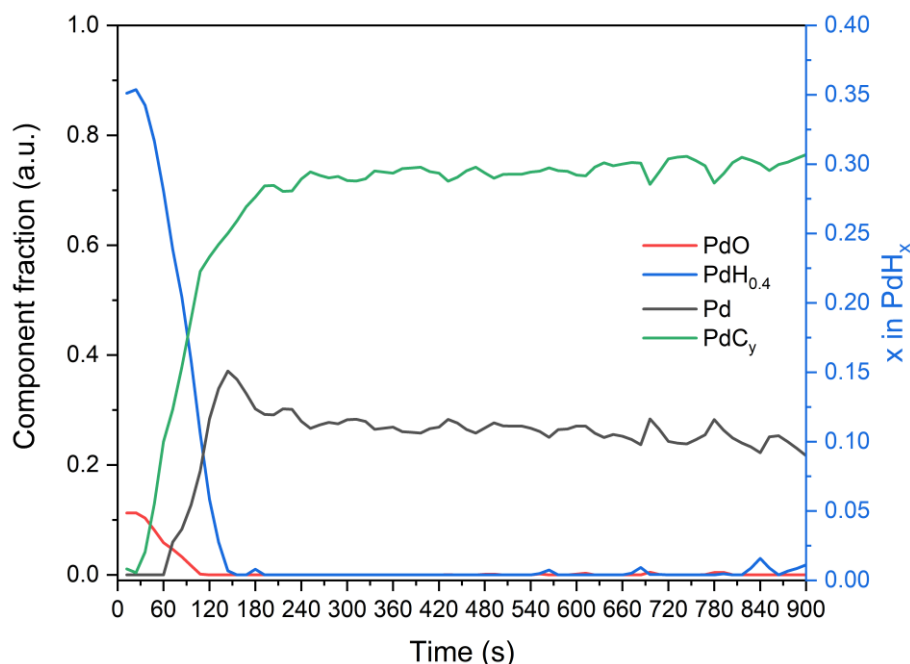


**Figure 4.7:** MCR-ALS of *in situ* XANES spectra collected at 50°C during furfural hydrogenation on 5 wt.% Pd/Al<sub>2</sub>O<sub>3</sub>. PdO component fraction (red), Pd component fraction (black), PdC (green) PdH (blue) component fraction are displayed on the right y-axis and H: Pd ratio is displayed on the left y-axis.

At  $t = 0$ , the initial fraction of hydrides in H<sub>2</sub>-saturated 2-propanol at 50°C is lower to what was achieved in 10 vol% H<sub>2</sub>/He at 30°C in **Figure 4.4** with a hydride fraction of 88% and an initial PdO fraction of 10%, the rest being the Pd metal component. Then, the concentration of hydrides decreases to zero with 180 s. Together with the changes associated with Pd metal and the hydrides component returned also an increase of the carbide. After exposure of the catalyst to the furfural solution for 30 min, the features in the XANES spectra changed towards those that are considered representative of Pd carbide species as shown in **Figure 4.1**.<sup>63</sup>

Analysis of the outlet solution in this experiment by gas chromatography (GC) revealed 5% conversion of furfural to both furan and furfuryl alcohol occurred, the former being the major product. We have performed a similar *operando* ATR-IR experiment in a dedicated cell, hence different, that revealed a higher furfural conversion (25%) but similar selectivity under the same conditions of temperature and pressure. The ATR-IR experiment was performed to observe the surface of the Pd/Al<sub>2</sub>O<sub>3</sub> catalyst from the perspective of the adsorbates evolving during furfural hydrogenation. The spectrum obtained after flowing a H<sub>2</sub>-saturated 2-propanol furfural solution for 30 min evidences the formation of adsorbed CO (**Figure 4.8**). The intense band at 1915 cm<sup>-1</sup> and the weak signal at 2000 cm<sup>-1</sup> were readily associated to bridged CO (CO<sub>B</sub>) and linear bonded CO (CO<sub>L</sub>), respectively<sup>89</sup>. The strong CO signals are accompanied by the carbonyl bands of dissolved furfural ( $\nu(\text{C}=\text{O})$  at 1704 and 1684 cm<sup>-1</sup>). The first information



from the vibrational experiment complementary to the XAS experiment is thus that decarbonylation of furfural occurred. Furan was identified at the end of the experiment using GC. The result is in agreement with the known decarbonylation activity of Pd-based catalysts.<sup>97</sup>

The XAS data show that the hydrides were consumed simultaneously (**Figure 4.7**) and that they were replaced by other species, whose features resemble those of carbides (**Figure 4.1**). The removal and consumption of the hydrides must occur because a reaction proceeds at the surface of the metal particles and its intermediates or by-products are able to cause the decay of the XAS signal of the hydrides. Because at this point in time CO covers the Pd surface, CO adsorption from 2-propanol was carried out at 50°C in the XAS cell after preparing the hydrides as described above.

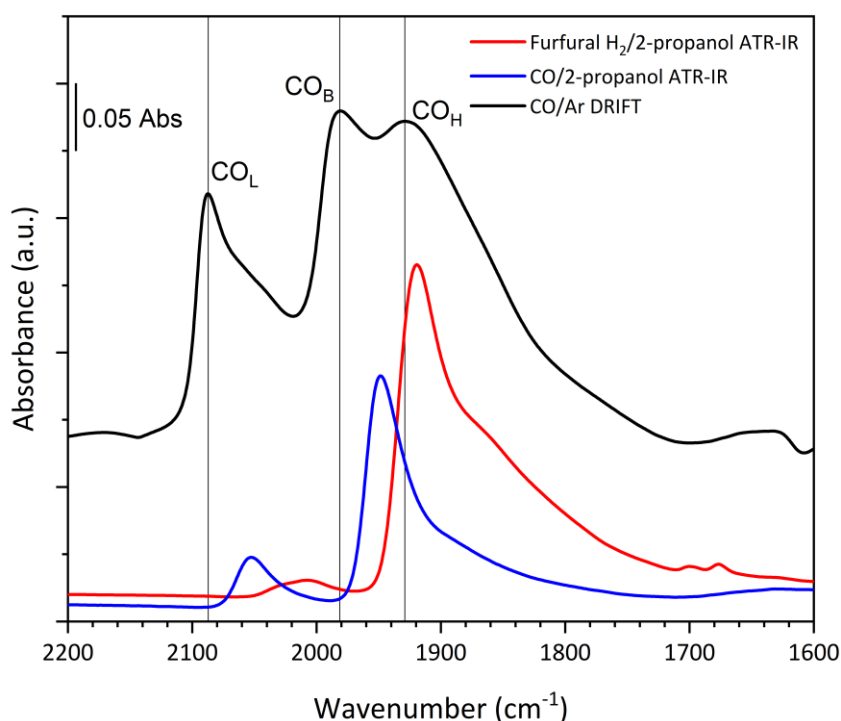


**Figure 4.8:** CO adsorption on 5 wt.% Pd/Al<sub>2</sub>O<sub>3</sub> in the gas phase (black) and from CO-saturated 2-propanol (blue). The red spectrum is an in situ ATR-IR spectrum obtained upon admittance of H<sub>2</sub>-saturated 2-propanol solution of furfural (5 mM) on the same catalyst. The gas phase CO adsorption spectrum is scaled by a factor 0.3.

Because adsorbed CO observed by ATR-IR derives from a chemical reaction (decarbonylation), it is interesting to compare the CO coverage and the Pd site occupancy with respect to the available Pd surface from both the gas phase and liquid phase experiments. The spectrum of adsorbed CO in a gas phase experiment (5 vol% CO/Ar; **Figure 4.8**) is similar to the transmission spectrum obtained for the same catalytic material.<sup>89</sup> Besides CO<sub>L</sub> and CO<sub>B</sub>, the hollow bonded CO (CO<sub>H</sub>) is present, which appears as a shoulder of CO<sub>B</sub> in 2-propanol, suggesting that CO<sub>H</sub> is less favourable in liquid phase. **Figure 4.8** shows that not only

adsorption of CO from the gas phase but also adsorption of CO from the liquid phase (CO-saturated 2-propanol) produces a different spectrum from that obtained during furfural hydrogenation. The most striking difference is the bathochromic shift of the CO bands by  $20\text{ cm}^{-1}$ . Moreover, the ratio of the integrated areas of the  $\text{CO}_\text{B}$  and  $\text{CO}_\text{L}$  signals ( $\text{CO}_\text{B}/\text{CO}_\text{L}$ ) was 7.7 in the case of CO adsorption in 2-propanol, while it reached a value of 44.6 in the experiment with furfural.

While we consider that the difference between adsorption of CO from gas phase and from 2-propanol may arise from the different experimental conditions under which adsorption was performed, but also because of the presence of a polar liquid environment (2-propanol), the explanation of the different behaviour during reaction and upon CO adsorption in the liquid environment is more difficult to rationalize. The shift observed during reaction could be attributed to the presence of furfural or the carbide phase, as reactive environment that influences the electronegativity of the surface. We consider the different  $\text{CO}_\text{B}/\text{CO}_\text{L}$  ratio as an indication that the coverage of Pd(111) sites by CO is lower in the presence of furfural and hydrogen than when only CO is present in solution. This might indicate that the Pd(111) sites that are free of CO can perform furfural hydrogenation to furfuryl alcohol, the competing reaction to furfural decarbonylation. The changes in the properties of CO uptake by the Pd nanoparticles are attributed to interaction of adsorbed CO from furfural decarbonylation with fragments of organic molecules deriving from furfural (e.g. furans).

## 4.4 Conclusions

We introduced a new method, where gas phase TPR experiments are combined with MCR-ALS and LCF analysis of XANES spectra, which allows quantification of palladium hydrides in both in gas and liquid phase experiments in a time resolved manner. The fate of the palladium hydride species was then determined upon their exposure to a solution of furfural. The presented method guaranteed to follow the change in concentration of the palladium hydride along time. First, hydrides were displaced upon introduction of furfural, which coincided with the adsorption of CO, observed by ATR-IR, originating from furfural decarbonylation. Second, The XAS spectra changed from those corresponding to hydrides, to those provided by interaction of Pd with C-containing species, likely deriving from the transformation of furfural. The possibility to follow the concentration of palladium hydride quantitatively, while selectively distinguishing from the palladium carbide, opens new possibilities for the study of liquid phase heterogeneous catalytic reactions.

# Chapter 5: Phosphorus promoted Ru/Al<sub>2</sub>O<sub>3</sub>

The present chapter is based on the postprint version of the publication: T. Fovanna, S. Campisi, A. Villa, A. Kambolis, G. Peng, D. Rentsch, O. Kröcher, M. Nachtegaal, D. Ferri, Ruthenium on phosphorus-modified alumina as an effective and stable catalyst for catalytic transfer hydrogenation of furfural, *RSC Advances*, **2020**, 10 (19), 11507-11516. T. Fovanna performed part of the experiments, analyzed and interpreted the data. The manuscript was written with the co-authors.

## 5.1 Introduction

Biomass can be converted into a pool of highly functionalized, platform molecules<sup>3,98</sup> to enable the synthesis of fine chemicals, pharmaceuticals, intermediates, polymers and additives. The production of value-added compounds from biomass involves catalytic transformations, where the catalyst design represents a key factor for achieving the desired efficiency and selectivity.<sup>99</sup> In this view, the catalytic transfer hydrogenation (CTH), consisting in the use of organic molecules as sources of hydrogen, represents a valid alternative, which minimizes safety hazards deriving from handling high pressure hydrogen gas.<sup>100</sup>

A large variety of metal-based catalysts have been proposed in the literature as alternatives for CTH<sup>101</sup> and include cobalt,<sup>102</sup> nickel,<sup>103</sup> copper,<sup>104</sup> platinum,<sup>105</sup> palladium<sup>106</sup> and ruthenium<sup>107</sup>. Ruthenium emerged by its superior activity and efficiency under liquid phase conditions and by its lower cost compared to other precious metals.<sup>108</sup> Ru/Al<sub>2</sub>O<sub>3</sub><sup>109–112</sup> and Ru on carbonaceous supports<sup>113</sup> are well studied hydrogenation catalysts. Interest in Ru as an effective metal for the hydrogenation of biomass-derived carbonyl compounds in the aqueous phase<sup>114–117</sup> has probably increased due to its unique oxophilicity and ability to dissociatively adsorb water molecules.<sup>118</sup> However, Ru-based catalysts often suffer from the lack of stability, due to passivation, poisoning or leaching of Ru species.<sup>119</sup> Besides the possibility to alloy Ru with Au to improve the stability for hydrogenation reactions,<sup>120</sup> modifiers and promoters can be used to increase the efficiency and the stability of the catalysts.<sup>121</sup> Organic linkers,<sup>122</sup> metal oxides<sup>123</sup> as well as heteroatoms introduced on the support<sup>124</sup> can commonly act as promoters by anchoring metal species, introducing defects or stabilizing particular oxidation states of the active metal.<sup>125</sup> P-containing functionalities (e.g. phosphates, phosphides) form a broad class of promoters, which are experiencing a growing interest in the field of heterogeneous catalysis for biomass valorization.<sup>126–137</sup> Besides acting as ligands for the stabilization of metal species, P introduces Brønsted acid sites on the support surface and promotes electron transfer phenomena resulting in enhanced activity.<sup>130,136</sup>

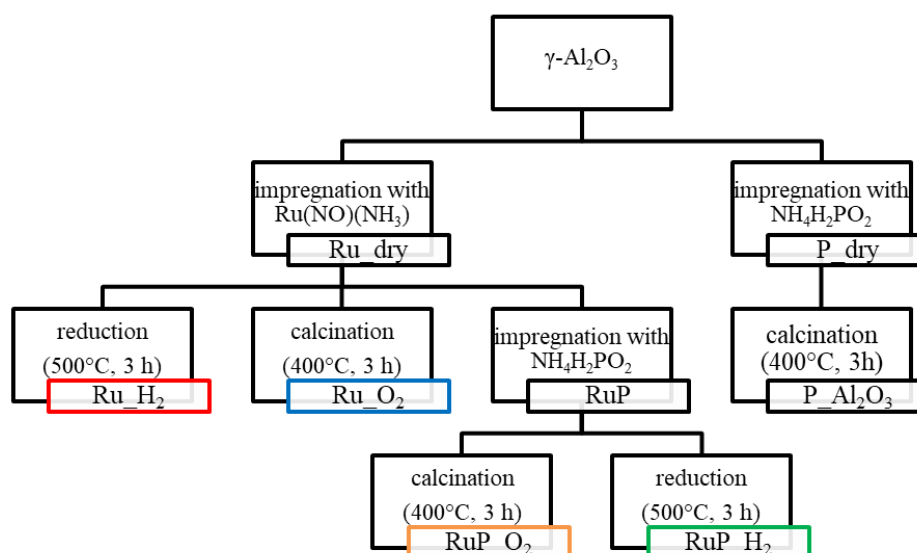
In this work, we investigate the effect of the modification of alumina with P on the catalytic performance of Ru towards CTH of furfural in the presence of isopropanol as hydrogen donor. A suite of characterization techniques (X-ray powder diffraction, X-ray absorption spectroscopy, attenuated total reflectance infrared spectroscopy, temperature programmed reduction, solid-state nuclear magnetic resonance spectroscopy, transmission electron microscopy) was used to clarify the nature, structure, speciation and coordination of Ru species

as well as of P functionalities on the alumina surface. This information allowed rationalizing the catalytic results in the frame of appropriate structure-activity relationships.

## 5.2 Experimental

### 5.2.1 Catalyst synthesis

The catalyst precursor (Ru<sub>dry</sub>) was obtained by impregnation of  $\gamma$ -Al<sub>2</sub>O<sub>3</sub> (PURALOX NWA155, Sasol; 132 m<sup>2</sup>/g) with a solution of ruthenium(III) nitrosyl nitrate (1.5 wt.% Ru(NO)(NO<sub>3</sub>)<sub>3</sub> in diluted HNO<sub>3</sub>, Sigma-Aldrich) in order to achieve 5 wt.% metal loading. After drying at 170 mbar / 60°C in a rotary evaporator, a portion of Ru<sub>dry</sub> was calcined in air in a muffle oven at 400°C for 3 h to obtain Ru<sub>O<sub>2</sub></sub>. A second aliquot of Ru<sub>dry</sub> was reduced at 500°C in 30 vol% H<sub>2</sub> (Ru<sub>H<sub>2</sub></sub>). A third portion was further impregnated with a solution of ammonium hypophosphite (NH<sub>4</sub>H<sub>2</sub>PO<sub>2</sub>, Sigma-Aldrich) to a P/Ru ratio of 1.4. After drying in a rotary evaporator at 60°C and 170 mbar, an aliquot of the material (RuP<sub>dry</sub>) was reduced in 30 vol% H<sub>2</sub> at 500°C for 4 h, cooled to 180°C in the same atmosphere and then under N<sub>2</sub> to ambient temperature. Finally, the powder was exposed to 1 vol% O<sub>2</sub> at room temperature for 30 min (sample labelled as RuP<sub>H<sub>2</sub></sub>). For comparison, a portion of RuP<sub>dry</sub> was calcined at 400°C (RuP<sub>O<sub>2</sub></sub>). An additional sample (P<sub>Al<sub>2</sub>O<sub>3</sub></sub>) was prepared by impregnation of  $\gamma$ -Al<sub>2</sub>O<sub>3</sub> with NH<sub>4</sub>H<sub>2</sub>PO<sub>2</sub> to achieve 5 wt.% P loading. The material was dried as described above then calcined at 400°C. The overall sample preparation is summarized in **Scheme 5.2**.



**Scheme 5.2.** Synthesis approach for the preparation of the various materials.

### 5.2.2 Characterization

*X-ray powder diffraction*-XRPD patterns were collected using a Bruker Advance D8 diffractometer (Cu-K $\alpha$  radiation) in the 2 $\theta$  range 15-90° with a step scan of 0.03°.

*Specific surface area*-N<sub>2</sub> physisorption was performed with a Quantachrome Autosorb-1 instrument at liquid N<sub>2</sub> temperature. Prior to N<sub>2</sub> adsorption, the sample was outgassed at 250°C for 3 h.

*Transmission electron microscopy*-Transmission electron micrographs were recorded using a JEOL 2010 at an acceleration of 200 keV and equipped with a LaB<sub>6</sub> filament, using the INCA software and a CCD camera (Orius, GATAN). The powders were suspended in isopropanol, and a 5  $\mu$ L drop of this suspension was deposited on a holey carbon film supported on 3 mm copper grid.

*Temperature programmed reduction*-H<sub>2</sub>-TPR experiments were carried out in a dedicated instrument (TPDRO 1100, ThermoScientific) equipped with a thermal conductivity detector (TCD). The sample (100 mg) was loaded at the bottom of a quartz reactor. H<sub>2</sub>-TPR profiles were collected in the temperature range of 30-500°C at a heating rate of 5°C/min in a gas flow of 10 vol% H<sub>2</sub>/Ar (20 mL/min).

*Nuclear magnetic resonance spectroscopy*-Single pulse magic angle nuclear magnetic resonance spectroscopy (MAS NMR) experiments were performed at room temperature on a Bruker Avance 400 MHz spectrometer using a 2.5 mm CP/MAS probe at spinning rates of 25 kHz. The <sup>27</sup>Al and <sup>31</sup>P NMR chemical shifts were referenced to external samples of a 1.1 M solution of Al(NO<sub>3</sub>)<sub>3</sub> in D<sub>2</sub>O and of solid NH<sub>4</sub>H<sub>2</sub>PO<sub>4</sub> at 0.0 ppm, respectively.

*X-ray absorption spectroscopy*-Transmission X-ray absorption spectra were obtained at the Ru K-edge (22117 eV) at the Swiss Norwegian beamline (SNBL) of the European Synchrotron Radiation Facility (ESRF, Grenoble, France) and the SuperXAS beamline of the Swiss Light Source (Paul Scherrer Institute, Switzerland) using 15 cm long ionization chambers filled with 1 bar N<sub>2</sub> and 1 bar Ar. A reference spectrum of a Ru metal mesh was measured simultaneously with the sample between the second and the third ionization sample for energy calibration. At SNBL, the white beam of a 0.8 T ESRF bending magnet was monochromatized by a Si(111) double crystal monochromator. Harmonic suppression was obtained by detuning the second crystal to 65% throughput. The beam size on the sample was set to 5 to 0.5 mm (l x h). At the SuperXAS beamline, the polychromatic beam from the 2.9 T bending magnet was collimated

by a Pt coated mirror at 2.5 mrad, monochromatized by a continuous scanning Si(111) channel cut monochromator and subsequently focused using a Pt coated toroidal mirror to a spot size of 100 x 100  $\mu\text{m}$  at the sample position. XAS spectra were background corrected, normalized and energy corrected using the Demeter software package.<sup>138</sup> Spectra of metallic Ru (foil) and RuO<sub>2</sub> were collected for reference purposes.

Operando experiments were carried out in a flow cell adapted for liquid phase experiments.<sup>42</sup> The catalyst (35 mg) was loaded between two quartz wool plugs. The cell was connected to a HPLC pump (Azura 4.1PS 10 mL/min head; Knauer) and set to a flow of 0.2 mL/min. At the outlet of the cell a backpressure regulator (KCB series, Swagelok) maintained the reactive environment in liquid phase at 16 bar. The catalyst bed was recorded dry at room temperature before allowing the Ar-saturated 2-propanol solution of furfural (5 mM; Sigma-Aldrich, 99.9%) to enter the cell. Quick EXAFS spectra were recorded for 1 min every 30 °C until the reactor reached 180°C. Once the desired reaction temperature was attained, the catalyst bed was left under reaction conditions for 30 min while collecting samples for analysis by gas chromatography (see below) every 15 min. In order to improve the signal to noise ratio, the time-resolved spectra were averaged over the whole acquisition period (1 min, 60 spectra). Fourier transform was performed in the k-range of 3-15  $\text{\AA}^{-1}$  for Ru-H<sub>2</sub> and 3-11  $\text{\AA}^{-1}$  for RuP-H<sub>2</sub>. The Fourier transformed spectra were not phase-shift corrected. A curve fitting analysis was carried out on the data in the R-range of 1.9-3.0  $\text{\AA}$ . Only the first coordination shell was considered and metallic Ru was used as reference. The amplitude reduction factor was set to 0.78 after fitting the EXAFS spectra of the Ru mesh.

*Pyridine adsorption*-The acidity of the materials was studied by adsorption of pyridine using attenuated total reflection infrared spectroscopy (ATR-IR). An aqueous slurry of the catalyst sample (10 mg in 1.5 mL) was allowed to dry overnight on the ZnSe internal reflection element (IRE, 45°, 52 x 20 x 2 mm; Crystran) under the fume-hood. The coated IRE was mounted in a home-made cell and installed on a commercial four-mirror vertical ATR-IR assembly (Specac) within the sample compartment of the IR spectrometer (Vertex 70; Bruker). Spectra were recorded at 20 kHz scanner velocity by averaging 60 scans at a spectral resolution of 4  $\text{cm}^{-1}$  using a liquid N<sub>2</sub> cooled MCT detector. The catalyst layer was equilibrated in cyclohexane at room temperature for 1 h prior to collection of the background spectrum. Then, a 5 mM pyridine solution in cyclohexane was allowed to enter the ATR-IR cell and adsorption was monitored for 30 min followed by desorption in cyclohexane for 30 min. For comparison purposes, pyridine adsorption was carried out also on H-ZSM5, a material

containing only Brønsted acid sites allowing for clear identification of pyridine adsorption on these sites (Si:Al mol ratio 11.3, ABCR, 379 m<sup>2</sup>/g, calcined at 550°C in air prior to use).

### 5.2.3 Catalytic activity

Catalytic experiments were carried out by at the University of Milano, Italy. Furfural hydrogenation was performed at 180°C, using a stainless steel reactor (30 mL capacity), equipped with heater, mechanical stirrer, gas supply system and thermometer. The furfural solution (15 mL; 0.3 M in 2-propanol) was added into the reactor at room temperature and the desired amount of catalyst (F/Ru ratio = 100 mol/mol) was suspended in the solution. The N<sub>2</sub> pressure was 5 bar. The mixture was heated to the reaction temperature and was then mechanically stirred (1250 rpm). At the end of the reaction, the autoclave was cooled to room temperature, N<sub>2</sub> flow stopped and the autoclave purged with flowing N<sub>2</sub>. Samples were removed periodically (0.2 mL) using a micro-syringe through a withdrawal valve and were analyzed by gas chromatography (HP 7820A gas chromatograph equipped with a capillary column HP-5 30 m x 0.32 mm, 0.25 µm Film; Agilent Technologies). Standard solutions of reactants and products were analyzed to determine separation times. Quantitative analysis was performed using an external standard (n-octanol). Identification of the products was performed using a Thermo Scientific Trace ISQ QD Single Quadrupole GC-MS equipped with a capillary column (HP-5 30 m x 0.32 mm, 0.25 µm Film; Agilent Technologies).

For catalyst recycling tests, each run was carried out under the same conditions (furfural = 0.3 M; F/Ru mol ratio, 100; 180°C, 5 bar N<sub>2</sub>). The catalyst was recycled to be used in the subsequent run (reaction times of 3 h each) after filtration without any further treatment.

## 5.3 Results and discussion

### 5.3.1 Catalyst preparation and characterization

The various materials that are compared in this study were prepared according to **Scheme 5.2**. Ruthenium was deposited on γ-Al<sub>2</sub>O<sub>3</sub> by wet impregnation from ruthenium(III) nitrosyl nitrate solution to attain a final metal loading of 5 wt.%. After drying, Ru<sub>dry</sub> underwent nitrosyl nitrate precursor decomposition either by calcination in air (Ru<sub>O<sub>2</sub></sub>) or by reduction in H<sub>2</sub> (Ru<sub>H<sub>2</sub></sub>). For both samples, specific surface areas of 169 and 163 m<sup>2</sup>/g were determined, respectively.



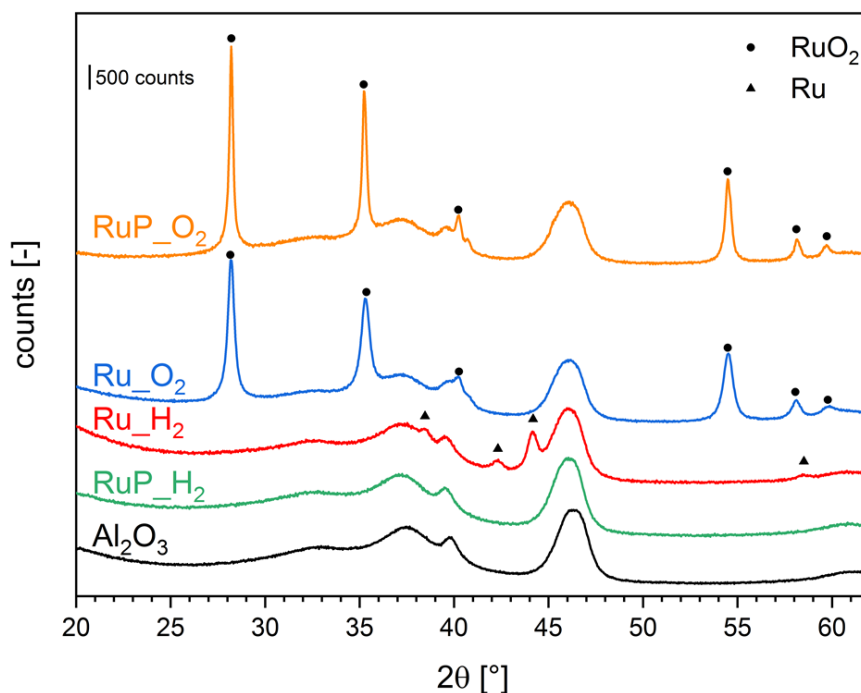


**Figure 5.1:** XRD patterns of Ru catalysts and of the Al<sub>2</sub>O<sub>3</sub> support.

The P-promoted catalysts were prepared similarly by sequential wet impregnation with ammonium hypophosphite. After impregnation with the ruthenium precursor, Ru<sub>dry</sub> was contacted with the phosphite containing solution. The material containing 7.5 wt.% P (RuP<sub>dry</sub>) was subsequently calcined (RuP<sub>O<sub>2</sub></sub>; 131 m<sup>2</sup>/g) or reduced (RuP<sub>H<sub>2</sub></sub>; 126 m<sup>2</sup>/g). The specific surface area of the resulting samples decreased to approximately the value obtained for the support (Al<sub>2</sub>O<sub>3</sub>, 132 m<sup>2</sup>/g).

The structural analysis by X-ray powder diffraction (XRPD, **Figure 5.1**) helped to identify the composition and structure of Ru containing crystallites. Calcination of the Ru precursors on P-free Al<sub>2</sub>O<sub>3</sub> (Ru<sub>O<sub>2</sub></sub>) and after impregnation with the P precursor (RuP<sub>O<sub>2</sub></sub>) produced large crystallites of RuO<sub>2</sub> as suggested by the presence of sharp reflections of this phase. Conversely, reduction (Ru<sub>H<sub>2</sub></sub>) produced metallic Ru crystallites of ca. 11 nm in diameter as estimated using the Scherrer equation (**Table D1 – Appendix**). The XRPD pattern of RuP<sub>H<sub>2</sub></sub> displayed only the reflections of the Al<sub>2</sub>O<sub>3</sub> support and no specific reflection of RuO<sub>2</sub> nor metallic Ru could be detected. Transmission electron micrographs of Ru<sub>H<sub>2</sub></sub> and RuP<sub>H<sub>2</sub></sub> (**Figure D1 – Appendix**) confirmed the absence of well-defined particles in RuP<sub>H<sub>2</sub></sub>. This observation suggests that the presence of phosphorous allowed Ru to disperse uniformly on Al<sub>2</sub>O<sub>3</sub> and prevented the growth of Ru or RuO<sub>2</sub> particles. It also provides a possible explanation for the observed lower increase of surface area after Ru wet impregnation compared to the corresponding P-free materials. On the other hand, phosphorous did not prevent the

formation of large RuO<sub>2</sub> crystallites when RuP<sub>dry</sub> was subjected to calcination at 400°C (sample RuP<sub>O<sub>2</sub></sub>). Hence, reduction is required to disperse Ru in the presence of phosphorous.

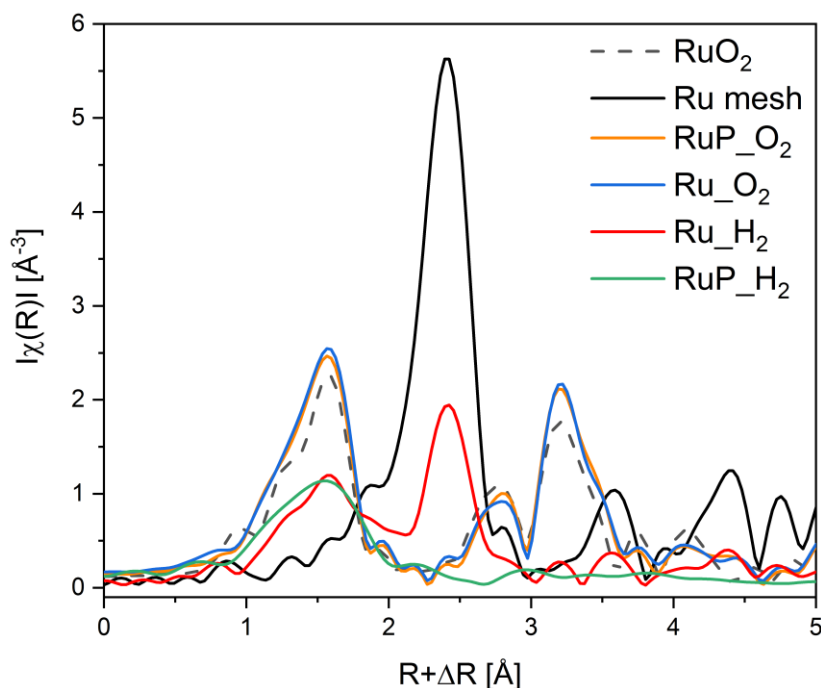


**Figure 5.2:** Ru K-edge FT-EXAFS of Ru catalysts and of the Ru<sup>0</sup> and RuO<sub>2</sub> references.

Information on the local environment of Ru was determined by analysis of the Ru K-edge X-ray absorption near edge structure (XANES, **Figure D2 – Appendix**) and extended X-ray absorption fine structure (EXAFS, **Figure 5.2**) spectra. The XANES spectra of Ru<sub>O<sub>2</sub></sub> and RuP<sub>O<sub>2</sub></sub> exhibited the typical white line of RuO<sub>2</sub> (**Figure D2 – Appendix**) confirming the presence of RuO<sub>2</sub> already identified by XRPD. The edge energy position of Ru<sub>H<sub>2</sub></sub> was close to that of metallic Ru while the edge of RuP<sub>H<sub>2</sub></sub> was shifted to higher energy suggesting the presence of partially oxidized Ru species. The attenuation of the features of the white line intensity of RuP<sub>H<sub>2</sub></sub> compared to the intensity of the Ru reference suggests the presence of small Ru domains. The FT-EXAFS spectra of the two reduced samples (**Figure 5.2**) are very different. Ru<sub>H<sub>2</sub></sub> presented coordination shells up to 10 Å, suggesting the presence of large Ru metal particles, while RuP<sub>H<sub>2</sub></sub> did not exhibit further coordination shells past the first Ru-O coordination shell (at ca. 1.6 Å). Hence, RuP<sub>H<sub>2</sub></sub> possessed smaller particles or clusters, thus justifying the absence of a Ru-containing phase in XRPD and of evident particles in TEM.

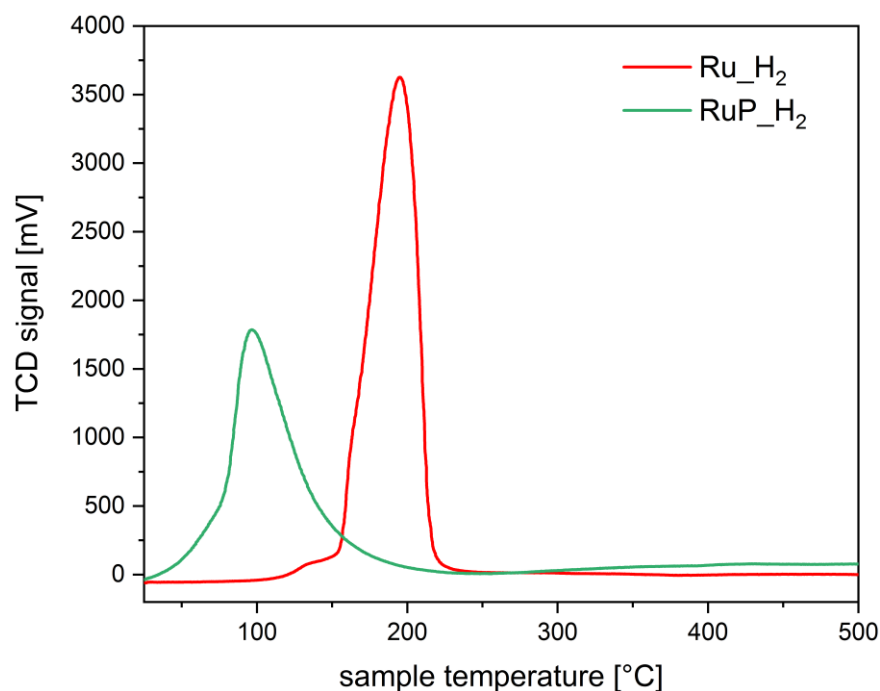


**Figure 5.3:** H<sub>2</sub>-TPR of Ru\_H<sub>2</sub> and RuP\_H<sub>2</sub>.

The differences in the extent of aggregation, the oxidation state and the coordination environment of Ru are expected to influence also the reactivity of Ru. Hence, the reducibility of the materials was investigated by temperature programmed reduction (H<sub>2</sub>-TPR). The H<sub>2</sub>-TPR profiles of Ru\_H<sub>2</sub> and RuP\_H<sub>2</sub> shown in **Figure 5.3** confirmed that the different Ru dispersion and aggregation also affected the reducibility of Ru. The P-free sample presented a reduction peak at 195°C, while highly dispersed Ru in sample RuP\_H<sub>2</sub> was already reduced at 98°C, in agreement with the increased difficulty to reduce small oxide particles than large particles. The opposite behavior displayed by the small Ru domains present on RuP\_H<sub>2</sub> reveals that phosphorous decreases the activation barrier for hydrogen dissociation on small Ru clusters.

Based on the characterization focused on Ru species, it appears clear that P induces an improvement of the dispersion of Ru on alumina. P groups stabilize Ru species of low nuclearity, which are characterized by a more pronounced tendency to split hydrogen compared to larger Ru species immobilized on P-free alumina.

Understanding the role of phosphorous includes also analysis of possible changes in the acidity of the samples. The type of acidity (Brønsted or Lewis) of Ru\_H<sub>2</sub> and RuP\_H<sub>2</sub> was investigated by adsorption of pyridine in cyclohexane solvent using ATR-IR (**Figure 5.4a**). The spectra of both samples (**Figure D3- Appendix**) exhibited signals of pyridine coordinated to Lewis acid sites (LAS) at 1448 cm<sup>-1</sup> ( $\nu_{19b}$ ) and 1610 cm<sup>-1</sup> ( $\nu_{8a}$ ).<sup>139</sup> The vibrations at 1540 cm<sup>-1</sup> ( $\nu_{19b}$  mode)

and 1637 cm<sup>-1</sup> ( $\nu_{8a}$ ) corresponding to the pyridinium ion coordinated to Brønsted acid sites (BAS) were negligible. Despite the similarities, significant information was obtained from the inspection of the band at ca. 1490 cm<sup>-1</sup>, which is attributed to the interaction of pyridine with both BAS and LAS. The intensity of this signal is typically higher than that of the signal at 1540 cm<sup>-1</sup> (BAS). It was centered at 1491 cm<sup>-1</sup> in the case of pyridine adsorbed on RuP\_H<sub>2</sub>, while the position changed to 1485 cm<sup>-1</sup> in the case of Ru\_H<sub>2</sub> (**Figure 5.4a**). While the signal was asymmetric in both samples, the spectra obtained after pyridine desorption clearly confirmed the existence of two signals close in energy. Pyridine adsorption on H-ZSM-5, which contains mainly BAS (**Figure D3 – Appendix**), shows the characteristic signals of BAS at 1540 and 1490 cm<sup>-1</sup>.<sup>140</sup> In the absence of the former signal, which is likely too weak to be detected in the spectrum of pyridine adsorbed on RuP\_H<sub>2</sub>, the signal at 1490 cm<sup>-1</sup> can be taken as evidence of a contribution from pyridine coordinated to BAS. Thus, phosphorous modified the acidity of alumina by increasing the tendency of the surface to donate protons.

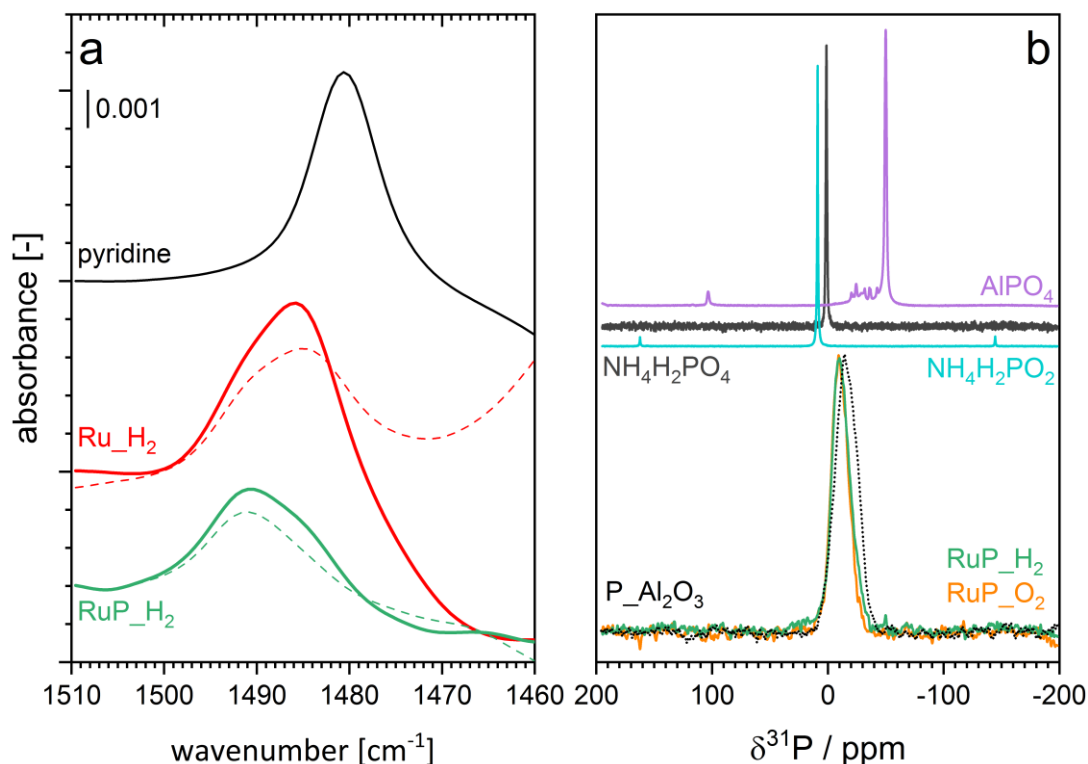


**Figure 5.4:** (a) Spectral region of interest of ATR-IR spectra of pyridine adsorption (solid) and desorption (dashed) on Ru\_H<sub>2</sub> and RuP\_H<sub>2</sub>. Enlarged region of the spectra are provided in **Figure D3 – Appendix D**. (b) <sup>31</sup>P MAS NMR spectra of RuP\_H<sub>2</sub>, RuP\_O<sub>2</sub> and of reference materials.

The interaction between P and alumina and thus the nature of phosphorous was studied by magic angle spinning nuclear magnetic resonance (MAS-NMR). The broad resonance at -10 ppm observed in the <sup>31</sup>P MAS-NMR spectra of RuP\_H<sub>2</sub> (**Figure 5.4b**) can be assigned to

surface phosphate species.<sup>141,142</sup> The same line shape was noticed in the spectrum of RuP\_<sub>2</sub>O<sub>7</sub>, indicating that the same phosphate species must be present in both cases irrespective of the synthesis conditions. The shift from the value of 0 ppm of the NH<sub>4</sub>H<sub>2</sub>PO<sub>2</sub> precursor provides an additional proof of the interaction of phosphorous with alumina by the formation of an amorphous aluminum phosphate species that is not visible by XRPD because it is not yet a well crystallized AlPO<sub>4</sub> phase. The similarity of the spectrum of P\_<sub>2</sub>O<sub>5</sub>/Al<sub>2</sub>O<sub>3</sub> to those of RuP\_<sub>2</sub>H<sub>2</sub> and RuP-O<sub>2</sub> confirmed that no specific interaction with Ru could be detected. No additional information was obtained from the <sup>27</sup>Al MAS-NMR data (**Figure D4 – Appendix**).

In summary, the characterization data indicate that phosphorous is present in the form of phosphate groups on the surface of alumina, likely anchoring sites for Ru species, thus ensuring the observed high metal dispersion and finally, it changes the acid properties of the surface by providing more BAS.

### 5.3.2 Catalytic activity

**Table 5.1** shows the selectivity and activity data of the prepared catalysts compared to a commercial 5 wt.% Ru supported on activated carbon (Ru/AC) as benchmark catalyst for the liquid phase CTH of furfural in batch conditions. We identified furfuryl alcohol as the major product for all materials.

Ru\_<sub>2</sub>O<sub>3</sub> and RuP\_<sub>2</sub>O<sub>7</sub> demonstrated the lowest activity, likely due to the fact that reduction of RuO<sub>2</sub> needs to take place first (**Figure 5.5a**). The hydrogen-treated sample (RuP-H<sub>2</sub>) exhibited the highest activity, 93% selectivity to furfuryl alcohol after 15 min of reaction and 58 (mol<sub>F0</sub>-mol<sub>Ft</sub>)·mol<sub>Ru</sub><sup>-1</sup>·h<sup>-1</sup> compared to 84% for the benchmark catalyst (38 (mol<sub>F0</sub>-mol<sub>Ft</sub>)·mol<sub>Ru</sub><sup>-1</sup>·h<sup>-1</sup>). This improved performance can be attributed to the superior reducibility and the presence of Ru metal. Ru/Al<sub>2</sub>O<sub>3</sub>-based catalysts did not produce 2-methylfuran, which was observed in the case of Ru/AC.

**Table 5.1.** Catalytic transfer hydrogenation of furfural on the indicated catalysts without pre-reduction.

Sample <sup>a</sup>	Activity <sup>b</sup>	Selectivity (%) <sup>f</sup>			
		furfuryl alcohol	tetrahydro furfuryl alcohol	2-methyl furan	ethers
Ru/AC	38	84 <sup>c</sup>	-	12 <sup>c</sup>	3 <sup>c</sup>
		80 <sup>d</sup>	2 <sup>d</sup>	16 <sup>d</sup>	2 <sup>d</sup>
Ru_H <sub>2</sub>	40	98 <sup>c</sup>	2 <sup>c</sup>	-	-
		96 <sup>e</sup>	1 <sup>e</sup>	-	3 <sup>e</sup>
RuP_H <sub>2</sub>	58	93 <sup>c</sup>	2 <sup>c</sup>	-	5 <sup>c</sup>
		81 <sup>e</sup>	3 <sup>e</sup>	2 <sup>e</sup>	14 <sup>e</sup>
Ru_O <sub>2</sub>	14	86 <sup>c</sup>	3 <sup>c</sup>	1 <sup>c</sup>	10 <sup>c</sup>
RuP_O <sub>2</sub>	18	70 <sup>c</sup>	18 <sup>c</sup>	1 <sup>c</sup>	9 <sup>c</sup>

<sup>a</sup> reaction conditions: F<sub>0</sub> = 0.3 M; F/Ru ratio = 100 mol/mol, 180°C, 5 bar N<sub>2</sub>. F<sub>0</sub>, initial concentration of furfural

<sup>b</sup> (mol<sub>F0</sub>-mol<sub>Fi</sub>)·(mol<sub>Ru</sub>)<sup>-1</sup>·h<sup>-1</sup>; mol<sub>F0</sub>, initial mol of F; mol<sub>Fi</sub>, mol of F at time i (i = 15 min)

<sup>c</sup> at 30% conversion

<sup>d</sup> at 50% conversion

<sup>e</sup> at 80% conversion

<sup>f</sup> selectivity is calculated as  $S_i = 100 \cdot \text{mol}_i \cdot (\text{mol}_{F0} - \text{mol}_{Fk})^{-1}$ ; mol<sub>F0</sub>, initial mol of F; mol<sub>Fk</sub>, mol of F at conversion value k (k = 30 and 80%)

Whether the additional acidity determined by pyridine adsorption impacts catalytic activity and selectivity cannot be completely excluded from the present data. Brønsted acidity was shown to promote etherification reactions<sup>143</sup> and **Table 5.1** shows that RuP\_H<sub>2</sub> promoted the production of ethers at 80% conversion of furfural (14% selectivity towards ethers) compared to the P-free catalysts but at the expense of selectivity to furfuryl alcohol. This may indicate that the presence of Brønsted acidity at the surface of the solid catalyst may be a strategy to direct the reaction towards etherification (**Figure D5 – Appendix**).

The stability of the catalysts to the reaction conditions and the liquid phase environment was evaluated by performing six consecutive recycling tests (**Figure 5.5b**). Both Ru\_H<sub>2</sub> and RuP\_H<sub>2</sub> experienced a decrease in furfural conversion between the first and the second run. However, the extent of activity loss was significantly higher for the P-free catalyst. Elemental analysis of the filtered solution evidenced 4% of Ru leaching in the case of RuP\_H<sub>2</sub> between the first and the second run and no further leaching in the subsequent runs. On the contrary, Ru\_H<sub>2</sub> leached 10% of Ru between the first and the second run, and another 5% in the subsequent catalytic test. For comparison, 7% of Ru leached into the solution in the case of Ru/AC in the same sequence.

These results indicate that besides increasing the dispersion and the reducibility of Ru, P strengthens the interaction between Ru and alumina. We consider this behavior a result of the increased dispersion of the active phase and the presence of phosphate groups.

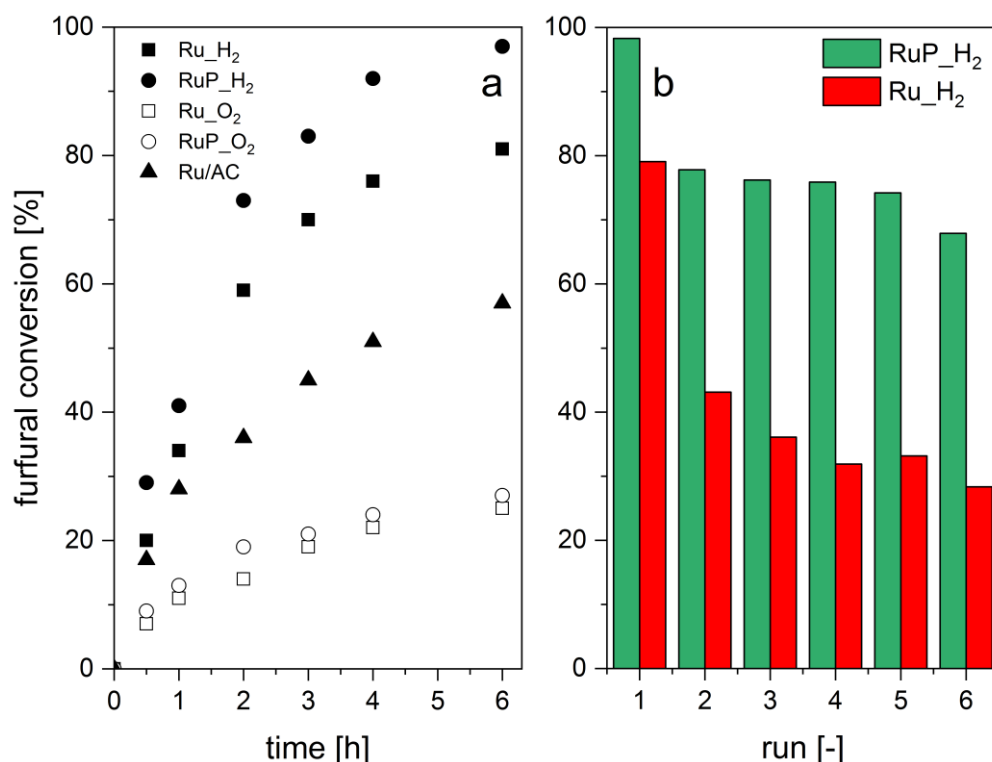


**Figure 5.5:** Catalytic transfer hydrogenation of furfural: (a) furfural conversion without catalyst pre-reduction and (b) consecutive leaching tests.

The effect of reduction of oxidized Ru species on the activity was investigated by reducing the Ru\_O<sub>2</sub> and RuP\_O<sub>2</sub> catalysts (7 bar H<sub>2</sub>, 150°C, 1 h) *in situ* prior to reaction. The catalytic activity and product selectivity are summarized in **Table 5.2**. The beneficial effect of the pre-reduction is evident from comparison with the data of **Table 5.1**. RuP\_O<sub>2</sub>, in particular, reproduced the same conversion profile of the reduced counterpart RuP\_H<sub>2</sub> (**Figure D6 – Appendix**), thus confirming the hypothesis that metallic ruthenium favors the hydrogenation reaction. *In situ* reduction produced a slight decrease in the activity of RuP\_H<sub>2</sub>, in agreement with the observation that the co-existence of RuO<sub>x</sub> species and Ru metal has a positive impact on the performance of Ru-based catalysts<sup>144</sup>. Therefore, the lower activity of pre-reduced RuP\_H<sub>2</sub> is ascribable to the complete reduction of the dispersed RuO<sub>x</sub> species (most likely Ru-OH species as indicated by EXAFS) present in the pristine catalyst. Whether remainders of oxidized Ru were present on Ru\_O<sub>2</sub> and RuP\_O<sub>2</sub> after reduction was not ascertained.

**Table 5.2.** Catalytic transfer hydrogenation of furfural on the indicated catalysts after *in situ* pre-reduction.

Sample <sup>a</sup>	Activity <sup>b</sup>	Selectivity (%) <sup>c</sup>			
		furfuryl alcohol	tetrahydro-furfuryl alcohol	2-methyl-furan	ethers
Ru/AC	42	80 <sup>c</sup>	-	18 <sup>c</sup>	1 <sup>c</sup>
		76 <sup>d</sup>	2 <sup>d</sup>	20 <sup>d</sup>	1 <sup>d</sup>
Ru_H <sub>2</sub>	38	84 <sup>c</sup>	4 <sup>c</sup>	-	10 <sup>c</sup>
RuP_H <sub>2</sub>	48	88 <sup>c</sup>	1 <sup>c</sup>	-	11 <sup>c</sup>
Ru_O <sub>2</sub>	30	70 <sup>c</sup>	18 <sup>c</sup>	1 <sup>c</sup>	9 <sup>c</sup>
RuP_O <sub>2</sub>	42	62 <sup>c</sup>	17 <sup>c</sup>	2 <sup>c</sup>	17 <sup>c</sup>

<sup>a</sup> reaction conditions: F<sub>0</sub> = 0.3 M; F/Ru ratio = 100 mol/mol, 180°C, 5 bar N<sub>2</sub>. F<sub>0</sub>, initial concentration of furfural

<sup>b</sup> (mol<sub>F0</sub>-mol<sub>Fi</sub>)·(mol<sub>Ru</sub>)<sup>-1</sup>·h<sup>-1</sup>; mol<sub>F0</sub>, initial mol of F; mol<sub>Fi</sub>, mol of F at time i (i = 15 min)

<sup>c</sup> at 30% conversion

<sup>d</sup> at 80% conversion

<sup>e</sup> selectivity is calculated as S<sub>i</sub> = 100·mol<sub>i</sub>·(mol<sub>F0</sub>-mol<sub>Fk</sub>)<sup>-1</sup>; mol<sub>F0</sub>, initial mol of F; mol<sub>Fk</sub>, mol of F at conversion value k (k = 30 and 80%)

Operando XAS experiments were performed on the most active of the pristine catalysts, i.e. Ru\_H<sub>2</sub> and RuP\_H<sub>2</sub> to monitor the Ru speciation under reaction in flow. **Figure 5.6** shows the FT-EXAFS spectra obtained while heating an Ar-saturated 2-propanol solution of furfural to 180°C. While the XANES region (**Figure D7 – Appendix**) demonstrates the reduction of both samples to Ru metal by a weakening of the white line at higher temperature, **Figure 5.6a** shows the appearance of a Ru-Ru shell of the metal phase in RuP\_H<sub>2</sub> at ca. 2.5 Å with a simultaneous gradual disappearance of the Ru-O shell (at ca. 1.5 Å). This process also occurs on Ru\_H<sub>2</sub>, but the reduction of the oxidized phase contributes to the increase in the fraction of Ru metal already present in the catalyst (at ca. 2.5 Å, **Figure 5.6b**). The less intense and broader contribution of the first Ru-Ru shell observed for RuP\_H<sub>2</sub> is an indication that the Ru particles formed upon reduction are smaller than in Ru\_H<sub>2</sub>, which is confirmed by the values of the Ru coordination number obtained from the fit of the first Ru-Ru shell (**Table 5.3**) of both catalysts (EXAFS fits are shown in **Figure D8 – Appendix**). Moreover, it is evident that the Ru-O species do not completely disappear during reaction in both catalysts, which can be related to the need of mixed RuO<sub>x</sub>/Ru interfaces.<sup>145</sup> After 30 min at 180°C, furfural conversion was 98 % on both RuP\_H<sub>2</sub> and Ru\_H<sub>2</sub>.



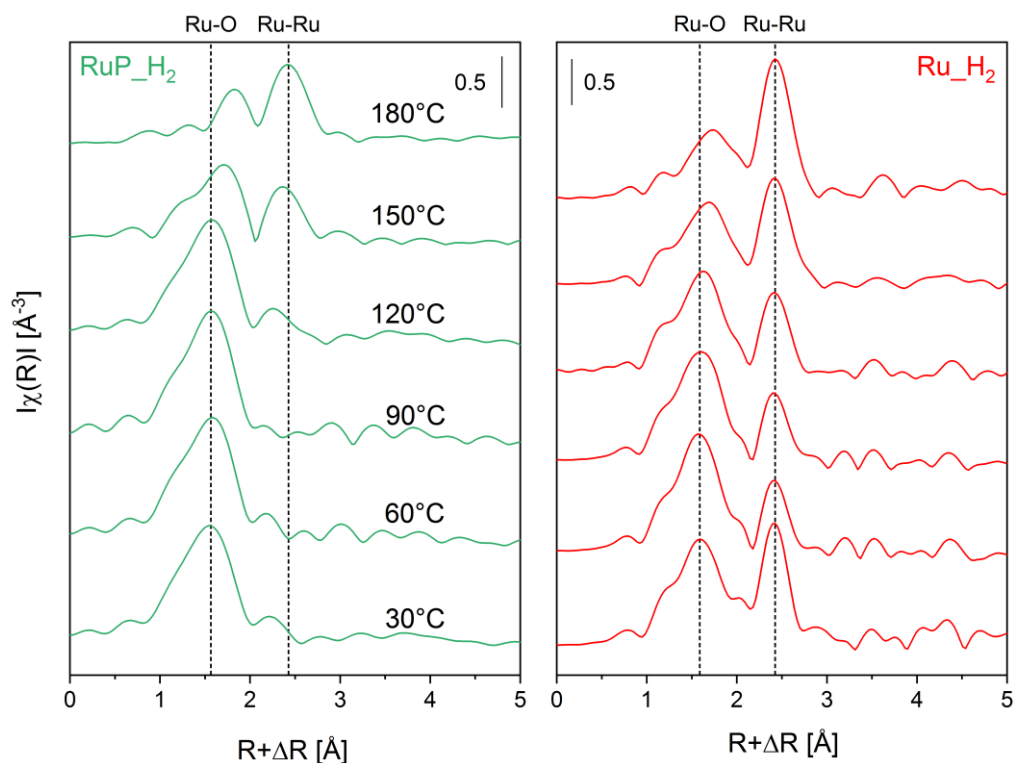


**Figure 5.6:** Operando non phase-shift corrected FT-EXAFS spectra at the Ru K-edge under reaction conditions of Ru\_H<sub>2</sub> and RuP\_H<sub>2</sub> determined from 30°C to 180°C. Conditions: 5 mM furfural in Ar-saturated 2-propanol at a flow rate of 0.2 mL/min, 16 bar and with 35 mg of material.

**Table 5.3.** EXAFS fitting results of operando spectra during continuous flow catalytic transfer hydrogenation of furfural.

Sample	CN <sup>a</sup>	R <sup>b</sup> (Å)	DW (Å <sup>2</sup> ) <sup>c</sup>	ΔE (eV) <sup>d</sup>	R factor <sup>e</sup>	Average size (nm) <sup>f</sup>
Ru_H <sub>2</sub>	8.12 ± 1.1	2.67 ± 0.01	0.006 ± 0.001	3.7 ± 1.0	0.024	1.2
RuP_H <sub>2</sub>	4.92 ± 1.0	2.67 ± 0.01	0.009 ± 0.002	3.6 ± 1.4	0.019	0.7

<sup>a</sup>Coordination number. <sup>b</sup>Interatomic distance. <sup>c</sup>Debye-Waller factor. <sup>d</sup>Shift in the edge energy.

<sup>e</sup>Defined as  $R = \sum_i [\text{Re}(\chi_e(R_i) - \chi_c(R_i))^2 + \text{Im}(\chi_e(R_i) - \chi_c(R_i))^2] / \sum_i [\text{Re}(\chi_e(R_i))^2 + \text{Im}(\chi_e(R_i))^2]$

<sup>f</sup>The average size was calculated using the hcp model as described in ref.<sup>146</sup>

## 5.4 Conclusion

The results from the characterization and from catalytic activity data indicate that addition of phosphorous changed significantly the dispersion and reducibility of Ru. Also, the type of acid site of the Al<sub>2</sub>O<sub>3</sub> support was modified from a Lewis-based material towards a more Brønsted-based material. While it is difficult to disentangle which effect is more critical

for catalytic activity and selectivity because of the vastly different Ru particle size in these catalysts, these combined effects improved the activity of Ru/Al<sub>2</sub>O<sub>3</sub> towards CTH of furfural to furfuryl alcohol. Further systematic study is needed to disentangle the role of the various parameters involved, such as particle size and P loading effects. Moreover, the nature of the binding mode of P to Al<sub>2</sub>O<sub>3</sub> and possibly to Ru should also be addressed in future studies. Phosphorous improved also the stability of Ru by reducing Ru leaching into the solution significantly.

# Chapter 6: Water inhibition of OME synthesis

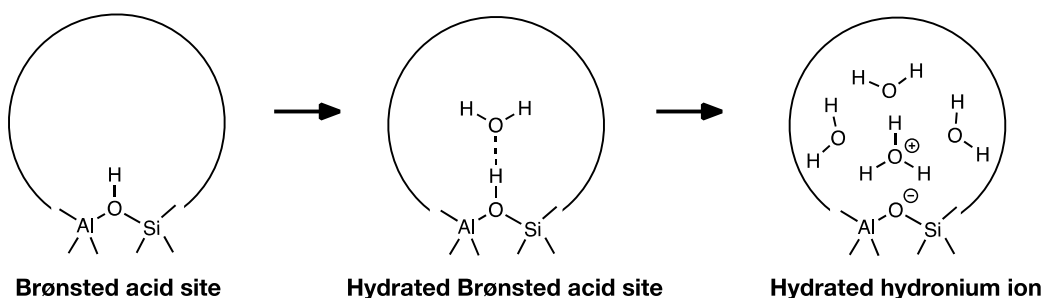
The present chapter is based on the accepted version of the publication: C. J. Baranowski, T. Fovanna, M. Roger, M. Signorile, J. Mc Caig, A. M. Bahmanpour, D. Ferri, O. Kröcher, Water inhibition of oxymethylene dimethyl ether synthesis over zeolite H-Beta: a combined kinetic and in situ ATR-IR study, *ACS Catalysis*. T. Fovanna performed the experiments related to the ATR-IR part, analyzed and interpreted the data. The manuscript was written with the co-authors.

## 6.1 Introduction

Zeolites are crystalline aluminosilicate materials with unique and advantageous features: silicon tetrahedra combine to form frameworks with large surface areas and well-defined pores of molecular dimensions. The one- to three-dimensional micropores of various sizes connected by channels and cages provide them with unique properties such as shape selectivity or activation by molecular confinement. Their acidity originates from the aliovalent substitution of a silicon framework atom by a trivalent metal cation, such as aluminum, generating a negative charge in the lattice balanced by a bridging hydroxyl group.<sup>147</sup> The chemical industry exploits heavily the catalytic properties of zeolites towards various reactions such as hydrogenation, alkylation or isomerization.<sup>148</sup> Despite extensive investigations, their activity for various chemical reactions has not yet been fully understood.

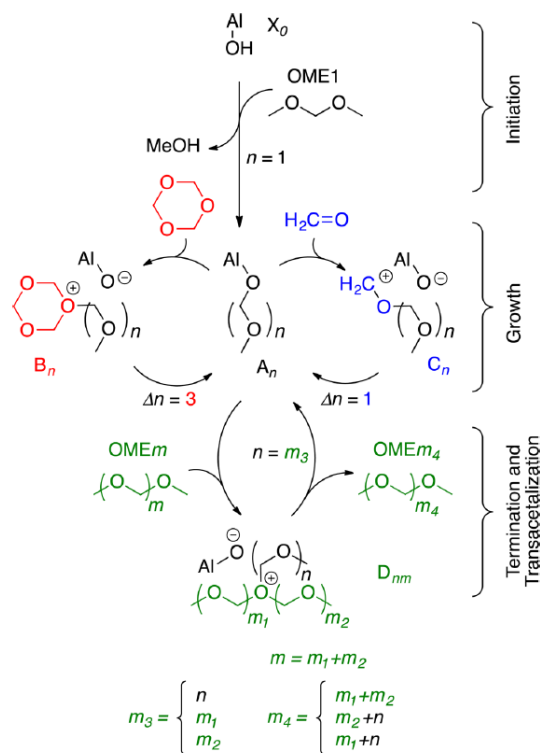
Both positive and negative influences of water on chemical reactions in zeolites have been reported. The dehydration rate of 1-propanol on an H-ZSM-5 zeolite was significantly hampered in the presence of water due to the stabilization of a reaction intermediate, which increased the activation energy.<sup>149</sup> On the contrary, catalytic cracking using zeolite Beta was improved by the presence of water in the feed, due to a better dispersion of hydrocarbons within the zeolite.<sup>150</sup> For the same reaction, the concentration of water in the zeolite is also a parameter which can positively or negatively affect the kinetics: low amounts of water increased the reaction rates for C-H bond activation by an order of magnitude, but had deleterious effect on the kinetics at higher concentrations.<sup>151</sup>

Recently, it was demonstrated that the presence of water changes the nature of the acidic sites in a zeolite from a bridging hydroxyl group to a stabilized hydronium cluster, as illustrated in **Scheme 6.1**.<sup>152,153</sup> Hydronium ions in the zeolite channels diminish the available pore volume and interact differently with reactants compared to a bridging hydroxyl group.<sup>154</sup> In liquid phase, the presence of water in the zeolite channels can have an important impact on the reaction rate and thus on the reaction mechanism. For instance, the reaction mechanism of cyclohexanol dehydration changes when the acid site transforms into a hydronium ion.<sup>155</sup> Similarly, protonation of olefins by hydronium ions must overcome a significantly higher energy barrier compared to a bridging hydroxyl group, leading to lower reaction rates.<sup>156</sup>



**Scheme 6.1.** Hydration of a Brønsted acid site in a zeolite channel.

The influence of water on the kinetics of polyoxymethylene dimethyl ether (OME) synthesis remains vague. OME is a new, promising candidate to replace Diesel fuel.<sup>157,158</sup> It can be used in virtually unmodified Diesel engines and is compatible with the current fuel distribution infrastructures.<sup>158</sup> Its soot-free combustion allows cleaner exhaust emissions from Diesel engines.<sup>159,160</sup> OME can be produced from methanol, a future platform molecule, or other sustainable sources such as biomass.<sup>161</sup> Regarding the reactants, generally, a methyl-end source reacts with an oxymethylene source to produce a Schulz-Flory distribution of OME.<sup>9,162</sup> Water is a co-product of the acetalization of methanol and hemiformals, or can be present as an impurity in the solvent used.



**Scheme 6.2.** Reaction pathways of OME chain growth, from ref 77.

The impact of water on the equilibrium parameters of the reaction has been studied by various authors. Zheng et al. reported that water induced hydrolysis of dimethoxymethane ( $\text{OME}_1$ ) to methanol and formaldehyde.<sup>163</sup> Water concentration above 5 wt.% led to a significant decrease in the OME yield. They also found a zeroth-order for water during OME synthesis from methanol and formaldehyde using Zr-alumina as the catalyst.<sup>164</sup> Burger et al. reported the production of large amounts of by-products when methanol or water was present during the synthesis.<sup>165</sup> Thus, the reaction route involving anhydrous reactants (i.e. trioxane = TRI and  $\text{OME}_1$ ) has been hitherto preferred. Silanol defects in ZSM-5 were also shown to be sufficient to catalyze TRI synthesis from FA.<sup>166</sup> Two reaction mechanisms were proposed to describe the synthesis of OME in anhydrous conditions using zeolite H-Beta: incorporation of formaldehyde (FA) from the *in situ* decomposition of TRI or direct incorporation of TRI into  $\text{OME}_1$  as shown in **Scheme 6.2**.<sup>167</sup> Both mechanisms have similar energy barriers, therefore, are believed to occur simultaneously.

A study from Lautenschütz et al. recently highlighted that the presence of small amounts of water in the reaction medium significantly increased the time to reach equilibrium for OME synthesis from TRI and  $\text{OME}_1$ .<sup>168</sup> They also revealed that zeolite H-Beta was more affected by water than acidic resins. However, they did not quantify, nor study the possible reasons which explained their observation. Therefore, this study aims at elucidating the effect of water on the kinetics of OME synthesis from  $\text{OME}_1$  and TRI using zeolite H-Beta. This objective was pursued by performing a kinetic study using various water concentrations in  $\text{OME}_1$ . Furthermore, attenuated total reflectance infrared (ATR-IR) spectroscopy was used to investigate the nature of the adsorbed species *in situ*. This technique is useful for studying the solid-liquid interfaces of catalytic systems, such as those which exist within zeolites.<sup>169</sup> The sensitivity of ATR-IR is improved by exploiting a modulation excitation (ME) approach combined with phase sensitive detection (PSD).<sup>38</sup> This allows an increase of the signal to noise ratio by averaging the sequence of repeated modulation periods and signal enhancement is achieved by conversion from the time domain to the phase domain. This facilitates the investigation of short-lived or low concentration species, such as transient adsorbates or intermediates. Combined with ATR-IR, these tools contributed to understand complex catalytic systems, where the solid-liquid interface plays a crucial role.<sup>39,170</sup>

## 6.2 Experimental

### 6.2.1 Materials

Trioxane (TRI, 99 %, Sigma-Aldrich), dimethoxymethane (OME<sub>1</sub>, 99.0 % from Sigma-Aldrich and 99.5 % from Acros), 2-propanol (LiChrosolv, hypergrade LC-MS, Merck), and pyridine (>99.0 %, Sigma-Aldrich) were used as received. Cyclohexane (99.8 %, analytical reagent grade, Fischer Chemical) was dried over molecular sieves (3A, 1-2 mm beads, Alfa Aesar) and filtered on microfiber filter (GF/D, Whatman) before use. In order to study the influence of water on the synthesis of OME, increasing amounts of water were added to OME<sub>1</sub>. The water content was determined by Karl-Fisher coulometric titrations using a Metrohm Titrando 737 instrument. Depending on the water concentration, the various OME<sub>1</sub> sources were named OME<sub>1</sub>-x-H<sub>2</sub>O, where x is the water content in wt.%. The zeolite H-Beta was obtained by calcination of NH<sub>4</sub>-Beta (Si/Al = 11, ABCR) at 550 °C (10°C·min<sup>-1</sup>) for 5 h. The water content of the chemicals used in this study is summarized in **Table 6.1**.

**Table 6.1.** Water content of the chemicals used in this study, measured by Karl-Fischer titration.

Chemical	wt.% H <sub>2</sub> O
OME <sub>1</sub> 99.0% (commercial)	0.436 ± 0.002
OME <sub>1</sub> 99.5% (commercial)	0.027 ± 0.003
OME <sub>1</sub> -0.4-H <sub>2</sub> O (synthetic from DMM 99.5%)	0.394 ± 0.064
OME <sub>1</sub> -0.2-H <sub>2</sub> O (synthetic from DMM 99.5%)	0.238 ± 0.040
TRI (commercial)	0.019 ± 0.002
Cyclohexane (commercial)	0.004 ± 0.002

### 6.2.2 Catalyst characterization

*X-ray powder diffraction* - X-ray powder diffraction patterns were recorded with a step size of 0.01° and acquisition period of 4 s per step using a D8 advance Bruker instrument (Cu K $\alpha$  radiation, with Ni filter) equipped with a 1D-LynxEye detector.

*Temperature programmed desorption-NH<sub>3</sub>* temperature programmed desorption (NH<sub>3</sub>-TPD) was carried out to calculate the concentration of acid sites using a Micromeritics Autochem 2920

II instrument. Typically, the sample (ca. 100 mg) was loaded in a U-shaped quartz tube and dried at 500 °C (2°C·min<sup>-1</sup>; 120 min hold time) under a He flow (50 mL·min<sup>-1</sup>). The sample was saturated with 1 vol% NH<sub>3</sub>/He at 100 °C for 1 h and flushed with He (50 mL·min<sup>-1</sup>) to remove physisorbed NH<sub>3</sub> prior to heating in He to 500 °C (10°C·min<sup>-1</sup>). Desorbed NH<sub>3</sub> was quantified with a calibrated thermal conductivity detector.

*Fourier transformed infrared spectroscopy*-Transmission infrared spectra were collected on a Bruker Vertex 70 Fourier transform spectrophotometer, equipped with a liquid N<sub>2</sub> cooled MCT detector by accumulating 32 scans at 4 cm<sup>-1</sup> resolution with a 20 kHz scanner velocity. The sample was examined in the form of a self-supporting pellet in a home-made quartz IR cell equipped with ZnSe windows (optical path, ca. 2 mm). Before measurement, the sample was heated under vacuum (< 10<sup>-3</sup> mbar) to 500 °C (5°C·min<sup>-1</sup>) for 1 h.

### 6.2.3 Catalytic study

Synthesis of OME was performed in glass reactors (Grace, 10 mL) with PTFE screw caps and a silicon sealing disk installed on a magnetic stirring plate. Before reaction, the catalyst powder was weighted and loaded in three to six reactors, which were dried overnight in the oven at 110 °C. To ensure minimal exposure to water, reactors were capped immediately after being removed from the oven and allowed to cool to ambient temperature (23 °C). OME<sub>1-x</sub>-H<sub>2</sub>O was then quickly inserted in the reactors to limit the uptake of moisture from the air by the zeolite, followed by the addition of TRI. All the experiments were performed with an OME<sub>1</sub>/TRI molar ratio of 3.3 and 0.5 wt.% of catalyst at a stirring speed of 450 rpm.

Conversion of trioxane (X<sub>TRI</sub>) and selectivity to OME<sub>3-5</sub> (S(OME<sub>3-5</sub>)) were used to quantify the synthesis of OME with various water concentrations and were defined as:

$$X_{TRI} = \frac{[TRI]_0 - [TRI]}{[TRI]_0} \times 100 \quad \text{Eq. (7.1)}$$

$$S(OME_{3-5}) = \frac{\sum_{i=3}^5 [OME]_i}{\sum_{i=2}^9 [OME]_i} \times 100 \quad \text{Eq. (7.2)}$$

The reactors were inserted in a thermostated water bath at the selected reaction temperature, which was considered as the start of the reaction. The analysis of the liquid samples, obtained after quenching the reactor in an ice bath, was carried out using an Agilent 7890B/5977A Series gas chromatogram-mass spectrometer (GC-MS) equipped with an HP-5 capillary column (length 30 m, outer diameter 0.32 mm, film 1.05 µm) and an automated liquid sampler.



#### 6.2.4 Modulation excitation attenuated total reflectance infrared spectroscopy study

The nature of adsorbates upon OME<sub>1</sub> and TRI adsorption-desorption and during reaction was investigated using ATR-IR spectroscopy. A suspension of the catalyst sample in 2-propanol (8 mg in 1.5 mL) was allowed to dry for 2 h on the ZnSe internal reflection element (IRE, 52 x 20 x 2 mm, 45°, Crystran). This resulted in the deposition of a uniform layer of catalyst on the IRE, which was then mounted in a homemade cell<sup>171</sup> and placed on a 4-mirrors ATR-IR assembly (Specac) in the sample chamber of the spectrometer (Vertex 70, Bruker). Solutions and neat solvent were provided from independent glass bottles, from which the liquid flow was set at 0.3 mL·min<sup>-1</sup> using a peristaltic pump (Reglo 100, Ismatec SA) connected to the outlet of the cell. At the inlet of the cell a 4-ports valve (Cheminert, VICI) enabled fast switching between two solutions. The solution switch was synchronized with the acquisition of the IR spectra using the spectrometer software (OPUS, Bruker). Spectra were recorded at 80 kHz scanner velocity by averaging 12 scans at 4 cm<sup>-1</sup> resolution using a liquid N<sub>2</sub> cooled MCT detector. In a typical experiment, the catalyst layer was equilibrated at room temperature in neat cyclohexane for 1 h prior to background collection. Experiments were performed with diluted solutions of OME<sub>1</sub> (15 mM-DMM 99.5% from Acros), TRI (5 mM) and water (0.7 mM) in cyclohexane, which was selected because of its simple IR spectrum. The low concentrations will allow for better detection of surface species under modulation conditions, while keeping the OME<sub>1</sub>/TRI ratio of 3:1.<sup>172</sup> The following concentration modulation excitation (ME) set of experiments was carried out: (i) TRI vs neat cyclohexane; (ii) OME<sub>1</sub> vs neat cyclohexane; (iii) TRI vs TRI + H<sub>2</sub>O; (iv) OME<sub>1</sub> vs OME<sub>1</sub> + H<sub>2</sub>O; (v) OME<sub>1</sub> + TRI vs OME<sub>1</sub>; (vi) OME<sub>1</sub> + TRI vs TRI (vii) OME<sub>1</sub> + TRI vs OME<sub>1</sub> + TRI + H<sub>2</sub>O. After the equilibration period and background collections, a typical ME experiment cycle consisted of introducing the first solution for 191 s then switching the second solution for 191 s, leading to a period of 382 s.

The interaction of OME<sub>1</sub> and TRI with the catalyst was also studied in the presence of pyridine. After an initial equilibration in cyclohexane for 1 h and background collection, a pyridine solution (5 mM in cyclohexane) was introduced to the catalyst layer for 30 min. Physisorbed pyridine was then removed by flowing neat cyclohexane for 30 min. After adsorption (30 min) and desorption (30 min) of OME<sub>1</sub> or TRI, the ME experiment was started by repeating experiments (i) and (ii), as described above.

A standard experiment consisted of 15 periods. Only the last 10 periods were averaged for improvement of the S/N ratio, while signal enhancement was obtained by phase sensitive

detection (PSD) using a MATLAB script. The phase domain spectra were obtained by mathematical treatment of the time-domain spectra according to the equation:

$$A_k(\varphi_k^{PSD}) = \frac{2}{T} \int_0^T A(t) \sin(k\omega t + \varphi_k^{PSD}) dt \quad \text{Eq. (7.3)}$$

where T is the length of a period,  $\omega$  is the stimulation frequency, k is the demodulation index,  $\varphi_k^{PSD}$  is the demodulation phase angle, and A(t) and A( $\varphi_k^{PSD}$ ) are the active species response in time- and phase-domain, respectively.<sup>173</sup>

### 6.2.5 Density functional theory simulation

Quantum chemical calculations were performed with the Gaussian 16 (rev. C01) code.<sup>174</sup> The IR spectra and the adsorption electronic energies, enthalpies and Gibbs free energies for relevant molecules, also interacting with a Brønsted acid site were simulated with the B3LYP hybrid DFT functional,<sup>175,176</sup> including dispersive forces through the Grimme D3 empirical scheme.<sup>177</sup> The structure of the molecules of interest, as such and interacting with a minimal Brønsted acid site model is shown in **Figure E1** and **Figure E2-Appendix**. The polarizable continuum model (PCM) was adopted to implicitly include the effect of solvent (i.e. cyclohexane), for the sake of a better comparison with the ATR-IR data.<sup>178</sup> During geometry optimization, all the atoms were described with the Pople 6-31+D(d,p) basis set.<sup>179</sup> Thermal corrections to enthalpy and Gibbs free energy corrections were computed at the same level of theory adopted for optimization.

## 6.3 Results and discussion

### 6.3.1 Physico-chemical characterization of the catalyst

The XRD pattern displayed the characteristic reflections of a zeolite Beta structure (**Figure E3 – Appendix**). NH<sub>3</sub> temperature programmed desorption (NH<sub>3</sub>-TPD) and pyridine adsorption by ATR-IR spectroscopy were used to study the acidic properties of the catalyst (**Figure E4 – Appendix**). An acidity of 0.880 mmol·g<sup>-1</sup> was obtained by quantification of the NH<sub>3</sub>-TPD results. The nature of the acidity was determined by ATR-IR. Signals ascribed to pyridine bound to the Brønsted acid sites (BAS) were detected at 1490, 1545 and 1638 cm<sup>-1</sup>.<sup>180</sup> Overall, H-Beta displayed strong Brønsted acidity. After drying the material at 500 °C under residual pressure below 10<sup>-3</sup> mbar for 1 h, an IR spectrum recorded in

transmission mode shows the main signals in the -OH stretching region at 3746 and 3611  $\text{cm}^{-1}$ , corresponding to the free external silanols and BAS respectively (**Figure E5 – Appendix**).<sup>181</sup>

### 6.3.2 Catalytic activity of zeolite H-Beta for OME synthesis in the presence of water

The synthesis of OME using TRI and OME<sub>1</sub> with various water concentrations was conducted at 30 °C and ambient pressure (**Figure 6.1**). Conversion of TRI reached equilibrium (96 %) within 30 min using OME<sub>1</sub> containing 0.03 wt.% H<sub>2</sub>O (OME<sub>1</sub>-0.03-H<sub>2</sub>O). Higher concentrations of water in OME<sub>1</sub> caused reduction of activity to negligible values: after 60 min, OME<sub>1</sub>-0.21-H<sub>2</sub>O and OME<sub>1</sub>-0.40-H<sub>2</sub>O reached a TRI conversion of only 1.8% and 1.1%, respectively. TRI conversion of 0.6% was obtained after 60 min using OME<sub>1</sub> from a different supplier with a water content of 0.44 wt.%. Thus, TRI conversion at 30 °C was almost negligible at water concentration as low as 0.21 wt.%. Hence, water had a deleterious effect on the kinetics of OME synthesis from TRI and OME<sub>1</sub>, which increased with increasing water concentration in OME<sub>1</sub>, in agreement with previous work.<sup>168</sup>

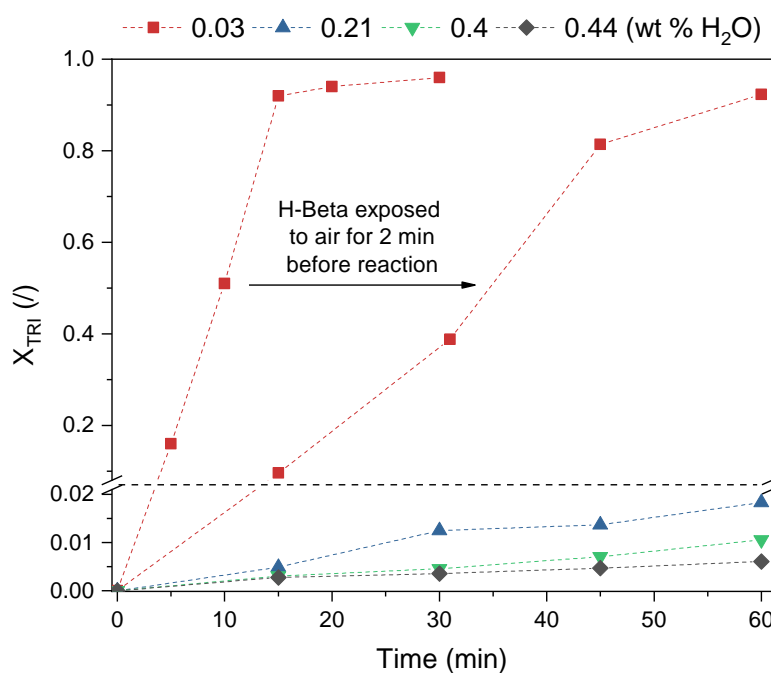


**Figure 6.1:** TRI conversion ( $X_{\text{TRI}}$ ) during synthesis of OME on H-Beta from OME<sub>1</sub> and TRI using various water concentrations in OME<sub>1</sub> ( $T = 30\text{ }^{\circ}\text{C}$ , 0.5 wt.% catalyst, molar ratio OME<sub>1</sub>:TRI = 3.3). OME<sub>1</sub> (0.44 H<sub>2</sub>O) was obtained from a different supplier.

A source of water that could significantly affect the performance of the catalyst is the moisture content of H-Beta. Therefore, the effect of catalyst pre-treatment on the performance of H-Beta was also tested. In the catalyst pre-treatment procedure, exposure to moisture from ambient air is typically minimized. When the catalyst was intentionally exposed to ambient air

for 2 min prior to reaction, TRI conversion dropped by factor of nine after 15 min compared to the standard pre-treatment procedure (**Figure 6.1**).

### 6.3.3 Modulation excitation attenuated total reflectance infrared spectroscopy

*In situ* ATR-IR experiments were performed to identify potential competitive adsorption processes between water and the reactants within the zeolite framework under reaction conditions that could be responsible for the inhibition effect of water on OME synthesis. To confirm that the reaction proceeded under the diluted reactants concentrations selected for ME experiments, catalytic tests performed in batch conditions (**Figure E6 – Appendix**) indicated that TRI conversion into OME and product selectivity were retained. The ME-ATR-IR experiments were carried out in a flow cell to increase the control on the reactive environment and to prevent accumulation of surface species, which can occur under batch conditions.<sup>182</sup>

#### 6.3.3.1 Adsorption-desorption of OME<sub>1</sub> and TRI on H-Beta

**Figure 6.2** shows two representative ATR-IR spectra (black, scaled by a factor 0.3) measured during modulation experiments of OME<sub>1</sub> (**Figure 6.2a**) and TRI (**Figure 6.2c**) in cyclohexane. In the OH region, the spectra exhibit a negative signal at 3650 cm<sup>-1</sup> and a broad positive signal at 3260 cm<sup>-1</sup>, which indicate consumption of the silanol groups and formation of hydrogen bonded species, i.e. adducts of OME<sub>1</sub> (Si-OH...OME<sub>1</sub>) and TRI (Si-OH...TRI). An important negative contribution at ca. 3450 cm<sup>-1</sup> appearing as high energy negative shoulder of the former band in the spectrum of the experiment with OME<sub>1</sub> seems absent in the case of TRI. In the spectrum obtained with TRI, this region is instead occupied by a signal at ca. 3470 cm<sup>-1</sup>. As it will become clearer in the following, this band is assigned to coordination of OME<sub>1</sub> to BAS.

The two time-resolved spectra also display a negative signal at ca. 1616 cm<sup>-1</sup> associated with physisorbed water. We explain the presence of water on the zeolite with the fact that during equilibration with the neat solvent prior to the modulation experiment, it was not removed entirely from the zeolite pores likely because of its poor solubility in cyclohexane. It thus became part of the background spectrum, but it was displaced by the subsequent flow of the TRI and OME<sub>1</sub> solutions. The significantly larger negative signal of desorbed water in the case of OME<sub>1</sub> (**Figure 6.2a**) implies that OME<sub>1</sub> displaces water more easily from the zeolite than TRI.

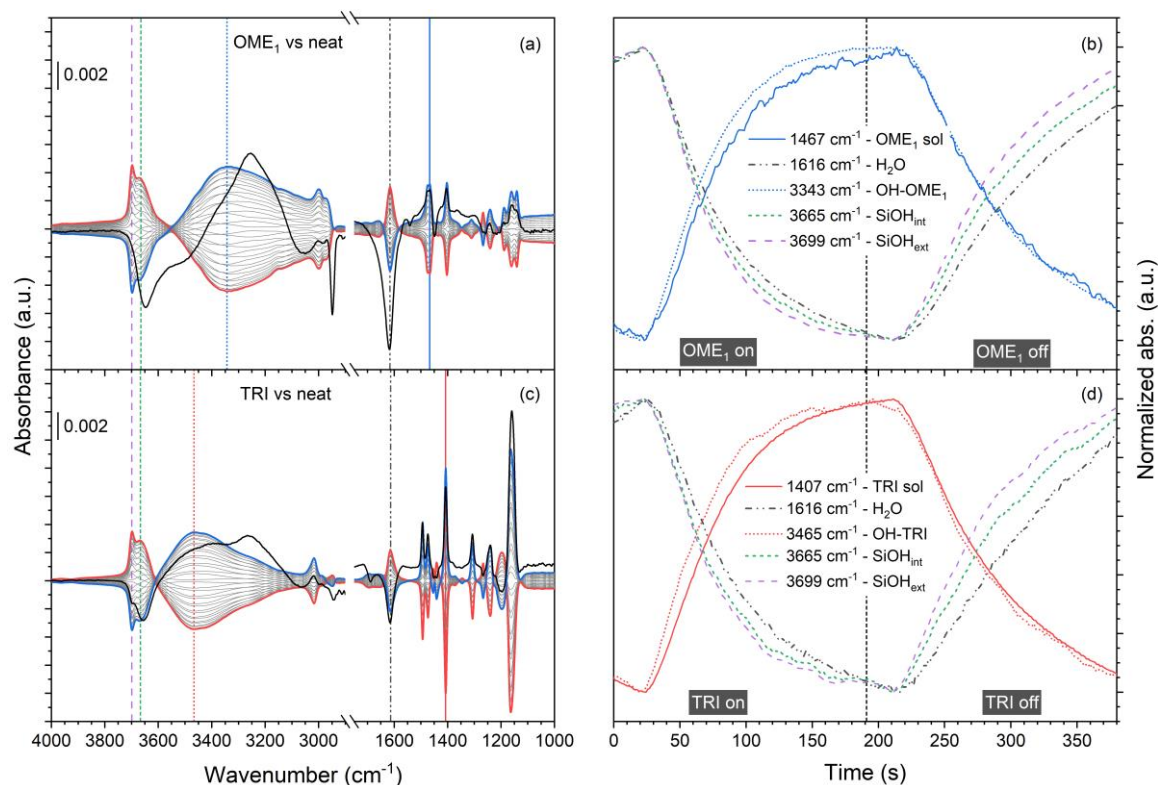


**Figure 6.2:** Phase-resolved ATR-IR spectra and time-dependent traces of modulation experiments: (a, b) OME<sub>1</sub> vs. neat solvent and (c, d) TRI vs. neat solvent. Vertical lines in (a, c) identify signals whose time-dependence is displayed in (b, d); the same line pattern and color are used. The time-resolved spectra (solid black line) in (a, c) are scaled by a factor 0.3.

The characteristic signals of OME<sub>1</sub> and TRI in the region below 1100 cm<sup>-1</sup> where C-O modes of ethers and their products can be expected are masked by the zeolite framework. Hence, we need to rely on the signals in the fingerprint region above 1100 cm<sup>-1</sup> based on comparison with the spectra of the reactants in cyclohexane and on simulation of the spectra of the most stable isomers of OME<sub>1</sub> (bent and linear, **Figure E7-Appendix**) and TRI (boat and chair, **Figure E8-Appendix**).<sup>183,184</sup> The normal mode analysis suggested that OME<sub>1</sub> and TRI adopt their most stable configuration, bent and boat forms, respectively. No additional signals that could be attributed to adsorbed species were observed in the ATR-IR spectra. The major difference between the time-resolved spectrum of **Figure 6.2a** and the spectrum of OME<sub>1</sub> is the intensity of the signal at 1141 cm<sup>-1</sup> (asymmetric stretch O-C-O mode,  $\nu_{as}(\text{OCO})$ ) relative to the other signals, e.g. at 1188 and 1161 cm<sup>-1</sup> (CH<sub>3</sub> rocking,  $\gamma(\text{CH}_3)$ ).<sup>183</sup> This observation may be taken as a crucial indication of the interaction of OME<sub>1</sub> with H-Beta as further discussed below.

The modulation experiment caused the spectra to vary periodically because of the repeated adsorption/desorption of OME<sub>1</sub> and TRI. Better evaluation of changes in the spectra can be obtained from phase sensitive detection (PSD). All the signals exhibiting the same sign (in

phase) of the bands in the adduct region were assigned to dissolved OME<sub>1</sub> or TRI. When OME<sub>1</sub> or TRI are present, they interact with the sample through such adducts. The periodic displacement of the solutions by the solvent contributed to the modulation of the signal at 1616 cm<sup>-1</sup>: water was periodically removed and partially restored because neat cyclohexane contains traces of water (0.004 wt.% by Karl-Fischer titration). The phase-resolved spectra present two peaks at 3699 and 3665 cm<sup>-1</sup> in both experiments that are assigned to perturbation of external (Si-OH<sub>ext</sub>) and internal silanol groups (Si-OH<sub>int</sub>), respectively.<sup>181,185</sup> While Si-OH<sub>ext</sub> appears of constant energy in all phase-resolved spectra, the signal of Si-OH<sub>int</sub> shifts suggesting the contribution of more than one silanol species. Remembering the 0.3 scaling factor of the time-resolved spectra of **Figure 6.2**, the fact that the signals of silanols are on the high energy shoulder of the negative signal at 3650 cm<sup>-1</sup> of the corresponding time-resolved spectrum suggests that the latter is mainly associated with the signal at 1616 cm<sup>-1</sup> and thus with water coordinated within the zeolite. The significantly low frequency values of the silanol signals compared to the values obtained for the dry material (3746 cm<sup>-1</sup>, **Figure E5-Appendix**) are due to the presence of the liquid environment, thus the cyclohexane solvent.<sup>186</sup> The difference in energy between the signals of the silanol group of dry and wet H-Beta ( $\Delta\nu = 47$  cm<sup>-1</sup>) suggests that a shift needs to be expected also for the vibrational signature of BAS. This falls at ca. 3610 cm<sup>-1</sup> in the spectrum of H-Beta (**Figure E5-Appendix**). We thus assign the strong negative signal at 3450 cm<sup>-1</sup> ( $\Delta\nu = 160$  cm<sup>-1</sup>) in the time-resolved spectrum of OME<sub>1</sub>, seemingly absent in the spectrum of TRI, to the consumption of the BAS upon interaction with OME<sub>1</sub>.<sup>181</sup> Because this signal is much weaker if not absent in case of TRI, we can already conclude that the interaction of BAS is stronger with OME<sub>1</sub> than with TRI.

The broad band centered at ca. 3400 cm<sup>-1</sup> of opposite sign with respect to the silanol bands is ascribed to the interaction of OME<sub>1</sub> or TRI with both types of silanol groups and the BAS. Despite originating likely from a number of signals due to adducts with various types of silanols, only adducts of OME<sub>1</sub> or TRI with silanol groups can be described with the maxima of these broad bands in the phase-resolved spectra. Maxima of the broad band at 3343 cm<sup>-1</sup> (**Figure 6.2a**) and at 3465 cm<sup>-1</sup> (**Figure 6.2c**) were assigned to Si-OH...OME<sub>1</sub> and Si-OH...TRI adducts, respectively. While the signals of silanol groups fall at the same position in both experiments because they belong to hydroxyl groups present on the H-Beta zeolite, the signals attributed to the adducts possess different position. Considering that the shift compared to the position of the silanol groups is proportional to the adsorption enthalpy,<sup>39</sup> the lower energy of the maximum for Si-OH...OME<sub>1</sub> compared to Si-OH...TRI reveals that also the bonding of

OME<sub>1</sub> to the silanol groups is stronger than that of TRI. OME<sub>1</sub> attracts the H atom more strongly than TRI.

The assignments were also based on the analysis of the time dependence of the normalized peak intensity of the band of each adduct, which were correlated to the concentration of the analogous species in solution (**Figure 6.2b and d**). Signals at 1465 (bending CH<sub>3</sub>,  $\delta(\text{CH}_3)$ ) and 1407 cm<sup>-1</sup> (CH<sub>2</sub> wagging,  $\omega(\text{CH}_2)$ ) were considered representative of dissolved OME<sub>1</sub> and TRI, respectively by comparison with the spectra of the pure compounds (**Figure E7 and F8-Appendix**). These bands were in phase with the broad -OH stretching band and exhibited opposite sign with respect to the signals of free silanol groups in agreement with the reversible consumption of silanol groups upon interaction with OME<sub>1</sub> and TRI and with the formation of the Si-OH...OME<sub>1</sub> and Si-OH...TRI adducts.

The phase-resolved spectra and the temporal dependence of selected vibrational bands allowed correlating the silanol groups consumption with the formation of Si-OH...OME<sub>1</sub> or Si-OH...TRI adducts. Selected phase-resolved spectra highlighted in **Figure 6.2a** and **Figure 6.2c** and those selected in **Figure E9-Appendix**, demonstrate that the adduct region of OME<sub>1</sub> is composed of at least two broad vibrational bands below the band at 3346 cm<sup>-1</sup> ( $\varphi^{\text{PSD}} = 110$  and 290°) that exhibit clearly distinct kinetics. The Si-OH<sub>ext</sub> (3698 cm<sup>-1</sup>) is negative at  $\varphi^{\text{PSD}} = 10^\circ$  and is accompanied by a positive signal at 3413 cm<sup>-1</sup> that we assign to Si-OH<sub>ext</sub>...OME<sub>1</sub>; the Si-OH<sub>int</sub> signal (3653 cm<sup>-1</sup>) is negative at  $\varphi^{\text{PSD}} = 200^\circ$  when a positive one appears at 3258 cm<sup>-1</sup> (Si-OH<sub>int</sub>...OME<sub>1</sub>). In **Figure 6.2**, this behavior is similar in the case of TRI, but the broad band at 3468 cm<sup>-1</sup> ( $\varphi^{\text{PSD}} = 110$  and 290°) seems composed of two very close signals at 3458 cm<sup>-1</sup> (attributed to Si-OH<sub>ext</sub>...TRI) and 3499 cm<sup>-1</sup> (Si-OH<sub>int</sub>...TRI). Even if the band is composed of various contributions, the corresponding species below this envelope exhibit very similar adsorption-desorption kinetics giving a symmetric shape to it. A significant difference in the kinetics of the silanols recovery is observed for both reactants in the desorption segment of the experiments (**Figure 6.2b,d**) that mirrors the difference observed in the phase-resolved data. While both types of silanols are modulated upon desorption of OME<sub>1</sub> or TRI, their temporal dependence shows that the external silanols are liberated earlier than the internal silanols, thus reminding of diffusion limitations for the reactant desorption.

The observation of the BAS, only interacting with the solvent, modulation in the phase-resolved spectra is difficult because several species are monitored in the same spectral region, i.e. the BAS being consumed by OME<sub>1</sub> together with the formation of at least two types of Si-OH...OME<sub>1</sub> adducts as interpreted from the phase-resolved spectra. However, a

signal appears at  $3553\text{ cm}^{-1}$  in the phase-resolved spectrum at  $\varphi^{\text{PSD}} = 10^\circ$  of **Figure E9-Appendix**, that we assign to modulation of BAS upon interaction with  $\text{OME}_1$  because it falls in the region of the BAS observed as a negative shoulder in the time-resolved spectrum at  $3450\text{ cm}^{-1}$ . The spectral contribution due to the formation of the adsorbate  $\text{BAS}\cdots\text{OME}_1$ , a weak broad band below  $3000\text{ cm}^{-1}$ , could not be observed.<sup>181</sup> The close values of all signals in the case of TRI (**Figure 6.2c**) do not allow to identify this signal in the phase-resolved data.

In the fingerprint region of **Figure 6.3**, the phase-resolved spectra mirror the modulation of the signals of  $\text{OME}_1$  and TRI. In the case of  $\text{OME}_1$ , the different ratio between the signals at  $1161$  and  $1141\text{ cm}^{-1}$  is evident again and suggests that adsorption-desorption causes an interaction with the zeolite that manifests in the change of intensity of the signal at  $1141\text{ cm}^{-1}$ . These assignments were further confirmed by performing the modulation experiments after pyridine adsorption. Spectral features at  $1490$ ,  $1545$  and  $1638\text{ cm}^{-1}$  confirmed the coordination of pyridine to BAS as pyridinium ion that did not desorb under the continuous flow of  $\text{OME}_1$  or TRI solutions (**Figure E10-Appendix**). The phase-resolved spectra obtained in the two modulation experiments with ( $\varphi^{\text{PSD}} = 0^\circ, 10^\circ, 200\text{-}360^\circ$ ) and without ( $\varphi^{\text{PSD}} = 20\text{-}190^\circ$ ) pyridine are presented in **Figure 6.3** to allow for a clearer comparison. Titration of the BAS with pyridine changed significantly the aspect of the phase-resolved spectra during  $\text{OME}_1$  modulation (**Figure 6.3a**). The adduct signal was blue-shifted from  $3300\text{ cm}^{-1}$  to  $3330\text{ cm}^{-1}$ , was more symmetric in presence of pyridine and was ideally composed of a single peak rather than the two peaks observed in absence of pyridine. As a result of pyridine adsorption on BAS, the broad peak observed at  $3553\text{ cm}^{-1}$  in **Figure 6.2a** was absent, thus confirming its assignment to BAS and suggesting that the BAS were not involved in the exchange of  $\text{OME}_1$ , because they were blocked by pyridine. Finally, the signal at  $1142\text{ cm}^{-1}$  exhibited an intensity closer to the solution values in the presence of pyridine relative to the peak of dissolved  $\text{OME}_1$  at  $1160\text{ cm}^{-1}$ . Hence, its lower intensity in the absence of pyridine is attributed to coordination of  $\text{OME}_1$  to the BAS via the oxygen atom.



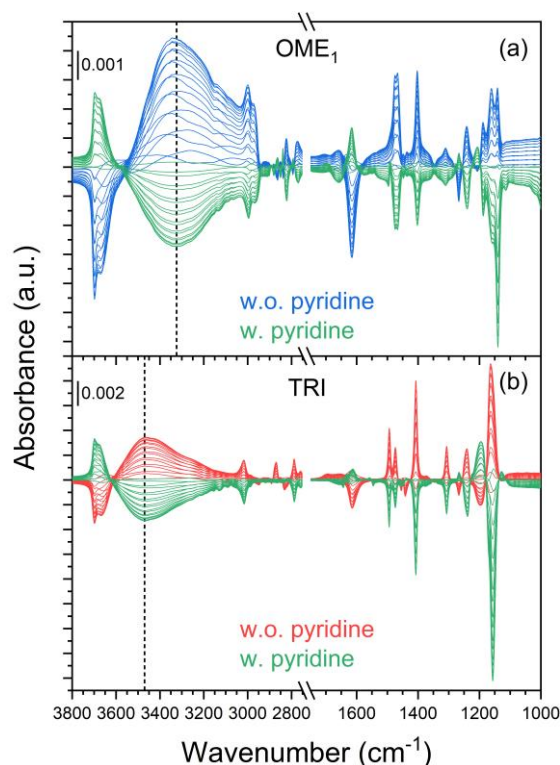


**Figure 6.3:** Phase-resolved ATR-IR spectra obtained from modulation experiments of (a) OME<sub>1</sub> vs. neat solvent and (b) TRI vs. neat solvent without (blue and red respectively;  $\varphi^{\text{PSD}} = 0^\circ, 10^\circ, 200 - 360^\circ$ ) and with (green;  $\varphi^{\text{PSD}} = 20 - 190^\circ$ ) pre-adsorbed pyridine.

The kinetics of adsorption and desorption is faster in the presence of pyridine. This can be observed in **Figure E11 – Appendix**, where the traces of the vibrational bands at 1160 cm<sup>-1</sup> and 1142 cm<sup>-1</sup> allow to follow the speed of appearance and disappearance of OME<sub>1</sub> in solution. In comparison, the two sets of phase-resolved spectra obtained from the modulation experiments with TRI were very similar irrespective of the presence of pyridine (**Figure 6.3b**) revealing that the interaction of TRI with BAS is less likely, under these experimental conditions. However, for both OME<sub>1</sub> and TRI the analysis of the time traces in the presence or absence of pyridine reveals that adsorbed species and occupancy of silanols exhibits faster kinetics when pyridine is binding to the BAS as shown in **Figure E12-Appendix**. Two interpretations can be provided for this behavior. On the one hand, a synergy between BAS and silanol groups affects the binding strength of the silanols. On the other hand, when pyridine is present in the zeolite framework, it prevents OME<sub>1</sub> or TRI to access the inner structure of the zeolite, therefore only sites available on the outside of the zeolite remain accessible for binding.

6.3.3.2 Effect of water concentration modulation on OME<sub>1</sub> and TRI adsorption-desorption

The effect of water on the interaction between H-Beta and OME<sub>1</sub> and TRI was studied by performing modulation experiments, in which the water content in the feed was varied against a constant concentration of each reactant (OME<sub>1</sub> vs OME<sub>1</sub> + H<sub>2</sub>O ; TRI vs TRI + H<sub>2</sub>O ; **Figure 6.4**). The resulting time-resolved spectra of **Figure 6.4a,c** resemble very much those of **Figure 6.2a,c**. In contrast, the band intensities obtained in the phase-resolved spectra of these modulation experiments are by an order of magnitude smaller compared to the intensities obtained in the absence of water (**Figure 6.2**). This is especially visible in the temporal dependence of the selected signals of OME<sub>1</sub> (**Figure 6.4b**), which are much noisier compared to the water-free adsorption-desorption experiment. The evident oscillations present in the kinetic traces that we associate with the pulsation induced by the peristaltic pump and the weak changes of the silanol groups and the absence of kinetic traces responding to the modulation of water, confirm that the later does not produce significant changes on OME<sub>1</sub> adsorption. The phase-resolved spectra (**Figure 6.4a**) do not display any characteristic signal of OME<sub>1</sub>, rather that of water at 1616 cm<sup>-1</sup> thus reflecting the addition and removal of water from solution.

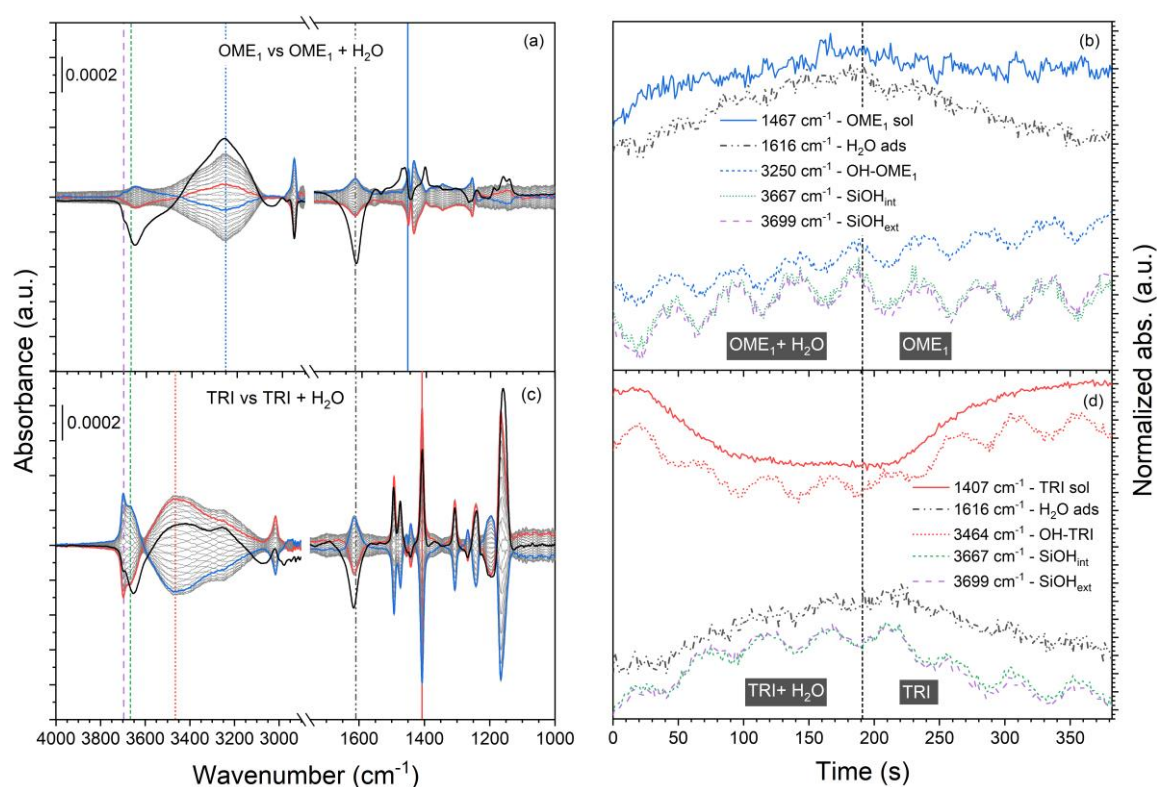


**Figure 6.4:** Phase-resolved ATR-IR spectra and time-dependent traces of modulation experiments: OME<sub>1</sub> vs. OME<sub>1</sub> + H<sub>2</sub>O (a, b) and TRI vs. TRI + H<sub>2</sub>O (c, d). Vertical lines in (a, c) identify signals whose time-dependence is displayed in (b, d); the same line pattern and color are used. The time-resolved spectra (solid black line) in (a, c) are scaled by a factor 0.02.

Regarding TRI adsorption-desorption, the phase-resolved spectra exhibit signals that are identical to those observed in **Figure 6.2c** indicating that a very similar process occurs during water modulation. The response of these signals in the time domain mirrored the concentration of water in the feed (**Figure 6.4d**), i.e. when water was introduced into the cell, the intensity of the signals of TRI decreased and it was restored when water was removed. Thus, TRI adsorption depends on the presence of water and a weaker interaction of TRI with the silanol groups than water can be inferred.

The observation that water did not perturb significantly the adsorption of OME<sub>1</sub> (**Figure 6.4b**) but strongly affected the adsorption of TRI (**Figure 6.4d**) unambiguously confirms that OME<sub>1</sub> bonded more strongly to the zeolite than water according to the surface affinity order: OME<sub>1</sub> > H<sub>2</sub>O > TRI.

#### 6.3.3.3 Reactants modulation under reactive conditions

The surface coverage of the catalyst under reaction conditions was also investigated by concentration modulation experiments (**Figure 6.5**). It is important to note that the two selected time-resolved spectra of **Figure 6.5a** and **Figure 6.5c** are essentially identical and are very similar to that in **Figure 6.2c** showing adsorption/desorption of TRI. However, the spectra of **Figure 6.5a,c** originate from two different experiments, OME<sub>1</sub> vs. OME<sub>1</sub> + TRI and TRI vs. OME<sub>1</sub> + TRI. Intensity and width differences with the spectrum in **Figure 6.2c** can be attributed to the overlap of the signals of OME<sub>1</sub> with those of TRI. Hence, irrespective of type of pulse sequence, TRI was the reactant with the strongest response to the concentration modulation.

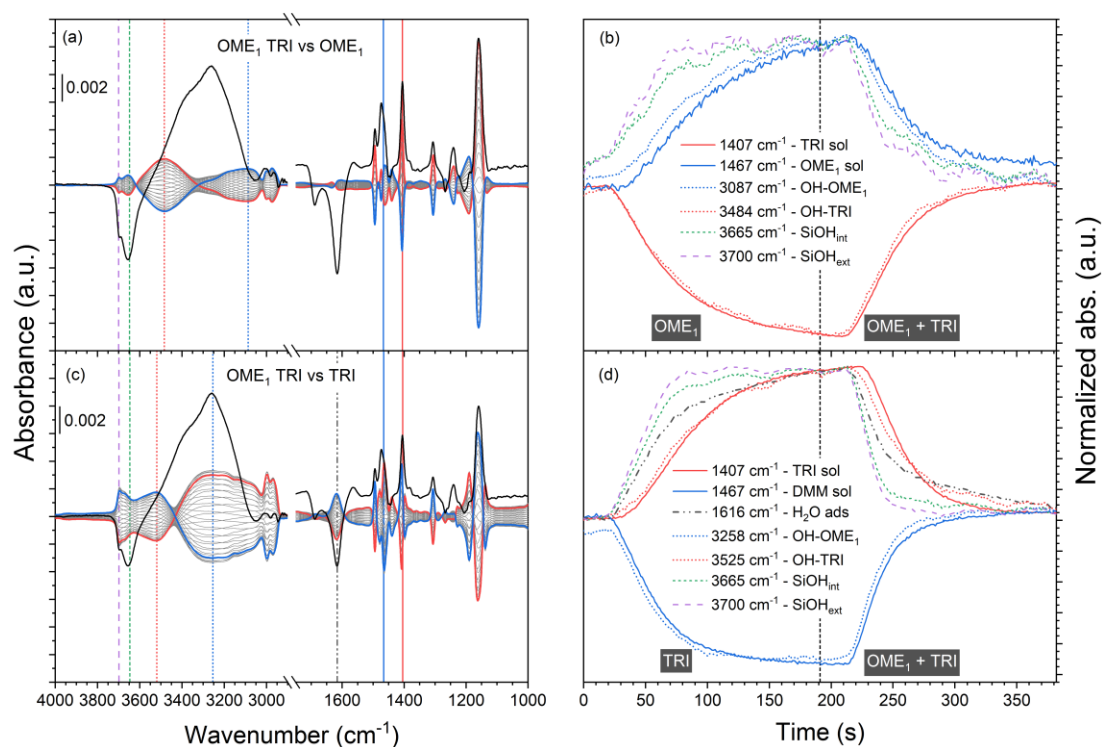


**Figure 6.5:** Phase-resolved ATR-IR spectra and time-dependent traces of modulation experiments: OME<sub>1</sub> + TRI vs. OME<sub>1</sub> (a, b) and OME<sub>1</sub> + TRI vs. TRI (c, d). Vertical lines in (a, c) identify signals whose time-dependence is displayed in (b, d); the same line pattern and color are used. The time-resolved spectra (solid black line) in (a, c) are scaled by a factor 0.1.

During modulation of TRI in OME<sub>1</sub> solution (OME<sub>1</sub> vs. OME<sub>1</sub> + TRI ; **Figure 6.5a**), the vibrational bands associated with the silanol groups displayed low intensity in the phase-resolved spectra indicating that modulation of TRI concentration did not impact the occupancy of those sites significantly likely because this interaction is dominated by OME<sub>1</sub>. The adduct region is significantly different from that of **Figure 6.2a**. A signal is modulated at 3484 cm<sup>-1</sup> that falls within the region of the signals of the BAS and a peak shape similar to the BAS observed on the dehydrated material (**Figure E5-Appendix**). Moreover, its intensity is larger than that of the silanol signals, while in the case of concentration modulation of OME<sub>1</sub> and of TRI, the change is roughly equal between the two signals. We take these observations to demonstrate the utilization of the BAS, rather than silanol groups, which are responding to the modulation of the reactants concentrations thus being involved in the reaction mechanism. The signals of dissolved TRI and of the Si-OH...TRI adducts were in phase opposition with both dissolved and coordinated OME<sub>1</sub>, which is evident in the time dependence of the signals (**Figure 6.5b**). The evolution of the signals of OME<sub>1</sub> (**Figure 6.5b**) and TRI (**Figure 6.5d**) is clearly delayed compared to the evolution of the silanol groups while this is not the case in **Figure 6.2b,d**. While the intensity of the Si-OH<sub>ext</sub> signal increases at the moment the TRI solution is removed and stabilizes after ca. 100 s, the signals of Si-OH<sub>int</sub> and OME<sub>1</sub> grow more

slowly and reach maximum intensity only at the end of the OME<sub>1</sub> pulse. Hence, the recovery of the silanol groups occurs before the increase in OME<sub>1</sub> concentration, both on the surface and in solution. Under reaction conditions, while displacing the TRI solution, the adducts of TRI are consumed first, thus freeing the silanol groups. This process may be responsible for the production of OME<sub>n</sub>. Despite the fact that we do not have evidence for the reaction occurring, because the effluent of the ATR-IR cell was not monitored, the decrease in the concentration of coordinated and dissolved OME<sub>1</sub> in correspondence of the pulses of TRI solution (**Figure 6.5b**) implies the consumption of OME<sub>1</sub>. The concentration of OME<sub>1</sub> should otherwise remain constant in this experiment. When the flow of the TRI solution is switched off, the concentration of OME<sub>1</sub> in solution and at the surface of the catalyst starts increasing after ca. 40 s, due to the delay generated by the dead volume between the switching valve and the cell, indicating that OME<sub>1</sub> consumption and thus reaction have stopped.

Similar observations can be made during the modulation experiment of OME<sub>1</sub> pulses in a continuous feed of TRI solution (**Figure 6.5c,d**). However, the Si-OH<sub>ext</sub> and Si-OH<sub>int</sub> signals were larger than during the modulation of TRI in the presence of OME<sub>1</sub>, indicating that a larger amount of silanol groups were consumed in the presence of OME<sub>1</sub>, in agreement with the higher affinity of OME<sub>1</sub> for the silanol groups compared to TRI demonstrated above. Hence, when TRI was constantly present in the reaction feed, it first reacted with OME<sub>1</sub> bound to the silanol groups. Furthermore, the modulation of OME<sub>1</sub> perturbed the signal of water at 1616 cm<sup>-1</sup>. In the time domain (**Figure 6.5d**), this signal was delayed compared to that of the silanol groups, which might reflect the adsorption of water to a stronger acid site. Overall, these two ME-ATR-IR experiments under reaction conditions demonstrate the occurrence of the reaction between OME<sub>1</sub> and TRI and the stronger interaction of OME<sub>1</sub> with the zeolite.

Finally, the concentration modulation experiment of water in a continuous feed of both reactants (OME<sub>1</sub> + TRI vs OME<sub>1</sub> + TRI + H<sub>2</sub>O, **Figure 6.6**) shows that under reaction conditions the phase-resolved spectra presented the spectral features of dissolved OME<sub>1</sub> and TRI. In the adduct region of the spectra, the same band at 3484 cm<sup>-1</sup> was present as in **Figure 6.5a** that was assigned to BAS. The time traces of the various selected maxima showed that only TRI in solution and the BAS were responding to the concentration modulation of water. This suggests that water was able to displace TRI but not OME<sub>1</sub> and confirms the affinity trend for the zeolite binding sites.

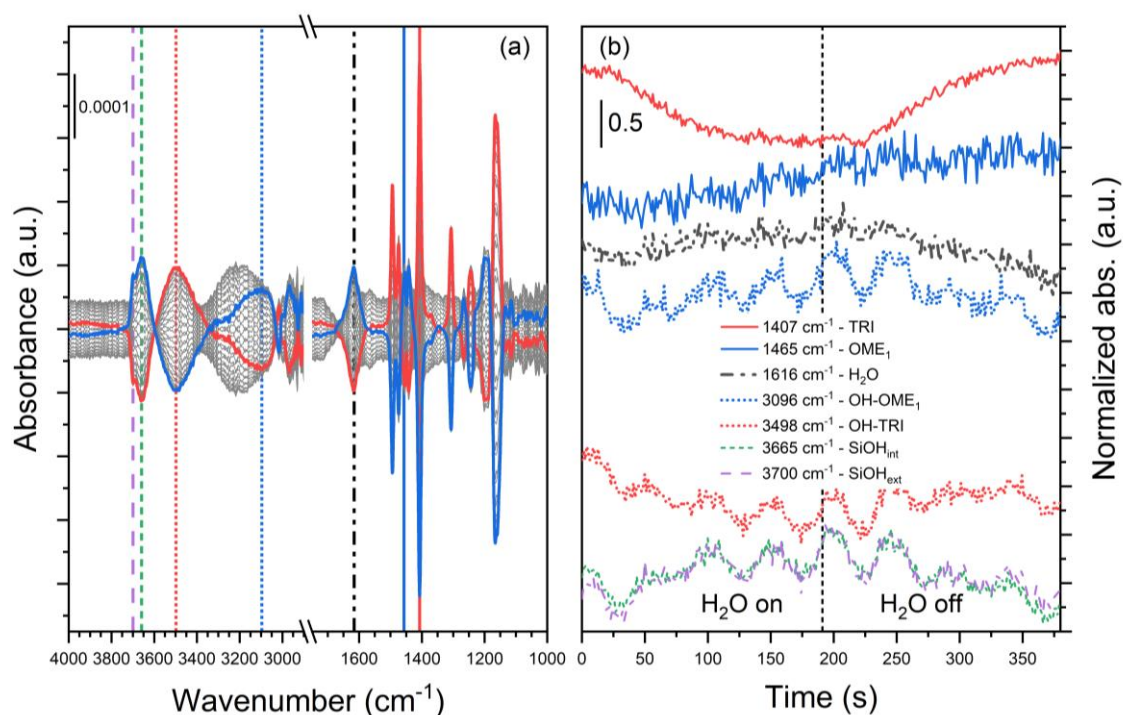


**Figure 6.6:** Phase-resolved ATR-IR spectra and time-dependent traces of modulation experiments: OME<sub>1</sub> + TRI vs. OME<sub>1</sub> + TRI + H<sub>2</sub>O. Vertical lines in (a) identify signals whose time-dependence is displayed in (b); the same line pattern and color are used.

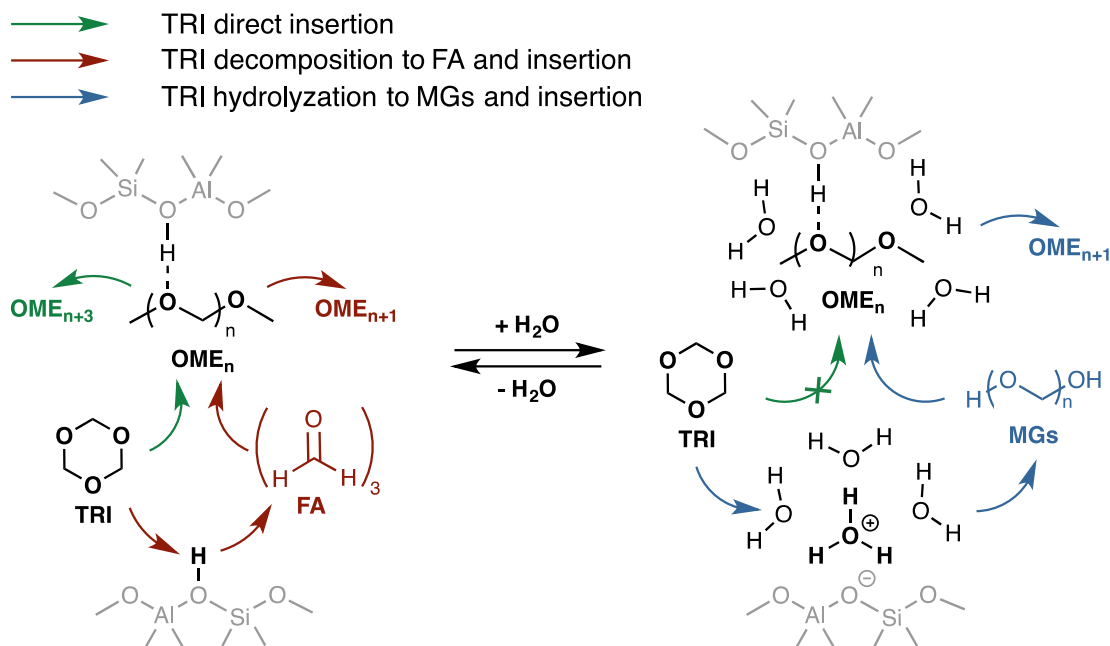
#### 6.3.3.4 Causes for zeolite deactivation due to water for OME synthesis

Water severely affected the kinetics of OME synthesis using TRI and OME<sub>1</sub> over an H-Beta zeolite. The ATR-IR study demonstrated that OME<sub>1</sub> possesses higher affinity for the zeolite binding sites compared to water and TRI, and that water competes predominantly with TRI for adsorption on the zeolite. Competitive adsorption of the reactants and water within the zeolite is thus considered the main cause for the kinetic inhibition of water. The poor interaction of TRI with the zeolite active sites due to the presence of water resulted in slower reaction kinetics (**Scheme 6.3**).

The adsorption-desorption experiments of OME<sub>1</sub> and TRI demonstrated that in cyclohexane the affinity of OME<sub>1</sub> for the surface is stronger than TRI. The higher adsorption enthalpy of OME<sub>1</sub> to the zeolite binding sites explains the higher resistance of OME<sub>1</sub> against competitive adsorption with water. On the contrary, the less strongly adsorbed TRI is much more susceptible to perturbation and displacement by water. We attribute the different affinity of water and TRI for the silanol groups to the greater ability of a water molecule/cluster to accommodate a proton than the C-O-C group of TRI. Under reaction conditions, modulation



of  $\text{OME}_1$  in the continuous presence of TRI affected more severely silanols occupancy compared to modulation of TRI in the presence of  $\text{OME}_1$ . Finally, modulation of water affected TRI adsorption more severely in the presence of both reactants.



**Scheme 6.3:** Schematic illustration of the proposed mechanism of kinetic water inhibition during OME synthesis on H-Beta zeolite.

The spectroscopic experiments with BAS poisoning by pyridine offer novel molecular level insights into the interaction of the reactants with the hydroxyl groups of the zeolite. Blockage of the BAS by pyridine significantly perturbed the interaction of  $\text{OME}_1$  with the catalyst surface, revealing that  $\text{OME}_1$  interacted with both the BAS and the silanol groups of the pristine catalyst. Conversely, no significant changes were observed in the case of TRI, suggesting that TRI did not bind to the BAS under these experimental conditions. Therefore, we assume that limited TRI adsorption to the zeolite active sites due to the presence of water was the main cause for the kinetic inhibition. TRI activation is required to provide oxymethylene units for OME growth, irrespective of the growth mechanism. The inability of TRI to adsorb on a BAS probably reduced the rate of decomposition of TRI into FA units. The presence of water also shifted the main growth mechanism from direct TRI insertion or TRI decomposition/FA incorporation, to the insertion of FA from methylene glycols groups, as shown in **Scheme 6.3**.

In order to further corroborate our proposed water inhibition mechanism, we computed the adsorption energies of  $\text{OME}_1$ , TRI and  $\text{H}_2\text{O}$  over a simple BAS model (B3LYP-D3/CBS level of theory). The simulation results show that all the considered adsorbates are

thermodynamically stable and their formation is favored in the selected temperature-pressure conditions (**Table 6.2**). As inferred from the experimental evidences, the stability of the adsorption on BAS follows the order:  $\text{OME}_1 > \text{H}_2\text{O} > \text{TRI}$ . By estimating the equilibrium constant of each adsorption process from the  $\Delta G$  values, the equilibrium population of the adducts can also be estimated. It is dominated by  $\text{OME}_1$ -BAS species, accounting for more than 95 % of the total adducts, regardless of the water concentration. Conversely, the  $\text{TRI}$ -BAS/ $\text{H}_2\text{O}$ -BAS ratio is strongly affected by the water content, being 1.4 at the highest water concentration considered in this work (0.44 wt.%), whereas it increases noticeably by a factor  $\sim 15$  (up to 20.8) when the water concentration drops to 0.03 wt.%. These estimates confirm that the accessibility of BAS by TRI is the key step for sustaining the synthesis of oligomerized OME.

**Table 6.2.** B3LYP-D3/CBS electronic energies ( $\Delta E$ ), enthalpies ( $\Delta H$ ) and Gibbs free energies ( $\Delta G$ ) for  $\text{OME}_1$ , TRI and  $\text{H}_2\text{O}$  with BAS (expressed in  $\text{kJ}\cdot\text{mol}^{-1}$ ).

Adsorbates	$\Delta E/\text{kJ}\cdot\text{mol}^{-1}$	$\Delta H/\text{kJ}\cdot\text{mol}^{-1}$	$\Delta G/\text{kJ}\cdot\text{mol}^{-1}$
$\text{OME}_1$ -BAS	-59.8	-53.2	-6.3
TRI-BAS	-50.0	-43.6	-0.3
$\text{H}_2\text{O}$ -BAS	-53.5	-46.6	-4.3

## 6.4 Conclusion

The presence of water in  $\text{OME}_1$  at concentrations as low as 0.21 wt.% strongly affected the activity of zeolite H-Beta for the synthesis of OME from TRI and  $\text{OME}_1$ . Even the short exposure of zeolite H-Beta to the humid atmosphere was sufficient to significantly hinder its performance due to the uptake of water. Additionally, a shift of the main OME growth mechanism was also observed from direct TRI insertion or TRI dissociation with subsequent incorporation of FA units, to TRI hydrolyzation to methylene glycols followed by insertion. Using ATR-IR spectroscopy, we studied TRI and  $\text{OME}_1$  adsorption modes, offering new perspectives on the molecular aspects of the reaction. The affinity of reactants for the zeolite surface followed the order:  $\text{OME}_1 > \text{H}_2\text{O} > \text{TRI}$ . While  $\text{OME}_1$  interacted with the silanol groups and the Brønsted acid sites, TRI bonded predominantly to the silanol groups. This trend was further confirmed by DFT simulations. Combined together, these results suggest that the kinetic inhibition of water was due to the inability of TRI to interact with the BAS, which prevented its direct insertion or decomposition to FA units.



In light of the present results demonstrating the impact of water concentration on the catalytic activity of H-Beta, future catalytic studies on OME should compare carefully zeolites performance with materials of different Si/Al ratio. Since zeolites with high Si/Al ratio are more hydrophobic, they accumulate less water in the pores, which in turn influences the reaction kinetics in the shown way. As exposure to ambient moisture greatly affected the catalytic activity, even a similar exposure to ambient moisture for a set of catalysts may not prove to be sufficient, as the hygroscopicity may vary across the tested catalysts. Similarly, when comparing zeolites of different structure types, increasing the dimension of the channels may increase water diffusion, and ultimately exposition to water in the pores. These studies should thus be performed with minimum exposure to air before reaction. Furthermore, the concentration of water in OME<sub>1</sub> should always be carefully considered so that catalytic activities can be compared across studies.



## Chapter 7: Conclusion and outlook

In this work, we have studied various aspects of catalysts and catalytic processes at the solid-liquid interface, e.g. the reduction of supported PdO, the formation of Pd hydrides, their quantification, their reactivity in a transient in time-resolved manner, Ru and P-modified Ru based catalysts and zeolites. In order to provide structural information mainly X-ray absorption spectroscopy, infrared spectroscopy and X-ray diffraction were used, while the measurements were made possible by the realization of a dedicated setup including reactor cells. The cells are designed to allow for monitoring structural changes of oxidation state and nature of adsorbates in a time-resolved manner. This is of particular interest to study the reactivity of species, such as the Pd hydrides, formed on the catalyst in the liquid environment exploiting tools that are already widely applied to study gas phase reactions.

While it was possible to design, manufacture and demonstrate a cell enabling the repetition of the same experiment with XAS and ATR-IR spectroscopies (Chapter 2), this cell was not systematically used within this work. Results obtained in various sections of the work obtained with dedicated cells for either XAS or ATR-IR clearly show the advantage of this combination. The potential of the combination of XAS and vibrational spectroscopies for the interrogation of solid-liquid interfaces spans from the study of supported metal nanoparticles and clusters to the study of catalytically active transition elements exchanged within the framework of zeolites. In Chapters 3-5, supported Pd and Ru catalysts have been studied especially by XAS but also by ATR-IR spectroscopy to try and combine the complementary information offered by the two methods. In Chapter 6, the increased level of understanding that is achieved by coupling ATR-IR with the ME approach for the study of cation-free zeolites has been demonstrated. The next step is to establish the changes in chemical behavior when cations are inserted in the zeolite structure, as these are used in a variety of relevant reactions in the fields of green and sustainable chemistry as well as of renewables such as biomass derived processes. It is clear that the use of a transient methodology such as ME together with the demonstrated spectroscopic technique opens up new avenues to study liquid phase processes taking place in a liquid, very similar to the gas phase counterpart that are already extensively studied.

Beside XAS and ATR-IR, XRD was used in Chapter 3 to study the reduction of PdO/Al<sub>2</sub>O<sub>3</sub>. XRD is very much complementary to those two methods, but the exploitation of XRD to study heterogeneously catalyzed liquid phase reactions is still

very limited because of the requirement of developed crystal phases and long range order. In contrast, pair distribution function (PDF) holds an enormous potential because information is delivered at length scales comprised between those studied by XAS and XRD. PDF would allow not only to bridge the gap between XRD and EXAFS, but it would also complement the overall mechanistic information by allowing a better distinction between Pd hydrides/carbides and metallic Pd due to larger lattice shift leading to better peak resolution and by taking into account the behavior of the metal oxide support, which is often neglected or not accessible. Other techniques such as UV-Vis and Raman spectroscopies could be exploited to study liquid phase reactions at solid catalysts but the opinion of the author is that they require suitable samples, in contrast to XAS and IR, which appear of more universal application.

The tools that have been shown in this work are available to perform more complex studies of that presented in Chapter 4. For example, support effects and especially solvent effects that are often crucial in liquid phase catalyzed reactions can be in principle tackled. As preliminary measurements not included in the thesis suggest, identification, quantification and time-resolved analysis of the consumption of Pd hydrides are ready to be expanded to various catalysts, hydrogenation reactions and solvents. This could greatly contribute to the rationalization of mechanisms in liquid phase reactions. While it is clear that Pd hydrides are not suitable for IR spectroscopy, the same approach could be applied to Pt-based catalysts where hydrides possess clear fingerprints in the 2000-1800  $\text{cm}^{-1}$  spectral range. Here, combination of XAS and ATR-IR using a single reactor cell could be very powerful to correlate the temporal behavior of the electronic and vibrational information of these species under reaction conditions.

A strong limitation that was encountered in the measurements at solid-liquid interfaces is the difficulty to monitor on-line reactants, products and by-products at comparable time resolution of the techniques used to determine the structure of the catalysts to be able to link catalyst structure with performance. The low concentration of  $\text{H}_2$  in the solvent as well as the ATR-IR cell design (flow over the catalyst rather than flow-through) certainly influenced the extent of surface processes observed spectroscopically and the extent of reactions, thus implying low conversion and low product concentrations. However, the problem here is really that typical analytical methods such as gas-chromatography for the analysis of products do not match the

time constraints imposed by the application of fast transients and of the ME approach. Time-resolution is in the order of the minutes rather of seconds and intervalled sampling (collection of a defined amount of liquid to be injected at given times) is typically carried out. ESI-TOF or table-top NMR instruments for on-line monitoring of the outlet solution could greatly improve the outcome of transient experiments such as those described in Chapter 4.

# Appendices

## Appendix A (Chapter 2)

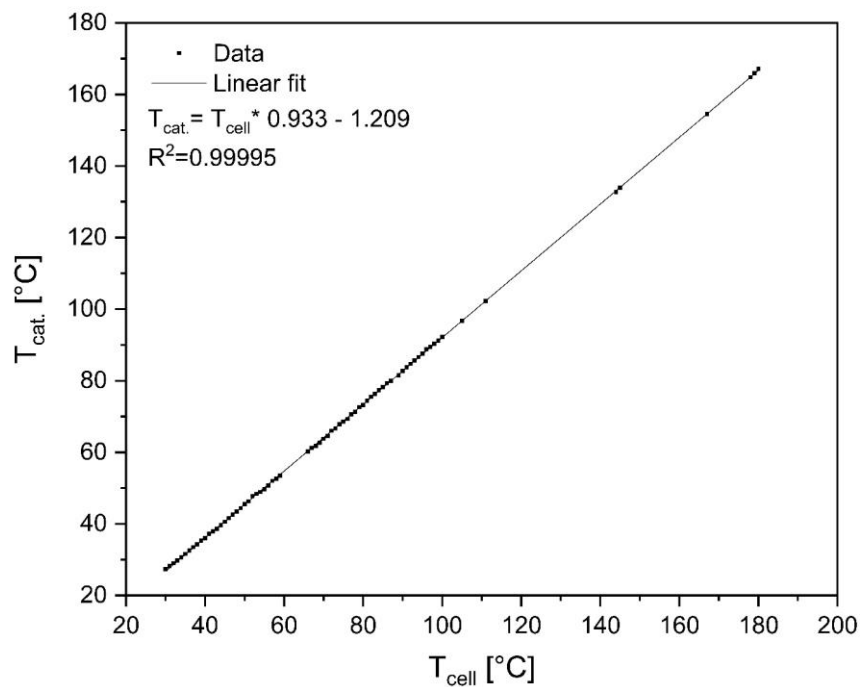


**Figure A1:** Temperature calibration of the catalyst bed. The cell was filled with 37 mg of  $Al_2O_3$  and a thermocouple was inserted in the bed ( $T_{cat.}$ ). The cell temperature was controlled via the temperature controller which is reading the temperature in the cell body ( $T_{cell}$ ). The cell was heated at  $2^{\circ}C$  from  $30^{\circ}C$  to  $180^{\circ}C$  setpoint of  $T_2$  while reading the output value from  $T_1$ .



**Figure A2:** Picture of the setup installed at the SuperXAS beamline (SLS, Switzerland).



## Appendix B (Chapter 3)

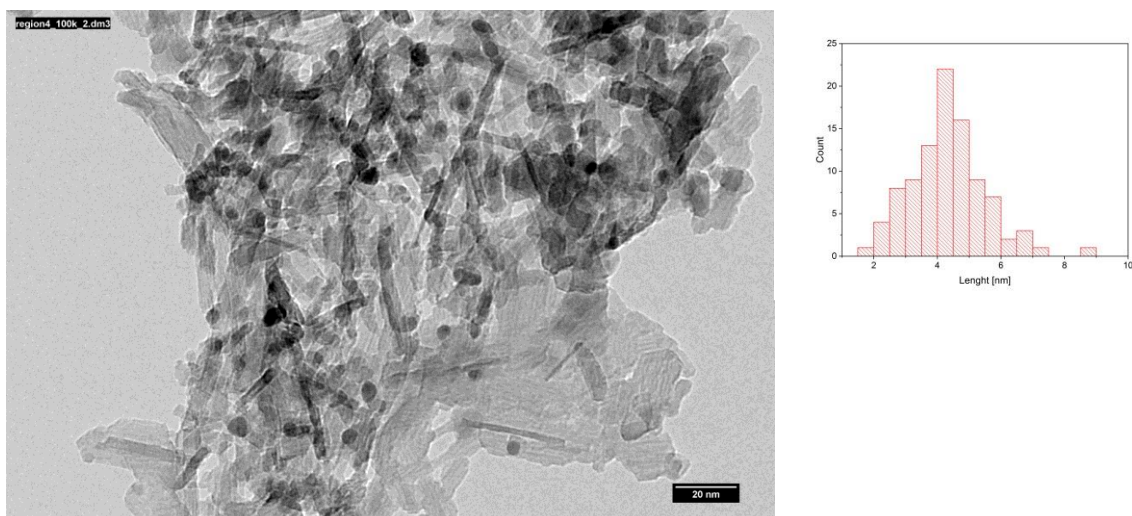


**Figure B1:** Electron micrograph of the catalyst and particle size distribution obtained from analyzing 97 particles on 10 micrographs.

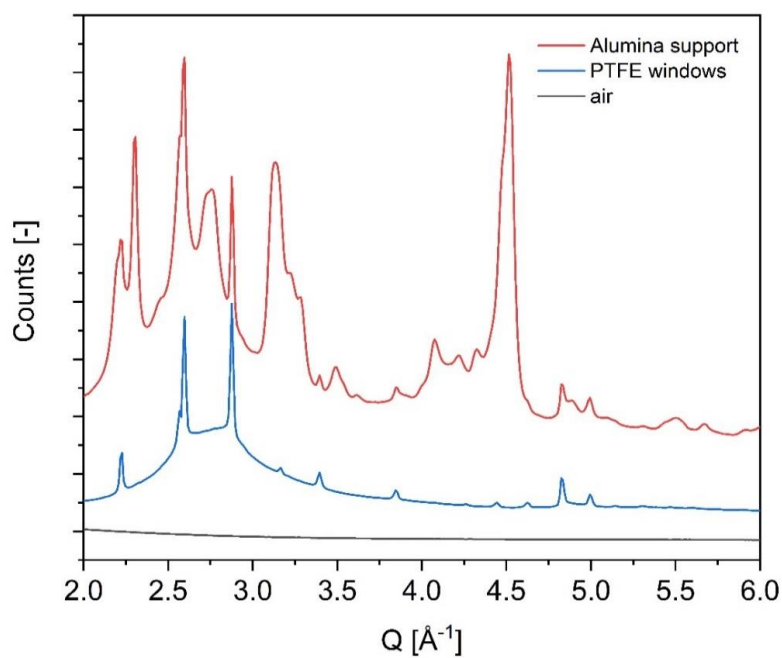


**Figure B2:** XRD pattern within the cell of the Al<sub>2</sub>O<sub>3</sub> support, the Teflon windows and the empty cell (air).

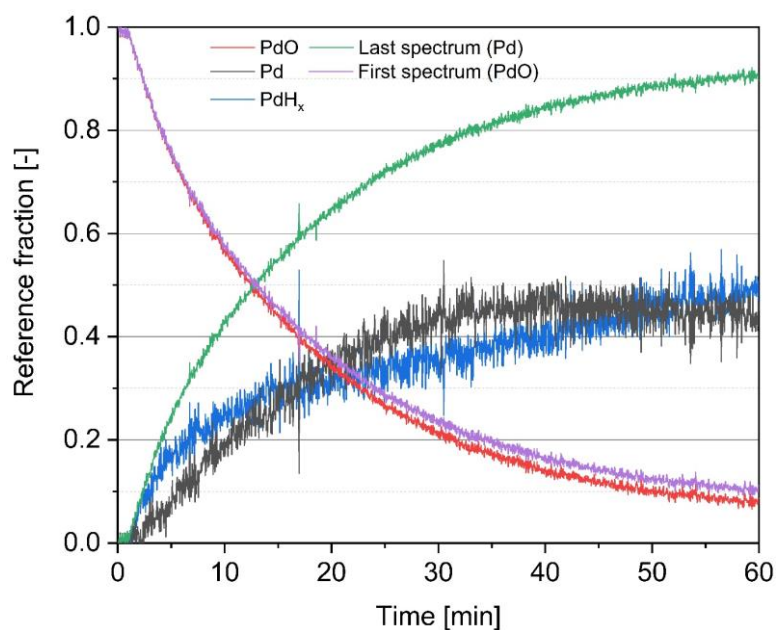


**Figure B3:** Comparison of XANES-LCF on the in situ reduction dataset. Once fitted with the three references and fitted with two references as the first and last spectra of the experiment.

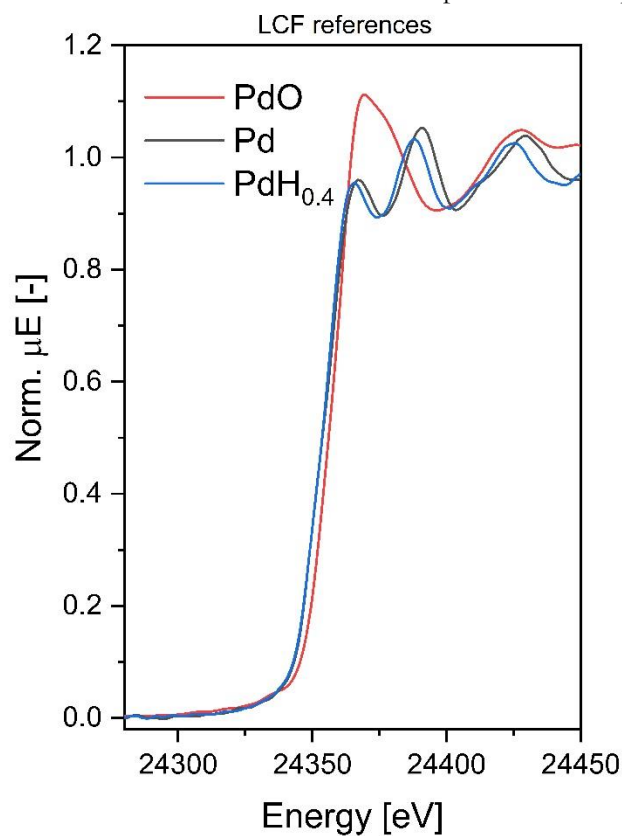


**Figure B4:** Reference spectra of obtained during gas phase experiment and used for XANES-LCF analysis.

**Table B1:** Fitting of the FT-EXFAS

Time [min]	CN <sup>a</sup>	R <sup>b</sup> (Å)	DW (Å <sup>2</sup> ) <sup>c</sup>	ΔE (eV) <sup>d</sup>	R factor <sup>e</sup>
5	0.8 +/- 0.6	2.76 +/- 0.010	0.001 +/- 0.004	9.2 +/- 0.8	0.055
10	3.5 +/- 1.9	2.78 +/- 0.04	0.007 +/- 0.004	5.7 +/- 2.5	0.032
15	5.8 +/- 2.4	2.77 +/- 0.02	0.010 +/- 0.004	4.1 +/- 2.5	0.035
20	6.6 +/- 2.2	2.76 +/- 0.02	0.009 +/- 0.003	3.2 +/- 2.0	0.028
25	7.1 +/- 2.0	2.76 +/- 0.02	0.008 +/- 0.003	3.1 +/- 1.8	0.029
30	8.8 +/- 1.2	2.77 +/- 0.01	0.010 +/- 0.001	2.9 +/- 0.9	0.019
35	9.0 +/- 1.1	2.76 +/- 0.01	0.010 +/- 0.001	2.8 +/- 0.8	0.013
40	9.1 +/- 1.4	2.76 +/- 0.01	0.011 +/- 0.011	2.0 +/- 1.3	0.024
45	9.1 +/- 1.3	2.77 +/- 0.01	0.008 +/- 0.001	2.9 +/- 1.0	0.023
50	9.6 +/- 0.9	2.77 +/- 0.01	0.009 +/- 0.001	2.6 +/- 0.6	0.008
55	9.5 +/- 1.0	2.78 +/- 0.01	0.009 +/- 0.000	2.7 +/- 0.7	0.010
60	9.7 +/- 1.0	2.78 +/- 0.01	0.008 +/- 0.001	3.3 +/- 0.7	0.010

<sup>a</sup> Coordination number. <sup>b</sup> Interatomic distance. <sup>c</sup> Debye-Waller factor. <sup>d</sup> Shift in the edge energy.

<sup>e</sup> Defined as

$$= \sum_i [\text{Re}(\chi_e(R_i) - \chi_c(R_i))^2 + \text{Im}(\chi_e(R_i) - \chi_c(R_i))^2] / \sum_i [\text{Re}(\chi_e(R_i))^2 + \text{Im}(\chi_e(R_i))^2]$$

## Appendix C (Chapter 4)

### TEM

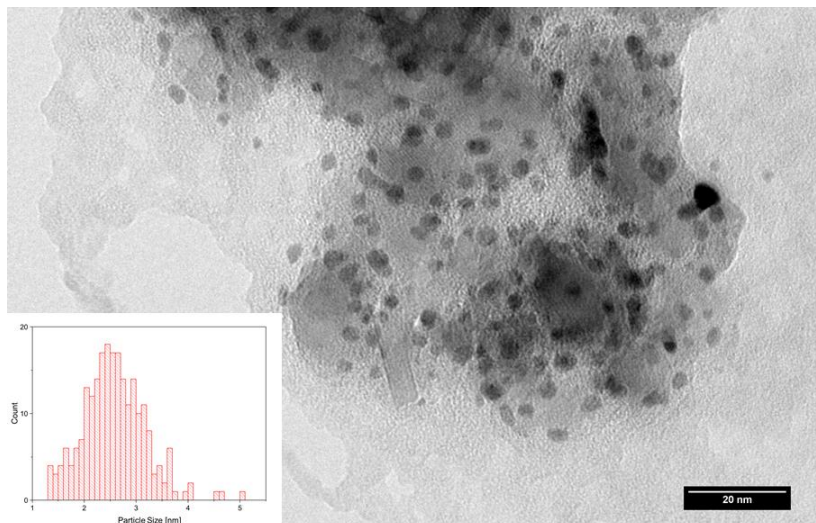


**Figure C1.** Transmission electron micrograph of the 5 wt.% Pd/Al<sub>2</sub>O<sub>3</sub> used in this study. Insert: Particle size distribution obtained from counting 230 particles.

### XRD

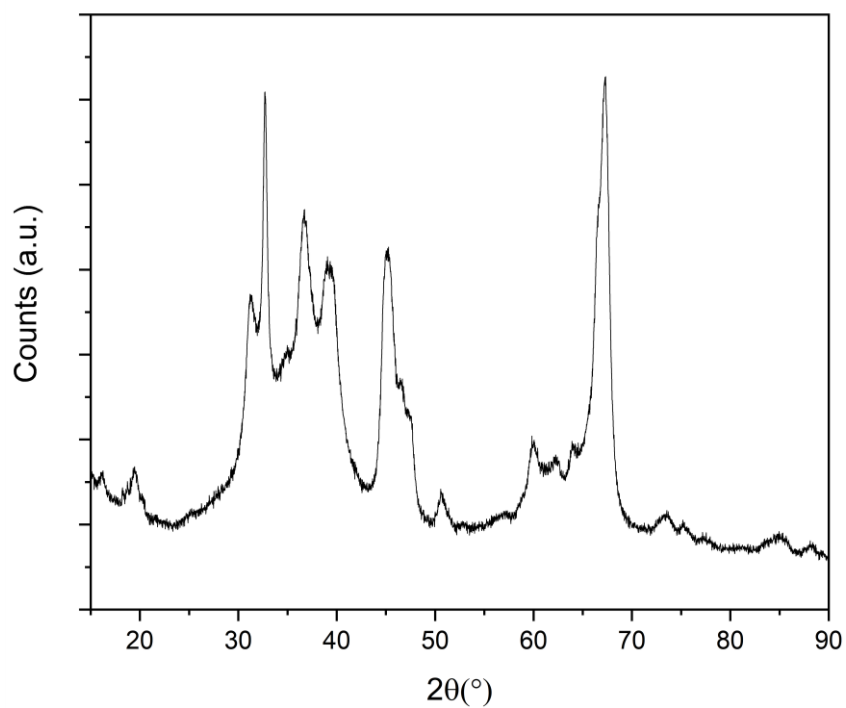


**Figure C2.** X-ray diffraction pattern of the 5 wt.% Pd/Al<sub>2</sub>O<sub>3</sub> catalyst used in this study.

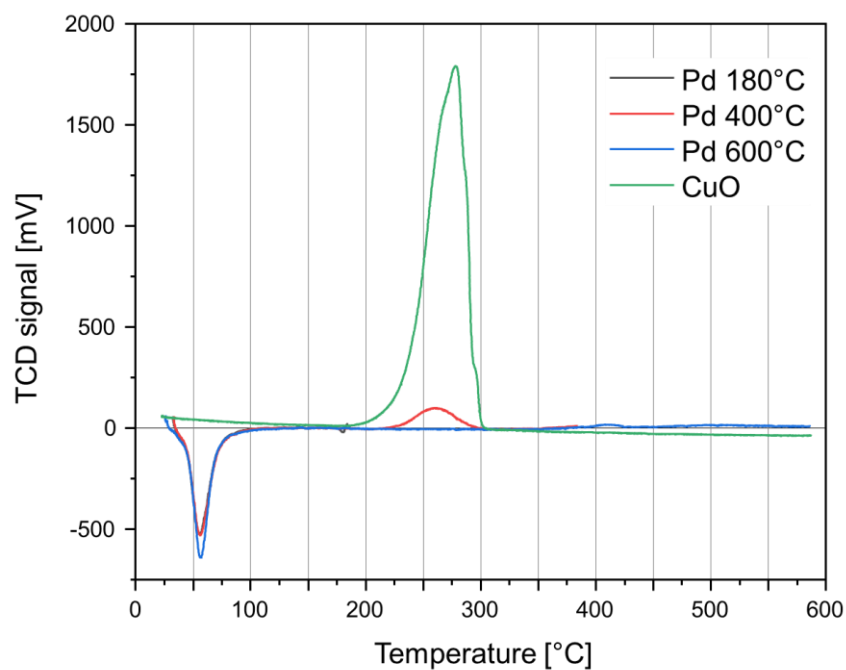


**Figure C3.** Comparison of the TPR experiments of Figure 2 with that of the CuO reference.

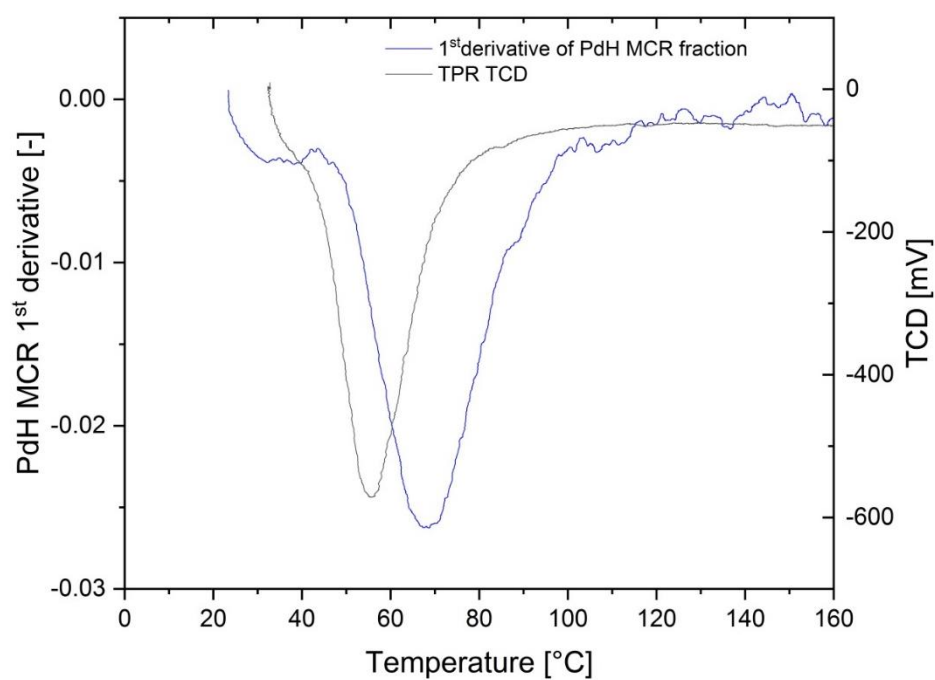


**Figure C4.** First derivative of the profiles shown in Figure 3 of the main text.

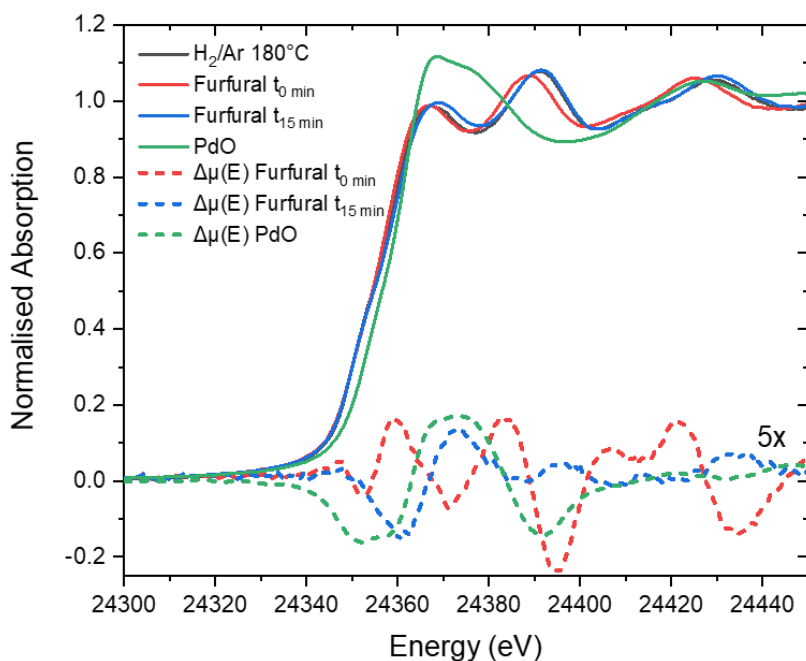


**Figure C5.** Selected Pd K-edge XANES spectra (solid line) from gas and liquid phase experiments. Difference spectra (dashed line), obtained by subtraction of the  $\text{H}_2/\text{Ar}$  180°C spectrum (Pd), from the other spectra. This exhibits the experimental XANES features associated to PdO, PdH and PdC.

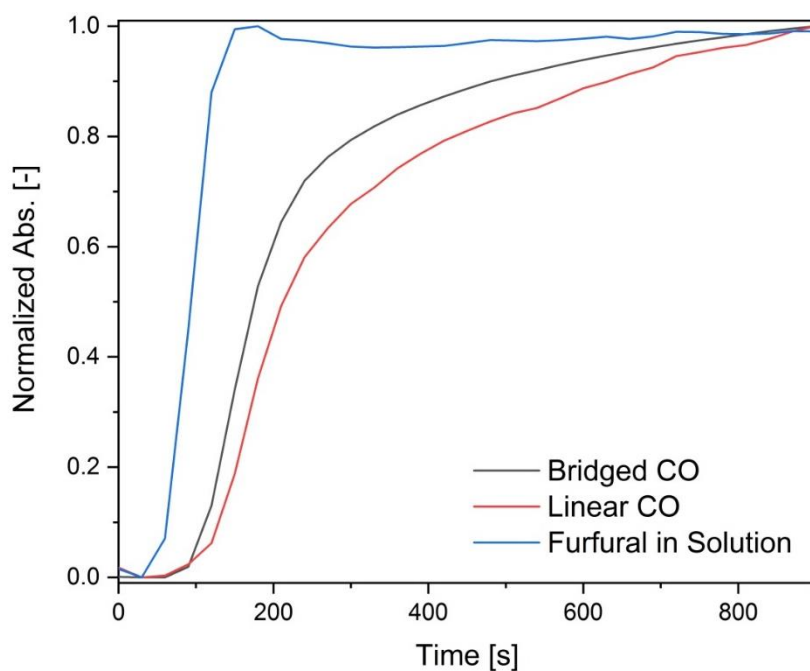


**Figure C6.** Evolution of signals after introduction of furfural  $\nu(\text{C}=\text{O})$  (blue),  $\text{CO}_\text{L}$  (red) and  $\text{CO}_\text{B}$  (grey) during the in situ ATR-IR experiment.

## Appendix D (Chapter 5)

### Transmission electron microscopy (TEM)

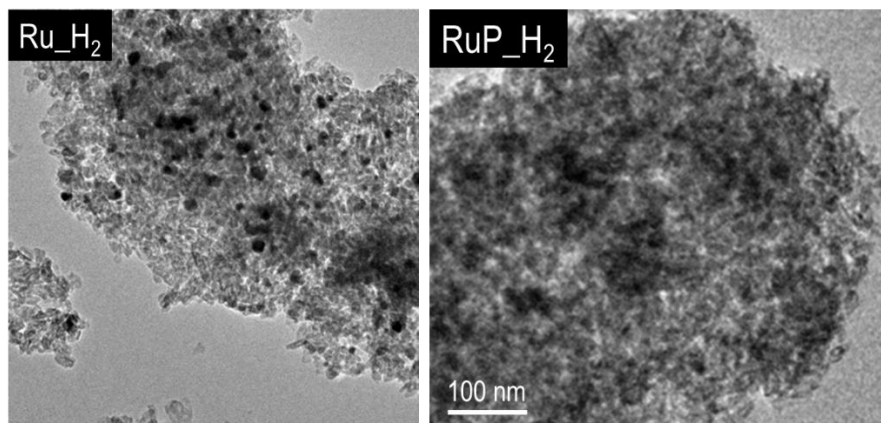


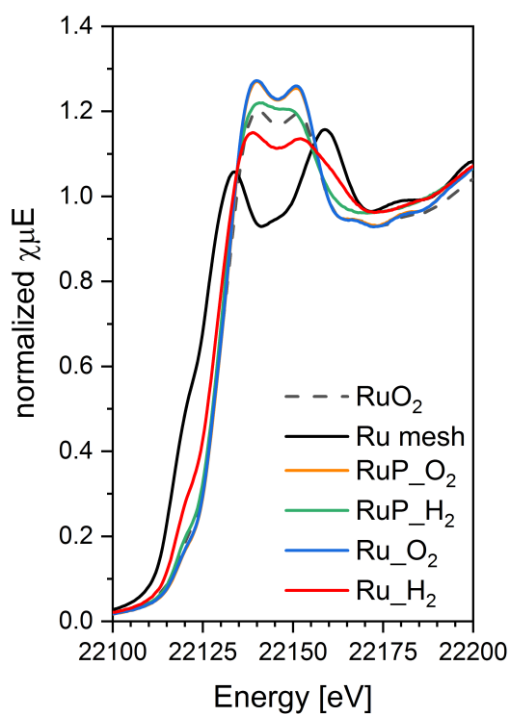
**Figure D1.** TEM micrographs of Ru\_H<sub>2</sub> and RuP\_H<sub>2</sub>. The same scale bar applies for both images.

Particles of ca. 10 nm diameter are observed in the case of Ru\_H<sub>2</sub>, while hardly any particle is discernible in the case of RuP\_H<sub>2</sub> in agreement with XRD (**Figure 5.1**) and EXAFS data (**Figure 5.2**).

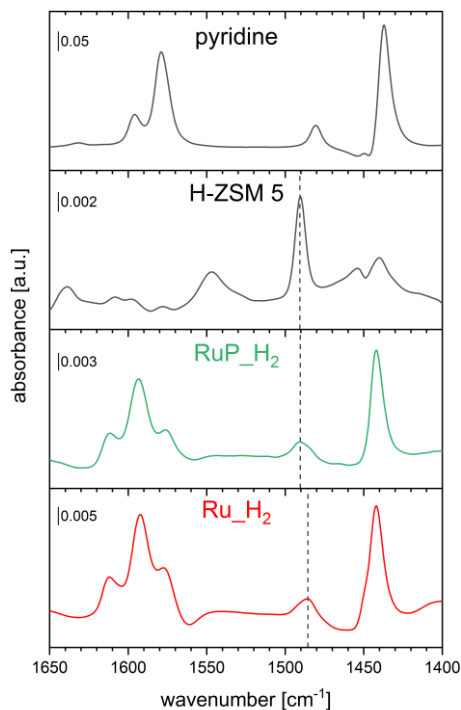
### X-ray diffraction (XRD)

**Table D1.** Crystallite size of Ru\_H<sub>2</sub> was obtained using the Scherrer equation. Peak maxima and full width half maximum (FWHM) were obtained by peak fitting using Gaussian function. The four peaks were obtained by subtraction of the diffractogram of Al<sub>2</sub>O<sub>3</sub> from that of Ru\_H<sub>2</sub> followed by baseline correction.

2 $\theta$ (°)	FWHM (-)	crystallite size (nm)	Average size (nm)	Error on average (nm)
38.55	0.7952	10.6	11.1	$\pm 0.6$
42.30	0.6567	12.9		
44.19	0.8160	10.5		
58.45	0.8695	10.5		

**X-ray absorption near edge structure spectroscopy (XANES)**

**Figure D2.** Ru K-edge XANES spectra of the various Ru catalysts and of the  $\text{RuO}_2$  and Ru mesh reference

**Pyridine adsorption using infrared spectroscopy**

**Figure D3.** ATR-IR spectra of pyridine adsorbed on the indicated samples and of a solution of pyridine in cyclohexane (10 mM).



The ATR-IR spectrum of pyridine adsorbed on H-ZSM 5 displays two clear bands at 1546 and 1490  $\text{cm}^{-1}$  that are associated with the pyridinium ion. While molecularly adsorbed pyridine on Lewis acid sites can contribute to the latter signal, its intensity and peak shape reveal that it is predominantly due to Brønsted acid sites. The spectrum obtained on RuP\_ $\text{H}_2$  exhibits the same signal (1490  $\text{cm}^{-1}$ ) but much weaker, while the signal observed for Ru\_ $\text{H}_2$  is clearly shifted to 1485  $\text{cm}^{-1}$  assigned to Lewis acid sites.

**$^{27}\text{Al}$  Magic angle spinning nuclear magnetic resonance ( $^{27}\text{Al}$  MAS-NMR)**

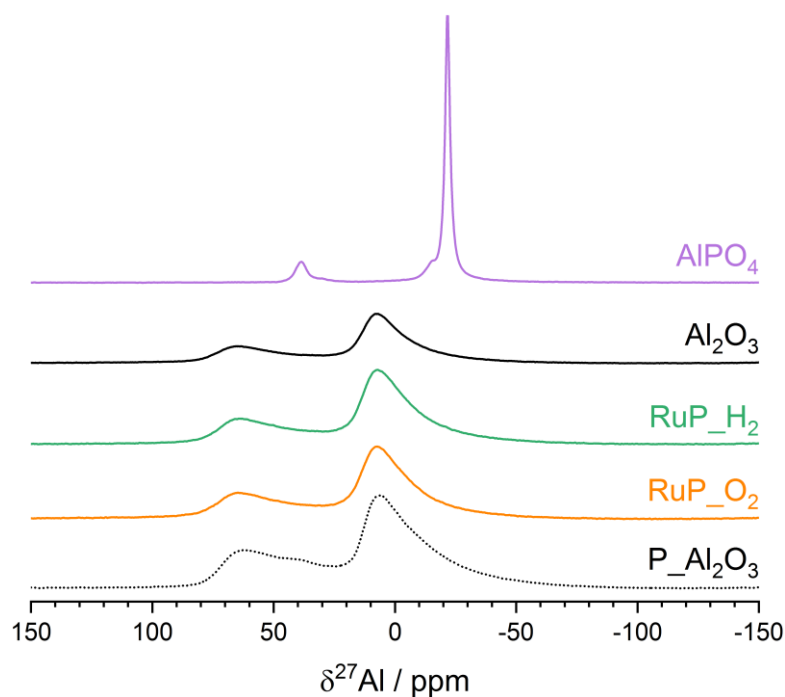


**Figure D4.**  $^{27}\text{Al}$  MAS-NMR spectra of RuP\_ $\text{H}_2$ , RuP\_ $\text{O}_2$  and of reference materials.

### Catalytic transfer hydrogenation of furfural without catalyst pre-reduction: selectivity towards furfuryl alcohol

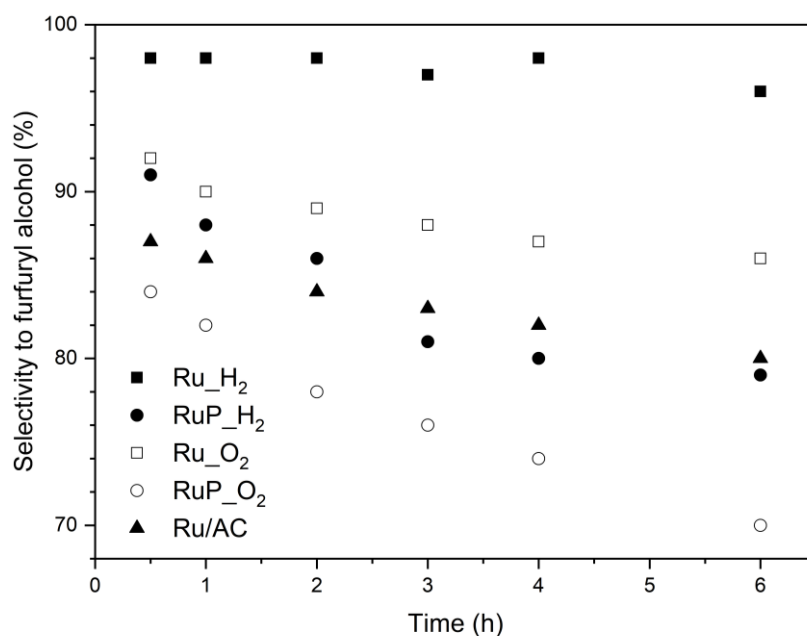


**Figure D5.** Selectivity to furfuryl alcohol under catalytic transfer hydrogenation conditions.

### Catalytic transfer hydrogenation of furfural after *in situ* reduction

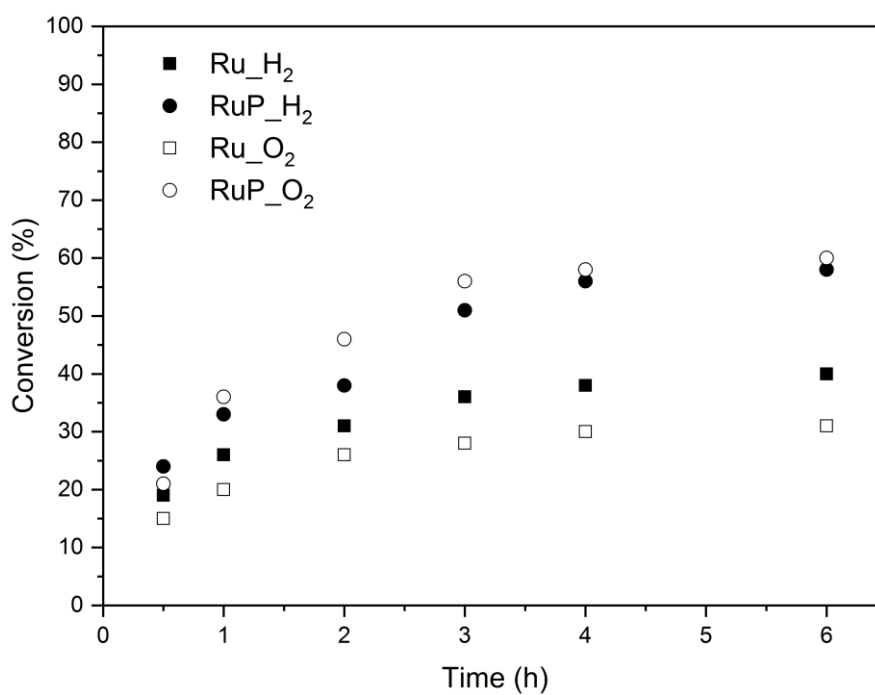


**Figure D6.** Conversion of furfural under catalytic transfer hydrogenation conditions. Materials were pre-reduced *in situ* before introduction of furfural in the reactor.

## Operando XANES

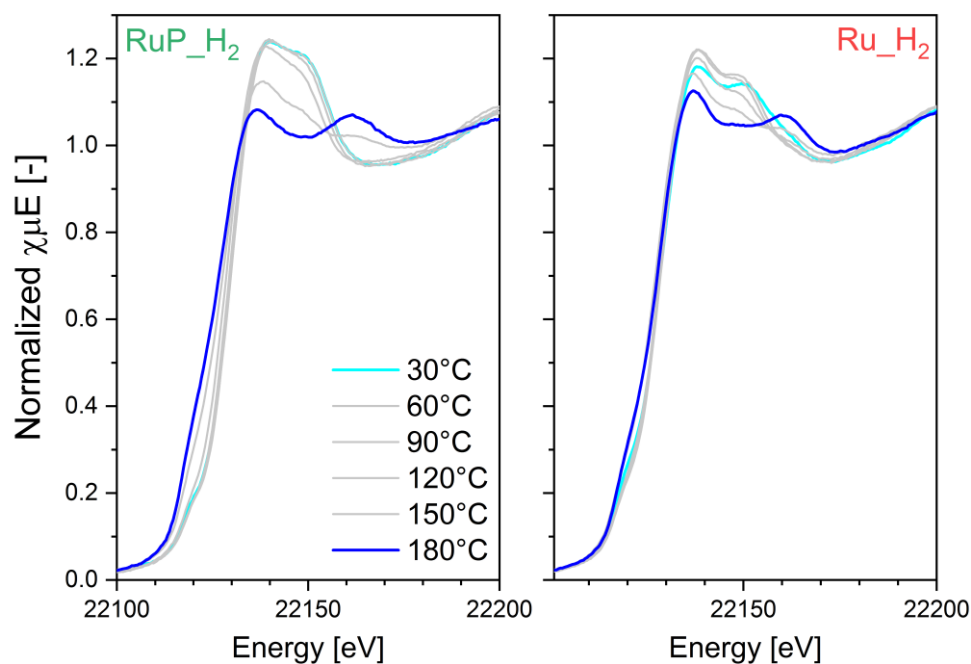


**Figure D7.** Operando Ru K-edge XANES spectra of RuP\_H<sub>2</sub> and Ru\_H<sub>2</sub> recorded during furfural hydrogenation at various temperatures.

## Fit of FT-EXAFS spectra

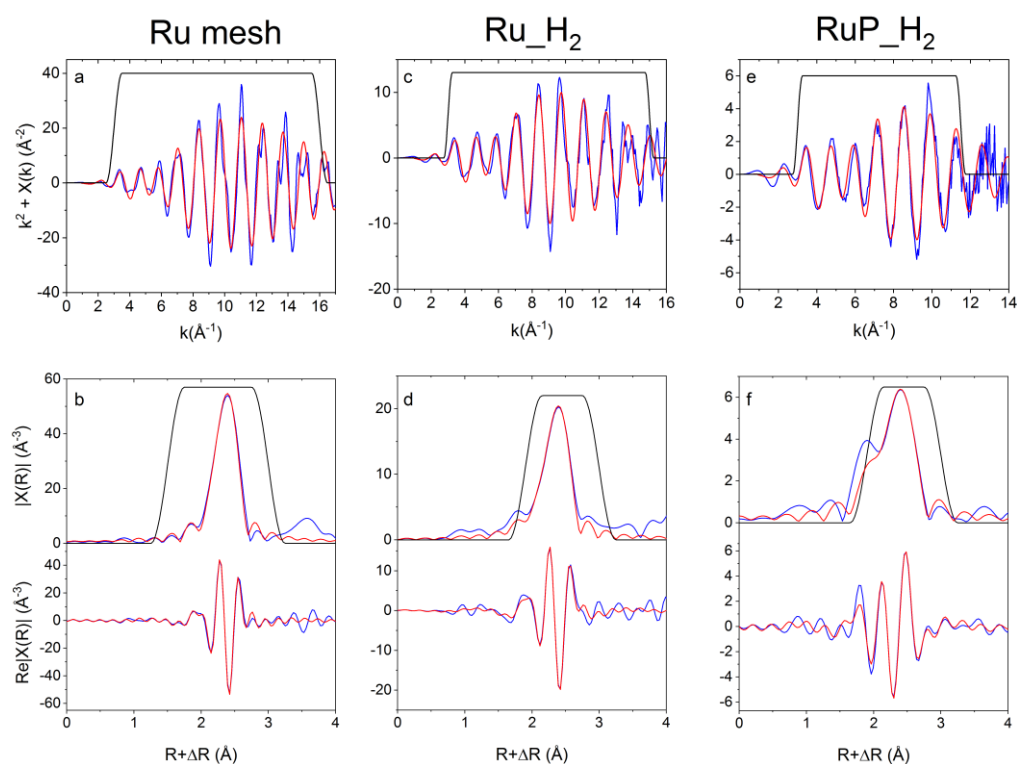


**Figure D8.** Operando Ru K-edge QEXAFS spectra obtained during furfural hydrogenation in Ar-saturated 2-propanol solution at 180°C and 16 bar. Spectra are the result of averaging of 60 spectra. (a, b) Ru mesh, (c, d) Ru\_H<sub>2</sub> sample, (e, f) RuP\_H<sub>2</sub> sample. (a,c,e)  $k^2$ -weighted  $\chi(k)$ , (b,d,f) magnitude  $|\chi(R)|$  and real part  $\text{Re}|\chi(R)|$  of the non-phase corrected Fourier transform spectra. Experimental data is shown in blue, fit results in red and fit window in black.

## Appendix E (Chapter 6)

### DFT simulations

#### 1.1. Models

DFT calculation aimed at supporting experimental evidences from both the kinetic and the ATR-IR study. The relative stability of the two most stable isomers of both OME<sub>1</sub> and TRI was evaluated.

The structure of the adopted molecular models is reported in **Figure E1**.

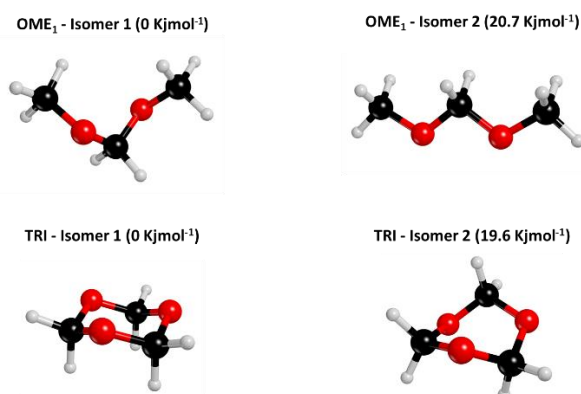


**Figure E1:** Molecular models of the most stable isomers of OME<sub>1</sub> and TRI adopted in the B3LYP-D3/CBS simulations. The relative stability ( $\Delta G$ ) of the isomers for of each molecule is reported in brackets.

We further simulated the interaction of OME<sub>1</sub>, TRI and water with a minimal BAS model and the optimized adduct structures are shown inFigure E2. We report here only the results concerning the adsorbates of the most stable isomers of both OME<sub>1</sub> and TRI over BAS, since adsorption does not alter significantly the relative stability of the isomers.

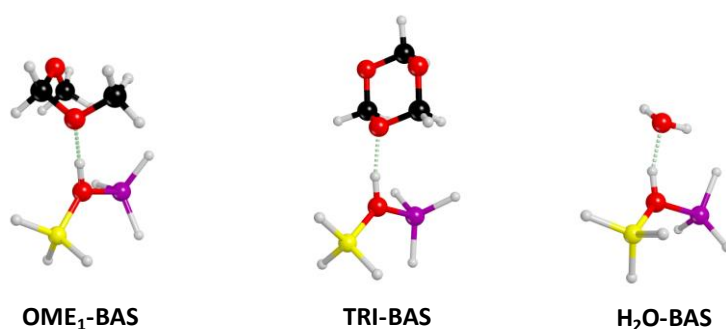


**Figure E2:** Molecular models of the OME<sub>1</sub>, TRI and H<sub>2</sub>O adsorbates with BAS, as adopted in the B3LYP-D3/CBS simulations. Colors: H (white), C (black), O (red), Al (pink) and Si (yellow).

## Catalyst characterization

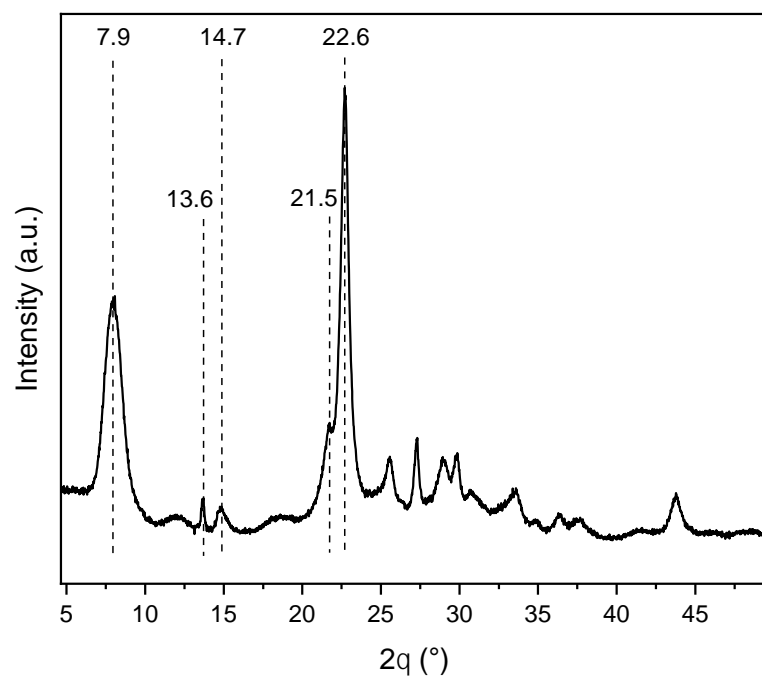


**Figure E3:** XRD pattern of zeolite H-Beta.

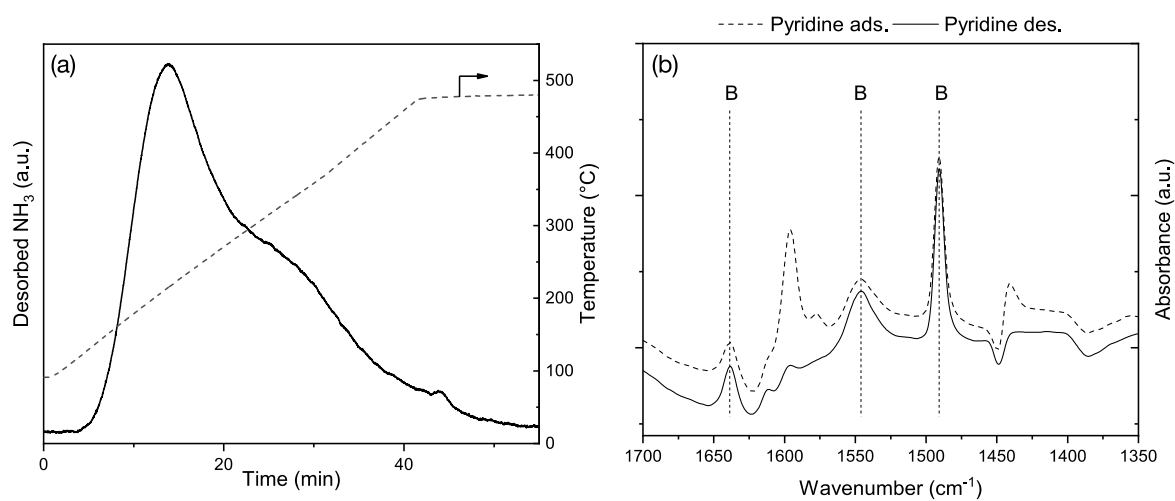


**Figure E4:** Characterization of the acidity of zeolite H-Beta by (a)  $\text{NH}_3$ -TPD and (b) pyridine adsorption (dash line) and desorption (solid line) in cyclohexane by ATR-IR spectroscopy (B indicates vibrational bands associated with pyridine bonded to Brønsted acid site).

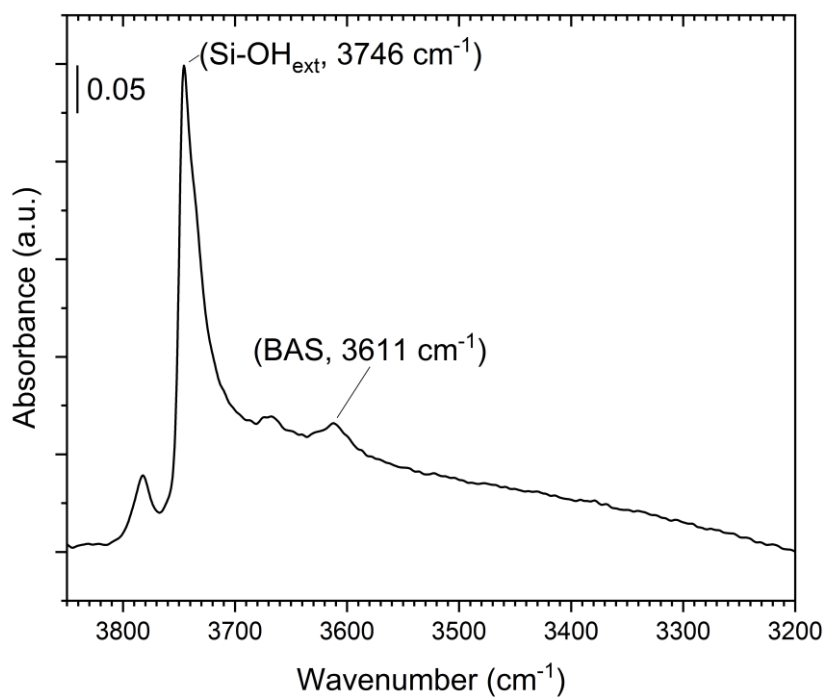


**Figure E5:** Transmission IR spectrum of H-Beta after drying for 1 h at 500 °C with residual pressure below 10<sup>-3</sup> mbar. BAS = 3611 cm<sup>-1</sup>, Si-OH<sub>ext</sub> = 3746 cm<sup>-1</sup>.

#### Modulation-excitation attenuated total reflectance infrared spectroscopy

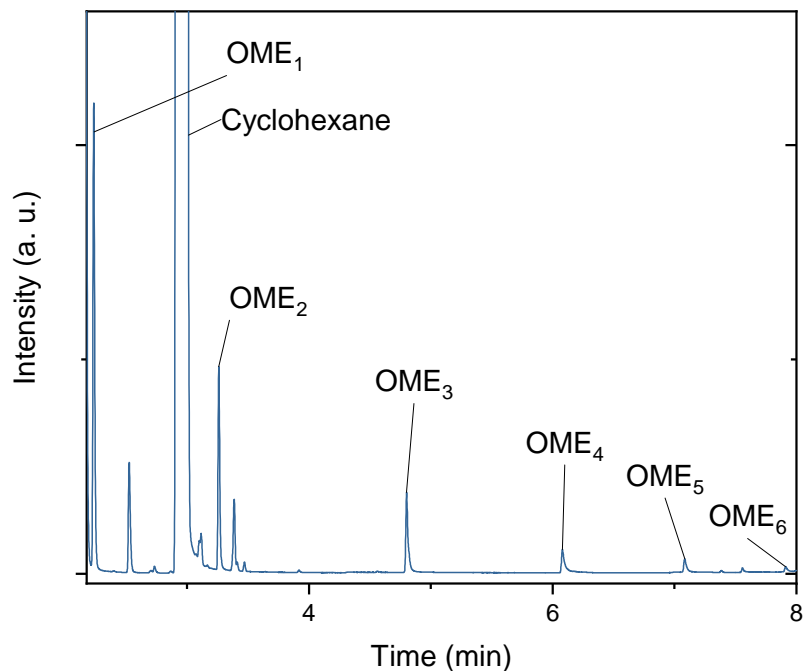


**Figure E6:** Chromatogram after 5 min of reaction of 10 mM DMM and TRI in cyclohexane (10 wt.% H-Beta and T = 25 °C).

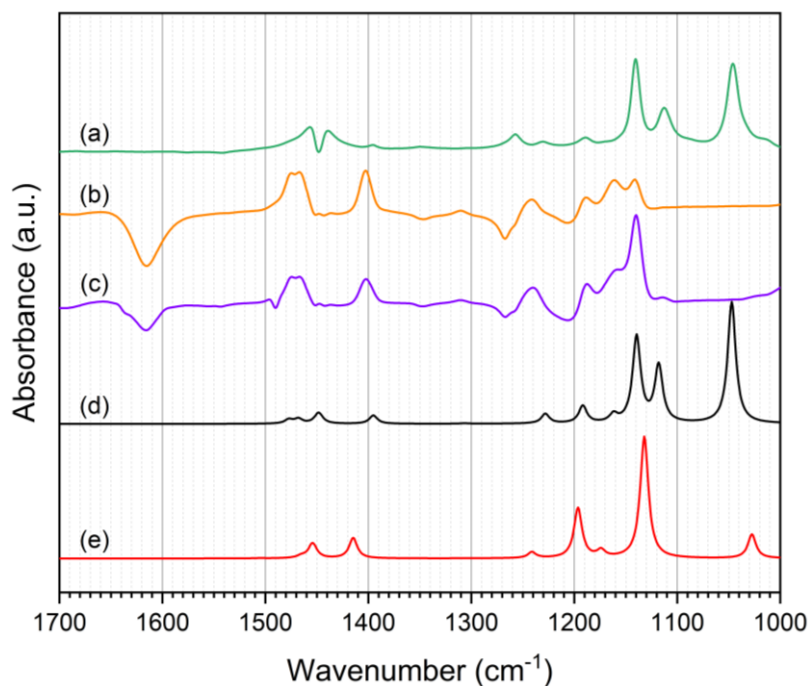


**Figure E7:** (a) IR spectrum of OME<sub>1</sub> in cyclohexane (10 mM). Phase-resolved spectra ( $\varphi^{\text{PSD}} = 290^\circ$ ) obtained during adsorption-desorption of OME<sub>1</sub> (b) with and (c) without pyridine. Simulated vibrational spectra of (d) bent and (e) linear isomers of OME<sub>1</sub> in cyclohexane.

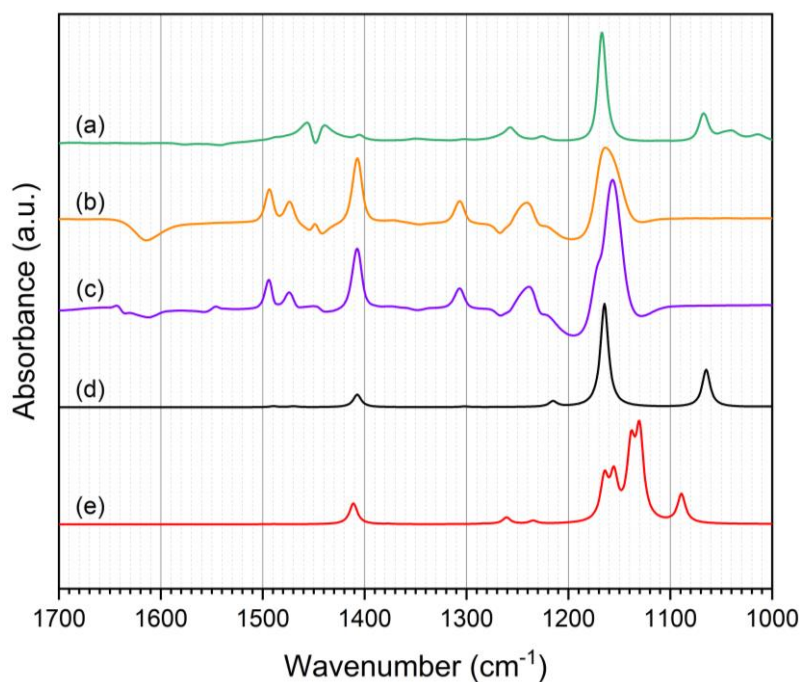


**Figure E8:** (a) IR spectrum of TRI in cyclohexane (10 mM). Phase-resolved ATR-IR spectra ( $\varphi^{\text{PSD}} = 290^\circ$ ) obtained during adsorption-desorption of OME<sub>1</sub> (b) with and (c) without pyridine. Simulated vibrational spectra of (d) chair and (e) boat isomers of TRI in cyclohexane.

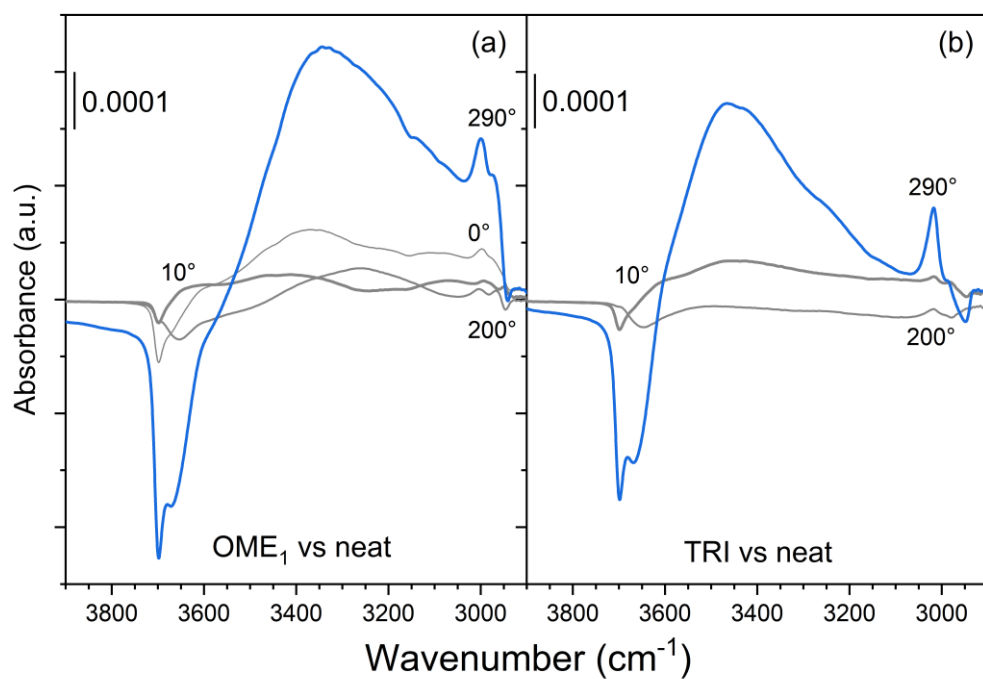


**Figure E9:** ATR-IR phase-resolved spectra during adsorption-desorption of (a) OME<sub>1</sub> and (b) TRI.

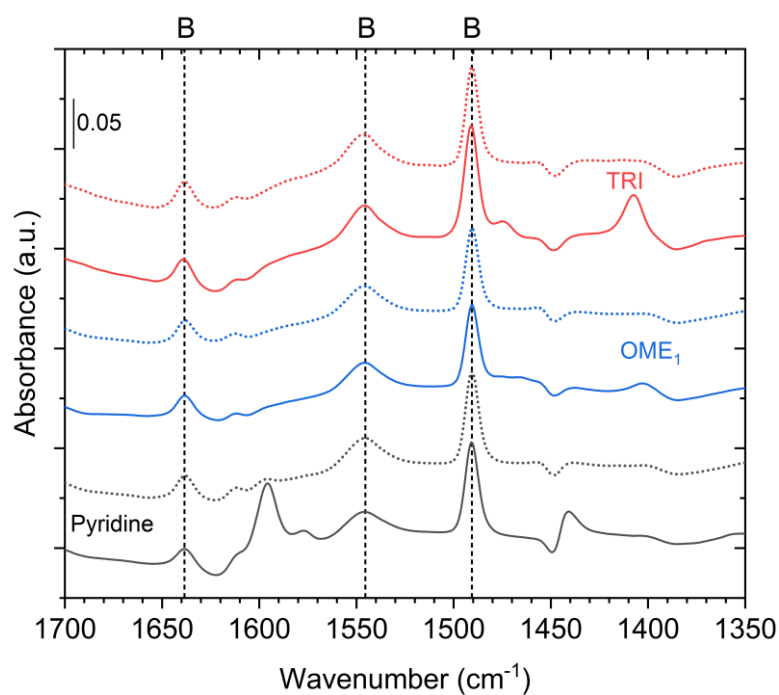


**Figure E10:** ATR-IR spectra obtained during adsorption (plain line) and desorption (dashed line) of pyridine (black), followed by adsorption-desorption of OME<sub>1</sub> (blue) and TRI (red) on H-Beta in cyclohexane.



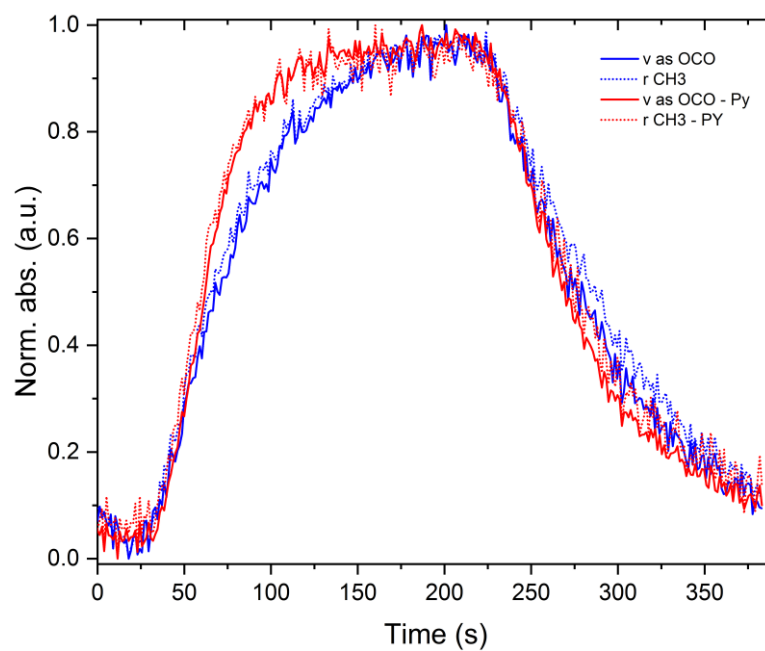


**Figure E11:** Time traces of vibrational bands at  $1160\text{ cm}^{-1}$  ( $CH_3$  rock – dotted line) and  $1142\text{ cm}^{-1}$  ( $\nu_{as}(OCO)$ -straight line) during OME1 adsorption-desorption experiments with (red) and without (blue) anchored pyridine.

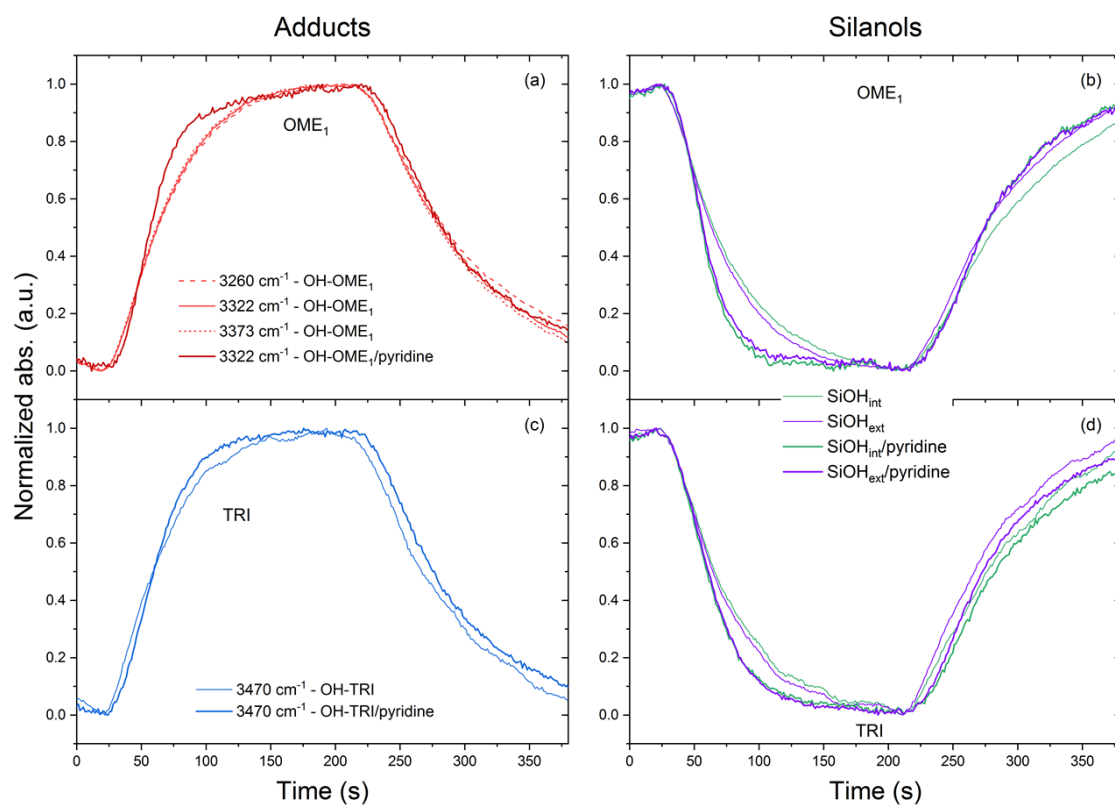


**Figure E12:** Comparison of time traces of the adduct region (a,c) and silanols (b,d) region during OME<sub>1</sub> (red) and TRI (blue) adsorption-desorption experiments with (thick lines) and without (thin lines) anchored pyridine.

# References

- (1) Zaera, F. Probing Liquid/Solid Interfaces at the Molecular Level. *Chem. Rev.* **2012**, *112* (5), 2920–2986. <https://doi.org/10.1021/cr2002068>.
- (2) Vassilev, S. V.; Baxter, D.; Andersen, L. K.; Vassileva, C. G. An Overview of the Chemical Composition of Biomass. *Fuel* **2010**, *89* (5), 913–933. <https://doi.org/10.1016/j.fuel.2009.10.022>.
- (3) Gallezot, P. Conversion of Biomass to Selected Chemical Products. *Chem Soc Rev* **2012**, *41* (4), 1538–1558. <https://doi.org/10.1039/C1CS15147A>.
- (4) Corma Canos, A.; Iborra, S.; Velty, A. Chemical Routes for the Transformation of Biomass into Chemicals. *Chem Rev* **2007**, *107* (6), 2411–2502. <https://doi.org/10.1021/cr050989d>.
- (5) Hoydonckx, H. E.; Van Rhijn, W. M.; Van Rhijn, W.; De Vos, D. E.; Jacobs, P. A. Furfural and Derivatives. In *Ullmann's Encyclopedia of Industrial Chemistry*; American Cancer Society, 2007. [https://doi.org/10.1002/14356007.a12\\_119.pub2](https://doi.org/10.1002/14356007.a12_119.pub2).
- (6) Lopez, G. M.; Martin, A. D. *Furfural: An Entry Point of Lignocellulose in Biorefineries to Produce Renewable Chemicals, Polymers, and Biofuels*; Sustainable Chemistry Series; World Scientific Publishing Company, 2018.
- (7) Chen, S.; Wojcieszak, R.; Dumeignil, F.; Marceau, E.; Royer, S. How Catalysts and Experimental Conditions Determine the Selective Hydroconversion of Furfural and 5-Hydroxymethylfurfural. *Chem. Rev.* **2018**, *118* (22), 11023–11117. <https://doi.org/10.1021/acs.chemrev.8b00134>.
- (8) J, F. L. E. O.; H, F. H. Copper Chromite Catalyst For Preparation Of Furfuryl Alcohol From Furfural, 1981.
- (9) Baranowski, C. J.; Bahmanpour, A. M.; Kröcher, O. Catalytic Synthesis of Polyoxymethylene Dimethyl Ethers (OME): A Review. *Appl. Catal. B Environ.* **2017**, No. 217, 407–420. <https://doi.org/10.1016/j.apcatb.2017.06.007>.
- (10) Shuai, L.; Luterbacher, J. Organic Solvent Effects in Biomass Conversion Reactions. *ChemSusChem* **2016**, *9* (2), 133–155. <https://doi.org/10.1002/cssc.201501148>.
- (11) Zaera, F. Probing Liquid/Solid Interfaces at the Molecular Level. *Chem. Rev.* **2012**, *112* (5), 2920–2986. <https://doi.org/10.1021/cr2002068>.
- (12) Bentrup, U. Combining in Situ Characterization Methods in One Set-up: Looking with More Eyes into the Intricate Chemistry of the Synthesis and Working of Heterogeneous Catalysts. *Chem. Soc. Rev.* **2010**, *39* (12), 4718–4730. <https://doi.org/10.1039/B919711G>.
- (13) Brückner, A. Looking on Heterogeneous Catalytic Systems from Different Perspectives: Multitechnique Approaches as a New Challenge for In Situ Studies. *Catal. Rev.* **2003**, *45* (1), 97–150. <https://doi.org/10.1081/CR-120015739>.
- (14) Newton, M. A.; Beek, W. van. Combining Synchrotron-Based X-Ray Techniques with Vibrational Spectroscopies for the in Situ Study of Heterogeneous Catalysts: A View from a Bridge. *Chem. Soc. Rev.* **2010**, *39* (12), 4845–4863. <https://doi.org/10.1039/B919689G>.
- (15) Bordiga, S.; Bonino, F.; Petter Lillerud, K.; Lamberti, C. X-Ray Absorption Spectroscopies : Useful Tools to Understand Metallorganic Frameworks Structure and Reactivity. *Chem. Soc. Rev.* **2010**, *39* (12), 4885–4927. <https://doi.org/10.1039/C0CS00082E>.

- (16) Singh, J.; Lamberti, C.; Bokhoven, J. A. van. Advanced X-Ray Absorption and Emission Spectroscopy: In Situ Catalytic Studies. *Chem. Soc. Rev.* **2010**, 39 (12), 4754–4766. <https://doi.org/10.1039/C0CS00054J>.
- (17) Mojet, B. L.; Ebbesen, S. D.; Lefferts, L. Light at the Interface: The Potential of Attenuated Total Reflection Infrared Spectroscopy for Understanding Heterogeneous Catalysis in Water. *Chem. Soc. Rev.* **2010**, 39 (12), 4643–4655. <https://doi.org/10.1039/C0CS00014K>.
- (18) Andanson, J.-M.; Baiker, A. Exploring Catalytic Solid/Liquid Interfaces by in Situ Attenuated Total Reflection Infrared Spectroscopy. *Chem. Soc. Rev.* **2010**, 39 (12), 4571–4584. <https://doi.org/10.1039/B919544K>.
- (19) Bürgi, T.; Baiker, A. Attenuated Total Reflection Infrared Spectroscopy of Solid Catalysts Functioning in the Presence of Liquid-Phase Reactants. In *Advances in Catalysis*; Gates, B. C., Knzinger, H., Eds.; Academic Press, 2006; Vol. 50, pp 227–283. [https://doi.org/10.1016/S0360-0564\(06\)50005-7](https://doi.org/10.1016/S0360-0564(06)50005-7).
- (20) Shi, H.; Lercher, J. A.; Yu, X.-Y. Sailing into Uncharted Waters: Recent Advances in the in Situ Monitoring of Catalytic Processes in Aqueous Environments. *Catal. Sci. Technol.* **2015**, 5 (6), 3035–3060. <https://doi.org/10.1039/C4CY01720J>.
- (21) Goormaghtigh, E.; Raussens, V.; Ruyschaert, J.-M. Attenuated Total Reflection Infrared Spectroscopy of Proteins and Lipids in Biological Membranes. *Biochim. Biophys. Acta BBA - Rev. Biomembr.* **1999**, 1422 (2), 105–185. [https://doi.org/10.1016/S0304-4157\(99\)00004-0](https://doi.org/10.1016/S0304-4157(99)00004-0).
- (22) Bürgi, T.; Baiker, A. Attenuated Total Reflection Infrared Spectroscopy of Solid Catalysts Functioning in the Presence of Liquid-Phase Reactants. In *Advances in Catalysis*; Gates, B. C., Knzinger, H., Eds.; Academic Press, 2006; Vol. 50, pp 227–283. [https://doi.org/10.1016/S0360-0564\(06\)50005-7](https://doi.org/10.1016/S0360-0564(06)50005-7).
- (23) Mojet, B. L.; Ebbesen, S. D.; Lefferts, L. Light at the Interface: The Potential of Attenuated Total Reflection Infrared Spectroscopy for Understanding Heterogeneous Catalysis in Water. *Chem. Soc. Rev.* **2010**, 39 (12), 4643–4655. <https://doi.org/10.1039/C0CS00014K>.
- (24) Andanson, J.-M.; Baiker, A. Exploring Catalytic Solid/Liquid Interfaces by in Situ Attenuated Total Reflection Infrared Spectroscopy. *Chem. Soc. Rev.* **2010**, 39 (12), 4571–4584. <https://doi.org/10.1039/B919544K>.
- (25) A. Mudunkotuwa, I.; Al Minshid, A.; H. Grassian, V. ATR-FTIR Spectroscopy as a Tool to Probe Surface Adsorption on Nanoparticles at the Liquid–Solid Interface in Environmentally and Biologically Relevant Media. *Analyst* **2014**, 139 (5), 870–881. <https://doi.org/10.1039/C3AN01684F>.
- (26) Shi, H.; A. Lercher, J.; Yu, X.-Y. Sailing into Uncharted Waters: Recent Advances in the in Situ Monitoring of Catalytic Processes in Aqueous Environments. *Catal. Sci. Technol.* **2015**, 5 (6), 3035–3060. <https://doi.org/10.1039/C4CY01720J>.
- (27) Mondelli, C.; Ferri, D.; Grunwaldt, J.-D.; Krumeich, F.; Mangold, S.; Psaro, R.; Baiker, A. Combined Liquid-Phase ATR-IR and XAS Study of the Bi-Promotion in the Aerobic Oxidation of Benzyl Alcohol over Pd/Al<sub>2</sub>O<sub>3</sub>. *J. Catal.* **2007**, 252 (1), 77–87. <https://doi.org/10.1016/j.jcat.2007.09.013>.
- (28) Wirz, R.; Ferri, D.; Baiker, A. ATR-IR Spectroscopy of Pendant NH<sub>2</sub> Groups on Silica Involved in the Knoevenagel Condensation. *Langmuir* **2006**, 22 (8), 3698–3706. <https://doi.org/10.1021/la053145y>.
- (29) Ferri, D.; Newton, M. A.; Di Michiel, M.; Chiarello, G. L.; Yoon, S.; Lu, Y.; Andrieux, J. Revealing the Dynamic Structure of Complex Solid Catalysts Using Modulated Excitation X-Ray Diffraction. *Angew. Chem. Int. Ed.* **2014**, 53 (34), 8890–8894. <https://doi.org/10.1002/anie.201403094>.

- (30) Holzwarth, U.; Gibson, N. The Scherrer Equation versus the “Debye-Scherrer Equation.” *Nat. Nanotechnol.* **2011**, 6 (9), 534–534. <https://doi.org/10.1038/nnano.2011.145>.
- (31) Shannon, I. J.; Maschmeyer, T.; Sankar, G.; Thomas, J. M.; Oldroyd, R. D.; Sheehy, M.; Madill, D.; Waller, A. M.; Townsend, R. P. A New Cell for the Collection of Combined EXAFS/XRD Data in Situ during Solid/Liquid Catalytic Reactions. *Catal. Lett.* **1997**, 44 (1), 23–27. <https://doi.org/10.1023/A:1018956520929>.
- (32) Liu, Y.-S.; Jeong, S.; White, J. L.; Feng, X.; Seon Cho, E.; Stavila, V.; Allendorf, M. D.; Urban, J. J.; Guo, J. In-Situ/Operando X-Ray Characterization of Metal Hydrides. *ChemPhysChem* **2019**, 20 (10), 1261–1271. <https://doi.org/10.1002/cphc.201801185>.
- (33) Bugaev, A. L.; Guda, A. A.; Lomachenko, K. A.; Srabionyan, V. V.; Bugaev, L. A.; Soldatov, A. V.; Lamberti, C.; Dmitriev, V. P.; van Bokhoven, J. A. Temperature- and Pressure-Dependent Hydrogen Concentration in Supported PdHx Nanoparticles by Pd K-Edge X-Ray Absorption Spectroscopy. *J. Phys. Chem. C* **2014**, 118 (19), 10416–10423. <https://doi.org/10.1021/jp500734p>.
- (34) Wirz, R.; Bürgi, T.; Baiker, A. Probing Enantiospecific Interactions at Chiral Solid–Liquid Interfaces by Absolute Configuration Modulation Infrared Spectroscopy. *Langmuir* **2003**, 19 (3), 785–792. <https://doi.org/10.1021/la026568y>.
- (35) Urakawa, A.; Wirz, R.; Bürgi, T.; Baiker, A. ATR-IR Flow-Through Cell for Concentration Modulation Excitation Spectroscopy: Diffusion Experiments and Simulations. *J. Phys. Chem. B* **2003**, 107 (47), 13061–13068. <https://doi.org/10.1021/jp0359889>.
- (36) Wirz, R.; Bürgi, T.; Lindner, W.; Baiker, A. Absolute Configuration Modulation Attenuated Total Reflection IR Spectroscopy: An in Situ Method for Probing Chiral Recognition in Liquid Chromatography. *Anal. Chem.* **2004**, 76 (18), 5319–5330. <https://doi.org/10.1021/ac049428x>.
- (37) Chiarello, G. L.; Nachtegaal, M.; Marchionni, V.; Quaroni, L.; Ferri, D. Adding Diffuse Reflectance Infrared Fourier Transform Spectroscopy Capability to Extended X-Ray-Absorption Fine Structure in a New Cell to Study Solid Catalysts in Combination with a Modulation Approach. *Rev. Sci. Instrum.* **2014**, 85 (7), 074102. <https://doi.org/10.1063/1.4890668>.
- (38) Müller, P.; Hermans, I. Applications of Modulation Excitation Spectroscopy in Heterogeneous Catalysis. *Ind. Eng. Chem. Res.* **2017**, 56 (5), 1123–1136. <https://doi.org/10.1021/acs.iecr.6b04855>.
- (39) Bürgi, T.; Baiker, A. In Situ Infrared Spectroscopy of Catalytic Solid-Liquid Interfaces Using Phase-Sensitive Detection: Enantioselective Hydrogenation of a Pyrone over Pd/TiO<sub>2</sub>. *J. Phys. Chem. B* **2002**, 106 (41), 10649–10658. <https://doi.org/10.1021/jp0255987>.
- (40) Niemantsverdriet, J. W. *Spectroscopy in Catalysis: An Introduction*; John Wiley & Sons, 2007.
- (41) Khawam, A.; Flanagan, D. R. Solid-State Kinetic Models: Basics and Mathematical Fundamentals. *J. Phys. Chem. B* **2006**, 110 (35), 17315–17328. <https://doi.org/10.1021/jp062746a>.
- (42) Chiarello, G. L.; Nachtegaal, M.; Marchionni, V.; Quaroni, L.; Ferri, D. Adding Diffuse Reflectance Infrared Fourier Transform Spectroscopy Capability to Extended X-Ray-Absorption Fine Structure in a New Cell to Study Solid Catalysts in Combination with a Modulation Approach. *Rev. Sci. Instrum.* **2014**, 85 (7), 074102. <https://doi.org/10.1063/1.4890668>.
- (43) Marchionni, V.; Kambolis, A.; Nachtegaal, M.; Kröcher, O.; Ferri, D. High Energy X-Ray Diffraction and IR Spectroscopy of Pt/Al<sub>2</sub>O<sub>3</sub> during CO Oxidation in a Novel Catalytic Reactor Cell. *Catal. Struct. React.* **2017**, 3 (1–2), 71–78. <https://doi.org/10.1080/2055074X.2016.1274118>.
- (44) C. Meunier, F. The Design and Testing of Kinetically-Appropriate Operando Spectroscopic Cells for Investigating Heterogeneous Catalytic Reactions. *Chem. Soc. Rev.* **2010**, 39 (12), 4602–4614. <https://doi.org/10.1039/B919705M>.

- (45) Ferri, D.; Bürgi, T.; Baiker, A. Probing Catalytic Solid-Liquid Interfaces by Attenuated Total Reflection Infrared Spectroscopy: Adsorption of Carboxylic Acids on Alumina and Titania. *Helv. Chim. Acta* **2002**, *85* (11), 3639–3656. [https://doi.org/10.1002/1522-2675\(200211\)85:11<3639::AID-HLCA3639>3.0.CO;2-2](https://doi.org/10.1002/1522-2675(200211)85:11<3639::AID-HLCA3639>3.0.CO;2-2).
- (46) Henke, B. L.; Gullikson, E. M.; Davis, J. C. X-Ray Interactions: Photoabsorption, Scattering, Transmission and Reflection  $E = 50\text{--}30,000$  EV,  $Z = 1\text{--}92$ . *At. Data Nucl. Data Tables* **1993**, *54* (2).
- (47) Gobert, S. R. L.; Kuhn, S.; Braeken, L.; Thomassen, L. C. J. Characterization of Milli- and Microflow Reactors: Mixing Efficiency and Residence Time Distribution. *Org. Process Res. Dev.* **2017**, *21* (4), 531–542. <https://doi.org/10.1021/acs.oprd.6b00359>.
- (48) H. S. Fogler, Elements of Chemical Reaction Engineering,... - Google Scholar [https://scholar.google.fr/scholar?hl=fr&as\\_sdt=0%2C5&q=H.+S.+Fogler%2C+Elements+of+Chemical+Reaction+Engineering%2C+Fourth+Edition%2C+2008%2C+Chapter+13%3A+Distributions+of+Residence+Times+for+Chemical+Reactors&btnG=](https://scholar.google.fr/scholar?hl=fr&as_sdt=0%2C5&q=H.+S.+Fogler%2C+Elements+of+Chemical+Reaction+Engineering%2C+Fourth+Edition%2C+2008%2C+Chapter+13%3A+Distributions+of+Residence+Times+for+Chemical+Reactors&btnG=) (accessed May 2, 2020).
- (49) Groppo, E.; Agostini, G.; Piovano, A.; Muddada, N. B.; Leofanti, G.; Pellegrini, R.; Portale, G.; Longo, A.; Lamberti, C. Effect of Reduction in Liquid Phase on the Properties and the Catalytic Activity of Pd/Al<sub>2</sub>O<sub>3</sub> Catalysts. *J. Catal.* **2012**, *287*, 44–54. <https://doi.org/10.1016/j.jcat.2011.11.018>.
- (50) Koos, P.; Gross, U.; Polyzos, A.; O'Brien, M.; Baxendale, I.; V. Ley, S. Teflon AF-2400 Mediated Gas–Liquid Contact in Continuous Flow Methoxycarbonylations and in-Line FTIR Measurement of CO Concentration. *Org. Biomol. Chem.* **2011**, *9* (20), 6903–6908. <https://doi.org/10.1039/C1OB06017A>.
- (51) Meemken, F.; Müller, P.; Hungerbühler, K.; Baiker, A. Simultaneous Probing of Bulk Liquid Phase and Catalytic Gas-Liquid-Solid Interface under Working Conditions Using Attenuated Total Reflection Infrared Spectroscopy. *Rev. Sci. Instrum.* **2014**, *85* (8), 084101. <https://doi.org/10.1063/1.4891188>.
- (52) M. Weckhuysen, B. Preface: Recent Advances in the in-Situ Characterization of Heterogeneous Catalysts. *Chem. Soc. Rev.* **2010**, *39* (12), 4557–4559. <https://doi.org/10.1039/C0CS90031A>.
- (53) Hughes, D. L. Applications of Flow Chemistry in Drug Development: Highlights of Recent Patent Literature. *Org. Process Res. Dev.* **2018**, *22* (1), 13–20. <https://doi.org/10.1021/acs.oprd.7b00363>.
- (54) Torborg, C.; Beller, M. Recent Applications of Palladium-Catalyzed Coupling Reactions in the Pharmaceutical, Agrochemical, and Fine Chemical Industries. *Adv. Synth. Catal.* **2009**, *351* (18), 3027–3043. <https://doi.org/10.1002/adsc.200900587>.
- (55) Augustine, R. L. *Heterogeneous Catalysis for the Synthetic Chemist*; CRC Press, 1995.
- (56) Joshi, S. S.; Ranade, V. V. *Industrial Catalytic Processes for Fine and Specialty Chemicals*; Elsevier, 2016.
- (57) Lopes, C. W.; Cerrillo, J. L.; Palomares, A. E.; Rey, F.; Agostini, G. An in Situ XAS Study of the Activation of Precursor-Dependent Pd Nanoparticles. *Phys. Chem. Chem. Phys.* **2018**, *20* (18), 12700–12709.
- (58) Groppi, G.; Cristiani, C.; Lietti, L.; Forzatti, P. Study of PdO/Pd Transformation over Alumina Supported Catalysts for Natural Gas Combustion. **2000**, *130*, 3081.
- (59) Caga, I. T.; Shutt, E.; Winterbottom, J. M. The Composition of Reduced Palladium Oxide and Its Behavior as a Catalyst for Liquid Phase Hydrogenation. *J. Catal.* **1976**, *44* (2), 271–280. [https://doi.org/10.1016/0021-9517\(76\)90397-3](https://doi.org/10.1016/0021-9517(76)90397-3).

- (60) Wimmers, O. J.; Arnoldy, P.; Moulijn, J. A. Determination of the Reduction Mechanism by Temperature-Programmed Reduction: Application to Small Iron Oxide (Fe<sub>2</sub>O<sub>3</sub>) Particles. *J. Phys. Chem.* **1986**, *90* (7), 1331–1337.
- (61) Hurst, N. W.; Gentry, S. J.; Jones, A.; McNicol, B. D. Temperature Programmed Reduction. *Catal. Rev.* **1982**, *24* (2), 233–309. <https://doi.org/10.1080/03602458208079654>.
- (62) Su, S. C.; Carstens, J. N.; Bell, A. T. A Study of the Dynamics of Pd Oxidation and PdO Reduction by H<sub>2</sub> and CH<sub>4</sub>. *J. Catal.* **1998**, *176* (1), 125–135. <https://doi.org/10.1006/jcat.1998.2028>.
- (63) Bugaev, A. L.; Guda, A. A.; Lazzarini, A.; Lomachenko, K. A.; Groppo, E.; Pellegrini, R.; Piovano, A.; Emerich, H.; Soldatov, A. V.; Bugaev, L. A.; Dmitriev, V. P.; van Bokhoven, J. A.; Lamberti, C. In Situ Formation of Hydrides and Carbides in Palladium Catalyst: When XANES Is Better than EXAFS and XRD. *Catal. Today* **2017**, *283*, 119–126. <https://doi.org/10.1016/j.cattod.2016.02.065>.
- (64) Clark, A. H.; Imbao, J.; Frahm, R.; Nachtegaal, M. ProQEXAFS: A Highly Optimized Parallelized Rapid Processing Software for QEXAFS Data. *J. Synchrotron Radiat.* **2020**, *27* (2). <https://doi.org/10.1107/S1600577519017053>.
- (65) Figueroa, S. J. A.; Prestipino, C. PrestoPronto: A Code Devoted to Handling Large Data Sets. In *Journal of Physics: Conference Series*; IOP Publishing, 2016; Vol. 712, p 012012.
- (66) Ravel, B.; Newville, M. ATHENA, ARTEMIS, HEPHAESTUS: Data Analysis for X-Ray Absorption Spectroscopy Using IFEFFIT. *J. Synchrotron Radiat.* **2005**, *12* (4), 537–541. <https://doi.org/10.1107/S0909049505012719>.
- (67) Newville, M.; Stensitzki, T.; Allen, D. B.; Ingargiola, A. *LMFIT: Non-Linear Least-Square Minimization and Curve-Fitting for Python*; Zenodo, 2014. <https://doi.org/10.5281/zenodo.11813>.
- (68) Bugaev, A. L.; Guda, A. A.; Lomachenko, K. A.; Lazzarini, A.; Srabionyan, V. V.; Vitillo, J. G.; Piovano, A.; Groppo, E.; Bugaev, L. A.; Soldatov, A. V.; Dmitriev, V. P.; Pellegrini, R.; van Bokhoven, J. A.; Lamberti, C. Hydride Phase Formation in Carbon Supported Palladium Hydride Nanoparticles by *in Situ* EXAFS and XRD. *J. Phys. Conf. Ser.* **2016**, *712*, 012032. <https://doi.org/10.1088/1742-6596/712/1/012032>.
- (69) Chase, Z. A.; Fulton, J. L.; Camaioni, D. M.; Mei, D.; Balasubramanian, M.; Pham, V.-T.; Zhao, C.; Weber, R. S.; Wang, Y.; Lercher, J. A. State of Supported Pd during Catalysis in Water. *J. Phys. Chem. C* **2013**, *117* (34), 17603–17612. <https://doi.org/10.1021/jp404772p>.
- (70) Fierro, J. L. G.; Peña, M. A.; González Tejuca, L. An XPS and Reduction Study of PrCoO<sub>3</sub>. *J. Mater. Sci.* **1988**, *23* (3), 1018–1023. <https://doi.org/10.1007/BF01154005>.
- (71) Chen, B.; Dingerdissen, U.; Krauter, J. G. E.; Lansink Rotgerink, H. G. J.; Möbus, K.; Ostgard, D. J.; Panster, P.; Riermeier, T. H.; Seebald, S.; Tacke, T.; Trauthwein, H. New Developments in Hydrogenation Catalysis Particularly in Synthesis of Fine and Intermediate Chemicals. *Appl. Catal. Gen.* **2005**, *280* (1), 17–46. <https://doi.org/10.1016/j.apcata.2004.08.025>.
- (72) Augustine, R. L. *Heterogeneous Catalysis for the Synthetic Chemist*; CRC Press, 1995.
- (73) Graham, T. On the Absorption and Dialytic Separation of Gases by Colloid Septa. *Philos Trans R Soc Lond.* **1866**, *156*.
- (74) Siebel, A.; Gorlin, Y.; Durst, J.; Proux, O.; Hasché, F.; Tromp, M.; Gasteiger, H. A. Identification of Catalyst Structure during the Hydrogen Oxidation Reaction in an Operating PEM Fuel Cell. *ACS Catal.* **2016**, *6* (11), 7326–7334. <https://doi.org/10.1021/acscatal.6b02157>.
- (75) Chase, Z. A.; Fulton, J. L.; Camaioni, D. M.; Mei, D.; Balasubramanian, M.; Pham, V.-T.; Zhao, C.; Weber, R. S.; Wang, Y.; Lercher, J. A. State of Supported Pd during Catalysis in Water. *J. Phys. Chem. C* **2013**, *117* (34), 17603–17612. <https://doi.org/10.1021/jp404772p>.

- (76) Flanagan, T. B.; Oates, W. A. The Palladium-Hydrogen System. *Annu. Rev. Mater. Sci.* **1991**, *21* (1), 269–304. <https://doi.org/10.1146/annurev.ms.21.080191.001413>.
- (77) Sakintuna, B.; Lamari-Darkrim, F.; Hirscher, M. Metal Hydride Materials for Solid Hydrogen Storage: A Review. *Int. J. Hydrog. Energy* **2007**, *32* (9), 1121–1140. <https://doi.org/10.1016/j.ijhydene.2006.11.022>.
- (78) Kishore, S.; Nelson, J. A.; Adair, J. H.; Eklund, P. C. Hydrogen Storage in Spherical and Platelet Palladium Nanoparticles. *J. Alloys Compd.* **2005**, *389* (1), 234–242. <https://doi.org/10.1016/j.jallcom.2004.06.105>.
- (79) Feenstra, R.; Griessen, R.; Groot, D. G. de. Hydrogen Induced Lattice Expansion and Effective H-H Interaction in Single Phase PdH c. *J. Phys. F Met. Phys.* **1986**, *16* (12), 1933. <https://doi.org/10.1088/0305-4608/16/12/008>.
- (80) Joshi, S. S.; Ranade, V. V. *Industrial Catalytic Processes for Fine and Specialty Chemicals*; Elsevier, 2016.
- (81) Selinsek, M.; Deschner, B. J.; Doronkin, D. E.; Sheppard, T. L.; Grunwaldt, J.-D.; Dittmeyer, R. Revealing the Structure and Mechanism of Palladium during Direct Synthesis of Hydrogen Peroxide in Continuous Flow Using Operando Spectroscopy <https://pubs.acs.org/doi/abs/10.1021/acscatal.7b03514> (accessed Sep 25, 2018). <https://doi.org/10.1021/acscatal.7b03514>.
- (82) Wang, J.; Wang, Q.; Jiang, X.; Liu, Z.; Yang, W.; Frenkel, A. I. Determination of Nanoparticle Size by Measuring the Metal–Metal Bond Length: The Case of Palladium Hydride. *J. Phys. Chem. C* **2015**, *119* (1), 854–861. <https://doi.org/10.1021/jp510730a>.
- (83) Bugaev, A. L.; Guda, A. A.; Lomachenko, K. A.; Lazzarini, A.; Srabionyan, V. V.; Vitillo, J. G.; Piovano, A.; Groppo, E.; Bugaev, L. A.; Soldatov, A. V.; Dmitriev, V. P.; Pellegrini, R.; Van, B.; Lamberti, C. Hydride Phase Formation in Carbon Supported Palladium Hydride Nanoparticles by in Situ EXAFS and XRD. *J. Phys. Conf. Ser.* **2016**, *712* (1). <https://doi.org/10.1088/1742-6596/712/1/012032>.
- (84) Dekura, S.; Kobayashi, H.; Ikeda, R.; Maesato, M.; Yoshino, H.; Ohba, M.; Ishimoto, T.; Kawaguchi, S.; Kubota, Y.; Yoshioka, S.; Matsumura, S.; Sugiyama, T.; Kitagawa, H. The Electronic State of Hydrogen in the  $\alpha$  Phase of the Hydrogen-Storage Material PdH(D)<sub>x</sub>: Does a Chemical Bond Between Palladium and Hydrogen Exist? *Angew. Chem. - Int. Ed.* **2018**, *57* (31), 9823–9827. <https://doi.org/10.1002/anie.201805753>.
- (85) Bugaev, A. L.; Srabionyan, V. V.; Soldatov, A. V.; Bugaev, L. A.; Bokhoven, J. A. van. The Role of Hydrogen in Formation of Pd XANES in Pd-Nanoparticles. *J. Phys. Conf. Ser.* **2013**, *430* (1), 012028. <https://doi.org/10.1088/1742-6596/430/1/012028>.
- (86) Bugaev, A. L.; Guda, A. A.; Lomachenko, K. A.; Srabionyan, V. V.; Bugaev, L. A.; Soldatov, A. V.; Lamberti, C.; Dmitriev, V. P.; van Bokhoven, J. A. Temperature- and Pressure-Dependent Hydrogen Concentration in Supported PdH<sub>x</sub> Nanoparticles by Pd K-Edge X-Ray Absorption Spectroscopy. *J. Phys. Chem. C* **2014**, *118* (19), 10416–10423. <https://doi.org/10.1021/jp500734p>.
- (87) Cassinelli, W. H.; Martins, L.; Passos, A. R.; Pulcinelli, S. H.; Santilli, C. V.; Rochet, A.; Briois, V. Multivariate Curve Resolution Analysis Applied to Time-Resolved Synchrotron X-Ray Absorption Spectroscopy Monitoring of the Activation of Copper Alumina Catalyst. *Catal. Today* **2014**, *229*, 114–122. <https://doi.org/10.1016/j.cattod.2013.10.077>.
- (88) Mariscal, R.; Maireles-Torres, P.; Ojeda, M.; Sádaba, I.; Granados, M. L. Furfural: A Renewable and Versatile Platform Molecule for the Synthesis of Chemicals and Fuels. *Energy Environ. Sci.* **2016**, *9* (4), 1144–1189. <https://doi.org/10.1039/C5EE02666K>.
- (89) Groppo, E.; Agostini, G.; Piovano, A.; Muddada, N. B.; Leofanti, G.; Pellegrini, R.; Portale, G.; Longo, A.; Lamberti, C. Effect of Reduction in Liquid Phase on the Properties and the Catalytic

- Activity of Pd/Al<sub>2</sub>O<sub>3</sub> Catalysts. *J. Catal.* **2012**, *287*, 44–54. <https://doi.org/10.1016/j.jcat.2011.11.018>.
- (90) Jaumot, J.; de Juan, A.; Tauler, R. MCR-ALS GUI 2.0: New Features and Applications. *Chemom. Intell. Lab. Syst.* **2015**, *140*, 1–12. <https://doi.org/10.1016/j.chemolab.2014.10.003>.
- (91) Ravel, B.; Newville, M. ATHENA, ARTEMIS, HEPHAESTUS: Data Analysis for X-Ray Absorption Spectroscopy Using IFEFFIT. *J. Synchrotron Radiat.* **2005**, *12* (4), 537–541. <https://doi.org/10.1107/S0909049505012719>.
- (92) Prestopronto by soonready <http://soonready.github.io/PrestoPronto/> (accessed Sep 25, 2018).
- (93) Griessen, R.; Strohfeldt, N.; Giessen, H. Thermodynamics of the Hybrid Interaction of Hydrogen with Palladium Nanoparticles. *Nat. Mater.* **2016**, *15* (3), 311–317. <https://doi.org/10.1038/nmat4480>.
- (94) Sá, J.; Arteaga, G. D.; Daley, R. A.; Bernardi, J.; Anderson, J. A. Factors Influencing Hydride Formation in a Pd/TiO<sub>2</sub> Catalyst. *J. Phys. Chem. B* **2006**, *110* (34), 17090–17095. <https://doi.org/10.1021/jp062205l>.
- (95) Paleček, D.; Tek, G.; Lan, J.; Iannuzzi, M.; Hamm, P. Characterization of the Platinum–Hydrogen Bond by Surface-Sensitive Time-Resolved Infrared Spectroscopy. *J. Phys. Chem. Lett.* **2018**, *9* (6), 1254–1259. <https://doi.org/10.1021/acs.jpcllett.8b00310>.
- (96) Bugaev, A. L.; Guda, A. A.; Lomachenko, K. A.; Srabionyan, V. V.; Bugaev, L. A.; Soldatov, A. V.; Lamberti, C.; Dmitriev, V. P.; van Bokhoven, J. A. Temperature- and Pressure-Dependent Hydrogen Concentration in Supported PdH<sub>x</sub> Nanoparticles by Pd K-Edge X-Ray Absorption Spectroscopy. *J. Phys. Chem. C* **2014**, *118* (19), 10416–10423. <https://doi.org/10.1021/jp500734p>.
- (97) Scholz, D.; Aellig, C.; Hermans, I. Catalytic Transfer Hydrogenation/Hydrogenolysis for Reductive Upgrading of Furfural and 5-(Hydroxymethyl)Furfural. *ChemSusChem* **2014**, *7* (1), 268–275. <https://doi.org/10.1002/cssc.201300774>.
- (98) Corma Canos, A.; Iborra, S.; Velty, A. Chemical Routes for the Transformation of Biomass into Chemicals. *Chem. Rev.* **2007**, *107* (6), 2411–2502. <https://doi.org/10.1021/cr050989d>.
- (99) Centi, G.; van Santen, R. A. *Catalysis for Renewables*; Centi, G., van Santen, R. A., Eds.; Wiley, 2007. <https://doi.org/10.1002/9783527621118>.
- (100) Gilkey, M. J.; Xu, B. Heterogeneous Catalytic Transfer Hydrogenation as an Effective Pathway in Biomass Upgrading. *ACS Catal.* **2016**, *6* (3), 1420–1436. <https://doi.org/10.1021/acscatal.5b02171>.
- (101) O'Driscoll; Leahy, J. J.; Curtin, T. The Influence of Metal Selection on Catalyst Activity for the Liquid Phase Hydrogenation of Furfural to Furfuryl Alcohol. *Catal. Today* **2017**, *279*, 194–201. <https://doi.org/10.1016/j.cattod.2016.06.013>.
- (102) Audemar, M.; Ciotonea, C.; De Oliveira Vigier, K.; Royer, S.; Ungureanu, A.; Dragoi, B.; Dumitriu, E.; Jérôme, F. Selective Hydrogenation of Furfural to Furfuryl Alcohol in the Presence of a Recyclable Cobalt/SBA-15 Catalyst. *ChemSusChem* **2015**, *8* (11), 1885–1891. <https://doi.org/10.1002/cssc.201403398>.
- (103) Liaw, B.-J.; Chiang, S.-J.; Tsai, C.-H.; Chen, Y.-Z. Preparation and Catalysis of Polymer-Stabilized NiB Catalysts on Hydrogenation of Carbonyl and Olefinic Groups. *Appl. Catal. Gen.* **2005**, *284* (1), 239–246. <https://doi.org/10.1016/j.apcata.2005.02.002>.
- (104) Gong, W.; Chen, C.; Fan, R.; Zhang, H.; Wang, G.; Zhao, H. Transfer-Hydrogenation of Furfural and Levulinic Acid over Supported Copper Catalyst. *Fuel* **2018**, *231* (March), 165–171. <https://doi.org/10.1016/j.fuel.2018.05.075>.



- (105) Taylor, M. J.; Durndell, L. J.; Isaacs, M. A.; Parlett, C. M. A.; Wilson, K.; Lee, A. F.; Kyriakou, G. Highly Selective Hydrogenation of Furfural over Supported Pt Nanoparticles under Mild Conditions. *Appl. Catal. B Environ.* **2016**, *180*, 580–585. <https://doi.org/10.1016/j.apcatb.2015.07.006>.
- (106) Palmer, R. E.; Jian, N.; Villa, A.; Dimitratos, N.; Catlow, C. R. A.; Chutia, A.; Wells, P. P.; Chan-Thaw, C. E.; Rogers, S. M.; Perdjon, M.; Thetford, A. Tandem Site- and Size-Controlled Pd Nanoparticles for the Directed Hydrogenation of Furfural. *ACS Catal.* **2017**, *7* (4), 2266–2274. <https://doi.org/10.1021/acscatal.6b03190>.
- (107) Ramirez-Barria, C.; Isaacs, M.; Wilson, K.; Guerrero-Ruiz, A.; Rodríguez-Ramos, I. Optimization of Ruthenium Based Catalysts for the Aqueous Phase Hydrogenation of Furfural to Furfuryl Alcohol. *Appl. Catal. Gen.* **2018**, *563* (April), 177–184. <https://doi.org/10.1016/j.apcata.2018.07.010>.
- (108) Su, J.; Yang, Y.; Xia, G.; Chen, J.; Jiang, P.; Chen, Q. For Producing Hydrogen in Alkaline Media. *Nat. Commun.* **2017**, *8*, 14969. <https://doi.org/10.1038/ncomms14969>.
- (109) Hoang, M.; Evangelisti, C.; Pertici, P.; Vitulli, G.; Maria Caporusso, A.; Marconi, G.; Turney, T. W.; Capannelli, G. Nanostructured Ruthenium on  $\gamma$ -Al<sub>2</sub>O<sub>3</sub> Catalysts for the Efficient Hydrogenation of Aromatic Compounds. *J. Organomet. Chem.* **2004**, *689* (3), 639–646. <https://doi.org/10.1016/j.jorganchem.2003.11.019>.
- (110) KELLNER, C. Effects of Dispersion on the Activity and Selectivity of Alumina-Supported Ruthenium Catalysts for Carbon Monoxide Hydrogenation. *J. Catal.* **2004**, *75* (2), 251–261. [https://doi.org/10.1016/0021-9517\(82\)90207-x](https://doi.org/10.1016/0021-9517(82)90207-x).
- (111) Kępiński, L.; Krajczyk, L.; Okal, J.; Zawadzki, M.; Tylus, W. The Use of Hydrogen Chemisorption for the Determination of Ru Dispersion in Ru/ $\gamma$ -Alumina Catalysts. *Appl. Catal. Gen.* **2006**, *319*, 202–209. <https://doi.org/10.1016/j.apcata.2006.12.005>.
- (112) Betancourt, P.; Rives, A.; Hubaut, R.; Scott, C. E.; Goldwasser, J. A Study of the Ruthenium-Alumina System. *Appl. Catal. Gen.* **1998**, *170* (2), 307–314. [https://doi.org/10.1016/S0926-860X\(98\)00061-1](https://doi.org/10.1016/S0926-860X(98)00061-1).
- (113) Oubenali, M.; Vanucci, G.; Machado, B.; Kacimi, M.; Ziyad, M.; Faria, J.; Raspolli-Galetti, A.; Serp, P. Hydrogenation of P-Chloronitrobenzene over Nanostructured-Carbon-Supported Ruthenium Catalysts. *ChemSusChem* **2011**, *4* (7), 950–956. <https://doi.org/10.1002/cssc.201000335>.
- (114) Panagiotopoulou, P.; Martin, N.; Vlachos, D. G. Liquid-Phase Catalytic Transfer Hydrogenation of Furfural over Homogeneous Lewis Acid-Ru/C Catalysts. *ChemSusChem* **2015**, *8* (12), 2046–2054. <https://doi.org/10.1002/cssc.201500212>.
- (115) Tukacs, J. M.; Bohus, M.; Dibó, G.; Mika, L. T. Ruthenium-Catalyzed Solvent-Free Conversion of Furfural to Furfuryl Alcohol. *RSC Adv.* **2017**, *7* (6), 3331–3335. <https://doi.org/10.1039/c6ra24723g>.
- (116) Xu, J.; Liu, F.; Wang, A.; Qiao, B.; Miao, S.; Su, Y.; Sun, H.; Li, L.; Zhang, T.; Cui, Y.-T.; Li, L.; Lang, R.; Jerome, F.; Liu, Q. Catalytic Cascade Conversion of Furfural to 1,4-Pentanediol in a Single Reactor. *Green Chem.* **2018**, *20* (8). <https://doi.org/10.1039/c8gc00039e>.
- (117) Jae, J.; Zheng, W.; Lobo, R. F.; Vlachos, D. G. Production of Dimethylfuran from Hydroxymethylfurfural through Catalytic Transfer Hydrogenation with Ruthenium Supported on Carbon. *ChemSusChem* **2013**, *6* (7), 1158–1162. <https://doi.org/10.1002/cssc.201300288>.
- (118) Michel, C.; Gallezot, P. Why Is Ruthenium an Efficient Catalyst for the Aqueous-Phase Hydrogenation of Biosourced Carbonyl Compounds? *ACS Catal.* **2015**, *5* (7), 4130–4132. <https://doi.org/10.1021/acscatal.5b00707>.

- (119) Wettstein, S. G.; Bond, J. Q.; Alonso, D. M.; Pham, H. N.; Datye, A. K.; Dumesic, J. A. RuSn Bimetallic Catalysts for Selective Hydrogenation of Levulinic Acid to  $\gamma$ -Valerolactone. *Appl. Catal. B Environ.* **2012**, *117–118*, 321–329. <https://doi.org/10.1016/j.apcatb.2012.01.033>.
- (120) Villa, A.; Chan-Thaw, C. E.; Campisi, S.; Bianchi, C. L.; Wang, D.; Kotula, P. G.; Kübel, C.; Prati, L. AuRu/AC as an Effective Catalyst for Hydrogenation Reactions. *Phys. Chem. Chem. Phys.* **2015**, *17* (42), 28171–28176. <https://doi.org/10.1039/c5cp00632e>.
- (121) Hutchings, G. J. Promotion in Heterogeneous Catalysis: A Topic Requiring a New Approach? *Catalysis Letters*. 2001, pp 1–12. <https://doi.org/10.1023/A:1016784122682>.
- (122) Yang, J.; Ma, J.; Yuan, Q.; Zhang, P.; Guan, Y. Selective Hydrogenation of Furfural on Ru/Al-MIL-53: A Comparative Study on the Effect of Aromatic and Aliphatic Organic Linkers. *RSC Adv.* **2016**, *6* (95), 92299–92304. <https://doi.org/10.1039/c6ra21701j>.
- (123) Jiménez-Gómez, C. P.; Cecilia, J. A.; Franco-Duro, F. I.; Pozo, M.; Moreno-Tost, R.; Maireles-Torres, P. Promotion Effect of Ce or Zn Oxides for Improving Furfuryl Alcohol Yield in the Furfural Hydrogenation Using Inexpensive Cu-Based Catalysts. *Mol. Catal.* **2018**, *455* (March), 121–131. <https://doi.org/10.1016/j.mcat.2018.06.001>.
- (124) Zhang, J.; Mu, X.; Zhang, B.; Fei, B.; Liu, X.; Chen, X. Tunable and Selective Hydrogenation of Furfural to Furfuryl Alcohol and Cyclopentanone over Pt Supported on Biomass-Derived Porous Heteroatom Doped Carbon. *Faraday Discuss.* **2017**, *202*, 79–98. <https://doi.org/10.1039/c7fd00041c>.
- (125) Gao, Z.; Yang, L.; Fan, G.; Li, F. Promotional Role of Surface Defects on Carbon-Supported Ruthenium-Based Catalysts in the Transfer Hydrogenation of Furfural. *ChemCatChem* **2016**, *8* (24), 3769–3779. <https://doi.org/10.1002/cctc.201601070>.
- (126) Xi, J.; Zhang, Y.; Xia, Q.; Liu, X.; Ren, J.; Lu, G.; Wang, Y. Direct Conversion of Cellulose into Sorbitol with High Yield by a Novel Mesoporous Niobium Phosphate Supported Ruthenium Bifunctional Catalyst. *Appl. Catal. Gen.* **2013**, *459*, 52–58. <https://doi.org/10.1016/j.apcata.2013.03.047>.
- (127) Lou, M.; Wang, R.; Zhang, J.; Tang, X.; Wang, L.; Guo, Y.; Jia, D.; Shi, H.; Yang, L.; Wang, X.; Sun, Z.; Wang, T. Optimized Synthesis of Nitrogen and Phosphorus Dual-Doped Coal- Based Carbon Fiber Supported Pd Catalyst with Enhanced Activities for Formic Acid Electrooxidation. *ACS Appl. Mater. Interfaces* **2019**, *11*, 6431–6441. <https://doi.org/10.1021/acsami.8b20736>.
- (128) Zhang, Z.; Sun, J.; Dou, M.; Ji, J.; Wang, F. Nitrogen and Phosphorus Codoped Mesoporous Carbon Derived from Polypyrrole as Superior Metal-Free Electrocatalyst toward the Oxygen Reduction Reaction. *ACS Appl. Mater. Interfaces* **2017**, *9* (19), 16236–16242. <https://doi.org/10.1021/acsami.7b03375>.
- (129) Heutz, F. J. L.; Erken, C.; Aguila, M. J. B.; Lefort, L.; Kamer, P. C. J. Heterogeneous Hydrogenation of Esters under Mild Conditions Using Solid-Supported Phosphorus–Ruthenium Catalysts. *ChemCatChem* **2016**, *8* (11), 1896–1900. <https://doi.org/10.1002/cctc.201600330>.
- (130) Campisi, S.; Bennici, S.; Auroux, A.; Carniti, P.; Gervasini, A. A Rational Revisiting of Niobium Oxophosphate Catalysts for Carbohydrate Biomass Reactions. *Top. Catal.* **2018**, *61* (18), 1939–1948. <https://doi.org/10.1007/s11244-018-0999-x>.
- (131) Liang, Q.; Shi, F.; Xiao, X.; Wu, X.; Huang, K.; Feng, S. In Situ Growth of CoP Nanoparticles Anchored on Black Phosphorus Nanosheets for Enhanced Photocatalytic Hydrogen Production. *ChemCatChem* **2018**, *10* (10), 2179–2183. <https://doi.org/10.1002/cctc.201701907>.
- (132) Martinelli, M.; Kumaran Gnanamani, M.; Hopps, S. D.; Sparks, D. E.; MacLennan, A.; Hu, Y.; Davis, B. H.; Jacobs, G. Effect of Phosphorus on the Activity and Stability of Supported Cobalt Catalysts for Fischer-Tropsch Synthesis. *ChemCatChem* **2018**, *10* (17), 3709–3716. <https://doi.org/10.1002/cctc.201800608>.

- (133) Radhakrishnan, R.; Do, D. M.; Jaenicke, S.; Sasson, Y.; Chuah, G. K. Potassium Phosphate as a Solid Base Catalyst for the Catalytic Transfer Hydrogenation of Aldehydes and Ketones. *ACS Catal.* **2011**, *1* (11), 1631–1636. <https://doi.org/10.1021/cs200299v>.
- (134) Machida, M. Rh Nanoparticle Anchoring on Metal Phosphates: Fundamental Aspects and Practical Impacts on Catalysis. *Chem. Rec.* **2016**, *16* (5), 2219–2231. <https://doi.org/10.1002/tcr.201600037>.
- (135) Chai, Y.-M.; Yan, K.; Liu, C.-G.; Lin, J.; Qin, J.; Liu, B.; Chi, J.; Dong, B.; Gao, W. Hydrogen Evolution Activity of Ruthenium Phosphides Encapsulated in Nitrogen- and Phosphorous-Codoped Hollow Carbon Nanospheres. *ChemSusChem* **2017**, *11* (4), 743–752. <https://doi.org/10.1002/cssc.201702010>.
- (136) Ding, Z. C.; Li, C. Y.; Chen, J. J.; Zeng, J. H.; Tang, H. T.; Ding, Y. J.; Zhan, Z. P. Palladium/Phosphorus-Doped Porous Organic Polymer as Recyclable Chemoselective and Efficient Hydrogenation Catalyst under Ambient Conditions. *Adv. Synth. Catal.* **2017**, *359* (13), 2280–2287. <https://doi.org/10.1002/adsc.201700374>.
- (137) Tuteja, J.; Choudhary, H.; Nishimura, S.; Ebitani, K. Direct Synthesis of 1,6-Hexanediol from HMF over a Heterogeneous Pd/ZrP Catalyst Using Formic Acid as Hydrogen Source. *ChemSusChem* **2014**, *7* (1), 96–100. <https://doi.org/10.1002/cssc.201300832>.
- (138) Ravel, B.; Newville, M. ATHENA, ARTEMIS, HEPHAESTUS: Data Analysis for X-Ray Absorption Spectroscopy Using IFEFFIT. *J. Synchrotron Radiat.* **2005**, *12* (4), 537–541. <https://doi.org/10.1107/S0909049505012719>.
- (139) Barzetti, T.; Selli, E.; Moscotti, D.; Forni, L. Pyridine and Ammonia as Probes for FTIR Analysis of Solid Acid Catalysts. *J. Chem. Soc. Faraday Trans.* **1996**, *92* (8), 1401–1407. <https://doi.org/10.1039/FT9969201401>.
- (140) Gould, N. S.; Xu, B. Catalyst Characterization in the Presence of Solvent: Development of Liquid Phase Structure-Activity Relationships. *Chem. Sci.* **2018**, *9* (2), 281–287. <https://doi.org/10.1039/c7sc03728g>.
- (141) Matam, S. K.; Otal, E. H.; Aguirre, M. H.; Winkler, A.; Ulrich, A.; Rentsch, D.; Weidenkaff, A.; Ferri, D. Thermal and Chemical Aging of Model Three-Way Catalyst Pd/Al<sub>2</sub>O<sub>3</sub> and Its Impact on the Conversion of CNG Vehicle Exhaust. *Catal. Today* **2012**, *184* (1), 237–244. <https://doi.org/10.1016/j.cattod.2011.09.030>.
- (142) Shin, E. W.; Han, J. S.; Jang, M.; Min, S. H.; Park, J. K.; Rowell, R. M. Phosphate Adsorption on Aluminum-Impregnated Mesoporous Silicates: Surface Structure and Behavior of Adsorbents. *Environ. Sci. Technol.* **2004**, *38* (3), 912–917. <https://doi.org/10.1021/es030488e>.
- (143) Nguyen, H.; Xiao, N.; Daniels, S.; Marcella, N.; Timoshenko, J.; Frenkel, A.; Vlachos, D. G. Role of Lewis and Brønsted Acidity in Metal Chloride Catalysis in Organic Media: Reductive Etherification of Furanics. *ACS Catal.* **2017**, *7* (10), 7363–7370. <https://doi.org/10.1021/acscatal.7b02348>.
- (144) Mironenko, A. V.; Vlachos, D. G. Conjugation-Driven “Reverse Mars-van Krevelen”-Type Radical Mechanism for Low-Temperature C–O Bond Activation. *J. Am. Chem. Soc.* **2016**, *138* (26), 8104–8113. <https://doi.org/10.1021/jacs.6b02871>.
- (145) Gilkey, M. J.; Panagiotopoulou, P.; Mironenko, A. V.; Jenness, G. R.; Vlachos, D. G.; Xu, B. Mechanistic Insights into Metal Lewis Acid-Mediated Catalytic Transfer Hydrogenation of Furfural to 2-Methylfuran. *ACS Catal.* **2015**, *5* (7), 3988–3994. <https://doi.org/10.1021/acscatal.5b00586>.
- (146) Beale, A. M.; Weckhuysen, B. M. EXAFS as a Tool to Interrogate the Size and Shape of Mono and Bimetallic Catalyst Nanoparticles. *Phys. Chem. Chem. Phys.* **2010**, *12* (21), 5562. <https://doi.org/10.1039/b925206a>.

- (147) Davis, M. E. Zeolite-Based Catalysts for Chemicals Synthesis. *Microporous Mesoporous Mater.* **1998**, *21* (4–6), 173–182. [https://doi.org/10.1016/S1387-1811\(98\)00007-9](https://doi.org/10.1016/S1387-1811(98)00007-9).
- (148) Weckhuysen, B. M.; Yu, J. Recent Advances in Zeolite Chemistry and Catalysis. *Chem. Soc. Rev.* **2015**, *44* (20), 7022–7024. <https://doi.org/10.1039/c5cs90100f>.
- (149) Zhi, Y.; Shi, H.; Mu, L.; Liu, Y.; Mei, D.; Camaioni, D. M.; Lercher, J. A. Dehydration Pathways of 1-Propanol on HZSM-5 in the Presence and Absence of Water. *J. Am. Chem. Soc.* **2015**, *137* (50), 15781–15794. <https://doi.org/10.1021/jacs.5b09107>.
- (150) Corma, A.; Marie, O.; Ortega, F. J. Interaction of Water with the Surface of a Zeolite Catalyst during Catalytic Cracking: A Spectroscopy and Kinetic Study. *J. Catal.* **2004**, *222* (2), 338–347. <https://doi.org/10.1016/j.jcat.2003.11.006>.
- (151) Chen, K.; Damron, J.; Pearson, C.; Resasco, D.; Zhang, L.; White, J. L. Zeolite Catalysis: Water Can Dramatically Increase or Suppress Alkane C-H Bond Activation. *ACS Catal.* **2014**, *4* (9), 3039–3044. <https://doi.org/10.1021/cs500858d>.
- (152) Vjunov, A.; Wang, M.; Govind, N.; Huthwelker, T.; Shi, H.; Mei, D.; Fulton, J. L.; Lercher, J. A. Tracking the Chemical Transformations at the Brønsted Acid Site upon Water-Induced Deprotonation in a Zeolite Pore. *Chem. Mater.* **2017**, *29* (21), 9030–9042. <https://doi.org/10.1021/acs.chemmater.7b02133>.
- (153) Wang, M.; Jaegers, N. R.; Lee, M.-S.; Wan, C.; Hu, J. Z.; Shi, H.; Mei, D.; Burton, S. D.; Camaioni, D. M.; Gutiérrez, O. Y.; Glezakou, V.-A.; Rousseau, R.; Wang, Y.; Lercher, J. A. Genesis and Stability of Hydronium Ions in Zeolite Channels. *J. Am. Chem. Soc.* **2019**, *141* (8), 3444–3455. <https://doi.org/10.1021/jacs.8b07969>.
- (154) Eckstein, S.; Hintermeier, P. H.; Zhao, R.; Baráth, E.; Shi, H.; Liu, Y.; Lercher, J. A. Influence of Hydronium Ions in Zeolites on Sorption. *Angew. Chem. Int. Ed.* **2019**, *58* (11), 3450–3455. <https://doi.org/10.1002/anie.201812184>.
- (155) Liu, Y.; Vjunov, A.; Shi, H.; Eckstein, S.; Camaioni, D. M.; Mei, D.; Baráth, E.; Lercher, J. A. Enhancing the Catalytic Activity of Hydronium Ions through Constrained Environments. *Nat. Commun.* **2017**, *8* (1), 14113. <https://doi.org/10.1038/ncomms14113>.
- (156) Liu, Y.; Baráth, E.; Shi, H.; Hu, J.; Camaioni, D. M.; Lercher, J. A. Solvent-Determined Mechanistic Pathways in Zeolite-H-BEA-Catalysed Phenol Alkylation. *Nat. Catal.* **2018**, *1* (2), 141–147. <https://doi.org/10.1038/s41929-017-0015-z>.
- (157) Burger, J.; Siegert, M.; Ströfer, E.; Hasse, H. Poly(Oxymethylene) Dimethyl Ethers as Components of Tailored Diesel Fuel: Properties, Synthesis and Purification Concepts. *Fuel* **2010**, *89* (11), 3315–3319. <https://doi.org/10.1016/j.fuel.2010.05.014>.
- (158) Lautenschütz, L.; Oestreich, D.; Seidenspinner, P.; Arnold, U.; Dinjus, E.; Sauer, J. Physico-Chemical Properties and Fuel Characteristics of Oxymethylene Dialkyl Ethers. *Fuel* **2016**, *173*, 129–137. <https://doi.org/10.1016/j.fuel.2016.01.060>.
- (159) Liu, H.; Wang, Z.; Wang, J.; He, X.; Zheng, Y.; Tang, Q.; Wang, J. Performance, Combustion and Emission Characteristics of a Diesel Engine Fueled with Polyoxymethylene Dimethyl Ethers (PODE3-4)/ Diesel Blends. *Energy* **2015**, *88*, 793–800. <https://doi.org/10.1016/j.energy.2015.05.088>.
- (160) Iannuzzi, S. E.; Barro, C.; Boulouchos, K.; Burger, J. Combustion Behavior and Soot Formation/Oxidation of Oxygenated Fuels in a Cylindrical Constant Volume Chamber. *Fuel* **2016**, *167*, 49–59. <https://doi.org/10.1016/j.fuel.2015.11.060>.
- (161) Zhang, X.; Oyedun, A. O.; Kumar, A.; Oestreich, D.; Arnold, U.; Sauer, J. An Optimized Process Design for Oxymethylene Ether Production from Woody-Biomass-Derived Syngas. *Biomass Bioenergy* **2016**, *90* (x), 7–14. <https://doi.org/10.1016/j.biombioe.2016.03.032>.

- (162) Hackbarth, K.; Haltenort, P.; Arnold, U. Recent Progress in the Production , Application and Evaluation of Oxymethylene Ethers. *Chem Ing Tech* **2018**, 90 (10), 1520–1528. <https://doi.org/10.1002/cite.201800068>.
- (163) Zheng, Y.; Tang, Q.; Wang, T.; Wang, J. Kinetics of Synthesis of Polyoxymethylene Dimethyl Ethers from Paraformaldehyde and Dimethoxymethane Catalyzed by Ion-Exchange Resin. *Chem. Eng. Sci.* **2015**, 134, 758–766. <https://doi.org/10.1016/j.ces.2015.05.067>.
- (164) Zhang, J.; Fang, D.; Liu, D. Evaluation of Zr–Alumina in Production of Polyoxymethylene Dimethyl Ethers from Methanol and Formaldehyde: Performance Tests and Kinetic Investigations. *Ind. Eng. Chem. Res.* **2014**, 53 (35), 13589–13597. <https://doi.org/10.1021/ie501231a>.
- (165) Burger, J.; Ströfer, E.; Hasse, H. Chemical Equilibrium and Reaction Kinetics of the Heterogeneously Catalyzed Formation of Poly(Oxymethylene) Dimethyl Ethers from Methylal and Trioxane. *Ind. Eng. Chem. Res.* **2012**, 51 (39), 12751–12761. <https://doi.org/10.1021/ie301490q>.
- (166) Ye, Y.; Yao, M.; Chen, H.; Zhang, X. Influence of Silanol Defects of ZSM-5 Zeolites on Trioxane Synthesis from Formaldehyde. *Catal. Lett.* **2019**, 150 (5), 1445–1453. <https://doi.org/10.1007/s10562-019-03040-x>.
- (167) Goncalves, T. J.; Arnold, U.; Plessow, P. N.; Studt, F. Theoretical Investigation of the Acid Catalyzed Formation of Oxymethylene Dimethyl Ethers from Trioxane and Dimethoxymethane. *ACS Catal.* **2017**, 7 (5), 3615–3621. <https://doi.org/10.1021/acscatal.7b00701>.
- (168) Lautenschütz, L.; Oestreich, D.; Haltenort, P.; Arnold, U.; Dinjus, E.; Sauer, J. Efficient Synthesis of Oxymethylene Dimethyl Ethers ( OME ) from Dimethoxymethane and Trioxane over Zeolites. *Fuel Process. Technol.* **2017**, 165, 27–33. <https://doi.org/10.1016/j.fuproc.2017.05.005>.
- (169) Müller, P.; Wolf, P.; Hermans, I. Insights into the Complexity of Heterogeneous Liquid-Phase Catalysis: Case Study on the Cyclization of Citronellal. *ACS Catal.* **2016**, 6 (5), 2760–2769. <https://doi.org/10.1021/acscatal.5b02493>.
- (170) Wirz, R.; Ferri, D.; Baiker, A. ATR-IR Spectroscopy of Pendant NH<sub>2</sub> Groups on Silica Involved in the Knoevenagel Condensation. *Langmuir* **2006**, 22 (8), 3698–3706. <https://doi.org/10.1021/la053145y>.
- (171) Ferri, D.; Bürgi, T.; Baiker, A. Probing Catalytic Solid-Liquid Interfaces by Attenuated Total Reflection Infrared Spectroscopy: Adsorption of Carboxylic Acids on Alumina and Titania. *Helv. Chim. Acta* **2002**, 85 (11), 3639–3656. [https://doi.org/10.1002/1522-2675\(200211\)85:11<3639::AID-HLCA3639>3.0.CO;2-2](https://doi.org/10.1002/1522-2675(200211)85:11<3639::AID-HLCA3639>3.0.CO;2-2).
- (172) Urakawa, A.; Bürgi, T.; Baiker, A. Sensitivity Enhancement and Dynamic Behavior Analysis by Modulation Excitation Spectroscopy: Principle and Application in Heterogeneous Catalysis. *Chem. Eng. Sci.* **2008**, 63 (20), 4902–4909. <https://doi.org/10.1016/j.ces.2007.06.009>.
- (173) Baurecht, D.; Fringeli, U. P. Quantitative Modulated Excitation Fourier Transform Infrared Spectroscopy. *Rev. Sci. Instrum.* **2001**, 72 (10), 3782–3792. <https://doi.org/10.1063/1.1400152>.
- (174) Frisch, M. J.; Trucks, G. W.; Schlegel, H. B.; Scuseria, G. E.; Robb, M. A.; Cheeseman, J. R.; Scalmani, G.; Barone, V.; Petersson, G. A.; Nakatsuji, H.; Li, X.; Caricato, M.; Marenich, A. V.; Bloino, J.; Janesko, B. G.; Gomperts, R.; Mennucci, B.; Hratchian, H. P.; Ortiz, J. V.; Izmaylov, A. F.; Sonnenberg, J. L.; Williams-Young, D.; Ding, F.; Lipparini, F.; Egidi, F.; Goings, J.; Peng, B.; Petrone, A.; Henderson, T.; Ranasinghe, D.; Zakrzewski, V. G.; Gao, J.; Rega, N.; Zheng, G.; Liang, W.; Hada, M.; Ehara, M.; Toyota, K.; Fukuda, R.; Hasegawa, J.; Ishida, M.; Nakajima, T.; Honda, Y.; Kitao, O.; Nakai, H.; Vreven, T.; Throssell, K.; Montgomery, J. A., Jr.; Peralta, J. E.; Ogliaro, F.; Bearpark, M. J.; Heyd, J. J.; Brothers, E. N.; Kudin, K. N.; Staroverov, V. N.; Keith, T. A.; Kobayashi, R.; Normand, J.; Raghavachari, K.; Rendell, A. P.; Burant, J. C.; Iyengar, S. S.; Tomasi, J.; Cossi, M.; Millam, J. M.; Klene, M.; Adamo, C.; Cammi, R.; Ochterski, J. W.; Martin, R. L.; Morokuma, K.; Farkas, O.; Foresman, J. B.; Fox, D. J.; Gaussian 16, R. C. 01; Gaussian, Inc., W. C. Gaussian 16, Revision C.01. Gaussian, Inc., Wallingford CT 2016.

- (175) Becke, A. D. A New Mixing of Hartree–Fock and Local Density-functional Theories. *J. Chem. Phys.* **1993**, 98 (2), 1372–1377. <https://doi.org/10.1063/1.464304>.
- (176) Lee, C.; Yang, W.; Parr, R. G. Development of the Colle-Salvetti Correlation-Energy Formula into a Functional of the Electron Density. *Phys. Rev. B* **1988**, 37 (2), 785–789. <https://doi.org/10.1103/PhysRevB.37.785>.
- (177) Grimme, S.; Antony, J.; Ehrlich, S.; Krieg, H. A Consistent and Accurate Ab Initio Parametrization of Density Functional Dispersion Correction (DFT-D) for the 94 Elements H–Pu. *J. Chem. Phys.* **2010**, 132 (15), 154104. <https://doi.org/10.1063/1.3382344>.
- (178) Tomasi, J.; Mennucci, B.; Cammi, R. Quantum Mechanical Continuum Solvation Models. *Chem. Rev.* **2005**, 105 (8), 2999–3094. <https://doi.org/10.1021/cr9904009>.
- (179) Ditchfield, R.; Hehre, W. J.; Pople, J. A. Self-Consistent Molecular-Orbital Methods. IX. An Extended Gaussian-Type Basis for Molecular-Orbital Studies of Organic Molecules. *J. Chem. Phys.* **1971**, 54 (2), 724–728. <https://doi.org/10.1063/1.1674902>.
- (180) Barzetti, T.; Selli, E.; Moschetti, D.; Forni, L. Pyridine and Ammonia as Probes for FTIR Analysis of Solid Acid Catalysts. *J. Chem. Soc. Faraday Trans.* **1996**, 92 (8), 1401. <https://doi.org/10.1039/ft9969201401>.
- (181) Bordiga, S.; Lamberti, C.; Bonino, F.; Travert, A.; Thibault-Starzyk, F. Probing Zeolites by Vibrational Spectroscopies. *Chem. Soc. Rev.* **2015**, 44 (20), 7262–7341. <https://doi.org/10.1039/c5cs00396b>.
- (182) Campisi, S.; Ferri, D.; Villa, A.; Wang, W.; Wang, D.; Kröcher, O.; Prati, L. Selectivity Control in Palladium-Catalyzed Alcohol Oxidation through Selective Blocking of Active Sites. *J. Phys. Chem. C* **2016**, 120 (26), 14027–14033. <https://doi.org/10.1021/acs.jpcc.6b01549>.
- (183) Wilmshurst, J. K. The Infrared and Raman Spectrum of Dimethoxymethane. *Can. J. Chem.* **1958**, 36 (1), 285–289. <https://doi.org/10.1139/v58-040>.
- (184) Kobayashi, M.; Iwamoto, R.; Tadokoro, H. Vibrational Spectra of Trioxane and Trioxane- d 6. *J. Chem. Phys.* **1966**, 44 (3), 922–933. <https://doi.org/10.1063/1.1726843>.
- (185) Bordiga, S.; Ugliengo, P.; Damin, A.; Lamberti, C.; Spoto, G.; Zecchina, A.; Spanò, G.; Buzzoni, R.; Dalloro, L.; Rivetti, F. Hydroxyls Nests in Defective Silicalites and Strained Structures Derived upon Dehydroxylation: Vibrational Properties and Theoretical Modelling. *Top. Catal.* **2001**, 15 (1), 43–52. <https://doi.org/10.1023/A:1009019829376>.
- (186) Molnár, E.; Tasi, G.; Kónya, Z.; Kiricsi, I. Infrared Spectroscopy Studies of Cyclohexene Hydrogenation and Dehydrogenation Catalyzed by Platinum Nanoparticles Supported on Mesoporous Silicate (SBA-15). Part 1: The Role of Particle Size of Pt Nanocrystals Supported on SBA-15 Silicate. *Catal. Lett.* **2005**, 101 (3–4), 159–167. <https://doi.org/10.1007/s10562-005-4883-5>.

# Scientific contributions

## Peer-reviewed publications

T. Fovanna, B. Horváth, H. Schiff, D. Ferri, Novel preparation of nanoparticles for molecules adsorption on Pd nanoparticles ATR-IR applications. *Manuscript in preparation*

T. Fovanna, A. H. Clark, M. Nachtegaal, O. Kröcher, D. Ferri, Quantification of Pd hydrides on Pd/Al<sub>2</sub>O<sub>3</sub> in liquid environment. *Manuscript in preparation*

T. Fovanna, G. Garin, I. Alxneit, A. H. Clark, S. Checchia, M. Di Michiel, O. Kröcher, M. Nachtegaal, D. Ferri, Combined in situ XAS and XRD studies of solvent mediated reduction of PdO nanoparticles by hydrogen. *Manuscript in preparation*

C. Baranowski, T. Fovanna, R. Maneka, M. Signorile, J. McCaig, A. Bahmanpour, D. Ferri, O. Kröcher, Water inhibition of oxymethylene dimethyl ether synthesis over zeolite H-Beta: A combined kinetic and in situ ATR-IR study, *ACS Catal.*, **2020**, *10*, 8106.

T. Fovanna, S. Campisi, A. Villa, A. Kambolis, G. Peng, D. Rentsch, O. Kröcher, M. Nachtegaal, D. Ferri, Ruthenium on phosphorous-modified alumina as effective and stable catalyst for catalytic transfer hydrogenation of furfural, *RSC Adv.*, **2020**, *10*, 11507

## Talks

Quantification of supported palladium hydride in liquid phase, NAM 26, Chicago (USA), 23.06.2019

Combined XAS and ATR-IR study of liquid phase selective hydrogenation, Operando VI, Malaga (Spain), 19.04.2018

## Posters

Combined XAS and ATR-IR study of liquid phase selective hydrogenation, ENE-NES seminar, PSI Villigen (Switzerland), 11.12.2019

Combined XAS and ATR-IR study of liquid phase selective hydrogenation, Condensed matter retreat, Brugg (Switzerland), 28-29.10.2019

Combined XAS and ATR-IR study of liquid phase selective hydrogenation, PSI Catalysis seminar, PSI Villigen (Switzerland), 17.01.2019

## References

Combined XAS and ATR-IR study of liquid phase selective hydrogenation, SCS Fall Meeting 2018, Lausanne (Switzerland), 09.09.2018

Cell design for combined XAS and ATR-IR, ENE-NES seminar, PSI Villigen (Switzerland), 27.04.2018

Furfural hydrogenation on P-promoted Ru/Al<sub>2</sub>O<sub>3</sub>, SCS Fall Meeting 2017, Bern (Switzerland), 21.08.2017

Furfural hydrogenation on P-promoted Ru/Al<sub>2</sub>O<sub>3</sub>, Summer School: Catalysis: fundamentals and practice, Liverpool (UK), 17.07.2017



# Curriculum Vitae

**Name** Thibault Xavier Florian Fovanna

**Date of birth** 18.12.1990

**Place of birth** Geneva, Switzerland

**Nationality** Swiss, French and Italian

## EDUCATION

02.2017 - current **PhD in chemistry:** “Liquid phase *in situ* spectroscopic investigations of heterogeneous catalysts” at EPFL and Paul Scherrer Institut

09.2014 - 07.2016 **Master of science in molecular and biological chemistry** combined with a **minor in management of technology** - EPFL  
Master thesis: “Scale-up studies of liquid-liquid extraction” at Novartis SA

09.2011 - 06.2014 **Bachelor of science in Chemistry** - EPFL  
*3<sup>rd</sup> year in exchange at **Imperial College London** as Erasmus student*

09.2010 - 06.2011 **Preparatory year** to enter EPFL (Cour de mathématiques spéciales - **CMS**)

08.2007 - 07.2010 **Apprenticeship as lab technician in chemistry** combined with professional technical maturity